UNIVERSITY OF SOUTHAMPTON

# Direct velocity feedback control of equipment vibration

by Marc Serrand

A thesis submitted for the degree of
*Master of Philosophy*

Signal Processing and Control Group
Institute of Sound and Vibration Research
Faculty of Engineering and Applied Science

April 2000

UNIVERSITY OF SOUTHAMPTON

# ABSTRACT

Faculty of Engineering and Applied Science

Institute of Sound and Vibration Research

Master of Philosophy

## Direct velocity feedback control of equipment vibration

by Marc Serrand

This study investigates the performance of the active strategy of Direct Velocity Feedback control (DVFB) in reducing vibration transmission from a flexible vibrating base to a mounted equipment structure. The first objective of coupling an active controller to existing passive mounts is to attenuate the low frequency amplification effect generated by the passive isolation system. Passive damping can be added in the mounts to limit this adverse effect but this decreases the high frequency performance provided by the passive isolation. In a previous study, a large vibration reduction was achieved using DVFB control on a rigid piece of equipment, whose rigid body modes were shown to be strongly reduced despite the flexibility of the base and without any effect on the high frequency isolation. The main advantage of absolute velocity feedback control is the extreme simplicity of the technique, which provides a decentralised control with a minimum of signal processing. Motivated by the good results obtained for the isolation of rigid equipment structures, this study extends the control strategy to the isolation of large flexible structures coupled to a flexible vibrating base structure by a set of passive isolators. Both the equipment and base structure flexibility has to be accounted for as well as the multi-transmission paths created by the use of several passive mounts. The final objective is not only to estimate the local reduction of the control at the mount junctions on the equipment structure but to assess the global effect of the control on the equipment structure dynamics

A simple rigid equipment mounted on a single mount is first considered to assess two practical methods of implementing the control, using either reactive or inertial actuation. An inertial actuator is shown to have stability limits at low frequencies, which are inherent to the actuator dynamics, whereas a reactive control force can provide an unconditionally stable plant to control. Inertial and reactive DVFB controls are then implemented on a mounted flexible composite panel at the mount junctions. Both single and multichannel controllers are considered in simulations and experiments. Both inertial and reactive controls exhibit low frequency instability that limits the maximum feedback gain. Because of the actuator dynamics, an inertial implementation appears to be more gain-limited than a reactive implementation, which provides strong local isolation above 100 Hz as each control channel then generates a skyhook damping effect. A large attenuation is thus obtained in the frequency range of passive isolation amplification for a reactive control, which is not destabilised by the longitudinal resonances occurring in the mounts. The experimental implementation of the reactive control also encounters stability problems at high frequencies which appear to be due to the actuator dynamics. The isolation effect of DVFB control is rather local but an implementation of three control channels, one at each mount junctions, provides global control over the equipment.

# Table of contents

## Chapter 2: Theory of Direct Velocity Feedback Control and the Skyhook Damping effect

## Chapter 3: Reactive actuation and Inertial actuation

## Chapter 4: Inertial implementation of DVFB control on a mounted flexible equipment

## Chapter 5: Reactive implementation of DVFB control on a mounted flexible equipment: Simulations

# Chapter 6: Reactive implementation of DVFB control on a mounted flexible equipment: Experiments

# Chapter 7: Conclusions

# List of figures

## Chapter 1

## Chapter 2

## Chapter 3

## Chapter 4

## Chapter 5

## Chapter 6

# List of tables

## Chapter 3

## Chapter 4

## Chapter 5

## Chapter 6

# List of symbols

| | |
|---|---|
| $a_m$ | Radius of one mount cross section |
| $A_m$ | Mount cross sectional area |
| $Att_{ij}$ | Percentage of vibration kinetic energy attenuation in the band [100 Hz - 1 kHz] at point $j$ for a control at point $i$ |
| $B$ | Bending stiffness of one mount |
| $c$ | Viscous damping constant of one massless mount |
| $c_a$ | Damping constant of the inertial actuator suspension |
| $c_{bm}$ | Modal damping of the $m^{\text{th}}$ mode of the base structure |
| $c_{crit}$ | Critical viscous damping |
| $c_{en}$ | Modal damping of the $n^{\text{th}}$ mode of the equipment structure |
| $c_{fm}$ | Phase velocity of flexural waves |
| $C_i$ | $i^{\text{th}}$ capacitor of the controller box circuit |
| $c_{lm}$ | Phase velocity of longitudinal waves |
| $c_t$ | Phase velocity of transversal waves |
| $d$ | Primary disturbance at the control sensor output |
| $\mathbf{d}$ | Primary disturbance vector at the control sensor outputs |
| $D$ | Bending stiffness of an isotropic plate |
| $D_j$ | Primary velocity disturbance at sensor output $j$ in the Laplace domain |
| $e$ | Error signal or response of the system under control at the control sensor output |
| $\mathbf{e}$ | Control system response vector at the control sensor outputs |
| $E_c$ | Young's modulus of the composite panel |
| $E_i$ | Estimate of the vibration kinetic energy over the mounted composite panel |
| $E_{ij}$ | Velocity response at point $j$ for a single-channel control at point $i$ in the Laplace domain |
| $E_k$ | Vibration kinetic energy of a controlled structure |
| $E_m$ | Young's modulus of elasticity of one rubber mount |
| $f_0$ | Primary excitation force |

| | |
|---|---|
| $f_a$ | Force generated by one secondary actuator |
| $f_b$ | Total force applied on the base structure |
| $\mathbf{f}_{be}$ | Global force vector at the mount junctions for the base and equipment structures |
| $\mathbf{f}_{b,e}$ | Global base force vector and global equipment force vector at the mount junctions |
| $\mathbf{f}_{bj,ej}$ | Base force vector and equipment force vector at mount junction $j$ |
| $f_e$ | Force applied by one inertial actuator on a rigid frame or total force applied on the equipment structure |
| $\mathbf{f}_j$ | Dynamic vector at mount junction $j$ |
| $\mathbf{f}_m$ | Global mount force vector |
| $\mathbf{f}_{m1j,m2j}$ | Mount force vector on the base and on the equipment at junction $j$ |
| $f_{mount}$ | Reactive force generated by one massless passive mount |
| $f_{nl}$ | Frequency of the $n^{th}$ longitudinal resonance in one rubber mount |
| $f_s$ | Control secondary force |
| $\mathbf{f}_s$ | Secondary force vector |
| $F_{/m}$ | Total force applied on the mounted equipment mass |
| $G$ | Plant response for single-channel control |
| $\mathbf{G}$ | Matrix of the plant response for multichannel control |
| $G_a$ | Plant response for direct acceleration feedback control |
| $G_d$ | Plant response for direct displacement feedback control |
| $G_{ii}$ | Plant response for a single-channel control at point $i$ |
| $G_{ji}$ | Transfer function between actuator input voltage at $i$ and control sensor output voltage at $j$ |
| $G_v$ | Plant response for direct velocity feedback control |
| $GM$ | Gain margin |
| $h$ | Feedback gain |
| $H$ | Response of a single-channel feedback controller |
| $\mathbf{H}$ | Matrix of a multichannel feedback controller |
| $h'$ | Thickness of an isotropic plate |
| $h_a$ | Feedback gain for direct acceleration feedback control |
| $h_d$ | Feedback gain for direct displacement feedback control |

| | |
|---|---|
| $h_m$ | Height of one rubber mount |
| $h_{max}$ | Maximum feedback gain |
| $h_v$ | Feedback gain for direct velocity feedback control |
| $\mathbf{I}$ | Identity matrix |
| $i_{in}$ | Input current in the inertial secondary actuator |
| $I_{m,xx,yy}$ | Area moment of inertia of one circular mount |
| $I_{xxact,yyact}$ | Moment of inertia of a reactive secondary actuator referring to the $x$ or $y$-axis |
| $j$ | Imaginary coefficient |
| $k$ | Axial static stiffness of one massless mount |
| $K$ | Experimental control gain provided by the controller box |
| $\mathbf{K}$ | Control gain matrix |
| $k_a$ | Axial stiffness of the inertial actuator suspension |
| $k_{bm}$ | Modal stiffness of the $m^{th}$ mode of the base structure |
| $k_e$ | Modal stiffness of the first resonance of the mounted equipment structure |
| $k_{en}$ | Modal stiffness of the $n^{th}$ mode of the equipment structure |
| $k_{fm}$ | Flexural wave number |
| $k_{lm}$ | Longitudinal wave number |
| $k_t$ | Transverse wave number |
| $L_e$ | Internal electrical inductance of one reactive secondary actuator |
| $l_{x,y,z}$ | Dimensions of the thick aluminium plate of the active isolator system in the $x$, $y$ and $z$-axis |
| $m$ | Mounted mass or modal order associated with the number of nodal lines in the $x$-direction |
| $m'$ | Density per unit cross section area of one rubber mount |
| $m_a$ | Inertial mass |
| $m_{act}$ | Mass of one reactive actuator |
| $M_b$ | Input mobility of the unconnected base structure at the mount junction |
| $\mathbf{M}_{b1}$ | Matrix of mobilities between the different mount junction locations on the base structure |
| $\mathbf{M}_{b2}$ | Matrix of mobilities between the excitation points and the response at the mount junction locations on the base structure |
| $M_{be}$ | Transfer mobility from force excitation on base structure to equipment velocity |

| | |
|---|---|
| $\mathbf{M}_{be1}$ | Global matrix of mobilities between the different mount junction locations on the uncoupled base and equipment structures |
| $\mathbf{M}_{be2}$ | Global matrix of mobilities between the primary excitation locations on the base structure and the response at the mount junction locations on the uncoupled base and equipment structures. |
| $m_{bm}$ | Modal mass of the $m^{\text{th}}$ mode of the base structure |
| $M_{cc}$ | Input mobility at the top of the equipment for fully-coupled inertial isolation system |
| $m_e$ | Modal mass of the first resonance of the mounted equipment structure |
| $M_e$ | Input mobility of the unconnected equipment structure at the mount junction |
| $\mathbf{M}_{e1}$ | Matrix of mobility between the different mount junction locations on the equipment structure |
| $M_{ee}$ | Input mobility of the equipment mounted on the base structure |
| $m_{en}$ | Modal mass of the $n^{\text{th}}$ mode of the equipment structure |
| $\mathbf{M}_r$ | Matrix of mobilities between excitation at the mount junctions and response at points of interest on the equipment structure |
| $M_{total}$ | Total mobility between secondary actuator force and the velocity at the control location or mechanical plant response |
| $M_{xf}^{kl}$ | Mobility between an excitation component $f$ at location $k$ and the velocity response $x$ at location $l$ |
| $M_{x,y,z}$ | Complex amplitudes of the moments referred to the $x$, $y$ and $z$-axis |
| $n$ | Modal order associated with the number of nodal lines in the $y$-direction |
| $N_{x,y,z}$ | Complex amplitudes of the forces in the $x$, $y$ and $z$-directions |
| $P_c$ | Power input at point $c$ into a structure by a control force applying perfect skyhook damping |
| $P_{in}$ | Total power input in the equipment structure |
| $R_e$ | Internal electrical resistance of one reactive secondary actuator |
| $R_i$ | $i^{\text{th}}$ resistor of the controller box circuit |
| $S$ | Sensitivity of the control accelerometers embedded in the inertial secondary actuators |
| $t$ | Time variable |
| $t_0$ | Time at instant 0 |
| $T$ | Transmissibility function |
| $T_1$ | Electric transfer function of the first sub-circuit of the controller box |

| | |
|---|---|
| $T_2$ | Electric transfer function of the second sub-circuit of the controller box |
| $T_a$ | Blocked inertial actuator response |
| $T'_a$ | Experimental blocked inertial actuator response |
| $T_e$ | Electric transfer function of the global circuit of the controller box |
| $u$ | Voltage signal driving one secondary actuator |
| $\mathbf{u}$ | Vector of secondary actuator input voltages |
| $\dot{u}_j$ | Complex amplitude of the linear velocity along the $x$-axis at point $j$ |
| $V_{0j}$ | Force normalised velocity response at point $j$ when no control is applied |
| $v_a$ | Velocity of the inertial mass |
| $v_b$ | Base structure velocity at mount junction |
| $\mathbf{v}_{be}$ | Global velocity vector at the mount junctions for the base and equipment structures |
| $\mathbf{v}_{b,e}$ | Global base velocity vector and global equipment velocity vector at the mount junctions |
| $\mathbf{v}_{bj,ej}$ | Base velocity vector and equipment velocity vector at mount junction $j$ |
| $v_c$ | Velocity at control location $c$ |
| $v_\mathrm{e}$ | Equipment structure velocity at mount junction |
| $v_{in}$ | Secondary actuator input voltage, or input voltage in the controller box |
| $V_{ij}$ | Force normalised velocity response at point $j$ for a single-channel control at point $i$ |
| $\mathbf{v}_j$ | kinematic vector at point $j$ |
| $\dot{v}_j$ | Complex amplitude of the linear velocity along the $y$-axis at point $j$ |
| $v_{out}$ | Output voltage of the controller box |
| $\mathbf{v}_m$ | Global mount velocity vector |
| $\mathbf{v}_{m1j,m2j}$ | Mount velocity vector on the base and on the equipment at junction $j$ |
| $\mathbf{v}_r$ | Velocity response vector at points of interest on the equipment structure |
| $\ddot{w}_a$ | Acceleration of the inertial mass |
| $W_\mathrm{b}$ | Base displacement |
| $W_e$ | Equipment mass displacement |
| $\dot{w}_j$ | Complex amplitude of the linear velocity along the $z$-axis at point $j$ |
| $x_b$ | Rigid base displacement |

| | |
|---|---|
| $\dot{x}_b$ | Rigid base velocity |
| $\ddot{x}_b$ | Rigid base acceleration |
| $x_e$ | Equipment mass displacement |
| $\dot{x}_e$ | Equipment mass velocity |
| $\ddot{x}_e$ | Equipment mass acceleration |
| $X_{ij}$ | Output voltage of the fictitious control sensor at point $j$ for single-channel control at point $i$ in the Laplace domain |
| $X_{pj}$ | Output voltage of the fictitious control sensor at point $j$ when no control is applied in the Laplace domain |
| $y$ | Control sensor output signal in the absence of primary disturbance |
| $\mathbf{y}$ | Vector of the control sensor output signals in the absence of primary disturbance |
| $Z_a$ | Impedance of the inertial actuator suspension |
| $Z_{aa}$ | Input impedance of the inertial actuator as seen from the bottom of the suspension at the connection with the equipment structure |
| $Z_e$ | Electrical impedance of one secondary reactive actuator |
| $Z_m$ | Impedance of one massless mount |
| $\mathbf{Z}_m$ | Mount impedance matrix |
| $Z_{fx}^{jl}$ | Mount impedance between a driving velocity $x$ at end $l$ of one mount and an effort $f$ at end $j$ of the same mount |
| $\alpha$ | Largest value of the real part of the plant response as it crosses the negative real axis of the Nyquist diagram |
| $\Delta$ | Frequency dependent determinant of the open loop frequency response of a multichannel controller |
| $\Delta_t$ | Spacing between two accelerometers for transverse wave number estimation |
| $\phi_{mn}$ | Axial mode shape function of the mode $(m,n)$ |
| $\eta$ | Modal hysteretic damping coefficient |
| $\varphi_{12}$ | Phase delay between two accelerometers |
| $\lambda_i^G$ | $i^{\text{th}}$ frequency dependent eigenvalue of the plant response matrix of a multichannel controller |
| $\lambda_i^{GH}$ | $i^{\text{th}}$ frequency dependent eigenvalue of the open loop frequency response of a multichannel controller |
| $\Lambda_{mn}$ | General normalisation factor of the axial mode $(m,n)$ |

| | |
|---|---|
| $\nu_e$ | Poisson's ratio of the composite panel |
| $\dot{\theta}_{xj,yj,zj}$ | Complex amplitudes of the angular velocity around the $x$, $y$ and $z$-axis at mount junction $j$ |
| $\rho$ | Density of an isotropic plate |
| $\rho_e$ | Density of the composite panel |
| $\omega$ | Frequency in radians per second |
| $\Omega$ | Normalised excitation frequency |
| $\omega_a$ | Blocked inertial actuator resonance frequency in radians per second |
| $\Omega_a$ | Excitation frequency normalised by the blocked inertial actuator resonance frequency |
| $\omega_c$ | Critical value of a specific frequency in radians per second |
| $\omega_e$ | First resonance of the mounted equipment structure in radians per second |
| $\omega_{mn}$ | Resonance of the structural mode $(m,n)$ in radians per second |
| $\omega_n$ | Resonance frequency of the mounted mass in radians per second |
| $\psi^{(x)}_{mn}$ | Rotational mode shape function of the mode $(m,n)$ associated with the rotation around the $x$-axis |
| $\psi^{(y)}_{mn}$ | Rotational mode shape function of the mode $(m,n)$ associated with the rotation around the $y$-axis |
| $\zeta_a$ | Passive damping ratio of the blocked resonance of the inertial actuator |
| $\zeta_{act}$ | Equivalent active damping ratio |
| $\zeta_e$ | Damping ratio of the first resonance of the mounted equipment structure |
| $\zeta_{pas}$ | Passive damping ratio of the heave mode of the rigid mounted piece of equipment |

# List of abbreviations

| | |
|---|---|
| ASAC | Active Structural Acoustic Control |
| AVC | Active Vibration Control |
| DVFB | Direct Velocity Feedback Control |
| SNR | Signal to Noise Ratio |

# Acknowledgements

I would like to thank Professor Stephen J. Elliott for his supervision, his availability all along this work and his trust in sending me to conferences. Many thanks also to Doctor Paolo Gardonio for his precious and constant scientific support and his technical advice. I will not forget my office colleagues and Tom for facing me for so long.

Et à d'autres...

# Chapter 1

# Introduction

Isolating a piece of equipment or any sensitive structure from a vibrating base structure is a very common problem in the field of mechanical engineering. Very little can usually be done to reduce the vibration of the base, which is often characterised by a complex dynamics and strict design requirements. Mechanical engineers have, for a long time, solved the problem of vibration isolation by designing passive isolation systems based on compliant material, such as rubber, to decouple the equipment dynamics from the base dynamics. Typically the base vibration is seismic, with an unpredictable waveform, so that passive isolators have to deal with broad band excitation spectra. However, passive systems for the isolation of equipment from base vibration involve an inherent compromise between good high frequency isolation, which requires low values of isolator damping, and limited excitation of the rigid body modes, which requires high values of isolator damping [1-7]. This trade-off is illustrated in Figure 1.2 which shows the modulus of the transmissibility function ,$T$, as defined in equation (1.1) and derived from the single degree of freedom isolation system in Figure 1.1.

$$T(j\omega)=\frac{W_e(j\omega)}{W_b(j\omega)}=\frac{1+2j\zeta_{pass}\Omega}{1-\Omega^2+2j\zeta_{pass}\Omega} \tag{1.1}$$

where

$W_e$ and $W_b$ are the equipment mass and base displacement respectively, $\Omega=\frac{\omega}{\omega_n}$ is the normalised excitation frequency, $\omega_n=\sqrt{\frac{k}{m}}$ is the resonance frequency, $\zeta_{pass}=\frac{c}{c_{crit}}$ is the passive damping ratio, $c$ is the passive damping constant, and $c_{crit}=2\sqrt{km}$ is the critical damping.

As the viscous damping in the mount and therefore the damping ratio increase, the rigid body resonance is attenuated but the high frequency efficiency of the isolation is reduced. The high frequency asymptotic value of the transmissibility of equation (1.1) is given by equation (1.2), from which it is clear that the transmissibility is proportional to the damping ratio in this frequency region.

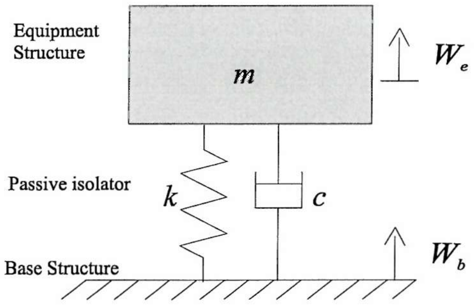

Figure 1.1. Single degree of freedom low frequency model of passive isolation system.

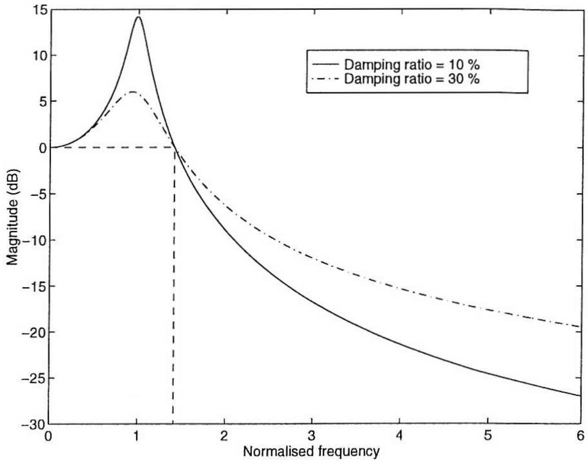

Figure 1.2. Transmissibility modulus for two different values of damping ratio

$$T(\omega \to +\infty) = -\frac{2j\zeta_{pass}}{\Omega} \tag{1.2}$$

The adverse effect of the passive damping at high frequencies is due to the fact that it increases the coupling between the base and the mounted structure. The net effect of a passive isolation, as shown in Figure 1.2, is to amplify the vibration transmission below $\omega_c = \sqrt{2}\omega_n$ and to provide some attenuation above this frequency. Soft mountings are generally used since they generate low rigid-body resonances of the mounted system and thus reduce the frequency band of vibration amplification. However, if the isolator mounting frequency is too low, there are potentially problems with static stability. Passive isolators thus provide, in general, an efficient way of reducing vibration transmission, but they are subject to various trade-offs when low frequency broad band excitations are involved. One should note that all these observations are also valid for the reciprocal situation of the isolation of a supporting structure from the vibration of a mounted system, although this is not the issue of interest in this thesis.

At low frequencies, where passive methods fail to be efficient, active control systems are known to be able to enhance the performance of many mechanical isolation systems, in structural dynamics [8, 9] as well as in acoustics [10]. It may be possible to couple an active device to the existing passive isolators in order to reduce the vibration transmitted to mounted structure, especially in the low frequency range of vibration amplification. This study reports an investigation into the effect of the control strategy called Direct Velocity Feedback (DVFB) control, in enhancing the vibration attenuation provided by a passive isolation to a suspended structure, termed as equipment. As already discussed, the design of passive mounting systems for the reciprocal problem of ground isolation from mounted machinery vibration generally follows the same rules as the isolation of a mounted equipment from a vibrating base structure. It can be noticed, however, that the two isolation schemes start to diverge as active isolation is introduced. The excitation spectrum of mounted machinery is often dominated by harmonic components so that feedforward control can then be implemented in place of feedback control. Active isolation from mounted system vibration using feedforward techniques has already been largely studied [11, 12].

Chapter 2 explains the use of DVFB control in the active isolation of equipment and how it enables, in principle, the synthesise of skyhook damping at the control point. A skyhook damping effect can strongly reduce the rigid body resonance shown in Figure 1.2 without debasing the high frequency performance of the passive device. The effect of skyhook damping generated by velocity feedback is well known [13] and has been shown to give strong isolation improvement on mounted rigid system [14-16]. The second interest of DVFB control, discussed in chapter 2, is its extreme simplicity as the secondary control force is directly proportional to the velocity monitored at the control point. Moreover, an extension of DVFB control to multichannel control gives a decentralised controller which greatly simplifies the wiring and reduce the number of operations to be performed by the controller on the control signals [17, 18]. Rules for the analysis of DVFB control stability are given in chapter 2 for single and multichannel control.

In chapter 2, perfect DVFB control, with an idealised control force, is presented. Chapter 3 tackles the practical issue of secondary force actuation, and in particular, unlike many studies on skyhook control [14, 19], the realistic situation of a flexible vibrating base structure is considered. No inertial ground is therefore available to react the secondary force off. Two ways of force actuation are then available in practise: a reactive actuation and an inertial actuation. Both of these methods are analysed in chapter 3 for the implementation of DVFB control of a rigid equipment mounted on a single dimension mount. The expression for the associated plant responses is derived and the stability characteristics of the control are discussed for each type of actuation. Restricting the control implementation analysis to a rigid equipment and to a single mount passive isolation enables us:

- to fully concentrate on the effect of the dynamics of the reactive or inertial actuator on the plant response and on the resulting control performance.

- to analyse the useful and practical issue of isolating mounted rigid equipment. For instance, the isolation of rigid boxes containing electronics.

The main outcome of this analysis was to demonstrate the unconditional stability of a reactive DVFB control system for rigid equipment mounted on a single mount, regardless of the base dynamics.

Controlling vibration transmission to a flexible structure is a challenge addressed very early in the development of active systems. The objective of controlling of large flexible aircraft or satellite panels motivated many researches and early studies on active vibration control (AVC) [20]. This is also a central interest in active structural acoustic control (ASAC), which tackles the mechanism of sound generation and attempts to control a vibrating structure in order to decrease the radiated acoustic power. In the second part of the thesis, consisting of chapters 4, 5 and 6, active isolation using DVFB control is extended to the control of flexible equipments. These are usually large structures that imply, in practise, multi-mount passive systems because of static stability requirements. There are then several connections between the base and the equipment structures and, therefore, as many vibration transmission paths to the equipment, so that multichannel control will be necessary to achieve good isolation.

A passive mounting system is usually designed for global attenuation of the suspended equipment. The strategies of DVFB control and skyhook damping are, however, local control strategies. They can be rather easily implemented in a global isolation scheme for rigid equipments [15, 16] but this is not necessary the case when flexible equipment structures are involved. The efficiency of DVFB control can be estimated locally on the flexible equipment at the control points, as done in chapters 4, 5 and 6, but it is clearly not the optimal objective of an active controller if enhancement of the passive isolation performance is to be achieved. Local control of the equipment structure at the junctions with the mounts is based on the idea that control is efficient when applied at the sources of disturbance [21]. In order to apply global control with a direct feedback strategy, the quantity to be considered should, in principle, be the power at the junctions between the mount and the equipment structure, which does not involve only kinematic information (velocity) but also dynamic information (force) [21-24]. The power relative to different degrees of freedom has, moreover, to be taken into account since not only axial but also rotational excitations in the mounts propagate to the equipment structure contributing to generate out-of-plane vibration. Gardonio showed in [25] that for a two plate system coupled by three passive isolators, an optimal feedforward control using a cost function of the square values of the velocities at the equipment plate junctions with the mounts was giving almost as good global vibration isolation over the equipment of harmonic disturbances as an optimal control using a cost function based on the input power estimation. This means that controlling only the velocity on the equipment at the junctions with the mounts may provide good control of the vibration transmission to the suspended equipment. The strategy of DVFB control does, however, not look for a perfect cancellation of the disturbances as a feedforward controller does but aims to add appropriate damping so that vibration transmission can be significantly reduced. Here lies a large interest of this study which is to estimate if the simple strategy of DVFB control can provide global out-of-plane vibration reduction over the whole suspended equipment sturcture. The existence of flexural waves in the mount and therefore the rotational excitation of the equipment is an extra challenge for the control since only axial control forces can be supplied by the secondary actuators used experimentally. Gardonio [25] showed that this could limit the control efficiency at high frequencies.

These questions are addressed in chapters 4, 5 and 6, which consider the performance of DVFB control in reducing bending vibration responsible for the out-of-plane displacement of a mounted flexible composite panel.

Chapter 4 presents an experimental analysis of the performance of an inertial implementation of DVFB control on a suspended composite panel equipment. Single-channel as well as multiple channel controls are investigated by control simulations based on the measurements of the appropriate plant responses. A real single-channel control is also implemented at one mount junction on the equipment panel. This chapter is largely focused on the local effect of the controller which is sufficient to clearly exhibit the limitations existing in the use of inertial devices to implement DVFB control.

In comparison to chapter 4, chapter 5 and chapter 6 study the performance of a reactive implementation of the control on a suspended composite panel equipment. Single and multiple channel controls are also considered. Close attention is paid to the stability of the control loop with a reactive implementation of the actuator, as it showed very interesting properties, as reported in chapter 3.

A model of the reactive isolation system designed for subsequent experiments is developed in chapter 5. It enables a first estimation of the control stability and, above all, of the global performance of the control by calculating the input power in the mounted panel under control at the mount junctions. Accounting for both axial and rotational excitation in the mount, the model allows us to discriminate between vibration transmitted by axial or by rotational excitation. It thus offers a useful benchmark of the real capacities of axial control forces.

Chapter 6 is focused on the experimental implementation of the control. The stability of different experimental control systems is assessed. Practical limitations on the use of high gain control are pointed out and analysed before implementing real single-channel controls and an equal gain multichannel control. The control effect is not only monitored at the mount junctions but also at five other locations on the equipment so that an estimate of the kinematic energy of the equipment panel can be obtained in order to determine the global isolation effect of the implementation of DVFB control on the equipment plate.

One should keep it mind that this study is dedicated to vibration control. This means that, even though active isolation of a flexible panel could be used in an ASAC study, any sound radiation control through active isolation of the mounted panel is beyond the scope of the work presented in this thesis. Reduction of the vibration pattern of a system does not automatically induce a reduction of the radiated acoustic power, since the dominant structural modes of vibration are not necessarily the modes of high radiation efficiency [26, 27]. Acoustic measurements should have been performed to test the effect of DVFB control on the radiation characteristics of the plate so that one should not see an attempt of ASAC in the work carried out.

The main contributions of this thesis are,

1) The development of analytic models for analysing the stability of single-channel DVFB systems with both reactive and inertial actuators.

2) The experimental investigation of multichannel DVFB systems with both reactive and inertial actuators.

3) The analysis of the effect of equipment and base flexibility on DVFB systems and the global effect of local controllers in such systems.

# Chapter 2

# Theory of Direct Velocity Feedback Control and the Skyhook Damping effect

## 2.1. The use of feedback control

To improve the performance of a passive isolation in reducing vibration transmission, a controller generally has to account for primary excitation of random type or transient disturbances. This implies that an active isolation system must be able to apply a broad frequency band control. The study reported in this thesis investigates vibration reduction on systems connected to a primary vibrating structure by passive mounts. The transmission paths are then clearly identified and reference excitation signals, at the connection points between the mounts and the vibrating base, are, in principle, available. The question of using a feedforward approach can therefore be addressed. A feedforward control system would be required to produce a model of the complete system dynamics in order to generate the correct secondary forces. The computation must be done digitally especially in the case of adaptative control. The time necessary to compute the optimal control output for a broad band control and the phase shifts associated with any digital system (analogue anti-aliasing and reconstruction filters, analogue-to-digital and digital-to-analogue converters) would quickly limit the optimal performance of such a controller. Finally the use of an optimal digital feedforward controller goes against the philosophy of keeping the control system simple.

A feedback system offers the possibility of good broad-band control by implementing a rather basic analogue controller. However, feedback generates an input into the system under control, a secondary force, which is already the result of the system response. This close loop feature is the cause of the danger of instability that limits the use of feedback system. The stability of the controller is therefore one of the main issues which must be addressed in this study when estimating the performance of the different control systems.

## 2.2. Single-channel skyhook damping

### 2.2.1. Single-channel feedback control

Figure 2.1 shows the block diagram of a typical single channel feedback control system for disturbance rejection.

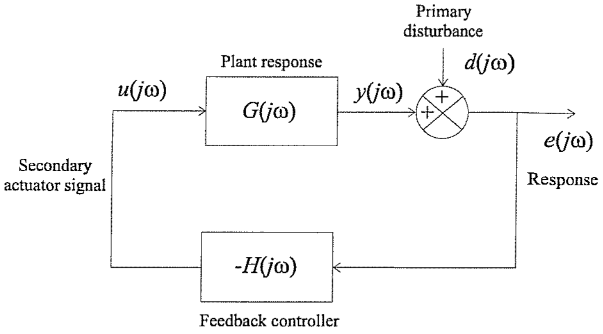

Figure 2.1. Electrical block diagram of single channel feedback control system.

The frequency response at the sensor output of the given equipment to a control force in the absence of any primary base excitation is that of the system under control, commonly termed the “plant”. It is convenient, in practise, to include the control actuator and the control sensor dynamics in the plant so G is now the transfer function between the signal input in the control actuator *u* and the output of the control sensor, *y*. The total response *e* of the system under control, also termed the error, is therefore the addition of the response to a secondary output, *y* with the contribution due the primary excitation acting on the base structure, also termed the primary disturbance, *d*. The total system output, *e*, is then fed back to the actuator input via a controller, defined by its frequency response, *H(jω)*. The negative sign in Figure 2.1 accounts for the negative feedback. For a stable system, the performance of such a feedback controller can be estimated using the sensitivity function defined in the frequency domain as the ratio between the control system response, *e* and initial disturbance, *d*.

$$\frac{e(j\omega)}{d(j\omega)}=\frac{1}{1+G(j\omega)H(j\omega)} \tag{2.1}$$

As discussed in many books on control [8, 28], if at a frequency ω the open loop frequency response *G(jω) H(jω)* has little phase shift and simultaneously a large enough gain so that,

$$\left|1+G(j\omega)H(j\omega)\right| >> 1 \tag{2.2}$$

then

$$\left|\frac{e(j\omega)}{d(j\omega)}\right| << 1 \text{ or } |e(j\omega)| << |d(j\omega)| \tag{2.3a, 2.3b}$$

At this frequency ω, the response of the mechanical system is then greatly reduced when the controller is acting. It is clear, on the other hand, that the system tends to instability as the open loop function approaches the value -1, since the denominator of the sensitivity function tends to zero. Another way to look at the notion of stability is to state that the control system will face some limitations if at one frequency $\omega_c$ the phase shift in the open loop frequency response is 180°. This means that the delay in the control loop is such that the controller has an effect on the system which is in-phase with the primary excitation and in which case

$$\frac{e(j\omega_c)}{d(j\omega_c)} = \frac{1}{1-|G(j\omega_c)H(j\omega_c)|} \tag{2.4}$$

The gain margin $GM$ can be defined as the gain increase (in dB), i.e. the increase in $|H(\omega_c)|$, necessary to cause instability.

$$GM(dB) = 20\,log_{10}\left|\frac{1}{G(\omega_c)H(\omega_c)}\right| = -20\,log_{10}|G(\omega_c)H(\omega_c)| \tag{2.5}$$

This brief description of a single-channel feedback control system demonstrates the importance of analysing the open loop function, since it gives a strong insight into the limitations and performance of a controller. The Nyquist representation is therefore a powerful experimental tool to assess the characteristics of a control system. It consists of plotting the real part versus the imaginary part of the open loop frequency response as ω varies along the frequency range of interest. The Nyquist criterion states that for a stable open loop system the closed loop system is also stable provided the Nyquist contour does not enclose the unstable point (-1,0*j*) [29, 30]. More practically, the Nyquist representation allows us to estimate the frequency ranges of expected reduction and amplification of the system vibration under control by looking at the distance of the open loop contour to the unstable point.

For DVFB control, the controller is a simple gain $h$ so that the Nyquist analysis of the open loop frequency response $GH$ can be reduced to the consideration of the plant response $G$ considering a unitary control gain ($h$=1). The value of the maximum gain, $h_{max}$, can then be easily determined looking at the largest value, $\alpha$, of the real part of the plant response as it crosses the negative real axis of the Nyquist diagram. The open loop response *GH* for a pure gain control will then hit the unstable point (-1,0*j*) for a feedback gain $h_{max}$ such that

$$h_{max} = \frac{1}{|\alpha|} \tag{2.6}$$

### 2.2.2. Skyhook damping versus direct displacement and acceleration feedback

A feedback control system requires the measurement of a quantity characterising the response of the system under excitation. Considering, as shown in Figure 2.2, a rigid piece of equipment of mass $m$ mounted on a vibrating base via a massless mount represented by a spring, $k$ and a passive damper, $c$, in series, three quantities are then available for basic feedback control: the displacement, $x_e$, the velocity, $\dot{x}_e$ and the acceleration of the equipment, $\ddot{x}_e$. Therefore, for a simple proportional control combining the three feedback possibilities, the secondary force can be defined as,

$$f_s = -h_d x_e - h_v \dot{x}_e - h_a \ddot{x}_e \tag{2.7}$$

where $h_d$, $h_v$ and $h_a$ are the control gains associated with the displacement, velocity and acceleration control signal respectively.

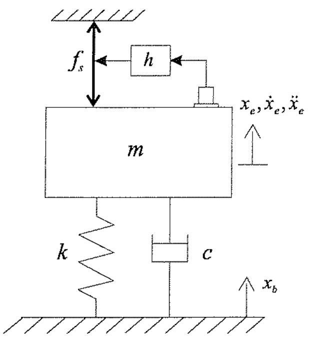

Figure 2.2. Skyhook feedback control on a SDOF isolation system

Considering the base to be rigid, the transmissibility factor $T$ can then be derived to assess the effect of each control strategies in improving the mounted mass isolation.

From Newton's second law of motion, it can be written that,

$$\sum F_{/m} = m\ddot{x}_e(t) \tag{2.8}$$

$$-k\left(x_e(t)-x_b(t)\right)-c\left(\dot{x}_e(t)-\dot{x}_b(t)\right)+f_s(t)=m\ddot{x}_e(t) \tag{2.9}$$

Since the system is linear, it can be written for an harmonic excitation of frequency ω,

$$(k+jc\omega)x_b(j\omega)-\left(k+h_d+jc\omega+jh_v\omega-h_a\omega^2\right)x_e(j\omega)=-m\omega^2x_e(j\omega) \tag{2.10}$$

where $f_s$ has been substituted from equation (2.7), and so

$$T(j\omega)=\frac{x_e(j\omega)}{x_b(j\omega)}=\frac{k+jc\omega}{k+h_d+j(c+h_v)\omega-(m+h_a)\omega^2} \tag{2.11}$$

The three strategies of displacement, velocity and acceleration feedback control leave the numerator in the expression for the passive transmissibility unchanged, whereas the absolute value of the denominator seems to increase, since the secondary force is only function of the equipment motion. This leads to an overall increase of the mounted system impedance for each feedback control but to different results in terms of performance as shown below in Figures 2.3(b), 2.4(b), 2.5(b) and illustrated by the representation of the mechanical effect of the controls in Figures 2.3(a), 2.4(a) and 2.5(a).

**Direct displacement feedback: $(h_v, h_a)=(0, 0)$**

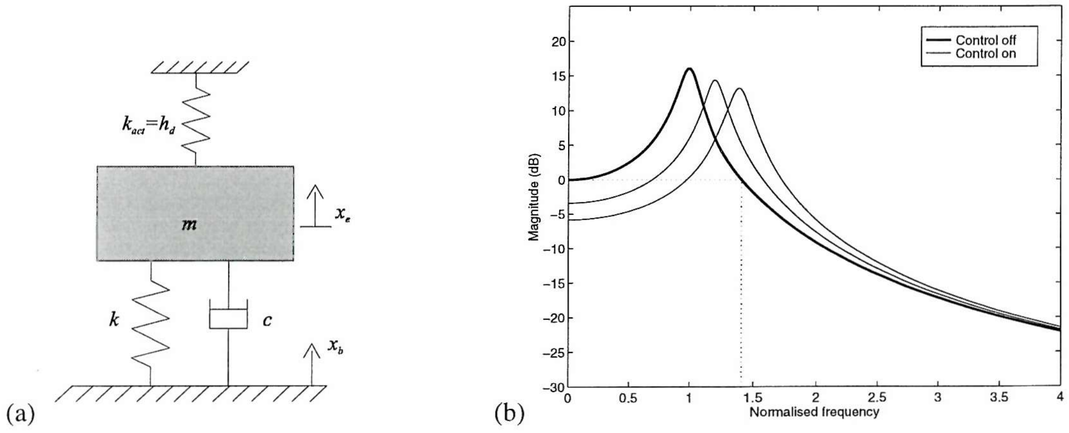

Figure 2.3. Mechanical representation of direct displacement feedback control on a SDOF isolation system (a) and corresponding performance compared to pure passive isolation, (b).

This is equivalent to adding an extra spring connecting the mounted mass to a fictitious inertial ground. The vibration level is then reduced at low frequencies. The resonance is shifted up in frequency but not significantly damped as desired. Therefore the control does not enable us to obtain a reduction of the vibration level over the whole frequency range. Moreover for the control to have an effect, the feedback gain $h_d$ must be of the order of magnitude of the mount stiffness $k$ which implies in practise a very high amplification of the displacement signal.

**Direct velocity feedback: ($h_d$, $h_a$)=(0, 0)**

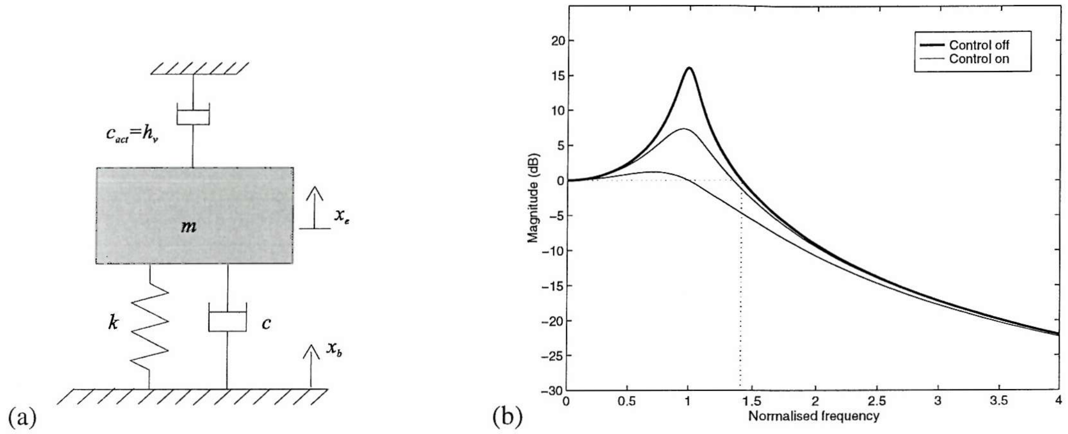

Figure 2.4. Mechanical representation of direct velocity feedback control on a SDOF isolation system (a) and corresponding performance compared to pure passive isolation, (b).

This is equivalent to connect the mounted mass to an inertial ground with a passive dashpot of damping constant $h_v$. This control is then called skyhook damping. It allows us to damp efficiently the resonance due to the passive isolation without debasing the high frequency performance of the passive isolator, unlike passive damping, since the secondary force is independent of the base velocity, $\dot{x}_b$. The main drawback of the passive isolation performance is thus suppressed and the good high frequency performance of the passive isolation remains unaltered. An equivalent active damping ratio can then be defined as

$$\zeta_{act} = \frac{h_v}{2\sqrt{km}} \tag{2.12}$$

**Direct acceleration feedback control: ($h_d$, $h_v$)=(0, 0)**

This is equivalent to adding a mass $h_a$ on top of the system. The already-good high frequency performance of the passive isolation is thus strongly improved. Moreover rather low feedback gains are required for the control to be effective. However the resonance is shifting down in frequency with an increasing amplitude since the global damping ratio decreases as the effective mass increases (2.11). Acceleration feedback does not enable to remove the limitation of a passive isolator since it does not attenuate the mounted system resonance.

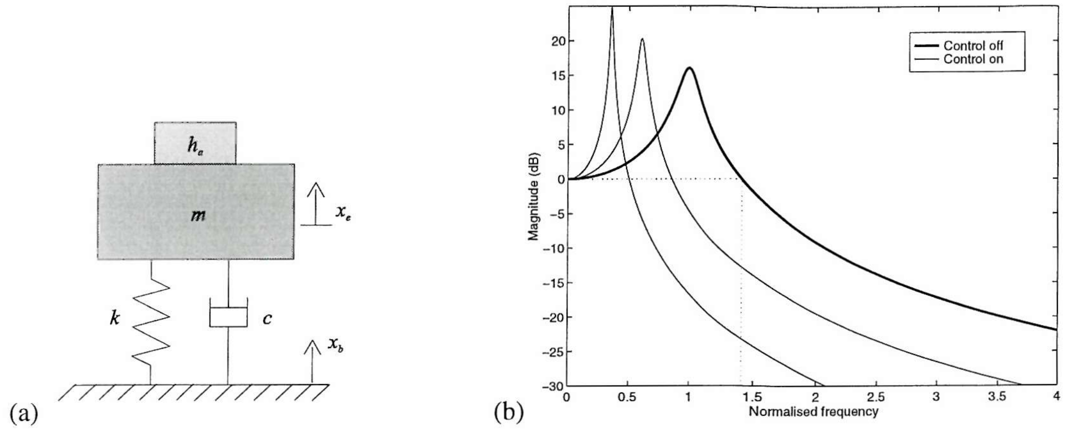

Figure 2.5. Mechanical representation of direct acceleration feedback control on a SDOF isolation system (a) and corresponding performance compared to pure passive isolation, (b).

### 2.2.3. Velocity feedback stability

It clearly appears that only direct velocity feedback (DVFB) enables us to attenuate efficiently and even to cancel the resonance of the mounted system which is what limits the efficiency of passive isolators. This good performance of DVFB can be easily understood looking at Figure 2.6 which shows the Nyquist plots of the plant responses for displacement, velocity or acceleration feedback. This is equivalent to look at the Nyquist plots of the corresponding open loop frequency responses with a gain factor, $h_d$, $h_v$ or $h_a$, as discussed in section 2.2.1. In Figure 2.6(b), the whole Nyquist contour is located in the positive real part of the plane. Therefore as the gain $h_v$ increases, the contour expands in the same half plane and each of its points goes further from the unstable point (-1,0*j*), thus providing disturbance attenuation at all frequencies. This positive real feature is characteristic of the input mobility function of a structure regardless of the system considered. The plant response $G_v$ for the lumped mass-isolator system in Figure 2.4 given in equation (2.13) is clearly an input mobility as the velocity response is collocated with the secondary force.

$$G_v = \frac{1}{jm\omega + c + k/_{j\omega}} \qquad (2.13)$$

Therefore its phase response is known to be between $\pm\frac{\pi}{2}$, which guarantees the open loop frequency response to be on the right hand side of the Nyquist plot. The control system is thus unconditionally stable and vibration reduction are expected at all frequencies, which explains the large disturbance reduction observed in Figure 2.4(b). This is not the case for displacement and acceleration feedback controls, for which part of the plant response contour lays in the negative real part half plane as shown in Figure 2.6 and expressed in equations (2.14) and (2.16).

$$G_d(j\omega) = \frac{1}{j\omega} \cdot G_v(j\omega) \tag{2.14}$$

$\Rightarrow -\frac{\pi}{2}$ rotation of the Nyquist plot of $G_v$ so that

$$-\pi < \angle G_d < 0 \tag{2.15}$$

and

$$G_a(j\omega) = j\omega \cdot G_v(j\omega) \tag{2.16}$$

$\Rightarrow \frac{\pi}{2}$ rotation of the Nyquist plot of $G_v$ and

$$0 < \angle G_a < \pi \tag{2.17}$$

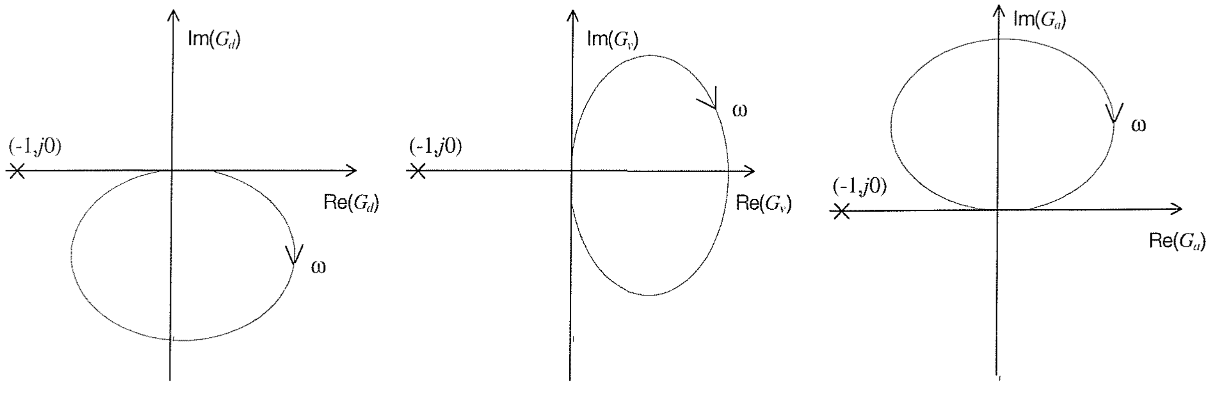

(a) (b) (c)

Figure 2.6. Standard shape of Nyquist plot of plant response for displacement (a), velocity (b), and acceleration (c) feedback on SDOF isolation system.

Direct displacement and acceleration feedback controls are still unconditionally stable when there is passive damping in the system, as the Nyquist contours do not cross the negative real axis. However, they generate vibration amplifications at high frequencies for displacement feedback and at low frequencies for acceleration feedback. Another interesting observation can be made on velocity feedback using this simple analysis of the different Nyquist plots. An extra $\frac{\pi}{2}$ or $-\frac{\pi}{2}$ phase shift can be added to the plant response $G_v$ without it crossing the negative real part axis. This means that velocity feedback is very robust to any unmodelled delays in the feedback control loop, usually due to the actuator, sensor dynamics or to the time required by the controller to process the control signal. The robustness of velocity feedback is discussed more mathematically by Fuller *et al.* [8].

### 2.2.4. Soft mounting

As noted in the previous section, skyhook damping is effectively applied in parallel with passive isolation, as the secondary force is directly applied on the mounted equipment. Such an active enhancement of the passive isolation is called soft mounting. Beard *et al.* [19] discussed the use of a secondary actuator in series with the passive mount. Such a control system is described as having a hard mounting. This involves the control of an intermediate mass situated below the passive isolator which renders the control less dependent on uncertain payload dynamics and thus provides a better system to control. For such a control system, however, the actuators require a large stiffness and are then typically made from piezoelectric materials. Their maximum displacement is of the order of 10 μm for a 1 cm long actuator which does not afford a sufficient throw to control the amplitude of the seismic vibration considered in this study for which electrodynamical devices are used.

## 2.3. Multichannel skyhook damping control

### 2.3.1. Decentralised DVFB control and skyhook damping

In the case of multi-mount isolation systems, either for flexible or rigid equipment control, several secondary forces are necessary for good control and therefore a multichannel controller is required. An equal gain decentralised collocated control is the most straightforward multichannel approach that can be designed. The implementation of such a controller is originally motivated by simplicity, rather than on the optimisation of performance. Keeping the controller simple allows us to fully concentrate on the mechanics of the system and the potential of the chosen control strategy. If strong vibration attenuation can be achieved with decentralised direct velocity feedback (DVFB) control, further reductions may then be possible using standard signal processing techniques on the sensor signals.

Considering a vibrating flexible structure acted on by inertially-reacted force actuators, Balas [31] showed that there were no stability limitations for decentralised collocated control using direct velocity feedback provided,

(*i*) equal number of collocated actuators and control sensors are used,

(*ii*) the actuators do not excite the modes associated with zero frequency (rigid body modes).

Since this study deals with the isolation of suspended structures, any rigid body modes of the mounted structure are controlled by the stiffness of the passive mounts. This prevents any zero-frequency modes from being present and thus condition (*ii*) is always satisfied.

A stable vibrating system controlled by $N$ independent channel using DVFB control is considered. At a time $t_0$, the plant dynamics are characterised by a kinetic energy $E_k(t_0)$. When an extra control loop is operating at a point $c$, the control sensor monitors a velocity $v_c(t_0)$ and the secondary actuator applies an ideal secondary force $f_s(t_0)$ such that,

$$f_s(t_0) = -hv_c(t_0) \tag{2.18}$$

the power input in the system is then,

$$P_c(t_0) = \frac{1}{2} Re\{f_s(t_0) \cdot v_c^*(t_0)\} \tag{2.19}$$

and

$$P_c(t_0) = \frac{1}{2} Re\left\{-h|v_c(t_0)|^2\right\} = -\frac{h}{2}|v_c(t_0)|^2 \tag{2.20}$$

Equation (2.20) shows that the power input on the control system at any time $t_0$ is negative and the resulting kinetic energy of the system is thus reduced by the effect of the extra loop. This discussion gives an insight into the stable properties of collocated DVFB, implementing perfect skyhook damping at each control point as represented in Figure 2.7 which illustrates the passive effect and therefore the stability of collocated multichannel DVFB control.

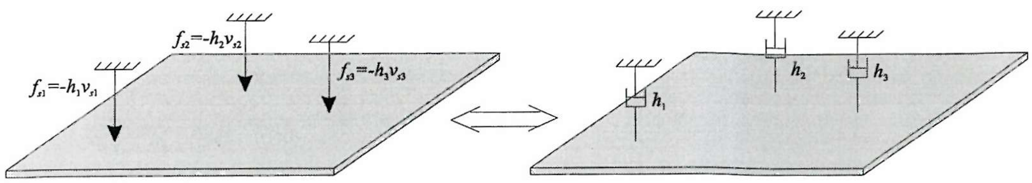

Figure 2.7. Equivalent mechanical effect of collocated multichannel DVFB control.

The complete proof of the control stability given by Balas is based on the assumption of perfect skyhook dampers, i.e. perfect control forces reacting off an infinite impedance ground as in Figure 2.7. Such a rigid ground is often not available in practise. The secondary forces must therefore react off another system, which may have significant dynamics, as considered in this study. Strictly speaking, the control is no longer collocated because of the contribution to the sensor output from this reactive force, and the control stability is not guaranteed. A large part of the implementation of DVFB control on the isolation systems presented in this thesis is dedicated to the analysis of the control stability.

### 2.3.2. Stability assessment for multichannel feedback control

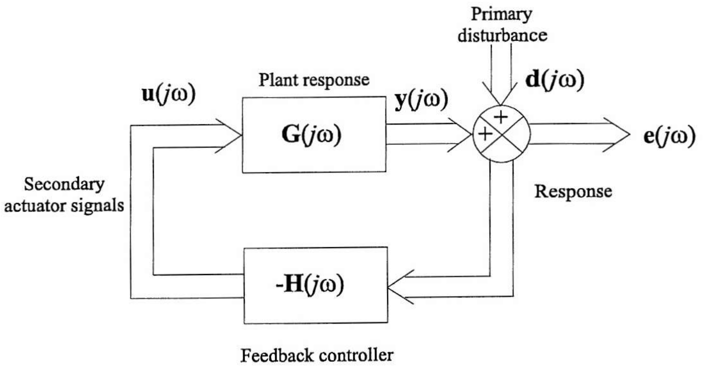

Figure 2.8. Electrical block diagram of multichannel feedback control system

For multichannel control, in the absence of primary excitation, the control signal at one point $i$, $y_i$ is the results of $N$ secondary actuators driven by the input signals $u_j$ so that:

$$y_i = \sum_{j=1}^{N} G_{ij} u_j \tag{2.21}$$

The plant response of the system is now defined by a matrix **G** of transfer functions between the points of control actuation and control sensing as

$$\mathbf{y} = \mathbf{G} \cdot \mathbf{u} \tag{2.22}$$

where **y** is the vector of the control signals at the sensor outputs in the absence of primary disturbance and **u** is the vector of secondary shaker input voltages. The controller operations are also defined by a matrix **H** relating the control sensor signals to the actuator driving voltages. The multichannel sensitivity function can then be written as

$$\mathbf{e} = (\mathbf{I} + \mathbf{GH})^{-1}\mathbf{d} \tag{2.23}$$

where **e** and **d** are the control system response vector and the primary disturbance vector respectively. The stability criterion can then be generalised such that the locus of the determinant $\Delta$ must not enclose the origin, where

$$\Delta(j\omega) = det(\mathbf{I} + \mathbf{G}(j\omega)\mathbf{H}(j\omega)) \tag{2.24}$$

Using the eigenvalue decomposition method, equation (2.24) can be written as

$$\Delta(j\omega) = \prod_{i=1\,to\,N} (1 + \lambda_i^{GH}(j\omega)) \tag{2.25}$$

where the $\lambda_i^{GH}(j\omega)$ are the $N$ frequency dependent eigenvalues of the open loop frequency response **GH** [30] which must each not encircle the (-1,*j*0) point for stability.

Multichannel DVFB control is a decentralised control strategy which means that one sensor is associated with one actuator such that the controller is composed of $N$ independent control loops. In other words, the controller does not couple the control loops and **H** is a diagonal matrix. Equal control gains were implemented in the experimental control systems so that the controller can be simply expressed as

$$\mathbf{H} = h\mathbf{I} \tag{2.26}$$

and so

$$\mathbf{GH} = h\mathbf{G} \tag{2.27}$$

The eigenvalues of the plant response matrix $\lambda_i^G$ are related to the eigenvalues of the open loop response by

$$\lambda_i^G = \frac{\lambda_i^{GH}}{h} \tag{2.28}$$

The stability assessment is then reduced to the analysis of the frequency dependent eigenvalues of the plant matrix **G**, as if *N* independent single-channel control systems were considered. The control gain is then limited by the eigenvalue associated with the most stringent stability condition.

# Chapter 3

# Reactive actuation and Inertial actuation

## 3.1. Introduction

As presented in chapter 2, absolute velocity feedback theoretically offers good control by adding active damping to a vibrating system. It is particularly useful in applications for the isolation of mounted systems, since it can provide a strong reduction and even cancellation of the extra resonances created by the insertion of passive mounts, without affecting the high frequency performance of the passive isolation. However, skyhook damping is an ideal implementation of DVFB control since it assumes, according to Newton's principle of force reaction, an extra structure with infinite impedance off which the secondary force can react, as shown in Figure 3.1(a). Perfect skyhook damping is therefore encountered in practise when DVFB control is implemented in parallel with the passive mounts, i.e. in a reactive way, to isolate a mounted system from a rigid vibrating base structure, as shown in Figure 3.1(b).

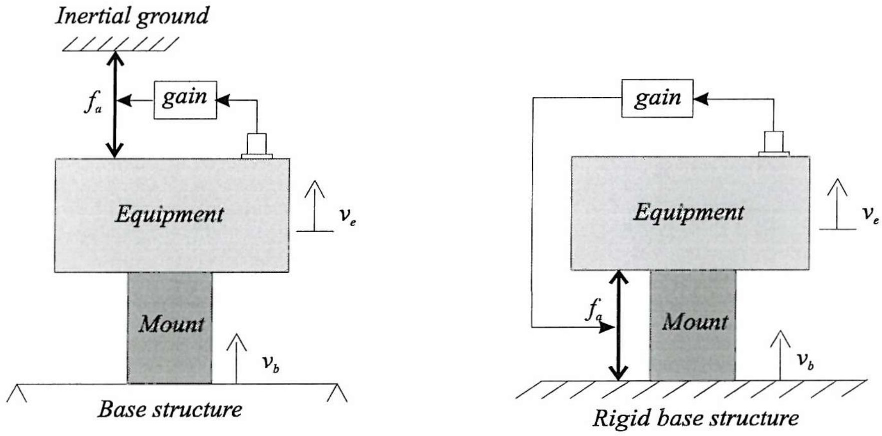

Figure 3.1. Schematic of theoretical (a) and practical (b) conditions for perfect skyhook damping.

This can be extended to the control of systems with base impedance much greater than the impedance of the equipment coupled to the passive mounts. The assumption of perfect skyhook damping for the use of reactive actuator may, however, be less and less satisfied as the frequency increases since resonances with significant magnitude can appear in the base structure whose dynamics must then be taken into account. Moreover, for a wide class of practical problems, the base structure has also a significant effect on the system dynamics at low frequencies, in the range of the blocked mounted equipment resonances. Therefore, the control study developed and summarised in this thesis has considered the realistic case of a flexible vibrating base structure in order to encompass all practical isolation system configurations.

Since an ideal inertial ground as shown in Figure 3.1(a) is not generally available, another support has to be found to react a control force off. There are two obvious practical methods of implementing the control in order to apply a secondary force on the suspended equipment.

- Reactive control: The control force $f_a$ is inserted between the base and the equipment in parallel with the passive isolation. A secondary force $f_a$ is thus generated on the equipment by reaction off the base structure as shown in Figure 3.2(a). This is known to provide perfect skyhook damping in the case of a rigid base as already discussed.

- Inertial control: An extra mass is mounted on the equipment to provide an inertial body, of mass $m_a$, on which the control actuator force, $f_a$, can react off. This generates a secondary force $f_s$ on the equipment which is different from $f_a$

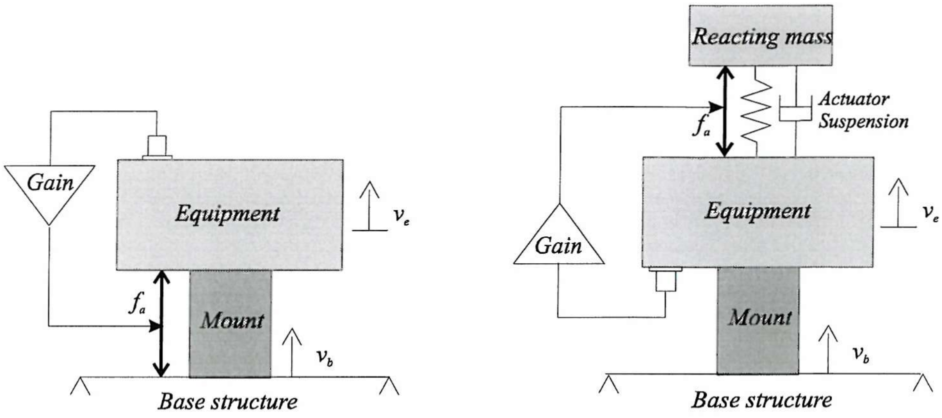

Figure 3.2. Principle schematic of direct velocity feedback control implementation using a reactive actuator (a) or an inertial actuator (b).

Unlike the perfect inertial ground, the flexible base as well as the actuator reacting mass $m_a$ are characterised by their own dynamics, which are going to modify the perfect plant response in equation (2.13). The stability and the performance of skyhook damping discussed by Balas has therefore to be reconsidered. This chapter is thus focused on the determination of the physical plant response for the two cases of reactive and inertial control implementation. We will consider here a single degree of freedom isolation problem in vertical translation since active controllers of suspended equipments are usually concerned with translational directions, as in the experimental works carried out in this thesis. Some of this work has also been reported by Elliott *et al* [32].

## 3.2. Reactive actuator for skyhook damping

This practical problem differs from theoretical skyhook control since the base is now considered flexible. The mounted equipment undergoes a primary disturbance generated by some excitation on the base structure. The secondary force reaction off the base can now be regarded as a second source of disturbance, since it will generate base vibration. This extra disturbance is transmitted through the mount to the mounted equipment, whose velocity is measured and then fedback to the controller. This mechanical feedback in the control will modify the plant response $G$ given in equation (2.13) and is potentially a source of instability. In other words, the plant under control is not the same as that considered above since the base dynamics is now accounted for. There is therefore the need to estimate the new plant response in order to assess the stability pattern of the control.

### 3.2.1. Analysis of the plant response expression for isolation of rigid equipments

The physical system is modelled as in Figure 3.3. The three elements; equipment, mount and base are connected together and using the mobility formulation when the two axial forces $f_e$ and $f_b$ operate, the velocity of the equipment $v_e$ can be written as,

$$v_e = M_{ee} f_e + M_{be} f_b \tag{3.1}$$

where $M_{ee}$ is the input mobility of the equipment when coupled to the rest of the system and $M_{be}$ is the transfer mobility from the force on the base, $f_b$ to the equipment velocity, $v_e$ when the system is coupled.

Expressions for $M_{ee}$ and $M_{be}$ can be derived using the three following quantities:

$M_e$, the input mobility of the unconnected equipment at location of the mount connection.

$M_b$, the input mobility of the unconnected mounted base at location of the mount connection.

$Z_m$, the impedance of the mount which characterises the mount properties. An unique quantity is sufficient since no resonances in the mount are taken into account. In other words, the mount is considered massless and thus modelled by a spring, $k$ and a damper, $c$, in parallel as shown in Figure

3.4. This assumption is correct in the low frequency range assuming that the passive isolation is very efficient and no controller effect is expected by the time resonances occur in the mount.

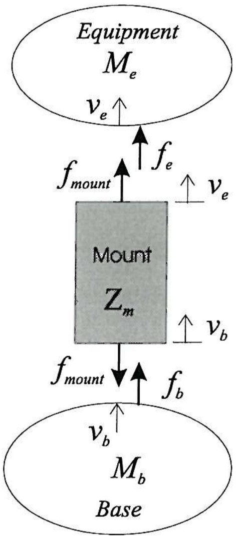

Figure 3.3. General block diagram for the isolation system representing the unconnected system elements.

When $f_b = 0$, it can be written from equation (3.1),

$$M_{ee} = \frac{v_e}{f_e} \tag{3.2}$$

Moreover

$$v_e = M_e\left[f_e + f_{mount}\right] = M_e\left[f_e + Z_m\left(v_b - v_e\right)\right] \tag{3.3}$$

and for the base

$$v_b = -M_b f_{mount} = M_b Z_{mount}\left(v_e - v_b\right) \tag{3.4}$$

$v_b$ can be written in term of $v_e$ using equation (3.4) and substituted in equation (3.3) so that from expression (3.2),

$$M_{ee} = \frac{M_e\left(1 + M_b Z_m\right)}{1 + Z_m\left(M_e + M_b\right)} \tag{3.5}$$

Similarly, for $f_e = 0$, using equation (3.1) it can be written that,

$$M_{be} = \frac{v_e}{f_b} \tag{3.6}$$

now

$$v_e = M_e f_{mount} = M_e Z_m (v_b - v_e) \tag{3.7}$$

and

$$v_b = M_b [f_b - f_{mount}] = M_b [f_b + Z_m (v_e - v_b)] \tag{3.8}$$

So that

$$M_{be} = \frac{M_e M_b Z_m}{1 + Z_m (M_e + M_b)} \tag{3.9}$$

As shown in Figure 3.4, a control actuator reacting between the equipment and the base structure generates a control force $f_a$ so that

$$f_e = f_a \text{ and } f_b = -f_a \tag{3.10, 3.11}$$

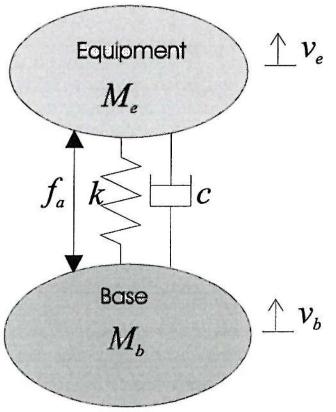

Figure 3.4. Principle schematic of the plant with massless mount using reactive actuator.

From equations (3.1) and (3.10, 3.11), $M_{total}$, the total effective mobility function from actuator force $f_a$ to equipment velocity $v_e$ is calculated as

$$M_{total} = \frac{v_e}{f_a} = M_{ee} - M_{be} \tag{3.12}$$

And then using equations (3.5) and (3.9) giving the expressions for the mobilities $M_{ee}$ and $M_{be}$ respectively,

$$M_{total} = \frac{M_e}{1 + Z_m\left(M_e + M_b\right)} \tag{3.13}$$

Since $M_{total}$ is proportional to the plant response $G$ defined in chapter 2 as the transfer function between secondary actuator input signal and control sensor output signal, expression (3.13) can be analysed to assess the stability of DVFB control using reactive actuator.

The total mobility function $M_{total}$ can be re-expressed thanks to equation (3.5) as,

$$M_{total} = \left(\frac{1}{1 + M_b Z_m}\right) M_{ee} \tag{3.14}$$

For a rigid base; i.e. perfect skyhook control, $M_b = 0$, and then $M_{total}$ is equal to $M_{ee}$. This bears out the fact that skyhook damping control is stable since $M_{ee}$ is an input mobility and thus fully passive which means that its phase is comprised between $-\pi/2$ and $\pi/2$. Expression (3.14) thus shows how the base dynamics affect a perfect skyhook control as considered in section 2, by adding an extra multiplicative term to the plant response.

No assumption on the base or the equipment structure has been made so far. However, a first category of problems to consider is the isolation of rigid equipment or stiff equipment which can be regarded as flexible only at high frequencies where the passive isolation is extremely efficient. A mounted box enclosing vibration sensitive electronic devices is a practical illustration of this class of isolation problems. Restricting the analysis to the simplest isolation problem possible also enables a strict assessment of the potentials of the actuation. A rigid system behaves as a masses $m$ so that at frequency $\omega$,

$$M_e = \frac{1}{j\omega m} \tag{3.15}$$

Using the lumped modelling of the mount as illustrated in Figure 3.4,

$$Z_m = \frac{k}{j\omega} + c \tag{3.16}$$

The actuator suspension can also be accounted for in the stiffness term $k$ and the damping term $c$ if its characteristics can not be neglected compared to the one of the passive mount. For the special case of a rigid equipment, the expression of the total mobility (3.13) can be rewritten as

$$M_{total} = \frac{1/j\omega m}{1+\left(k/j\omega + c\right)\left(1/j\omega m + M_b\right)} = \frac{1}{j\omega m + \left(k/j\omega + c\right)\left(1 + j\omega m M_b\right)} \tag{3.17}$$

A phase analysis of expression (3.17) can now be carried out in order to investigate the stability of the control as discussed in chapter 2. Noticing that $M_b$ is an input mobility, i.e. fully passive then,

$$-\frac{\pi}{2} < \angle M_b < \frac{\pi}{2} \tag{3.18}$$

therefore

$$0 < \angle\left(1 + j\omega m M_b\right) < \pi \tag{3.19}$$

strictly since damping is accounted for in the base structure. Moreover,

$$-\frac{\pi}{2} < \angle\left(c + k/j\omega\right) < 0 \tag{3.20}$$

So that

$$-\frac{\pi}{2} < \angle\left(c + k/j\omega\right) \cdot \left(1 + j\omega m M_b\right) < \pi \tag{3.21}$$

The first term of the denominator in expression (3.17), $j\omega m$, does not modify the phase limit of equation (3.21) and then,

$$-\frac{\pi}{2} < \angle\frac{1}{M_{total}} < \pi \tag{3.22}$$

The phase of the total mobility is then bounded as

$$-\pi < \angle M_{total} < \frac{\pi}{2} \tag{3.23}$$

The absolute value of the phase of the total mobility, $M_{total}$, is never greater than $\pi$. Therefore, the Nyquist plot of $M_{total}$ never crosses the negative real axis. Since $M_{total}$ is, in principle, proportional to the plant response $G$ and the controller is a simple feedback gain, equation (3.23) is equivalent to the condition

$$-\pi < \angle GH < \frac{\pi}{2} \tag{3.24}$$

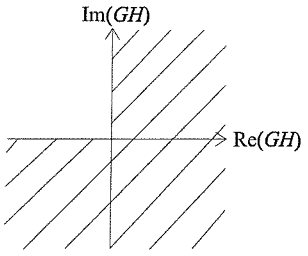

Figure 3.5. Possible region for the Nyquist plot of the plant using a reactive actuator.

Therefore, DVFB control of a rigid equipment mounted on a single mount is in principle unconditionally stable regardless of the dynamics of the base. This is an important result since it allows us to generalise the use of skyhook damping strategy to flexible and even very flexible base structure.

Even if the control is guaranteed to be stable, vibration amplifications may arise under the controller action since the phase of $M_{total}$ and then of the plant response $G$ could, in principle, get close to $-\pi$. This does not occur in practise. Assuming no damping in the mount, $c = 0$, equation (3.13) becomes

$$M_{total} = \frac{1}{j\omega m + {}^{k}\!/_{j\omega} + kmM_b} \tag{3.25}$$

Once again, going through the same process of phase analysis and noticing that $M_b$ in an input mobility it turns out that

$$-\frac{\pi}{2} < \angle M_{total} < \frac{\pi}{2} \qquad \text{when } c = 0 \tag{3.26}$$

When there is no damping in the mount, the control is fully passive which means that vibration reduction on the equipment is achieved at all frequencies, as already discussed in chapter 2. In practise, this statement is also satisfied at low frequencies since

$$c << \frac{k}{\omega} \tag{3.27}$$

and then

$$Z_m \approx \frac{k}{j\omega} \tag{3.28}$$

So that only vibration reduction is expected at low frequencies for any value of control gain.

### *Base vibration under equipment control*

When control is applied three forces acting on the base can be identified: the primary excitation $f_0$, the action of the passive mount reacting off ($-f_{mount}$) and the reactive control force, ($-f_a$) so that,

$$v_b = M_b\left(f_0 - f_{mount} - f_a\right) \tag{3.29}$$

Assuming the control is stable, the equipment velocity is driven to 0 as the gain increases to infinity, so that the sum of the forces acting on the rigid equipment is zero.

$$f_{mount} + f_a = 0 \tag{3.30}$$

Equation (3.29) becomes

$$v_b = M_b f_0 \tag{3.31}$$

The only contribution to the motion of the base structure is thus the primary excitation $f_0$. For an infinite gain control the base responds only to the primary force $f_0$ as if it was uncoupled from the rest of the system.

### 3.2.2. Experimental implementation

An experimental rig was designed to validate the theoretical conclusions drawn in the previous section on the stability of reactive implementation of DVFB control for the isolation of a SDOF rigid equipment.

### *Experimental set up*

The experimental isolation system consists of a unit called “the active isolator system”, which was designed by Gardonio [33], set on a flexible rectangular steel plate [16]. The active isolator system, shown in Figure 3.6, is composed of the equipment to be isolated and both the passive and the active isolation elements gathered in two identical active mounts. Each active mount is made of a hollow rubber cylinder bounded by two aluminium discs; this constitutes the passive isolation. Inside each rubber cylinder a steel rod connects the moving part of the control shaker, set on top of the thick mounted plate, with the bottom disc of the piece of rubber; this constitutes the active isolation. A reactive force can thus be generated in parallel of the passive isolation as shown in Figure 3.6(b). The suspended equipment gathers the suspended plate which is a thick aluminium plate and the two control shakers bolted to it. The whole system is symmetrical.

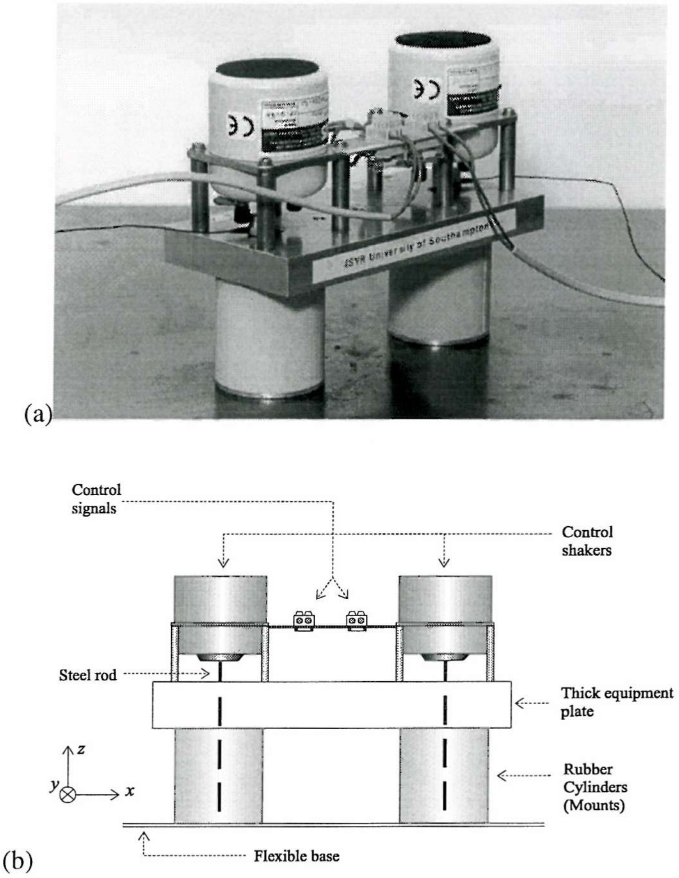

Figure 3.6. Photograph (a) and corresponding schematic (b) of the active isolator system

Once the active isolator system is set on a vibrating structure, the motion of the piece of equipment can be described as a combination of a heave motion (translation along $z$-axis) and a pitching motion (rotation around $y$-axis). The associated modes are very low in frequency compared to the first flexible modes of the equipment which is very stiff. It can then be regarded as a two degrees of freedom rigid body in the frequency range of interest for active isolation. Similarly the first resonances in the mount occur at high frequencies in comparison with the mounted rigid body resonance frequencies [33], at which the passive isolation is supposed to be very efficient. The rubber cylinders can then be modelled as lumped systems so that the global isolation device is simply modelled by the 2 DOF system shown in Figure 3.7.

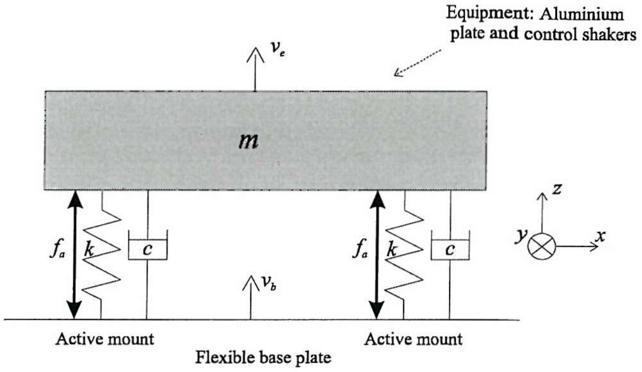

Figure 3.7. Low frequency model of the active isolator system.

Tables 3.1 and 3.2 give the physical and geometrical characteristics of the active isolator system according to the model presented in Figure 3.7. These values are the ones used in the simulations presented in this section.

| PARAMETER | VALUE |
|---|---|
| Equipment plate dimensions | $l_x \times l_y \times l_z$ = 200x100x18 mm |
| Density | 2700 Kg/m$^3$ |
| Mass of the aluminium plate | 1.08 Kg |
| Mass of the control shakers | 2×0.91 Kg |
| Total mass of the equipment | $m$ = 2.9 Kg |
| Moment of inertia of the equipment around $y$-axis | 4×10$^{-2}$ Kg.m$^2$ |
| Distance between mounts | 134 mm |

Table 3.1. Geometrical and physical characteristics of the equipment.

| PARAMETER | ACTIVE MOUNT |
|---|---|
| external diameter | 60 mm |
| internal diameter | 40 mm |
| height | 60 mm |
| axial stiffness | $k$ = 24000 N/m |
| including shaker suspension | ($k_a$ = 3900 N/m) |
| total viscous damping | $c$ = 18 Ns/m |

Table 3.2. Main characteristics of one rubber mount.

The active isolator system was set on a 2 mm thick steel plate clamped on two opposite edges (dimension 700 mm) and free at the others (500 mm). This plate constitutes the vibrating base structure and was excited by a primary shaker. For the purpose of running simulations before any control implementation, the base structure has been modelled using a modal decomposition according to Warburton's expressions for beam mode shapes and rectangular plate resonances [34]. Details of the modelling are given in [16]. An experimental analysis was conducted to validate the plate model. The first base plate resonances was measured at 32.5 Hz and predicted at 44.8 Hz. The discrepancies at low frequencies between the model and the measurements are due to the boundary conditions which do not behave as perfect clamped boundary at low frequencies. Better matching is observed for higher modes. The blocked heave resonance of the active isolator is calculated to be 20.5 Hz and measured at 19.1 Hz. The first base resonance and the mounted system resonance thus lie close to each other and so the base structure is regarded as flexible in the frequency range of active control efficiency.

To recover a single degree of freedom isolation system, the primary shaker was placed at the centre of the base structure so that only symmetrical modes of the base plate were excited. The active isolator system was then glued symmetrically at the centre of the base structure so that only the symmetrical modes of the base structure couple with the heave motion of the active isolator system. Furthermore the control sensor was positioned at the centre of gravity of the suspended equipment to avoid to monitor any potential residual pitching contribution in the control signal. The system can then be regarded as a single mount, single channel control system provided the control actuators are driven in phase.

### *Control loop*

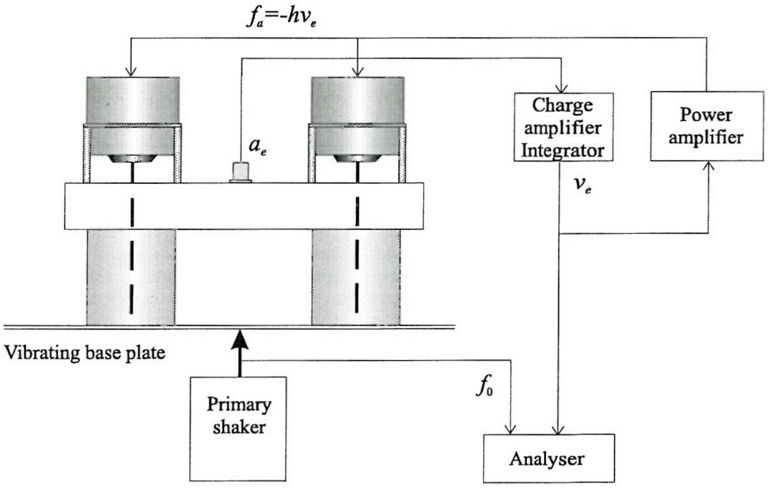

Figure 3.8. Experimental control setting and feedback loop.

The control sensor monitors the acceleration on the equipment. The sensor is a standard accelerometer B&K type 4375 connected to a charge amplifier which performs an analogue integration to obtain a signal proportional to the system velocity. The signal is then amplified through a power amplifier and fedback in both secondary actuators driven in phase, thus implementing DVFB control. (In Figure 3.8, the accelerometer and the charge amplifier are assumed to create a perfect velocity sensor).

### *Plant response measurement*

The measured plant response is the frequency response from the secondary actuator driving signal to the output signal of the charge amplifier. It was scaled by the gain factor applied by the charge amplifier on the velocity signal $v_e$ and by the efficiency of the secondary shakers; quantity defined in Newtons per volt (N/v), to obtain a corrected plant response that could be compared to $M_{total}$. $M_{total}$, the total mobility, is the simulated plant response which does not take the sensor and actuator behaviours into account.

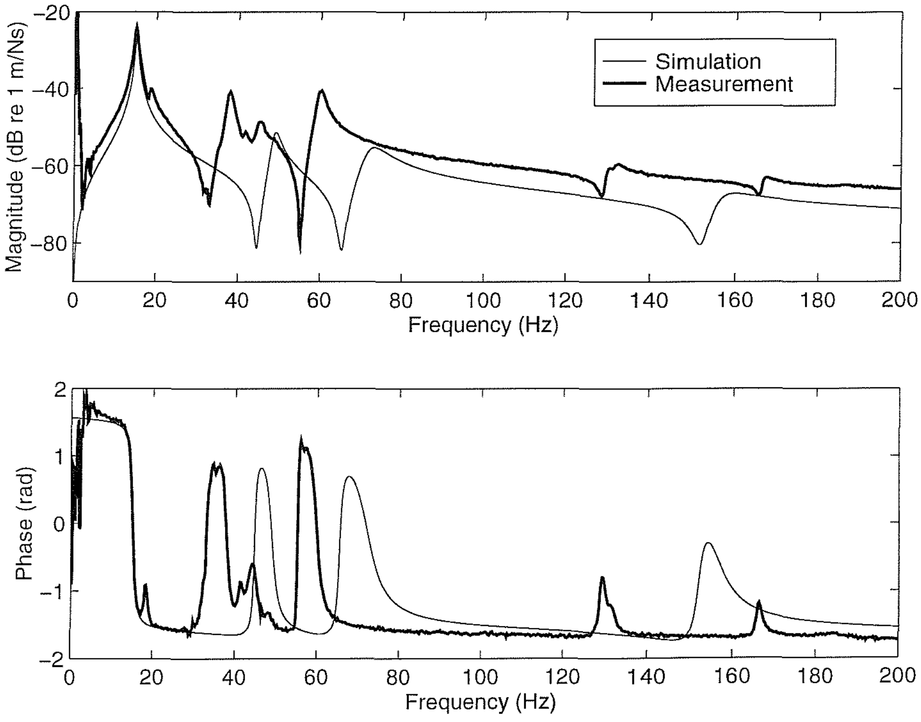

Figure 3.9. Magnitude and phase of the simulated and measured plant response for reactive control of rigid equipment.

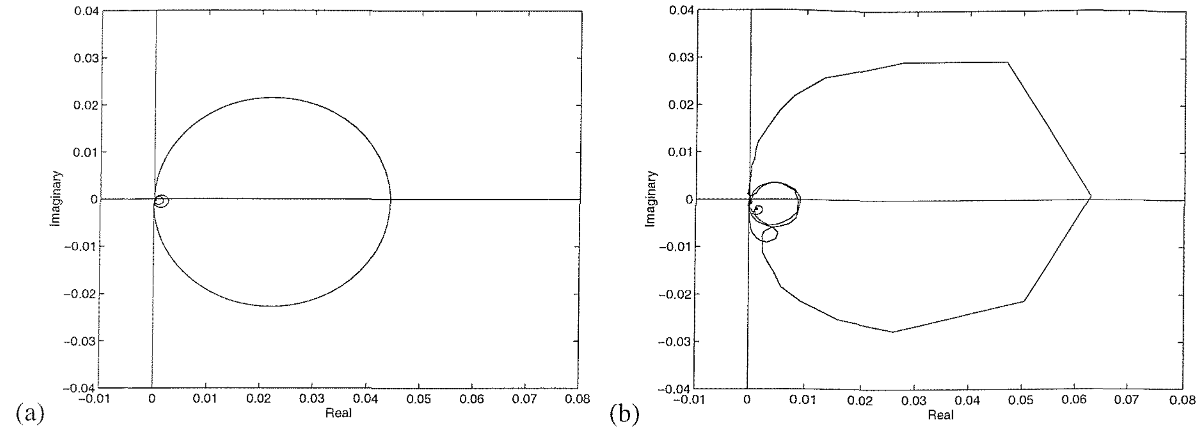

Figure 3.10. Nyquist plots of the simulated (a) and measured (b) plant responses for reactive control of rigid equipment.

Figure 3.9 compares the magnitude and phase of the simulated and measured plant response and Figure 3.10 presents the associated simulated, (a), and measured, (b), Nyquist plots. A rather good agreement is observed between the two contours mainly characterised by the large loop due to the mounted equipment resonance. Smaller loops can be noticed close to the origin. These are the effects of the base plate resonances on the mounted equipment. Almost the whole counter lies in the real part half plane. Not only does this satisfy the stability condition, but the system under control appears to be almost passive. It is in fact not fully passive unlike perfect skyhook damping, as observed in Figure 3.11(b). Moreover, ideal skyhook damping would offer a better control since the mounted equipment resonance loop is larger as shown in Figure 3.11(a).

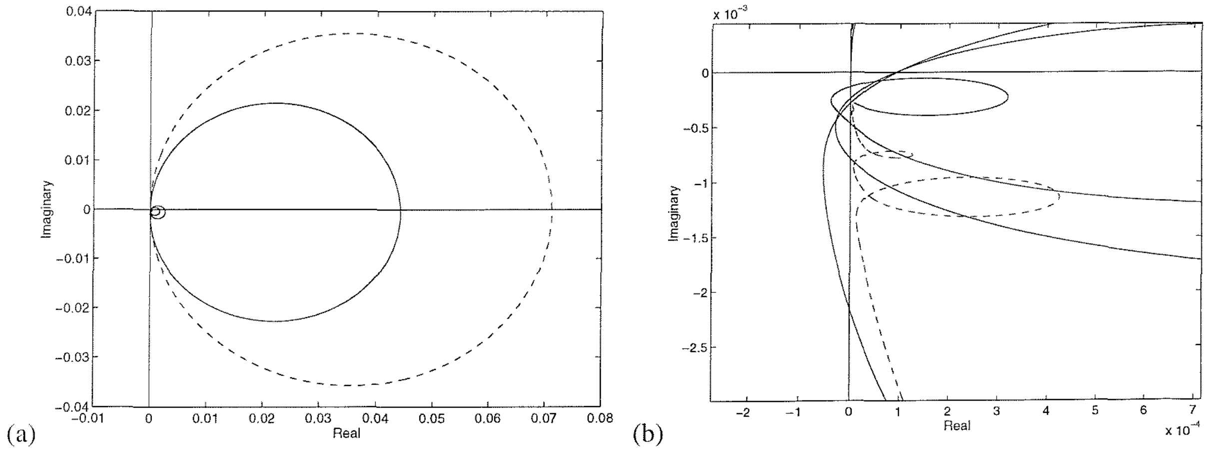

Figure 3.11. Simulated plant responses for rigid equipment control using reactive actuation (—) and perfect skyhook damping (---). Global Nyquist plot (a), zoom around the origin (b).

Going back to the general expression of the total mobility of the system under control, equation (3.17) can be rewritten as

$$M_{total} = \frac{1}{j\omega m + {}^{k}\!/_{j\omega} + c + kmM_b + j\omega mcM_b} \tag{3.32}$$

The phase response can only be significantly greater than $-\pi/2$ if the denominator of equation (3.32) is dominated by the term $j\omega mcM_b$ and provided the base structure is mass controlled so that

$$M_b \approx \frac{j\omega}{k_b} \tag{3.33}$$

and then

$$M_{total} \approx -\frac{k_b}{\omega^2 mc} \tag{3.34}$$

where $k_b$ is the equivalent modal stiffness of the base structure. Equation (3.34) also implies that the third term in the denominator, $kmM_b$, is negligible compared to $j\omega mcM_b$, which is equivalent to

$$\omega >> \frac{k}{c} \tag{3.35}$$

In practice, equation (3.35) is satisfied at rather high frequencies, where the first term in the denominator of equation (3.32), $j\omega m$, has then a large effect on the plant response so that equation (3.34) is not satisfied anymore.

This brief analysis explains why, in practise, the phase of the plant response does not approach $-3\pi/2$ closely, as noticed experimentally and shown in Figure 3.11(b). This prevents any strong control amplification. This conclusion must be balanced by the fact that no modal overlap in the base structure is taken into account in this analysis.

### *Control performance*

Thanks to the very stable characteristics of the control system, very high gains have been applied in the practical control implementation. The maximum experimental physical gain $h_{max}$ used was equal to 1800. This enables to achieve huge vibration reduction over the whole frequency range of interest as shown in Figures 3.12(a) and 3.12(b) for three values of control gain. The higher the control gain,

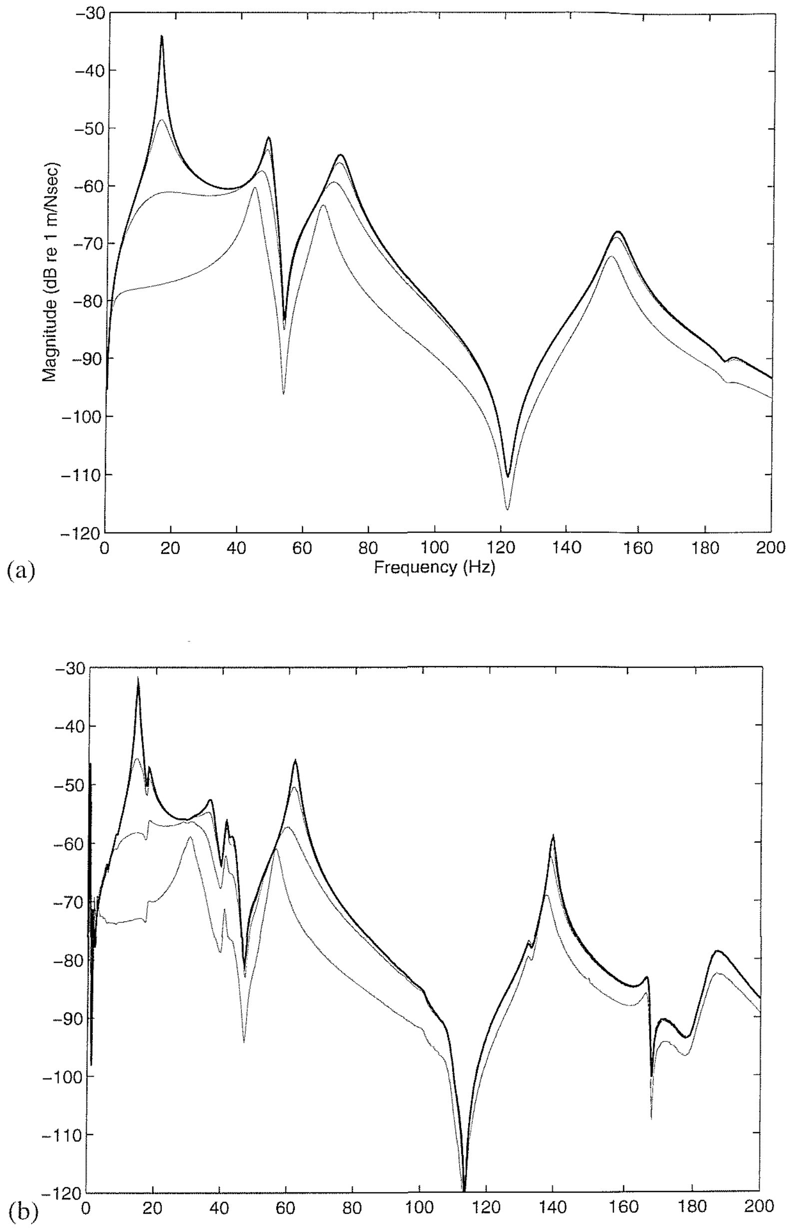

Figure 3.12. Simulated (a) and measured (b) velocity of the equipment per unit primary force for heave control using reactive actuators. Results are shown for the passive system (control off) (bold line) and three values of physical control gain $h$ (faint line): 55, 278 and 1800, which give progressively lower values of response.

the larger the vibration attenuation. The gain values are listed in Table 3.3 with the corresponding equivalent active damping ratio $\zeta_{act}$ that defines the control damping effect.

$$\zeta_{act} = \frac{h}{c}\zeta_{pass} \tag{3.36}$$

where $\zeta_{pass}$ is the passive damping ratio of the heave mode of the active isolator system and is equal to 4.8 %.

| Feedback gain $h$ | Active damping ratio $\zeta_{act}$ |
|---|---|
| 55 | 14.6 % |
| 280 | 74.7 % |
| 1800 | 480.0 % |

Table 3.3. Values of the control gain and equivalent active damping ratios for reactive actuator.

In order to obtain a good estimation of the control performance, Figure 3.12 shows the controlled equipment velocity normalised by the primary excitation $f_0$, which was almost unaffected by the controller, unlike the base velocity $v_b$, since the primary shaker impedance is very large. The main objective of DVFB control is well achieved since the resonance of the mounted rigid system is attenuated by up to 40 dB at 15 Hz. As expected from the theory and the plant response measurement, the control shows some efficiency at higher frequencies and allows attenuation of the disturbances generated by the base resonances: by up to 6 dB for the first mode and 14 dB for the third base structure mode. The control effect decreases uniformly with frequency as the passive isolation becomes more efficient, but no amplification is observed which is in agreement with the previous discussion on the plant response.

In practise, velocity is a difficult quantity to monitor at low frequencies. The charge amplifier associated with the accelerometer does not perform a perfect integration and therefore the low frequency velocity is badly estimated. This is due to the low-pass filtering operation of the integrator which adds phase shift in the close loop response. The power amplifier also presents a roll off frequency which creates an extra phase shift at low frequencies. Therefore, in practise, the electronics involved in the control drives the control system to instability for the use of very high control gains. This is not obvious in Figure 3.12(b) since it occurs at very low frequencies. However, strong equipment vibration reductions can be obtained before any significant vibration amplifications are noticed.

The experimental implementation of DVFB control on a SDOF system using reactive actuator bears out the theory developed in section 3.2.1, that the control is mechanically unconditionally stable in case of rigid equipment isolation on a single mount. The Nyquist plot of the plant response does not significantly enter the negative real part half plane and very large improvements of the passive isolation can then be obtained. The practical consideration of phase shift in the control loop at low frequencies prevents the use of infinite gains and sets a limitation on the overall vibration reduction achievable.

## 3.3. Inertial actuator for skyhook damping

### 3.3.1. Analysis of the plant response expression

The use of an inertial actuator for control allows us to decouple the secondary force from the flexible base structure as it reacts off the suspended inertial mass of the actuator, $m_a$, as shown in Figure 3.13. The total secondary force $f_s$ applied on the equipment in the upwards direction is now the combination of the force due to the actuator $f_a$ and that due to the actuator suspension so that

$$f_s = -f_a - Z_a(v_e - v_a) \tag{3.37}$$

where $Z_a$ is the impedance of the actuator suspension, $v_a$ is the actuator mass velocity and $v_e$ is the velocity of the equipment, as shown in Figure 3.13. The negative sign in front of $f_a$ comes from the convention that a positive actuator force $f_a$ is associated with an expansion of the free shaker.

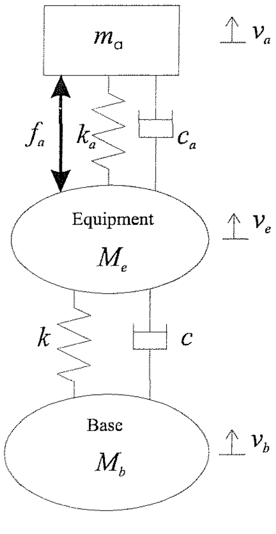

Figure 3.13. Schematic of inertial control.

Applying Newton's second law on the moving actuator mass $m_a$, at frequency ω it can be written that,

$$f_a + Z_a(v_e - v_a) = j\omega m_a v_a \tag{3.38}$$

so that

$$v_a = \left(\frac{1}{Z_a + j\omega m_a}\right) f_a + \left(\frac{Z_a}{Z_a + j\omega m_a}\right) v_e \tag{3.39}$$

Substituting equation (3.39) in expression (3.37), the secondary force $f_s$ on the system can now be expressed as a function of $f_a$ and $v_e$ as,

$$f_s = -\left(\frac{j\omega m_a}{Z_a + j\omega m_a}\right) f_a - \left(\frac{j\omega m_a Z_a}{Z_a + j\omega m_a}\right) v_e \tag{3.40}$$

If the equipment is fixed, $v_e = 0$, the transmissibility function relating the secondary force $f_s$ to an actuation force $f_a$ can be defined by

$$T_a = \frac{f_s}{f_a} = -\frac{j\omega m_a}{Z_a + j\omega m_a} \tag{3.41}$$

This transmissibility term is the blocked force response of the actuator and is illustrated in Figure 3.14. For an actuator suspension equivalent to a spring of stiffness $k_a$ in parallel with a damper of constant $c_a$, then

$$T_a = \frac{\omega^2 m_a}{k_a + j\omega c_a - \omega^2 m_a} \tag{3.42}$$

The amplitude of the secondary force is therefore equal to the force $f_a$ generated by the actuator for frequencies $\omega$ well above the blocked actuator resonance $\omega_a$. Then $T_a \approx -1$, where the minus sign account for the convention that a positive actuator input voltage and thus a positive feedback force $f_a$ will push the equipment downwards. At high frequencies, the secondary force $f_s$ is thus independent of the actuator dynamics. The control can then produce perfect skyhook damping. Equation (3.42) can be written as

$$T_a = -\frac{\Omega_a^2}{\Omega_a^2 - 1 - 2j\zeta_a\Omega_a} \tag{3.43}$$

where $\Omega_a = \omega/\omega_a$, $\omega_a = \sqrt{k_a/m_a}$ and $\zeta_a = c_a/2\sqrt{k_a m_a}$ are the normalised frequency, resonance frequency and damping ratio of the actuator.

Equation (3.40) can now be re-expressed as,

$$f_s = T_a f_a - Z_{aa} v_e \tag{3.44}$$

where

$$Z_{aa} = \frac{j\omega m_a Z_a}{Z_a + j\omega m_a} \tag{3.45}$$

is the input impedance of the inertial actuator as seen from the bottom of the suspension at the connection with the equipment.

When the isolation system shown in Figure 3.13 is excited by the actuator with a force $f_a$, it creates on the mounted equipment a secondary force $f_s$ such as the equipment responds with a velocity $v_e$ such as,

$$v_e = M_{ee} f_s \tag{3.46}$$

where $M_{ee}$ is the input mobility of the equipment coupled to base structure via the mounting system as already defined in section 3.2.1. The secondary force $f_s$ on the mounted equipment is then, from equation (3.44),

$$f_s = \frac{T_a}{1 + Z_{aa} M_{ee}} f_a \tag{3.47}$$

The equipment velocity response $v_e$ per unit actuator force $f_a$ which is proportional to the plant response is now obtained, combining equation (3.44) and (3.47).

$$\frac{v_e}{f_a} = \frac{T_a M_{ee}}{1 + Z_{aa} M_{ee}} \tag{3.48}$$

As already mentioned, a positive force $f_a$ is assumed to be a negative force contribution on the equipment, which already accounts for the minus sign in the control loop. A minus sign in front of the blocked transmissibility term is therefore added to be consistent with the equivalent expression derived in section 3.2.1 and with the control theory presented in chapter 2. The expression for the total mobility response is then,

$$M_{total} = -T_a M_{cc} \tag{3.49}$$

where

$$M_{cc} = \frac{M_{ee}}{1 + Z_{aa} M_{ee}} \tag{3.50}$$

is the input mobility at the top of the equipment for the full coupled system with base, mount, equipment and inertial actuator as shown in Figure 3.14.

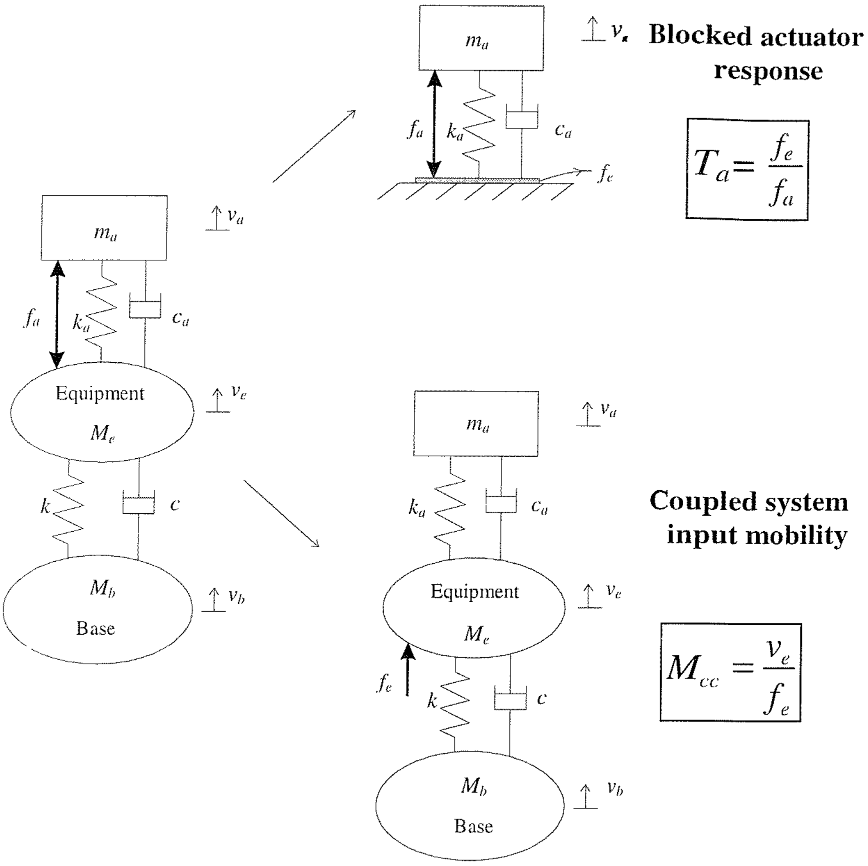

Figure 3.14. Schematic of the plant response decomposition for inertial control.

The phase analysis of the total plant response can be deduced from equation 3.49. First of all, $M_{cc}$ is an input mobility and is therefore fully passive, i.e. with a real part always positive so that

$$-\frac{\pi}{2} < \angle M_{cc} < \frac{\pi}{2} \tag{3.51}$$

strictly since passive damping is considered in the system. The perturbation in the plant response is introduced by the transmissibility term since,

$$0 < \angle - T_a = \angle \frac{\Omega_a^2}{\Omega_a^2 - 1 - 2j\zeta_a \Omega_a} < \pi \tag{3.52}$$

which adds a significant phase shift below the resonance of the blocked actuator $\omega_a$ as shown in Figure 3.15 for a typical response of blocked actuator and therefore,

$$-\frac{\pi}{2} < M_{total} < \frac{3\pi}{2} \tag{3.53}$$

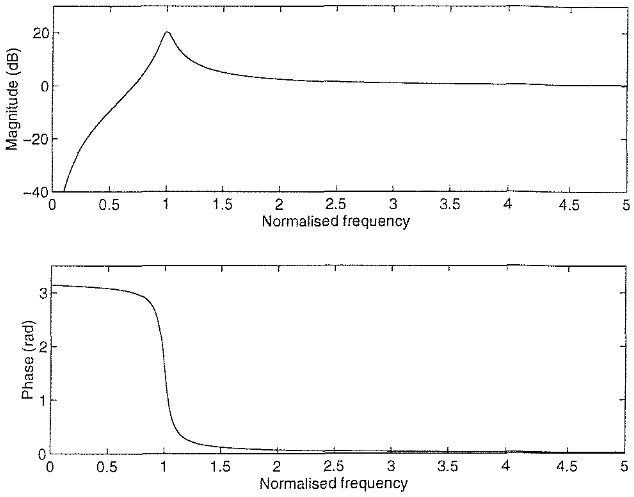

Figure 3.15. Magnitude and phase of ($-T_a$) for a typical inertial actuator.

It is known that reacting a force off a mass is very difficult at low frequencies as the mass is characterised by a small impedance The energy provided by the actuator is then mainly transformed into a motion of the inertial mass which explains the small amplitude of the actuator response in Figure 3.15 at low frequencies and therefore of the secondary force $f_s$. At the actuator resonance $\omega_a$, the absolute value of the blocked actuator response is large and a large control force can be applied on the equipment. However, there is still an associated phase shift of $\pi/2$ and the DVFB control is then equivalent to a perfect acceleration feedback control of the coupled isolation system with inertial mount on top. Above $\omega_a$, no instability can occur in the system since

$$0 < \angle(-T_a) < \frac{\pi}{2} \tag{3.54}$$

and then

$$-\frac{\pi}{2} < \angle M_{total} < \pi \tag{3.55}$$

Far above the blocked actuator resonance $-T_a \approx 1$, so that,

$$M_{total} \approx M_{cc} \tag{3.56}$$

$M_{total}$ is then passive and only reduction of the equipment vibration can be expected when DVFB control is implemented. This is because the inertial mass mobility becomes so large that the actuator force $f_a$ seems to react off a rigid ground as represented in Figure 3.16.

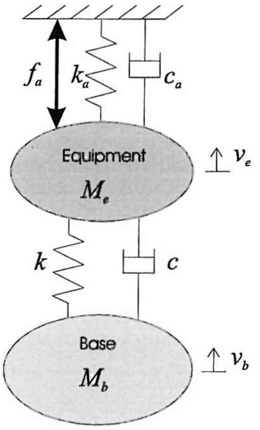

Figure 3.16. High frequency model of the plant with inertial actuator.

To illustrate the effect of the actuator dynamics on the plant response, a simple system consisting of a rigid mass mounted on a vibrating base is considered. For simplification, the base is assumed to be rigid as shown on Figure 3.17 so that its dynamics can be neglected. This does not restrict the analysis since $M_{cc}$ is still an input mobility with a phase oscillating between $\pm\pi/2$, even if the problem can now be regarded as 2 DOF system.

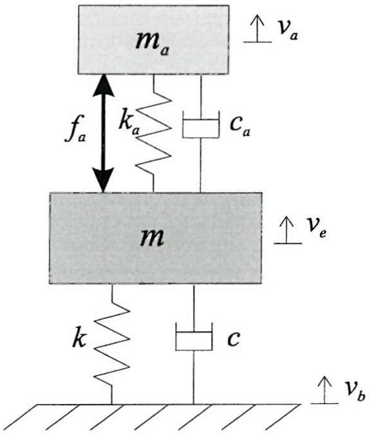

Figure 3.17. Simplified isolation system on a rigid base using inertial actuator.

The characteristics of the actuator, $m_a$ and $k_a$, are adjusted so that the blocked actuator resonance is half of the mounted equipment resonance $\omega_e = \sqrt{k/m}$. Figure 3.18 shows the magnitude, phase and Nyquist plot of the total mobility function (mechanical plant response). The first resonance of the coupled system, around 20 Hz, is mainly related to the inertial mass motion whereas the second one at 60 Hz can be called the equipment resonance even if it is different from the uncoupled resonance $\omega_e$ which is equal to 50 Hz. This is not true if $\omega_a$ is much closer to $\omega_e$ since the two mass motions are then strongly coupled.

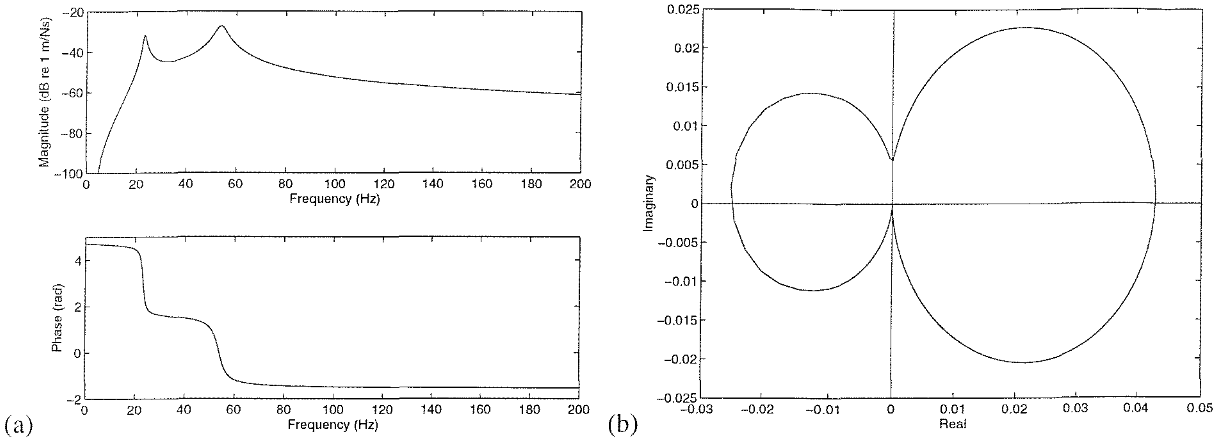

Figure 3.18. Magnitude and phase (a) and Nyquist plot (b) of the plant response for inertial control of a suspended mass mounted on a rigid vibrating base structure.

Above 40 Hz, as the system dynamics is dominated by the mounted equipment dynamics, the phase of the total mobility varies from $\pi/2$ to $-\pi/2$ asymptotically, as shown in Figure 3.18(a). In the Nyquist contour, this is responsible for the large loop in the positive real part half plane. Good control is thus expected at high frequencies. However, when the system motion is controlled by the actuator behaviour, below 30 Hz, the actuator resonance being not separated from the equipment resonance by an anti-resonance, an extra phase shift is introduced into the mobility response so that the phase now varies from $3\pi/2$ to $\pi/2$ at low frequencies. This is represented in the Nyquist plot in Figure 3.18(b) by the extra smaller loop in the left hand side of the plane, which induces a stability limitation in the control as the contour crosses the negative imaginary axis. Direct velocity feedback (DVFB) control is therefore gain limited when an inertial actuator is used.

### 3.3.2. Maximum control gain and maximum attenuation

Under certain assumptions, which are usually satisfied in practise, a simple analytical expression for the maximum physical gain $h_{max}$ can be derived as well as for the corresponding maximum attenuation.

The phase response of the total mobility $M_{total}$ will be $\pi$ very close to $\omega_a$ if the actuator dynamics is well decoupled from the isolation system, i.e. $\omega_a \ll \omega_e$, where $\omega_e$ is the first resonance of the mounted equipment for the general isolation case illustrated in Figure 3.13. Under this condition and provided the actuator is significantly damped, it can be shown that

$$M_{cc}(\omega_a) \approx M_{ee}(\omega_a) \tag{3.57}$$

Assuming the first resonance of the mounted equipment $\omega_e$ does not significantly overlap with the higher order resonances of the mounted equipment then, below and around $\omega_e = \sqrt{k_e/m_e}$,

$$M_{ee} = \frac{j\omega/m_e}{\omega_e^2 - \omega^2 + 2j\zeta_e\omega_e\omega} \tag{3.58}$$

where $\zeta_e$ is the passive damping ratio associated with the first resonance of the isolation system. $m_e$ and $k_e$ are the corresponding modal mass and modal stiffness. They can often be, in practise, regarded as the mass of the mounted equipment $m$ and the passive mount stiffness $k$ but not in case of a very flexible base or equipment structure. Then,

$$M_{ee}(\omega_a) \approx \frac{j\omega_a}{m_e\omega_e^2} \tag{3.59}$$

and from equation (3.57)

$$M_{cc}(\omega_a) \approx \frac{j\omega_a}{m_e\omega_e^2} \tag{3.60}$$

It is also clear, from equation (3.43), that

$$T_a(\omega_a) = 1/2j\zeta_a \tag{3.61}$$

Assuming perfect actuator and sensor, the open loop response can be expressed in term of the total mobility and the physical control gain as

$$GH = hM_{total} \tag{3.62}$$

As already discussed, providing $\omega_a \ll \omega_e$, instability in the system will arise at a frequency close to $\omega_a$ so that, according to equation (3.62), the maximum gain $h_{max}$ that can be applied to the system is,

$$h_{max} = -\frac{1}{M_{total}(\omega_a)} \tag{3.63}$$

and using equation (3.49),

$$h_{max} = \frac{1}{T_a(\omega_a) M_{cc}(\omega_a)} \tag{3.64}$$

now using equations (3.60) and (3.61)

$$\boxed{h_{max} = 2\zeta_a m_e \frac{\omega_e^2}{\omega_a} = c_a \frac{k_e}{k_a}} \tag{3.65}$$

The maximum attenuation will in practice occur around the first mounted equipment resonance $\omega_e$. $M_{ee}$ is then damping controlled in which case, since $M_{cc}(\omega_e) \approx M_{ee}(\omega_e)$,

$$GH(\omega_e) \approx -T_a(\omega_e)\left(\frac{1}{2m_e \zeta_e \omega_e}\right)h \tag{3.66}$$

and $T_a(\omega_e) \approx 1$. The maximal attenuation in dB is defined as

$$Att_{max}(dB) = 20\, log\left(1 + GH_{max}(\omega_e)\right) \tag{3.67}$$

and

$$GH_{max}(\omega_e) = h_{max} M_{total}(\omega_e) \approx \frac{\zeta_a \omega_e}{\zeta_e \omega_a} \tag{3.68}$$

so that

$$\boxed{Att(dB) = -20\, log\left(\frac{\zeta_e \omega_a}{\zeta_e \omega_a + \zeta_a \omega_e}\right)} \tag{3.69}$$

The two expressions for the maximum control gain and the maximum vibration attenuation show that in order to obtain a large gain margin and therefore good control of the mounted equipment, the actuator must be significantly damped and its blocked resonance must be much smaller than the first mounted equipment resonance $\omega_e$. A small actuator resonance also allows us to reduce the low frequency range of control amplification.

### 3.3.3. Experimental implementation

*Experimental setting*

The conclusions drawn from the theoretical analysis in the previous two sections were validated on a modified form of the experimental setting already used for the reactive implementation of direct velocity feedback control in section 3.2. The two electrodynamic control shakers used to apply a reactive secondary force were disconnected so that the rigid equipment was only the thick aluminium receiving plate. One of these shakers was then put on top of the centre of the rigid receiver, as shown on Figure 3.19, so that its mass acts as the inertial mass $m_a$.

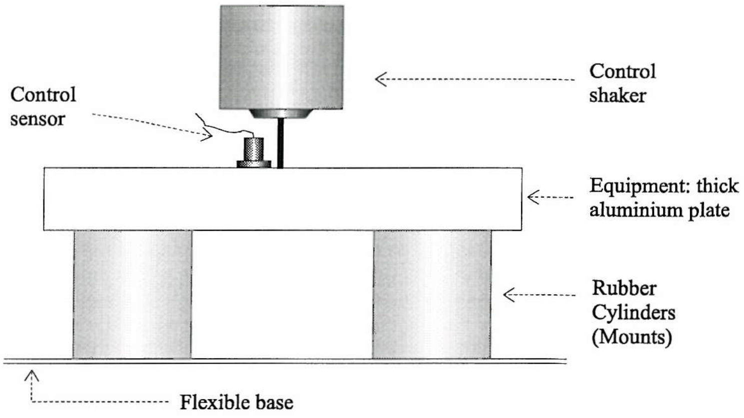

Figure 3.19. Schematic of the experimental isolator system with the inertial actuator.

Simulations were also performed using the same model as developed for the study of reactive feedback control. The passive mount parameters were slightly changed by the removal of the reactive actuators and the parameters $m_a$, $c_a$ and $k_a$ of the suspended actuator were added to the model, as presented in Figure 3.20. The new parameter values are listed in Table 3.4.

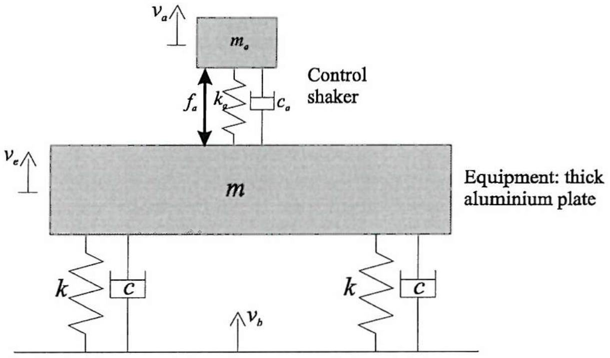

Figure 3.20. Low frequency model of the experimental isolator system with the inertial actuator.

As for the experimental implementation of reactive control, the base structure was excited by a primary shaker generating a force $f_0$ at the centre of the base plate so that the mounted equipment could only be excited in vertical translation. The control sensor was also positioned at the centre of gravity of the equipment, as seen in Figure 3.19 to avoid any strong residual pitching motional component. The control loop is similar to the one described in the reactive control setting except that only one secondary actuator is now fed with the control signal.

| Parameters | Equipment mounted plate | Blocked inertial actuator |
|---|---|---|
| mass | $m = 1.08$ Kg | $m_a = 0.91$ Kg |
| total stiffness | $2\,k = 40\,000$ N/m | $k_a = 3900$ N/m |
| viscous damping | $2\,c = 17.7$ Ns/m | $c_a = 5.8$ Ns/m |
| natural frequency | $\omega_e = 23.5$ Hz | $\omega_a = 10.4$ Hz |
| damping ratio | $\zeta_e = 2.4$ % | $\zeta_a = 4.8$ % |

Table 3.4. Characteristics of the experimental isolator system and inertial actuator.

### *Plant response measurement*

The measured plant response is the frequency response between the output signal of the charge amplifier and the signal input in the secondary actuator. It was then scaled as previously described in section 3.2 to be compared to the simulated mobility function $M_{total}$. Figure 3.21 shows the magnitude and phase of the simulated and scaled measured plant responses whereas Figure 3.22 presents the associated Nyquist plots. The model exhibits good agreements with the experimental results so that the measured gain margin of the control can be checked by the simulations.

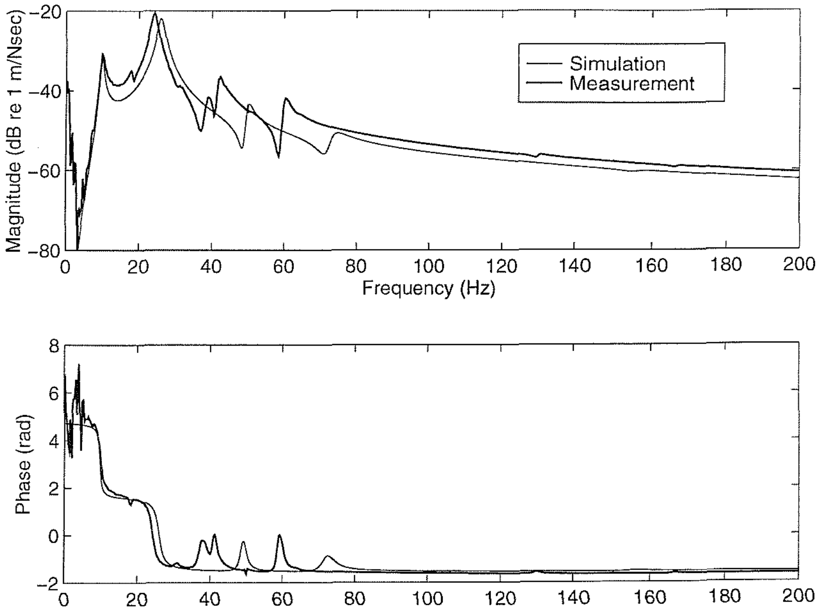

Figure 3.21. Magnitude and phase of the simulated ($M_{total}$) and measured plant responses for inertial control.

The magnitude of the measured plant response exhibits two main peaks. The first one at 9.5 Hz is the mounted actuator resonance which is very close to the value of the blocked actuator resonance. This means that the actuator dynamics can be regarded as reasonably well decoupled from the mounted equipment. The second peak occurs at 23.5 Hz on the measured plot, 2 Hz lower than the simulation. It is due to the mounted mass heave resonance and is therefore mainly associated with a motion of the mass $m$. The measurement offers a very poor coherence at low frequencies because of a low SNR but the phase response does clearly show the extra $\pi$ phase shift induced by the actuator dynamics which leads to a first phase jump from $3\pi/2$ to $\pi/2$. As the frequency increases, the mounted equipment dynamics become of primary influence and generate a second phase jump from $\pi/2$ to $-\pi/2$. Other phase variations are noticed above $\omega_e$, as the result of the base plate resonances, but do not fall below $-\pi/2$ and thus do not threaten either the stability or the efficiency of the control, as already discussed in the theoretical analysis. The higher order resonances due to the plate dynamics seem to be filtered out at relatively low frequencies in the plant response, at around 80 Hz. This illustrates the characteristic of inertial control which decouples quite efficiently the control force from the base structure dynamics.

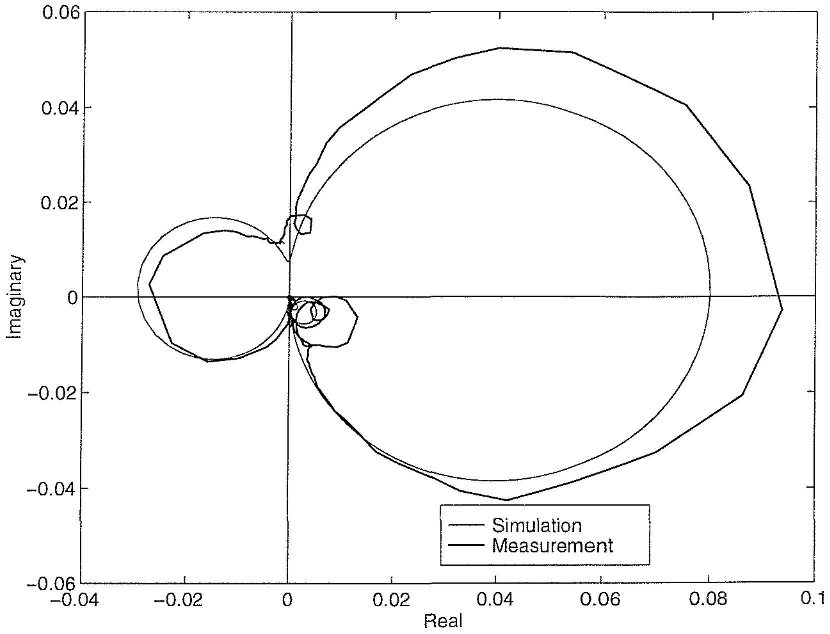

Figure 3.22. Nyquist plot of the simulated ($M_{total}$) and measured plant responses for inertial control.

In term of the Nyquist representation, the contour of the plant draws a clear loop inside the negative real part half plane as the actuator mass resonates on top of the equipment as shown in Figure 3.22. A pure gain control is thus clearly limited. The second plant phase jump associated with the main equipment resonance is represented by a large loop in the stable half plane. Smaller resonant loops can also be noticed as the base plate resonances affect the equipment vibration. As discussed in the theoretical development of the plant response, an inertial implementation of velocity feedback offers a very clean plant to control at high frequencies but is gain limited because of the low frequency behaviour of the coupled secondary actuator.

*Control performance*

The experimental and simulation performance are presented in Figure 3.23(a) and 3.23(b) when the controller is not running and for two values of feedback gain: $h = 11$ and about $h_{max}$, equal to 36 in the experiment and to 30 in the simulation.

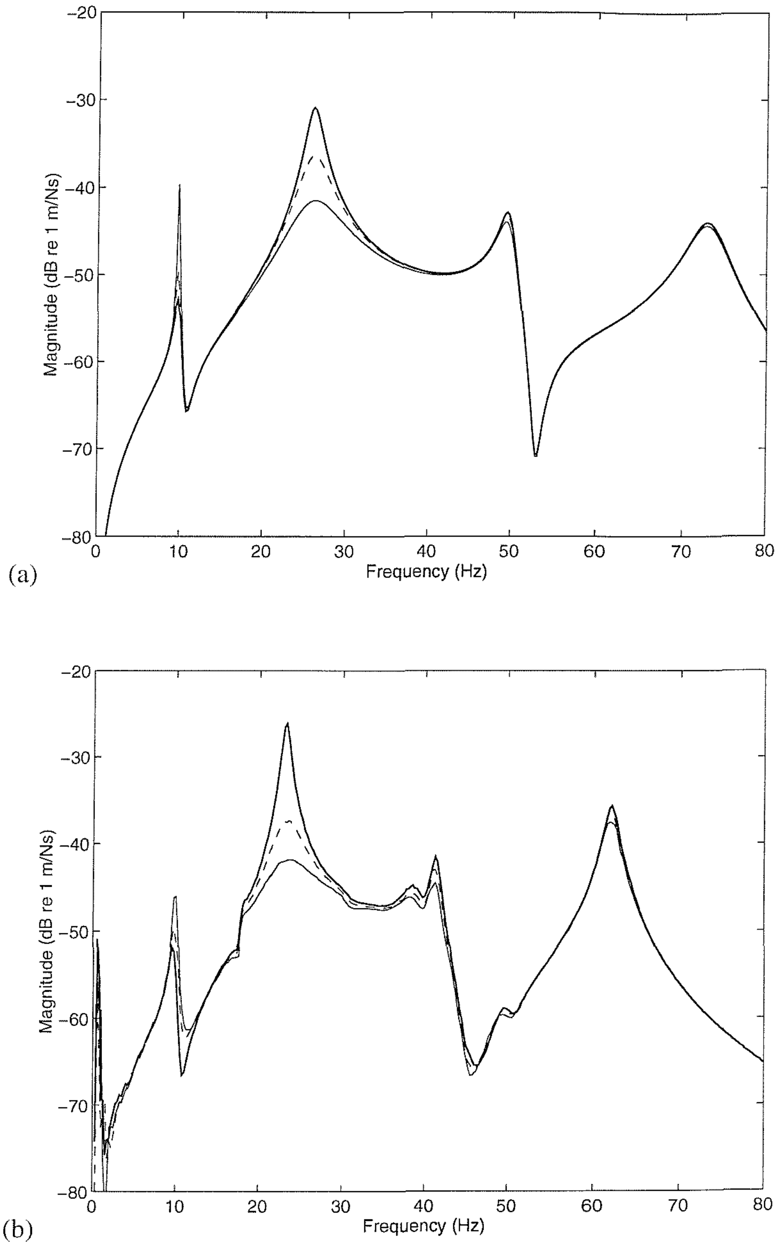

Figure 3.23. Simulated (a) and measured (b) equipment velocity per unit primary base excitation force. Results are shown for the passive system (control off) (bold line) and for two values of control gain (dashed and faint line) for which the higher gain (faint line) is close to instability.

When control is implemented, significant attenuation of the first mounted system resonance is obtained at 23.5 Hz. This good result is balanced by an amplification of the equipment vibration below 14 Hz and by a net increase at the actuator resonance around 9.5 Hz, since the contour of the open loop response starts to approach the unstable point as the control gain is gradually increased. Onset of instability is experimentally observed for an experimental gain of 36 which provides about 15 dB attenuation of the main equipment resonance, 13 dB according to the simulations whereas the predicted value of maximum attenuation given by equation (3.69) is 16 dB. No further reduction can be achieved. The attenuation is rather small at high frequencies since the feedback gain is limited and therefore the controller does not have enough control power to improve the isolation provided by the passive mounts. The results in Figure 3.23 are thus presented on a more restricted frequency range than these in Figure 3.12 for reactive control.

## 3.4. Conclusions

Since in practice no inertial ground is available to react a secondary force off, there exist two obvious practical ways of implementing absolute velocity feedback control on mounted systems, which have been detailed in this chapter: the reactive implementation, where the secondary force reacts off the flexible vibrating base structure and the inertial implementation, requiring an extra suspended mass to react the secondary force off. Restricting the study to single degree of freedom isolation systems, the first strategy was proved to be unconditionally stable in the special but realistic case of rigid equipment control. In practise, the low frequency phase shift in the control loop and especially in the transducer conditioning electronics drives the system to instability for very high control gains. In this rather academic exercise, the interest was however focused on the mechanical response of the control system in order to assess its potential. It appeared that a reactive implementation of velocity feedback provided very large enhancements of the passive isolation, cancelling the low frequency amplification caused by the passive isolators.

Not so good performance were obtained by the inertial controller which was proved to be gain limited. Expressions for the maximum control gain and maximum attenuation were derived. They show that to be efficient, the natural frequency of the inertial actuator has to be low in comparison with the dynamics of the suspended system and it should have a rather large internal damping. Under these conditions, high frequency reduction can be expected but vibration amplification will still be observed at the vicinity of the secondary actuator resonance. The actuator resonance can be reduced by increasing the inertial mass or setting a very soft suspension but this is likely to induce static limitations and design problems. Inertial actuation must, however, be considered since it can easily be set on top of a mounted structure in a self-contained control unit whereas a reactive actuator must be integrated into the passive mount which is technologically challenging. Moreover, inertial actuation does not require us to identify a passive transmission path and can be used on any vibrating structure independently of mounting systems. This is illustrated mathematically by expression (3.49) which is independent of the passive isolation since $M_{cc}$ only has to be an input mobility. Finally, the use of electronic compensators should be investigated at low frequencies as they could increase the gain margin of the inertial controller.

# Chapter 4

# Inertial implementation of DVFB control on a mounted flexible equipment

## 4.1. Introduction

As outlined in the introduction chapter, the objective of this chapter is now to extend the principle of DVFB to the control of mounted flexible equipment structure. In practice this means we have to deal with multi-mount systems and therefore with multi-structural transmission path problems. Both the equipment and the base structures are considered flexible so that no assumption is made on the main system elements unlike in chapter 3. This analysis is therefore a strong assessment of the potentials of inertial DVFB in controlling vibration transmission to suspended structures. The use of DVFB control for active isolation of mounted structures is based on two ideas, as outlined in chapter 1:

- DVFB control can implement skyhook damping under certain conditions, which is known to strongly reduce vibration at the control location.

- The source of disturbances, i.e. the connections of the equipment structure with the passive isolation, is a sensible location for local control.

This very simple control strategy differs, however, from an optimal active isolation which would consider:

- The power input in the equipment structure at the mount junctions as the control quantity. This would require us to take into account both velocity and input force at the mount junctions to insure a global control of the equipment.

- the possibility of centralised or internal model control to take full advantage of the different control channels and to guarantee the stability of the controller.

In this study, vibration control is first attempted at the control locations but a local vibration reduction at the mount junctions does not guarantee an overall reduction of the dynamics of the equipment structure. A global reduction of the equipment structure vibration is however desired.

Therefore, in this chapter, as in chapters 5 and 6, the different analysis attempt to estimate the global isolation effect of a DVFB control implemented on the equipment structure at the mount junctions.

In this chapter, an inertial implementation of the control is experimentally investigated using an experimental arrangement lent by the Aero-Structures Department at DERA Farnborough. This rig was designed with reference to an aircraft fuselage, where passive isolation is inserted between the external metallic fuselage, subject to vibration excitation, and the internal shell. This was done to assess the extend to which local active control at the junctions with the passive isolation could reduce the structural sound transmission through this double panel system: from the external fuselage to the internal panel inside the aircraft body. The analysis reported here is not an ASAC study however, since it only considers vibration isolation. The test rig should thus strictly be regarded as two flexible structures coupled by passive isolators. The acoustic power radiated by the mounted panel is not estimated and any noticeable reduction of the radiated sound may be considered as a bonus. The experimental test rig, based on a practical application offers, however, a relevant framework for an experimental analysis.

This chapter first presents the inertial control test rig and the main expected effects of the inertial actuators on the system dynamics. Simulations for single channel control based on measured plant responses are then produced and discussed. The results for real time implementation of a single-channel control system are also presented. Finally simulations for a multichannel controller based on the measured plant response are performed and the limitations of DVFB control using inertial actuators is addressed.

## 4.2. The experimental test rig

The fuselage of a civil aircraft is a double shell system. The external skin is an aluminium shell stiffened by a longitudinal set of elements, the stringers, and a transversal set of elements, the frames. Light honeycomb composite panels or trim panels constitute the equipment structure, in our terms, which has to be isolated from the external excitation generated on the aluminium shell by flow turbulence or engine noise. The disturbance is propagated along the stiffeners and through a set of rubber mounts which is inserted to isolate the internal composite shell from the external metallic structure vibration. The primary disturbances can be considered directly applied on the stringers and the experimental test rig is therefore composed of three main elements: an aluminium U-shape beam or stringer for the base structure, 3 rubber mounts for the passive isolation and a rectangular composite panel or trim panel for the equipment structure. The material and dimensions of the three different elements constituting the isolation system are listed in Table 4.1.

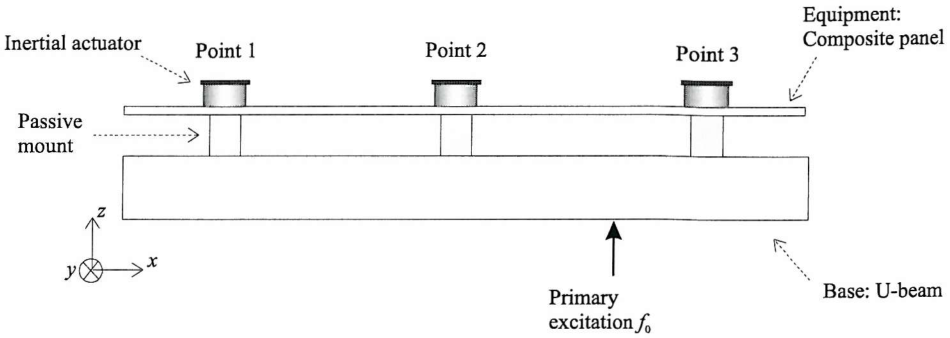

Figure 4.1. Schematic of the experimental test rig.

| | Main dimensions (in mm along $\vec{x}$ and $\vec{y}$) | Height (in mm) | Thickness (in mm) | Material |
|---|---|---|---|---|
| Equipment panel | 756 x 556 | ** | 4 | Composite |
| U-beam | 756 x 23 | 23 | 1.5 | Aluminium |
| 1 mount | ∅ = 30 | 30 | ** | Hard rubber |

Table 4.1. Main characteristics of passive elements in the coupled isolation system.

| Point | Position (*x*,*y*) in mm |
|---|---|
| 1 | (278,125) |
| 2 | (278,377) |
| 3 | (278,630) |

Table 4.2. Positions of the mount/actuator junctions on the equipment panel.

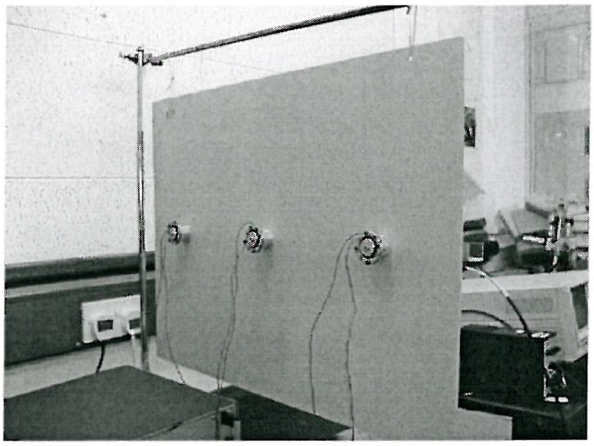

Figure 4.2. Photograph of the three inertial control actuators on the centre line of the composite panel.

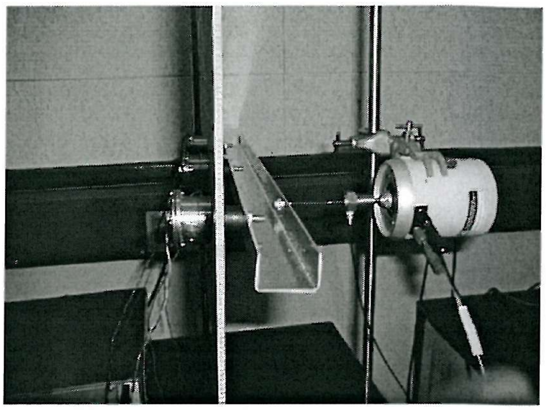

Figure 4.3. The connection between actuator and mount through the composite panel.

Three inertial shakers are bolted on the equipment composite trim panel at the vertical of the junctions with the rubber mounts, as shown in Figures 4.1 and 4.3. The coordinates of the mount/actuator junctions on the panel are given in Table 4.2.

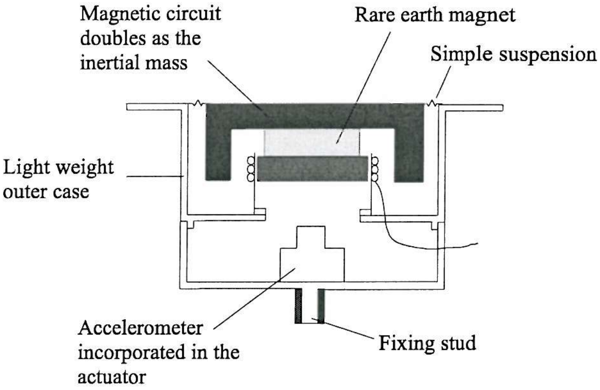

Figure 4.4. Sketch of the internal design of the inertial actuator

Figure 4.4 shows a sketch of the internal design of one inertial actuator. The permanent magnet is suspended by an elastomeric suspension so that it is centred on top of the coil which is fixed to the body of the actuator. Current in the coil moves the magnet up and down which also acts as the inertial mass and therefore is able to generate an axial control force. The inertial mass, $m_a$, is equal to 77 g and the actuator suspension can be characterised by a static axial stiffness, $k_a$, which was estimated to be equal to 23 kN/m. An embedded accelerometer positioned on the actuator body enables the measurement of the local response of the system at the control location. Accounting for viscous damping in the secondary control actuator, the global system can then be represented as shown in Figure 4.5, where the shaker suspension is modelled as a spring in parallel with a viscous damper and the actuator body by a point mass on the equipment panel which has an effect on the system dynamics as the frequency increases. This low frequency model of the secondary actuation devices is good enough in the frequency band of interest.

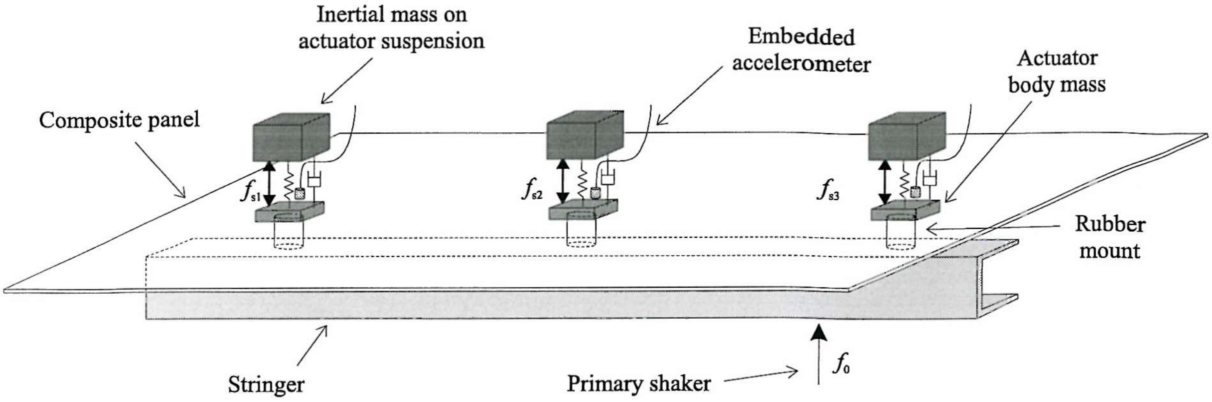

Figure 4.5. Schematic of the global isolation system with modelled representation of the control actuators.

## 4.3. Expected performance and control limitations

### 4.3.1. Effect of rotation excitation

As already mentioned in chapter 1, the inertial controller can only apply a vertical control force in the *z*-direction whereas both axial displacement *w* and rotation $\theta_x$ and $\theta_y$ around $\vec{x}$ and $\vec{y}$ occurs along the U-beam, generating axial but also rotational excitation at the bottom of the mounts. In principle, perfect control of the vibration transmission would also require secondary actuators able to generate rotational excitations by applying two control moments $M_{sx}$ and $M_{sy}$. Gardonio [25] illustrated the effects of the rotation on the vibration transmission in the case of two aluminium plates connected by a set of three rubber mounts. He showed by simulations that, for the system he considered, such rotational effects were small at low frequencies but increased with frequency. The implementation of only an axial control system was sufficient to give good reductions in vibration transmission since the role of an active controller is to supplement the unsatisfactory low frequency performance of a passive isolation. At higher frequencies, around 1 kHz, the rotational excitation in the mount limited the control performance obtained by Gardonio, but the passive isolation was significant in this frequency range.

For the system considered in this study, however, a strong extra rotational excitation $\theta_x$ is likely to arise since the primary excitation applied at the centre of the bottom flange of the U-beam will tend to twist the beam around the *x*-axis, as shown in Figure 4.6. Even if the high frequency effect of rotational excitation is compensated by the efficiency of the passive isolation, this could constitutes a limitation to the performance of the active control.

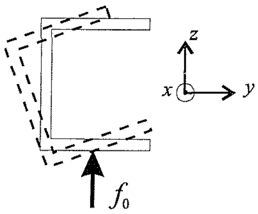

Figure 4.6. Twisting effect of the primary excitation on the base structure.

However, since any rotational excitation is coupled with vertical displacement over the panel, an axial control force directly proportional to the axial velocity of the system at the control point may have a control effect on the rotational excitation undergone by the equipment panel. Moreover, two control forces due to two control actuators acting on the equipment can apply a control moment and may thus have a control authority on the rotational vibration provided the distance between the two control actuators is smaller that half the wavelength in the mounted equipment panel. This short discussion on the coupling between translation and rotation in the system illustrates the complexity of designing a perfect full control for vibration transmission to a mounted system. In the low frequency range [0-1 kHz], which is going to be considered here, an axial actuation is however expected to be efficient enough to proceed to the analysis of DVFB control.

### 4.3.2. The secondary actuator dynamics

The plant response for a single channel DVFB control using an inertial shaker is proportional to the total mobility $M_{total}$ derived in chapter 3 and given by equation (4.1).

$$M_{total} = -T_a M_{cc} \tag{4.1}$$

where $M_{cc}$ is the input mobility of the isolation system coupled with the inertial actuator at the control location and $T_a$ is the blocked actuator response. Such a control system is, in a way, independent of the different elements of the mechanical system, since the only assumption made in the stability discussion in chapter 3 is that $M_{cc}$ is an input mobility. Equation (4.1) is therefore valid for a single channel DVFB inertial control in the case of vibration isolation of a flexible structure as it would be valid for any mechanical system. Therefore, as discussed in chapter 3, the secondary actuator dynamics will set the boundary between the low frequency band of control amplification and the high frequency band of control vibration reduction. A first estimation of the control capacities for a single channel but also for a multichannel implementation can then be drawn from the measurement of the blocked actuator response $T_a$. $T_a$, as defined in chapter 3, is the ratio between the force generated by the blocked actuator on the reacting mass, $f_a$, and the effective secondary force applied on the blocking frame, $f_e$. Similarly, the experimental transmissibility $T_a'$ is defined as the ratio between the voltage input in the current amplifier which drives the secondary actuator, $v_{in}$, and the resulting blocked secondary force $f_e$.

$$T_a' = \frac{f_e}{v_{in}} \tag{4.2}$$

This quantity is convenient since it is easy to measure and allows us to include the current amplifier and the whole electro-mechanical behaviour of the actuator in the plant response. Further details are given in section 4.4, describing the experimental control loop and providing the full definition of the experimental plant response.

$T_a'$ was measured by fixing one inertial actuator to a rigid frame. The input voltage $v_{in}$ is easy to monitor whereas the resulting force was estimated by measuring the acceleration of the inertial mass with a B&K accelerometer, type 4375, and using the relation

$$f_e = m_a \ddot{w}_a \tag{4.3}$$

the mass of the accelerometer being negligible compared to the inertial mass $m_a$.

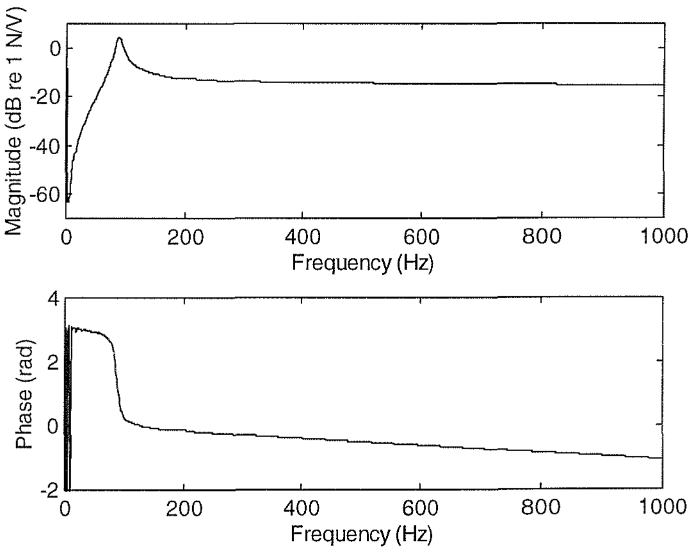

Figure 4.7. Blocked actuator force response per unit voltage input in the driving current amplifier.

Figure 4.7 shows the measured transmissibility ($-T_a'$). As expected from the actuator modelling in section 4.2, the inertial shaker appears to behave as a SDOF mechanical system, characterised by one main peak at 88 Hz which is the resonance of the inertial mass on its suspension, since the actuator is driven by a constant current and so is unaffected by the back e.m.f effect. Below this frequency, the control force is small as a result of the small impedance of the inertial mass. It also presents a phase shift compared to the secondary force required for perfect skyhook damping which is given by the phase response of ($-T'_a$). As discussed in chapter 3, the low frequency dynamics of the actuator is going to limit the control gain by introducing instability in the control system. Amplifications are expected below 100 Hz. Above about 150 Hz the inertial mass motion becomes very small and the actuator can apply perfect secondary force, independent of frequency and without phase shift with the actuator input signal. The phase of the actuator response seems however to drop slightly below 0° as the frequency increases. This will not affect the system stability in the frequency range of control but will slightly change the control force in comparison with the perfect skyhook force expected from the system mechanics. This phase drop may be due to the increase of the actuator electrical impedance as the inductance of the coil starts to have an effect on the actuator response at high frequencies or to phase shifts in the driving amplifier.

The actuator dynamics appear more likely to induce control limitation than the rotational excitation from the base structure discussed above.

### 4.3.3. Initial passive analysis

The system was hung vertically using soft elastic strings attached to the equipment composite plate to obtain free boundary conditions, as shown in Figure 4.8.

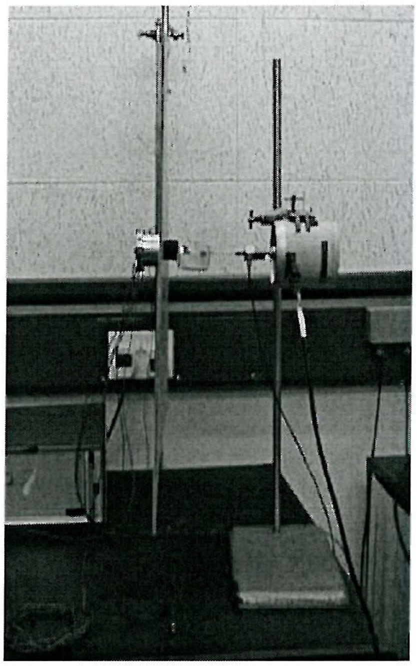

Figure 4.8. The experimental isolation system excited by an axial primary force.

Figure 4.9. shows the measured velocity response at the point 1 on the equipment panel for the global isolation system per unit primary excitation $f_0$ applied on the U-beam, as shown in Figures 4.5 and 4.8.

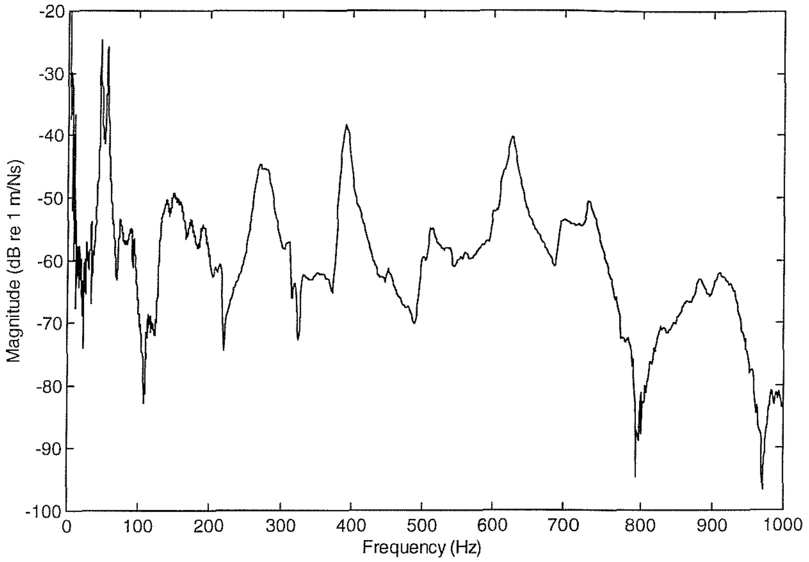

Figure 4.9. Disturbance at point 1. Passive velocity response per unit primary excitation.

The static stiffness of one of the rubber mount was measured to be equal to 57 kN./m which is too large to create an obvious mass-spring-mass resonance effect between the base beam, mounts and composite panel, since the equipment panel and the base structure behave as rigid bodies only at very low frequencies. The passive mounts appear, however, to provide passive isolation above 600 Hz as the vibration level at point 1 goes down by almost 40 dB from 600 Hz to 1 kHz. Further isolation improvement from the active controller is therefore very unlikely above 1 kHz. The passive response is low below 40 Hz. Several resonances are observed below the measured inertial actuator resonance, amongst which two strong ones are apparent at 46.5 Hz and 55.5 Hz. The mobility $M_{cc}$ at the control point 1 is likely to be characterised by these two resonances. At any resonance, the input mobility $M_{cc}$ is damping controlled and has a small phase shift, so that, if the expression for the experimental plant response for single-channel control is

$$G = -T_a' M_{cc} \tag{4.4}$$

the phase response of the plant at 46.5 Hz and 55.5 Hz is such that

$$\angle G \approx \angle - T_a' \approx \pi \tag{4.5}$$

A more detailed analysis of the stability for the three single-channel control systems studied is provided in the following section. However, equation (4.5) illustrates that the resonances in the passive system below the actuator resonance $\omega_a$, as well as the resonance $\omega_a$ itself, are one of the main threat to the stability of inertial DVFB control. A simple measurement of the passive response of the system can thus tell us a lot about the problems and limitations that the controller is likely to encounter.

Figure 4.10 shows the input mobility measured at one random position on the composite panel uncoupled from the rest of the system. The measurement position was chosen so as to avoid any obvious nodal lines, so that most of the low frequency modes in the panel response would be measured. Figure 4.11 shows the velocity response at mount junction 1 on the base beam, uncoupled from the rest of the system, per unit excitation $f_0$ applied at the driving point as shown in Figure 4.5.

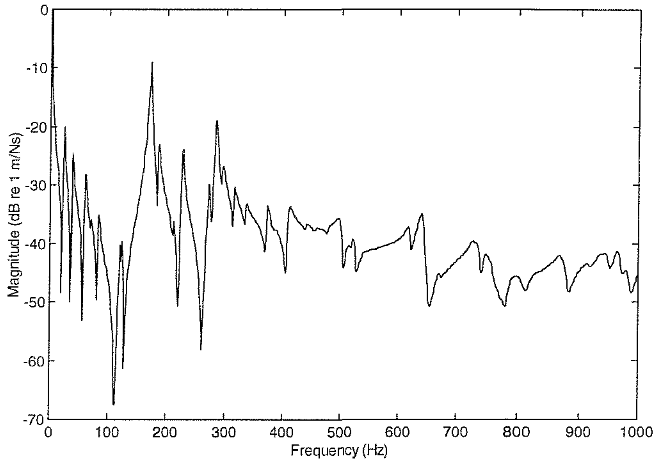

Figure 4.10. Measured random input mobility on the equipment composite panel.

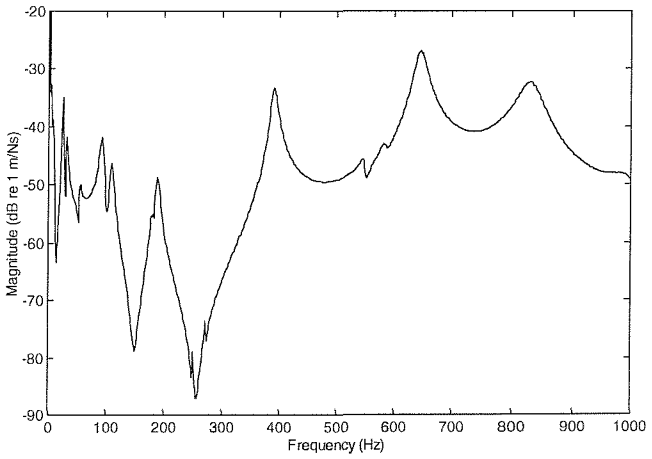

4.11. Measured transfer mobility at point 1 on the uncoupled U-beam per unit excitation $f_0$.

Both systems are characterised by several low frequency resonances. The panel is very flexible with a first resonance for the mode (1,1) as low as 23.5 Hz and with little damping in the low frequency modes. This would suggest that the two sharp peaks observed in the system passive response in Figure 4.9 at 46.5 Hz and 55.5 Hz are directly associated with the panel dynamics. The base beam also presents a relatively dense modal distribution at low frequencies which first appears surprising with respect to the apparent rigidity of the aluminium beam in bending. The high frequency modal distribution also looks less dense than at low frequencies which is an other unexpected results for beam vibration in bending. The first modes in the beam are in fact probably due to the rotation of the beam around the $x$-axis as already discussed in section 4.3.1 and illustrated in Figure 4.6. The large flexibility of the U-beam in torsion is easily noticed by exerting a torsional effort at the two ends of the beam.

The flexible characteristics of the equipment and base structures explain the low frequency resonances observed in the passive response of the system below the inertial actuator resonance $\omega_a$. One should note that a significant number of modes of the equipment panel may not have a large effect in the measured response of the control system, since the mounts are connected along the centre line in the $x$-direction, which is a principal nodal line of the plate. These modes may however be slightly excited by the mount rotations. They are not, however, controllable by the axial actuator devices available and can not be monitored at the mount junctions.

Finally, resonances in mounts should not affect the system dynamics in the frequency range of interest since the first longitudinal resonance of the rubber mounts has been calculated to be 2730 Hz and the first flexural resonance around 6000 Hz according to the model detailed in chapter 5. The mounts can thus be regarded as lumped springs and dashpots in the frequency range of interest.

It appears from this brief passive analysis of the elements involved in the control system that a simple DVFB control using inertial actuators is going to hit two major limitations. The first one, developed in chapter 3, is the actuator resonance itself which will generate a peak in the plant response associated with an undesired phase shift. The second one comes from the system element flexibility which generates resonance maxima in the low frequency range of expected control amplification. One could also add the rotational excitation of the beam as a third limitation since it seems to be significant and uncontrollable with axial actuation devices.

## 4.4. Control loop description

### 4.4.1. General presentation

Each control accelerometer is wired to its associated control shaker through the same control loop. Figure 4.12 shows the structure of one control channel and Figure 4.13 presents a photograph of different elements of the control loop.

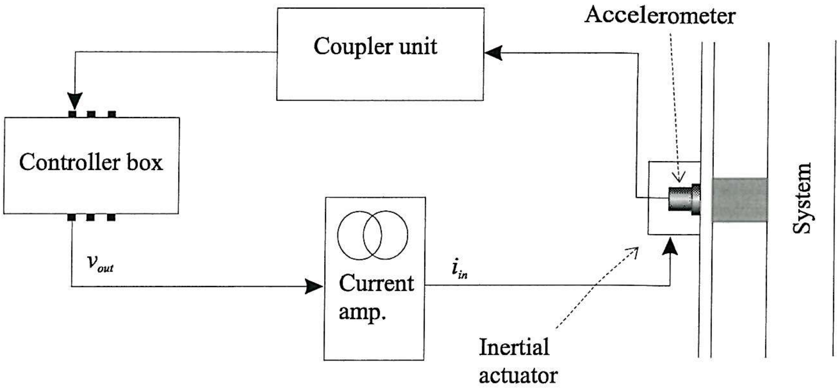

Figure 4.12. Schematic of one experimental control channel.

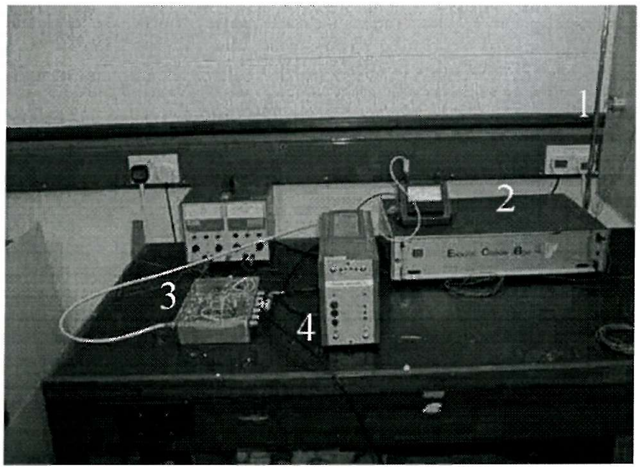

Figure 4.13. Photograph of one control channel.

The equipment panel response is monitored by the embedded accelerometer (1) whose signal is fed to a coupler unit, the *endevco* coupler box (2), which acts as a charge amplifier and provides phantom power necessary for the accelerometer operation. This unit can deal with 24 independent channels and is thus common to the three control channels. The voltage output, ideally proportional to the panel acceleration for a flat frequency response of the accelerometer with coupler unit, is then fed to a control box (3) which has a double action of integration and amplification. The amplitude of the resulting signal can be modulated to provide different control gain. Finally, the control box output is fed to a constant current amplifier which drives the control shaker.

### 4.4.2. Controller box

The control box is composed of four different sets of three connections, constituting three independent channels with two inputs and two outputs each. Only one set of inputs, "acceleration input" and one set of outputs were used in this investigation. Details for one channel electronical circuit is shown in Figure 4.14. The circuit in Figure 4.14 can be divided into two sub-circuits.

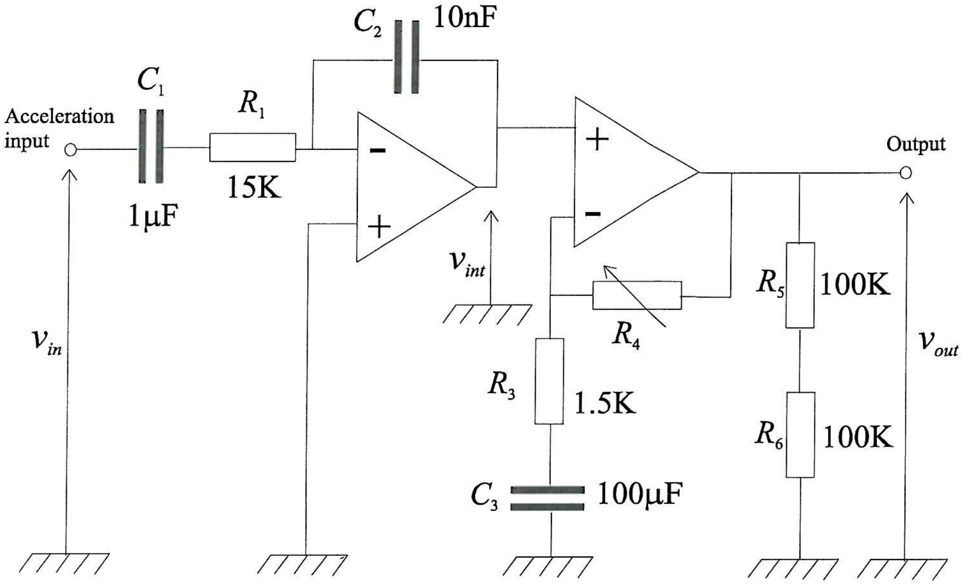

Figure 4.14. Electronical circuit for one channel of the controller box.

The first sub-circuit can be defined by the electrical transfer function

$$T_1 = \frac{v_{int}}{v_{in}} = -\frac{C_1}{C_2}\frac{1}{1 + jR_1C_1\omega} \tag{4.6}$$

where $v_{in}$ and $v_{int}$ are the input voltage and intermediate voltage respectively. This can be re-expressed as,

$$T_1 = -\frac{1}{R_1C_2}\cdot\frac{1}{j\omega}\cdot\frac{j\omega}{1/R_1C_1 + j\omega} \tag{4.7}$$

Sub-circuit 1 acts as an integrator circuit. The integration is effective at frequencies above the roll-off frequency, $\omega_1$, of the high-pass filter defined by the third ratio in the expression of $T_1$ ($\omega_1=1/R_1C_1$ equal to 10.6 Hz). The integration is associated with a scaling factor $1/R_1C_2$. The sub-circuit also acts as an invertor so that the negative feedback required by the DVFB control can be implemented. At low frequencies, because of the equivalent high-pass filter, no integration effect can be expected and the circuit just multiplies the input voltage by a negative factor. This is likely to generate the same low frequency phase shift effect as already pointed out in chapter 3.

Similarly the second sub-circuit is defined by the electrical transfer function

$$T_2 = \frac{v_{out}}{v_{int}} = 1 + \frac{jR_4C_3\omega}{1+jR_3C_3\omega} \tag{4.8}$$

where $v_{out}$ is the controller output voltage.

This second circuit is the control gain stage. Above 10 Hz, a high frequency simplification can be made so that

$$T_2 = \frac{R_4}{R_3} \tag{4.9}$$

The second sub-circuit acts as a simple constant gain amplifier. The gain can be adjusted, within a dynamic range of 30 dB, by changing the value of the resistor $R_4$.

Above 10 Hz, the global electrical transfer function of the controller is therefore,

$$T_e = T_1T_2 = -\frac{R_4}{R_1R_3C_2}\cdot\frac{1}{j\omega}\cdot\frac{j\omega}{1/_{R_1C_1}+j\omega} \tag{4.10}$$

The controller box can then be regarded as an integrator associated with:

- an invertor allowing negative feedback.
- a amplifier of adjustable gain $K=\dfrac{R_4}{R_1R_2C_2}$ of dynamic range equal to 30 dB
- a high-pass filter of cut -off frequency equal to 10.6 Hz whose characteristics are shown in Figure 4.15.

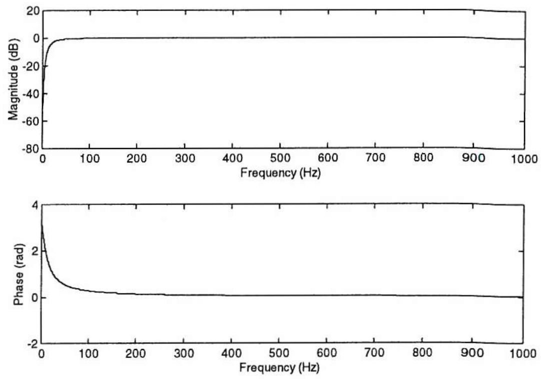

Figure 4.15. Magnitude and phase response of the low-pass filtering operation of the controller box.

The control loop represented in Figure 4.12 can now be redrawn as shown in Figure 4.16.

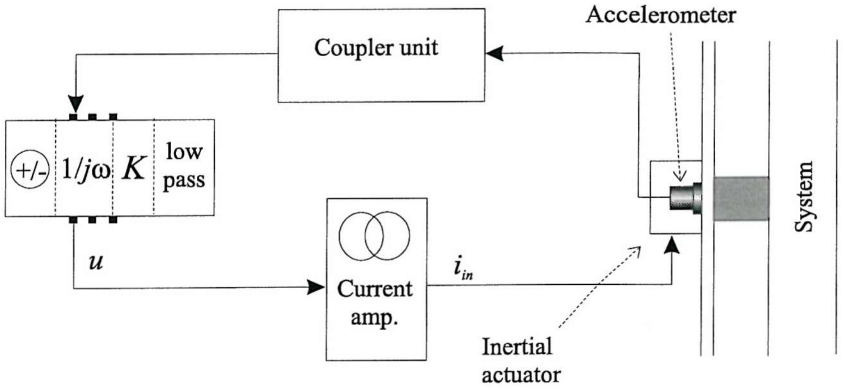

Figure 4.16. Schematic of one experimental control channel with detailed controller box effects.

In order to perform control simulation based on the measured plant response using the Nyquist method discussed in chapter 2, the experimental plant response has to be defined so that the controller has a pure amplification effect. The output of the coupler unit can then be numerically integrated and divided by the sensitivity $S$ of the accelerometer, to give a signal, $y$, differing from the exact velocity of the system only by the normalised frequency response of the accelerometer coupled to the *endevco* box. The sensitivity $S$ can then be applied at the control stage as an extra gain factor. The low-pass filtering operation caused by the non-perfect integration of the acceleration signal can also be integrated in the plant as part of a new fictitious velocity sensor. This manipulation is equivalent to a change in the position of the different operations performed by the controller box and to account for the accelerometer sensitivity at the sensing stage. This is valid since all the elements in the loop behave linearly. The effective control loop is then as shown in Figure 4.17.

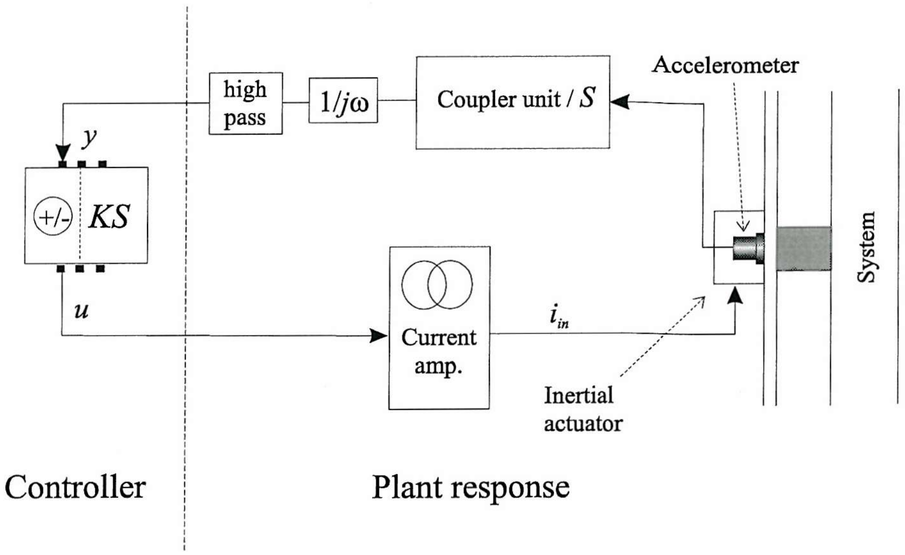

Figure 4.17. Schematic of one rearranged experimental control channel.

This rearrangement allows us to define a meaningful and convenient plant response $G$ for single channel control.

$$G = \frac{y}{u} \tag{4.11}$$

where $y$ can be regarded as the output voltage of a velocity sensor and where the controller is a pure amplification gain as discussed in the block diagram for DVFB control. $G$, as defined in (4.11) is also convenient for easy experimental estimation since it includes the sensor, actuator dynamics and the current amplifier. Expression (4.11) defines the general expression for the different plant responses analysed and assessed in this study.

## 4.5. Single channel control

### 4.5.1. Experimental control quantities

In the Laplace domain, the response $X_{ii}$ of the system under control at the control point is estimated by the sensitivity function, as derived in chapter 2,

$$\frac{X_{ii}(s)}{X_{Pi}(s)} = \frac{1}{1 + G_{ii}(s)h_i} \tag{4.12}$$

where $h_i$ is the control gain which is equal to $KS$ and $X_{pi}(s)$ is the primary disturbance measured at point $i$. $G_{ji}(s)$ is the transfer function, as defined in equation (4.11), between an excitation at $i$ and a response at $j$. In this special case, $i=j$ and $G_{ii}(s)$ is the plant response for control at position $i$. Since three accelerometers are available, it is possible to calculate the effect of the single-channel control on the output of the two other sensors. For a control at point $i$, the response of the system at point $j$ under linear behaviour is,

$$X_{ij}(s) = X_{Pj}(s) + G_{ji}(s)U_i(s) \tag{4.13}$$

where $X_{ij}(s)$ is the system response at point $j$ under control at point $i$ and $U_i(s)$ is the voltage output from the controller feedback to the plant so that,

$$X_{ij}(s) = X_{Pj}(s) - h_i G_{ji}(s) X_{ii}(s) \tag{4.14}$$

and therefore using equation (4.12)

$$\frac{X_{ij}(s)}{X_{Pj}(s)} = 1 - \frac{G_{ji}(s)h_i}{1+G_{ii}(s)h_i}\frac{X_{Pi}(s)}{X_{Pj}(s)} \tag{4.15}$$

Equation (4.15) is a general expression for the performance of a single-channel controller at the three sensor location $j$ and for $i=j$, equation (4.15) is identical to equation (4.12). Control simulations thus only require us to measure the passive response of the system under primary excitation at the mount junctions on the composite panel and the nine different transfer functions $G_{ji}(s)$ (strictly speaking, only 6 of them if the reciprocity principle was used, assuming identical actuators and sensors) which will also be necessary for the analysis of the multichannel controller. Only the three plant responses $G_{ii}(s)$ are, however, necessary to assess the stability of the different single channel controls.

Equations (4.12) and (4.15) are derived according to the formulation of the experimental plant response in equation (4.11) so that the quantities $X$ take into account the low frequency filtering effect of the controller box. In practice, the measured velocity responses are obtained by integrating and scaling by $S$ the output of the coupler unit. Equations (4.12) and (4.15) can then be expressed in more physical terms as

$$\frac{E_{ii}(s)}{D_i(s)} = \frac{1}{1+G_{ii}(s)h_i} \tag{4.16}$$

and
$$\frac{E_{ij}(s)}{D_j(s)} = 1 - \frac{G_{ji}(s)h_i}{1+G_{ii}(s)h_i}\frac{D_i(s)}{D_j(s)} \tag{4.17}$$

where $E_{ij}(s)$ is the velocity response at point $j$ under control at $i$ and $D_j(s)$ is the primary velocity disturbance at points $j$. They are the quantities used in the analysis of the control performance.

### 4.5.2. Plant responses and stability analysis

The experimental plant responses have been defined so that the controller acts as a perfect amplifier. As discussed in chapter 2, the stability for a single channel DVFB control at point $i$ can then now be assessed by simply analysing the Nyquist plot of the measured plant response $G_{ii}$. The stability of the three single-channel control systems, implemented subsequently at each mount junction, is discussed below using the Nyquist method.

#### *Control at point 1*

Figure 4.18 shows the modulus and phase of the plant response for a control implementation at point 1, $G_{11}$.

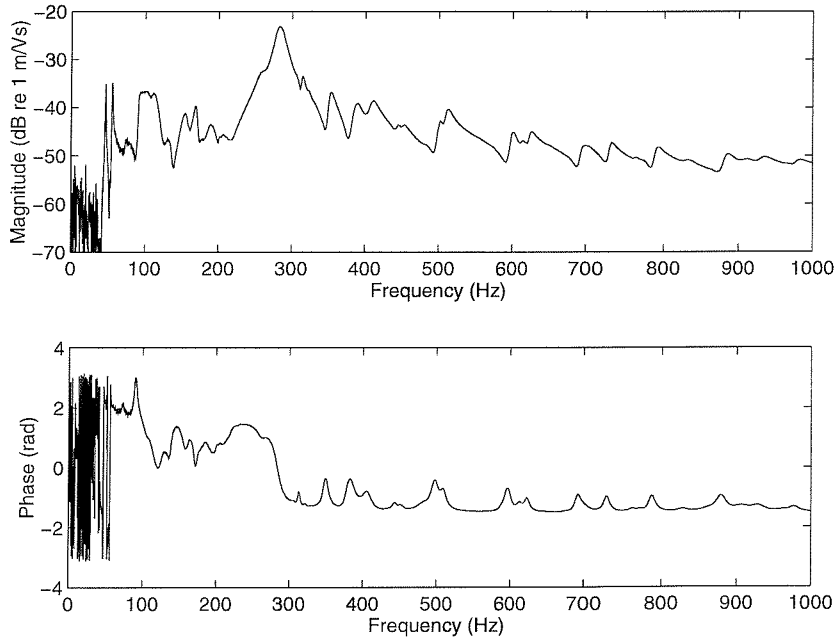

Figure 4.18. Magnitude and phase of the measured plant response for a single channel-control at point 1.

Below 40 Hz, the amplitude of the plant response is very low as observed in Figure 4.9 for the passive analysis of the system. The low mechanical response of the system is moreover accentuated by the low-pass filtering operation mentioned in the previous section. The secondary excitation then has two sharp resonances at 46.5 Hz and 55.5 Hz, which were also clearly seen in the passive study of the system. They are associated with a phase almost equal to $\pi$ and give rise to the two main loops located in the unstable half plane of the Nyquist plot in Figure 4.19.

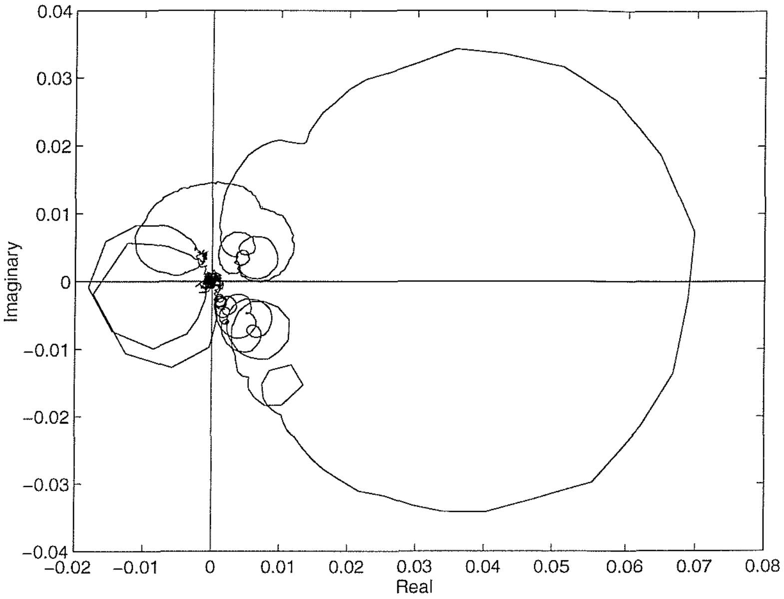

Figure 4.19. Nyquist plot of the measured plant response for a single-channel control at point 1.

The amplitude of the loop centred around the 55.5 Hz resonance as it crosses the negative real axis is the largest of the two and will induce instability in the system for a control gain larger than 52.5. The phase of the plant response is also equal to $\pi$ at 90 Hz, as the inertial actuator resonates, which may constitute another threat for the control stability. In this case, however, the amplitude of the plant response at 90 Hz is much smaller than at 55.5 Hz and therefore the inertial actuator resonance does not directly limit the control gain. It is interesting to note the large influence of the simple actuator dynamics on the control, as discussed in section 4.3. Below 90 Hz, the phase of the plant response is greater than $\pi/2$ so that the Nyquist locus is almost entirely located in the negative real part half plane of the Nyquist diagram. Above 90 Hz, the phase decreases very quickly with frequency and oscillates between $-\pi/2$ and $\pi/2$, so that the Nyquist plot is located in the positive real part half plane. The plant response is largest in the frequency band [250-350 Hz] as the passive isolation amplifies the vibration of the mounted equipment. The resonance at 280 Hz gives rise to large loop in the positive real part half plane of the Nyquist diagram, so that feedback control is expected to have a significant attenuation effect here. Above 300 Hz, the magnitude of the plant response drops regularly with frequency as the passive isolation becomes more and more efficient. The control effect will then be reduced at high frequencies as the passive isolation offers increasing vibration attenuation since the secondary force is proportional to the measured control velocity. Therefore no further large reduction is expected from the active isolation.

### *Control at point 2*

Figure 4.20. shows the magnitude and phase of the plant response $G_{22}$ when a single-channel DVFB control is implemented at point 2 and Figure 4.21. shows its Nyquist representation.

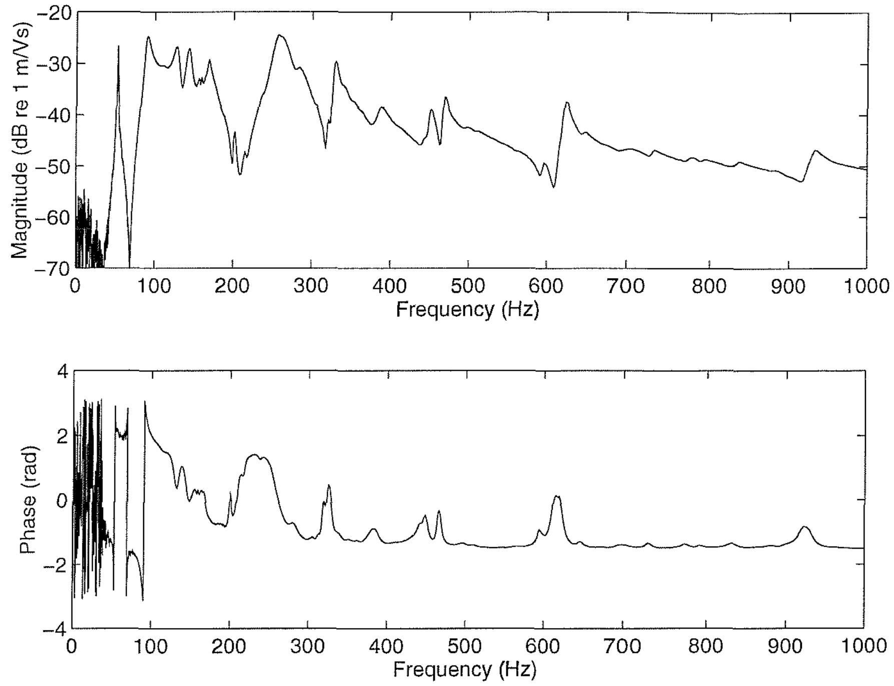

Figure 4.20. Magnitude and phase of the measured plant response for a single-channel control at point 2.

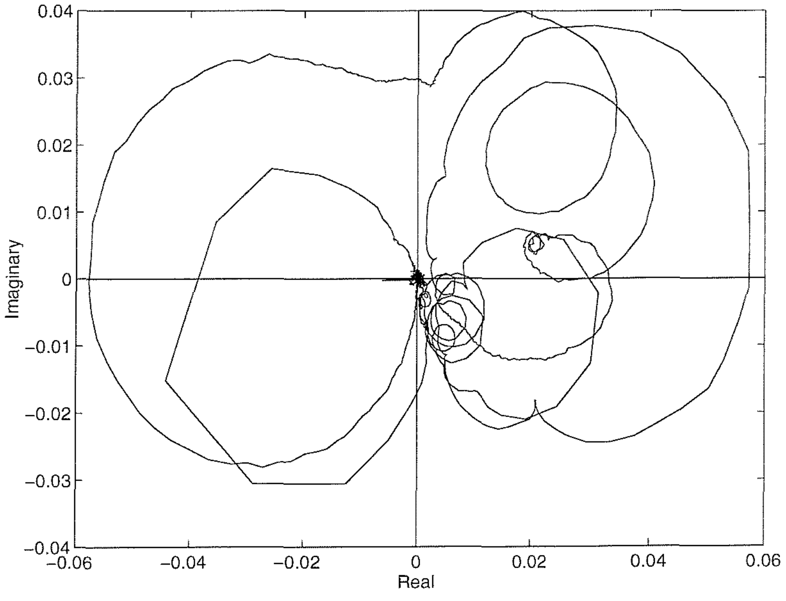

Figure 4.21. Nyquist plot of the measured plant response for a single-channel control at point 2.

$G_{22}$ presents the same main characteristics as observed in the analysis of $G_{11}$ since the control stability strongly relies on the secondary actuator dynamics. The phase of the plant response is such that above 90 Hz the Nyquist contour lies in the stable half plane whereas below 90 Hz it is located in the unstable one. Two large loops cross the negative real axis of the Nyquist plot at 90 Hz and 55.5 Hz. The largest one is related to the resonance of the inertial actuator which, in this case, is going to limit the control gain to a maximum value of 17. This low value of gain is partly due to the rather large dynamics at the centre of the composite panel where point 2 is located. The second loop is associated with the sharp resonance at 52.5 Hz, clearly shown in Figure 4.20. This is likely to be the same resonance as the mode observed at 55.5 Hz in $G_{11}$, which looked shifted as the result of a cancellation effect with the 46.5 Hz resonance. This would mean that the 46.5 Hz resonance is not picked up by the second control accelerometer, which is very likely since point 2 is located at the intersection of the two central nodal lines of the uncoupled equipment panel where a larger number of modes than at point 1 are neither observable nor excited by an axial force. As noticed for $G_{11}$, the magnitude of the plant response decreases at high frequencies and below 40 Hz, where no real control effect is then to be expected.

### *Control at point 3*

Figure 4.22. shows the magnitude and phase of the plant response $G_{33}$ when a single-channel DVFB control is implemented at point 3 and Figure 4.23. shows its Nyquist representation.

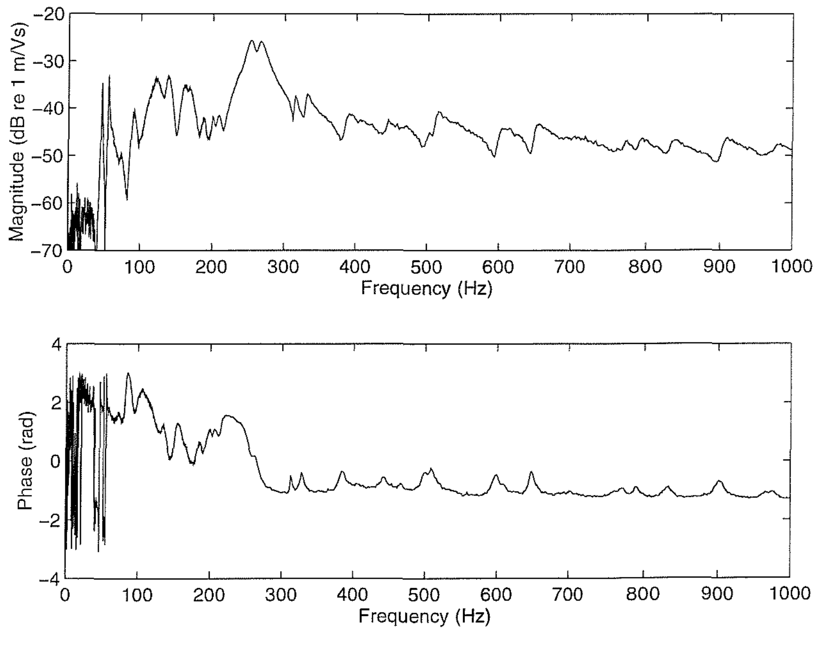

Figure 4.22. Magnitude and phase of the measured plant response for a single-channel control at point 3.

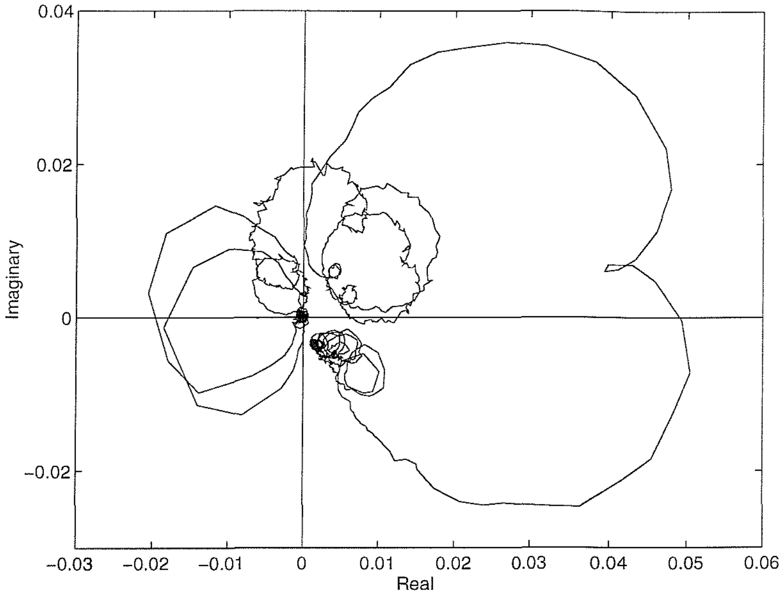

Figure 4.23. Nyquist plot of the measured plant response for a single channel-control at point 3.

Because of the system symmetry, the plant response $G_{33}$ presents some similarities with $G_{11}$. For a perfect symmetrical system with identical actuators and sensors and neglecting the mechanical impedance of the primary shaker, $G_{11}$ and $G_{33}$ would be identical. It thus exhibits the same sharp resonances at 46.5 Hz and 55.5 Hz. As for a control at point 1, the resonance of the secondary actuator is not the direct cause of instability, which will be first introduced by the amplification of the resonance at 55.5 Hz, which limits the feedback gain to a maximum value of 48. The inertial actuator dynamics have still the effect of defining the low frequency range, below 90 Hz, as the band of expected vibration amplification and the high frequency band as the range of expected vibration reduction. As for the two other control implementations, the greatest attenuation will be obtained in the frequency band [250 Hz - 350 Hz] where the passive isolation has an adverse influence on the equipment vibration. It is represented on the Nyquist plot in Figure 4.23 by the large loop in the stable half plane, of almost same radius as for $G_{11}$ and $G_{22}$.

The different single-channel control loops appear to be strongly gain limited, especially at point 2 where the control accelerometer is blind to numerous modes of the system that may still be excited by the rotation of the mount. As a control gain is applied, the control is either limited by the rapid increase of a system resonance located below $\omega_a$ or by the increase of the secondary actuator resonance itself. In either case, however, the inertial actuator dynamics dictate the general phase pattern of the different plant responses, as discussed in chapter 3 and in section 4.3. The response at the control points will thus generally be amplified below $\omega_a$ and attenuated above $\omega_a$.

### 4.5.3 Control performance

For each single-channel control at point $i$, the response at the three accelerometer locations $j$ has been computed according to equation 4.17 and using the nine measured transfer functions $G_{ji}$. Nine force normalised velocity response spectra $V_{ij}(j\omega)$ has thus been defined as,

$$V_{ij}(j\omega)=\frac{E_{ij}(j\omega)}{F_0(j\omega)} \tag{4.18}$$

where $E_{ij}(j\omega)$ is the system velocity response at point $j$ for a control implementation at point $i$. $F_0(j\omega)$ is the frequency response of the primary force excitation used to normalised the velocity response such as to obtain a reliable estimate to be compared to the normalised passive response of the system at point $j$, defined as,

$$V_{0j}(j\omega)=\frac{D_j(j\omega)}{F_0(j\omega)} \tag{4.19}$$

This two quantities enable us to estimate the control performance of each single-channel controller not only at the control location but also at the location of the two other control accelerometers. The nine plots of the system responses $V_{ij}$ are shown below in the faint line, overlaid with the corresponding passive response $V_{0j}$ plotted in bold line. The control results are shown for a maximum value of control gain to provide a benchmark of the maximum attenuation achievable in the reduction frequency band.

***Control at point 1***

The system responses at point 1, 2 and 3 are simulated for a maximum control gain at point 1 only of 52.5. The response at the control point $V_{11}$ over the whole frequency of interest is shown in Figure 4.24. It is dominated by the two spikes at 46.5 Hz and 55.5 Hz. Already predominant in the passive response, they are strongly amplified by feedback control, as shown in the zoomed picture in Figure 4.25, and eventually drive the system to instability. The control can then be regarded as dangerous for the overall system, but interesting observations on inertial control are, however, provided by a further analysis of the controller effects over the whole frequency range.

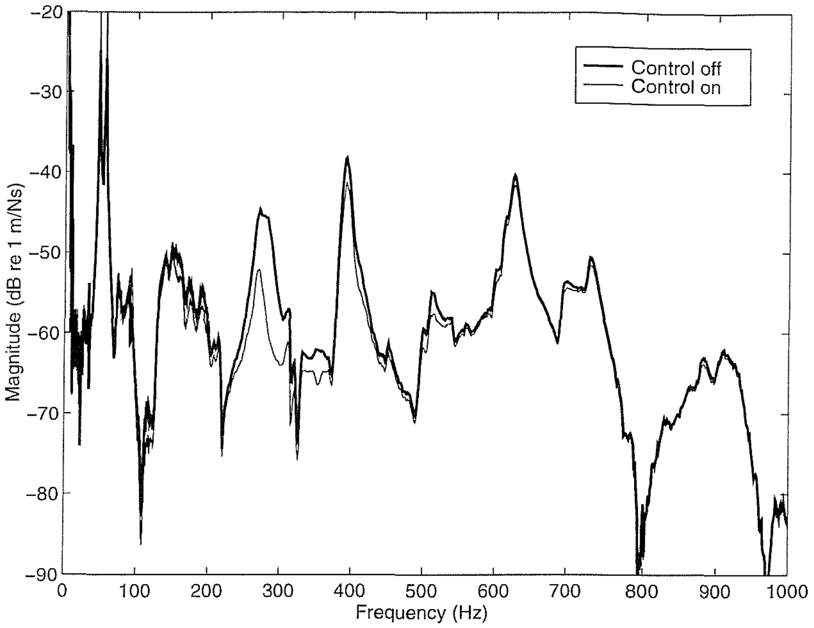

Figure 4.24. Measured passive response $V_{01}$ and simulated controlled velocity response $V_{11}$ at the control point for a control at point 1.

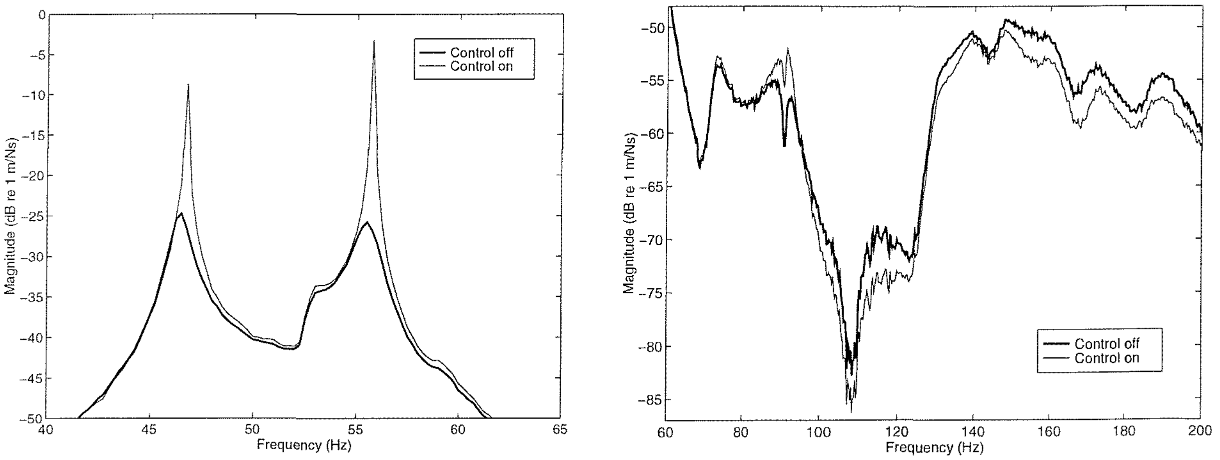

Figure 4.25. Zoomed picture of the passive response $V_{01}$ and of the simulated controlled response $V_{11}$ showing the onset of instability.

Figure 4.26. Zoomed picture of the passive response $V_{01}$ and of the simulated controlled response $V_{11}$ around the secondary actuator resonance.

Figure 4.26 illustrates very clearly the importance of the inertial actuator resonance on the controller performance. Below 94 Hz, the vibration level at the control point is amplified, whereas only vibration reductions are achieved above this frequency, as the control starts implementing perfect skyhook damping. The control does not have any significant effect above 550 Hz, as expected from the plant response analysis, since the passive isolation starts to be efficient and dominates the effect of the control system which is relatively small under the double effect of small control gain and small amplitude of the plant response at high frequencies. For the same reasons the system response is unaffected by feedback control below 40 Hz. Maximum broad band attenuation is observed in the frequency range [250 Hz -300 Hz], as expected from the plant response analysis, with a 7 dB reduction at 280 Hz.

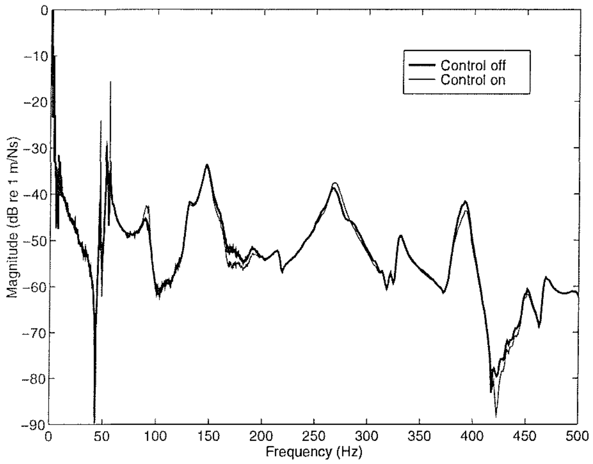

Figure 4.27. Passive and simulated controlled responses at point 2 for control at point 1, $V_{02}$ and $V_{12}$.

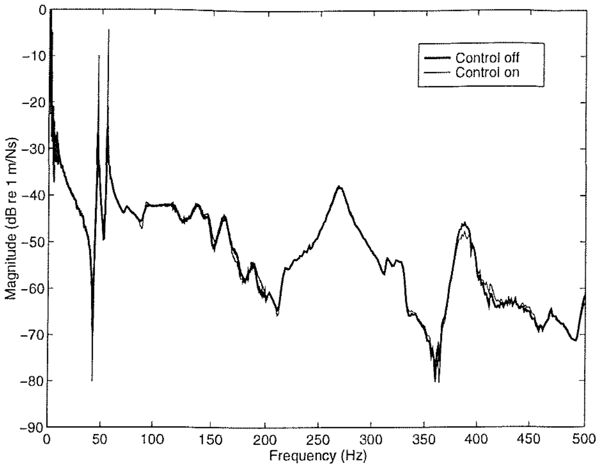

Figure 4.28. Passive and simulated controlled responses at point 3 for control at point 1, $V_{03}$ and $V_{13}$.

Figures 4.27 and 4.28 show the effect of a control at point 1 at the two other accelerometer locations, at points 2 and 3. Results are given for a reduced frequency band since no significant control effect can be noticed above 500 Hz. Apart from the large increases at 46.5 Hz and 55.5 Hz due to the onset of instability, no significant effect of the control is noticed on the equipment panel at points 2 and 3, even in the frequency range [250 Hz - 300 Hz]. Some control effect at point 3 could have, however, been expected, since, from their symmetrical locations, points 1 and 3 tend to have a similar response to the modes of the isolation system. Attenuation of a resonance at point 1 (270 Hz for instance) thus does not seem to induce a reduction of the associated mode over the system, since no such reduction is observed at point 3. This single-channel control system appears to generate a strict local reduction in the velocity of the composite panel.

### *Control at point 2*

Figure 4.29 presents the force normalised velocity $V_{22}$ simulated for a maximum control gain equal to 17, as determined from the plant response analysis. Because of this very small gain, the range displayed is limited to 500 Hz, as no further isolation improvements were noticed above this frequency. As for a control implementation at point 1, the controller has no effect on the system below 50 Hz.

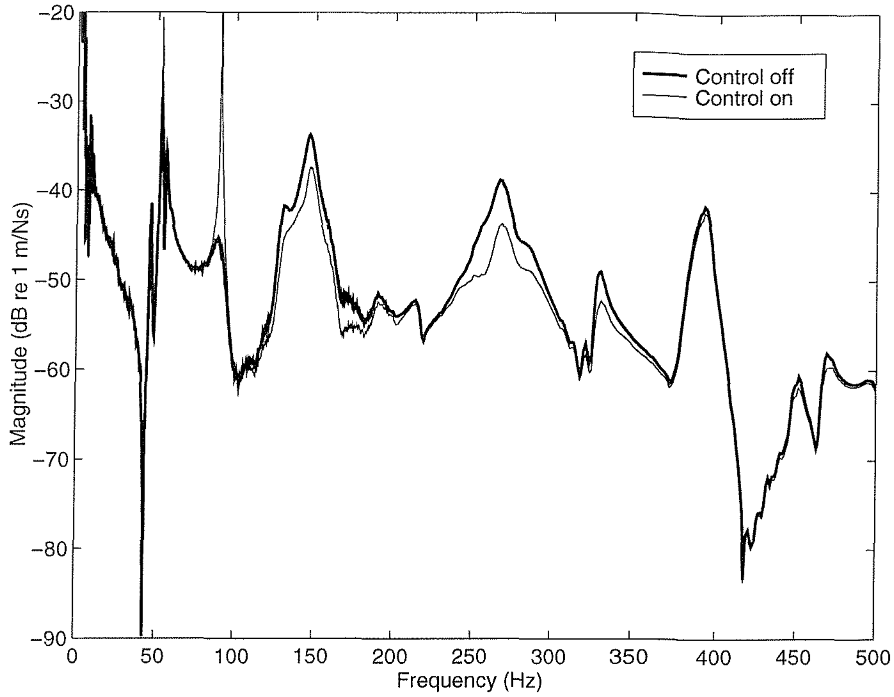

Figure 4.29. Measured passive velocity response $V_{02}$ and simulated controlled velocity response $V_{22}$ at the control point for a control at point 2.

The main point to be observed is the large increase due to being close to instability; in this case at 90 Hz because of the inertial actuator effect. A sharp increase is also observed at 52.5 Hz as pointed by the Nyquist plot of the plant response $G_{22}$. Figure 4.29 illustrates once more the effect of the dynamics of the inertial actuator, as above 100 Hz, only vibration reduction is achieved. The reductions are limited by the very low gain due to the very reactive dynamics of the system at 90 Hz and only 2-3 dB attenuation are obtained in a frequency range centred around 150 Hz. The largest vibration reduction again occurs around 270 Hz as the vibration level goes down by 4-5 dB.

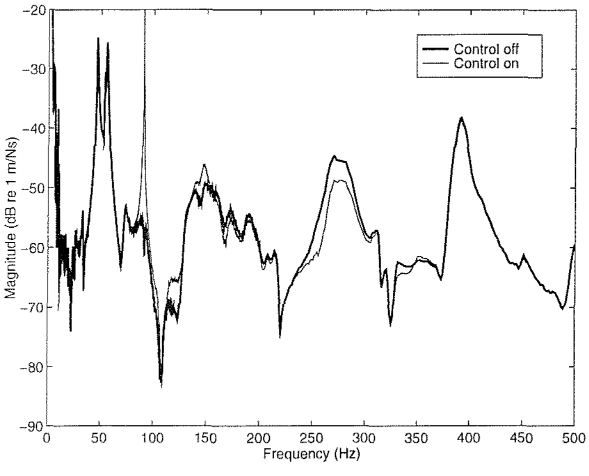

Figure 4.30. Passive and simulated controlled responses at point 1 for control at point 2, $V_{01}$ and $V_{21}$.

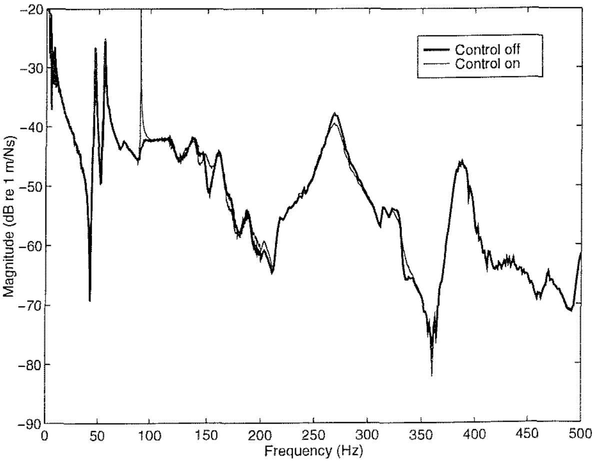

Figure 4.31. Passive and simulated controlled responses at point 3 for control at point 2, $V_{03}$ and $V_{23}$.

Figures 4.30 and 4.31 show the response at points 1 and 3 for a maximum gain control at point 2. Apart from the unstable features, the control seems to have some effect at point 1, unlike the previous single channel control implementation. The vibration level thus goes down by up to 3-4 dB at 270 Hz and small vibration attenuation is observed between 250 Hz and 300 Hz. Small amplification is also noticed around 150 Hz but without real consequences on the system vibration. Very small attenuation is observed in the range [250 Hz - 300 Hz] at point 3 so that the control at point 2 appears to generate, to a certain extend, a global reduction of the system vibration in this band.

***Control at point 3***

Figure 4.32 presents the force normalised velocity $V_{33}$ simulated for a maximum control gain of 48. The main effects of a control at point 3 are similar to the ones observed in the two other control implementations.

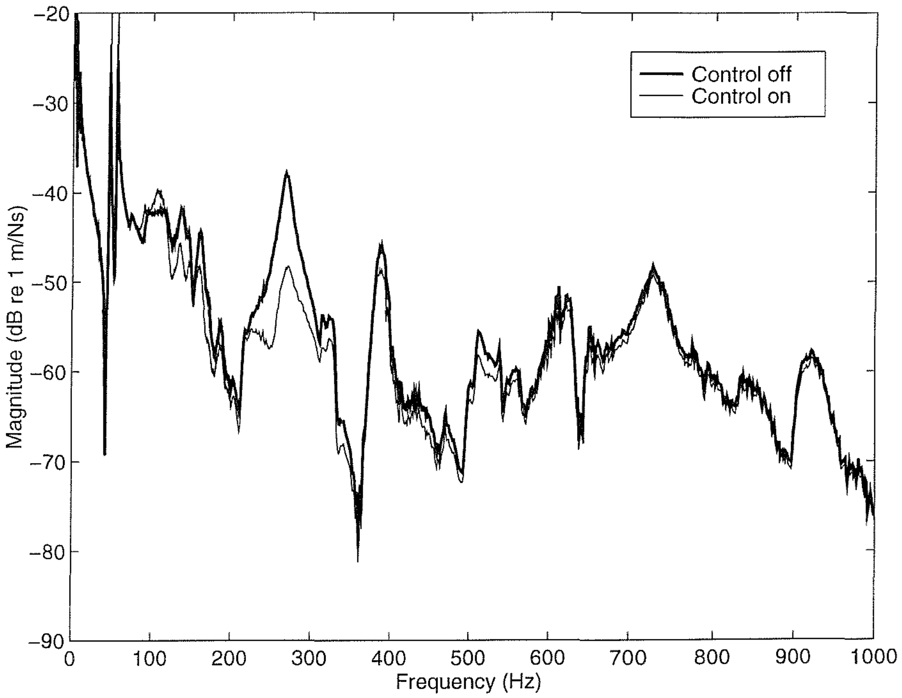

Figure 4.32. Measured passive velocity response $V_{03}$ and simulated controlled velocity response $V_{33}$ at the control point for a control at point 3.

As for control at point 1, instability arises in the system through the fast increase of the 55.5 Hz resonance. A large amplification also occurs at 46.5 Hz. The control shows attenuation effects above the secondary actuator resonance $\omega_a$ with significant reduction in the band [230 Hz - 350 Hz], up to 10 dB at 270 Hz. No real control benefit can be recovered above 500 Hz for the same reasons of low control gain and decreasing plant response magnitude already discussed.

Apart from the onset of instability at 55.5 Hz and the large increase at 46.5 Hz, control at point 3 as a little effect at point 1 as shown in Figure 4.33. 1-2 dB reduction are observed between 130 Hz and 270 Hz. and vibration amplification arises around 120 Hz.

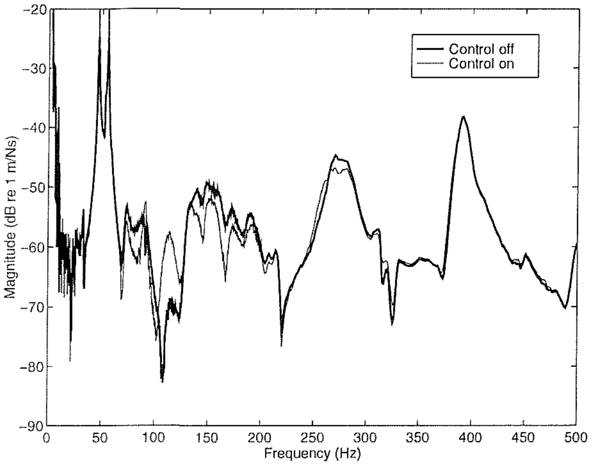

Figure 4.33. Passive and simulated controlled responses at point 1 for control at point 3, $V_{01}$ and $V_{31}$.

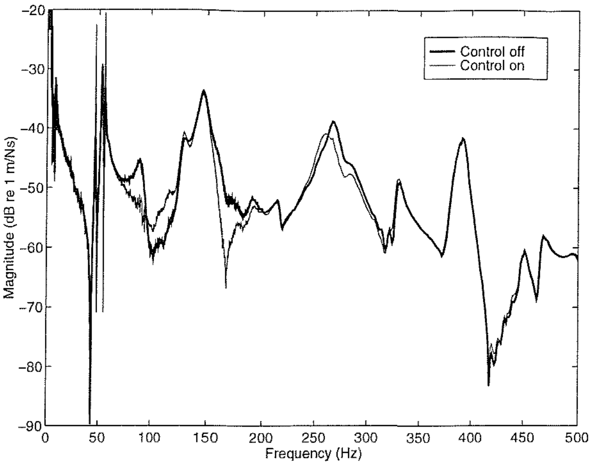

Figure 4.34. Passive and simulated controlled responses at point 2 for control at point 3, $V_{02}$ and $V_{32}$.

At point 2, the control generates small vibration amplifications and reductions in the frequency band [70 Hz - 300 Hz] but does not significantly affects the global velocity response above 60 Hz, as shown in Figure 4.34.

### 4.5.4. Summary of single-channel implementation of inertial DVFB control

Similar characteristics come out of the analysis of the three different single-channel controls. The three sets of simulations illustrate the strong limitation induces by an inertial actuator, that sets an inherent limit in term of feedback gain. Below the inertial actuator resonance $\omega_a$, only vibration amplification is expected, and any low frequency resonance of the system is strongly increased and can threatened the system stability. If no resonances occur in the system below $\omega_a$, instability will still appear at $\omega_a$, as shown in chapter 3 for rigid equipment isolation. An inertial implementation of DVFB control ensures, however, vibration reduction at high frequencies at the control point, since it tends to implement skyhook damping. The performance of an inertial DVFB control can therefore be characterised as a control strategy which is rather independent of the passive system dynamics.

The vibration reduction observed at the control point seem to generate, to some extend, vibration reduction at the two other mount connections on the equipment plate. However the small amplitude of the attenuation and, in general, the small control effect observed at the uncontrolled points do not enable us to draw definite conclusions on the response of the whole equipment panel to a single-channel control implementation. It appeared that the three single-channel controllers had only a local efficiency which seems reasonable since DVFB control is a local control strategy, unlike a control based on the input power which seeks to minimise the global equipment vibration. To help in the analysis of the "cross effect" of one controller, the attenuation above 100 Hz has been estimated in term of vibration energy at each accelerometer position $j$ for each control implementation at point $i$, using the numerical version of the following expression,

$$Att_{ij}(\%) = 100 * \left( 1 - \frac{\int_{f=100Hz}^{1kHz} \left| V_{ij} \right|^2 df}{\int_{f=100Hz}^{1kHz} \left| D_{0j} \right|^2 df} \right) \tag{4.20}$$

where $f$ is the frequency (in Hz). The system response is only taken into account above 100 Hz to avoid the instability effect that would corrupt the estimation. Results are shown in Table 4.3.

| | Measured at 1 | Measured at 2 | Measured at 3 |
|---|---|---|---|
| Control at 1 | 38.4% | 12.8% | 1.4% |
| Control at 2 | 6.0% | 46.7% | 2.9% |
| Control at 3 | 13.4% | 12.2% | 23.5% |

Table 4.3. Percentage of vibration kinetic energy attenuation at the mount junctions on the composite panel in the band [100 Hz - 1 kHz] for the three single-channel control systems.

Table 4.3 provides interesting information on the net attenuation effect of the different control systems. The diagonal terms of the table are the largest since they represent the attenuation at the control points. It appears that good local control is achieved at point 2 whereas, amongst the three control implementations, a control at point 2 tolerates the smallest feedback gain. Control at point 2 appeared, from the plots, to have a larger effect at the uncontrolled points than a control implementation at point 1, but the net isolation effect at points 1 and 3 of a control at 2 is in fact very small. The reason is that not only reductions but also vibration amplifications were observed above 100 Hz at these points which is connected with the fact that several panel modes do not contribute strongly to the response at point 2. Control at point 3 does give significant performance at points 1 and 2.

### 4.5.5. Experimental implementation of single-channel control at point 1

Real single-channel control was experimentally implemented at point 1. Results are only shown at the control point in Figure 4.35 for two values of gains: $h$=54, which is close to 52.5, the estimated maximum gain, and $h_{max}$=110, which is the largest experimental gain applied before the onset of instability. This unexpected large gain value seems to be the consequence of non linearity in the current source driving the control shaker or in the controller box which may saturate as the sensor output becomes too large. This enables us to apply a gain that is twice that expected and therefore larger vibration attenuation is achieved above 100 Hz. As seen from the simulations, the band of larger reduction is [250 Hz - 300 Hz]. The vibration level is reduced by 16 dB at 280 Hz for a gain of 110 and by 10 dB for a gain of 54, which is 3 dB better than estimated by the simulations for a maximum gain of 52.5. Significant reductions are also observed at 400 Hz where the control provides 8 dB and 4 dB attenuation for these two gains respectively. Isolation enhancements are also noticed up to 1 kHz. If the maximum gain is different from the one estimated, the general features of the control commented in section 4.5.4 are reproduced in practice. Vibration attenuation is achieved above 100 Hz and sharp amplification occurs below 100 Hz. Only the amplitude of vibration attenuation is changed by this unexpected value of maximum control gain.

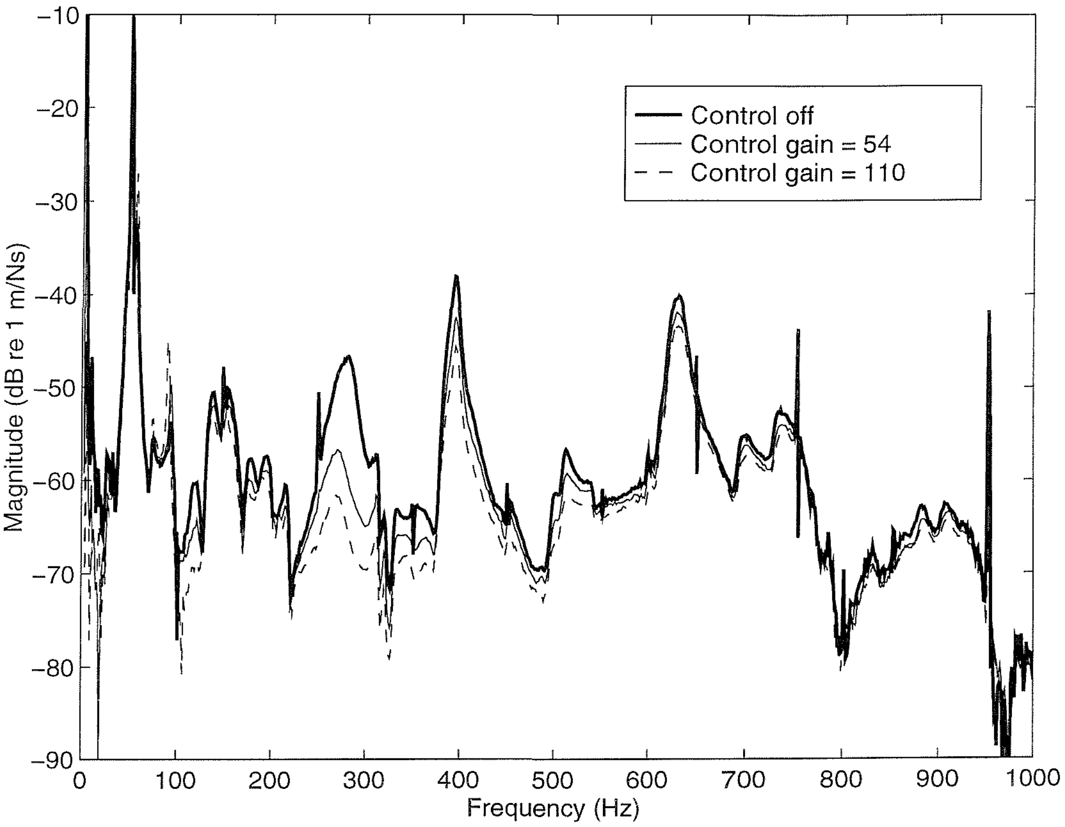

Figure 4.35. Measured passive velocity response $V_{01}$ and measured controlled velocity response $V_{11}$ at control point 1 for two values of control gain.

Over the range [100 Hz - 1000 Hz], the vibration energy is thus attenuated by 64.3% at the control point for a maximum gain of 110 and by 47.9% for a gain of 54 whereas it was estimated at 38.4% for a control gain of 52.5.

## 4.6. Multichannel control

### 4.6.1. Plant response and stability analysis

Simulations are now performed for a three-channel decentralised control system, in which all the control loops studied in the previous section are closed simultaneously. The objective is here to assess the performance of a local control based on DVFB operating at each mount connection. The nine transfer functions $G_{ji}$ measured for the analysis of the single channel controllers are now required in the stability analysis, since the plant response is now the matrix **G** made of the $G_{ji}$ transfer functions, as presented in chapter 2.

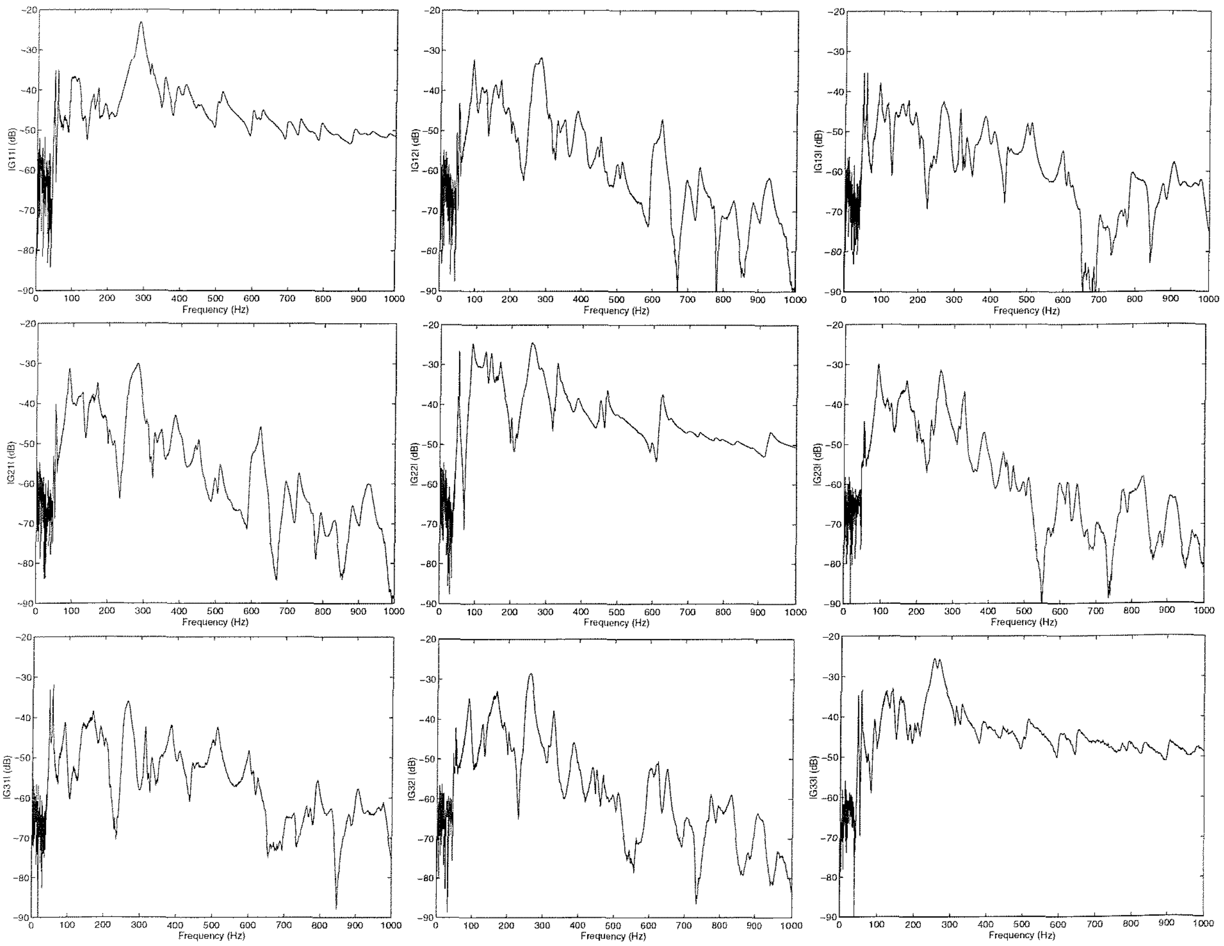

Figure 4.36. Magnitude of the elements of the measured matrix plant response.

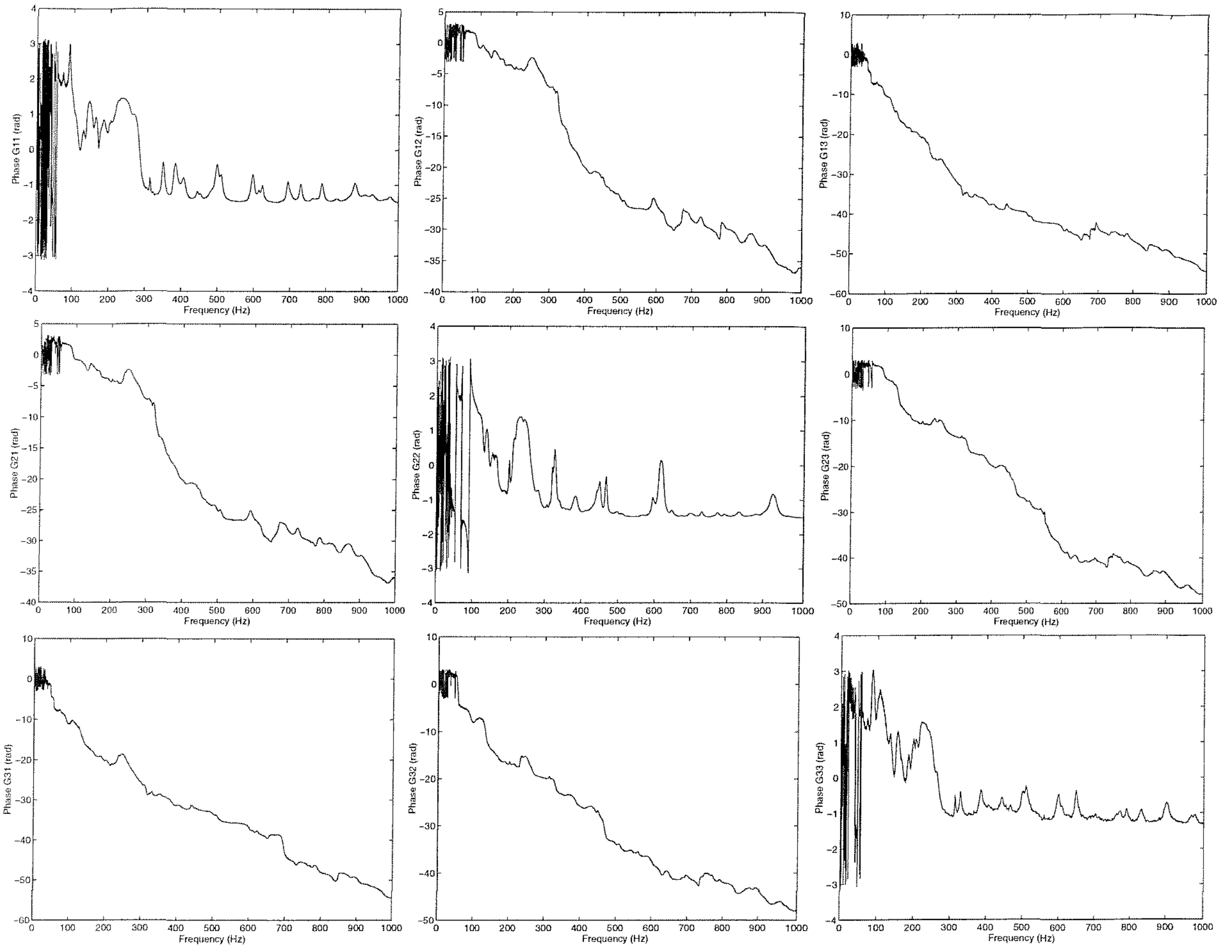

Figure 4.37. Phase of the elements of the measured matrix plant response.

In this case of a three channel-controller,

$$\mathbf{G} = \begin{bmatrix} G_{11} & G_{12} & G_{13} \\ G_{21} & G_{22} & G_{23} \\ G_{31} & G_{32} & G_{33} \end{bmatrix} \tag{4.21}$$

where the frequency dependence of these quantities are not made explicit for simplification of the notation.

Figure 4.36 shows the plots of the magnitude of the elements constituting the plant response matrix **G**. Figure 4.37 shows the different phase responses of the plant matrix whose cross-plots illustrate the mechanical delay between sensors and actuators as one control sensor is not located at the same position as one of the secondary actuators.

As discussed in chapter 2, the system stability can be studied by evaluating the frequency dependent eigenvalues of the open loop **GH** and applying the Nyquist method. For constant gain control, identical for each loop so that **H** is diagonal and time invariant, the Nyquist method is very convenient since it was shown to simplify to the determination of the eigenvalues of the plant matrix **G** alone. If the magnitude each diagonal term $G_{ii}$ in Figure 4.36 is much larger than the magnitude of the two cross terms of the same row, at each frequency, the control channels are mechanically weakly coupled and the eigenvalues of **G** are almost equal to the corresponding single-channel control plant responses $G_{ii}$, so that the maximum gain values estimated for the single-channel control systems can be used for the three-channel control implementation without any risk of instability. For the system considered, it appears, however, from Figure 4.36 that below 500 Hz, the cross terms of the plant response matrix can not be neglected and have to be taken into account in the stability assessment of the multichannel control. This mechanical coupling between the control channels was already pointed in the previous study by the discussion on the effect of a single-channel control at the two other sensor locations.

Figures 4.38, 4.39 and 4.40 show the Nyquist plots of the three eigenvalues $\lambda_1$, $\lambda_2$ and $\lambda_3$. Each of this eigenvalues are in principle more or less associated with the plant response $G_{ii}$ of one of the three single-channel control systems and common features between the two corresponding quantities are therefore expected. However, because of the mechanical coupling existing between the three channels and the noise in the measurement, it is difficult to track the eigenvalue $\lambda_i$ that corresponds to $G_{ii}$ and the Nyquist plots in Figures 4.38, 4.39 and 4.40 thus exhibit some discontinuities as one eigenvalue seems to switch to another one as the frequency changes. This does not corrupt the stability analysis for equal gain control, however, and the maximum feedback gain tolerated can still be properly estimated.

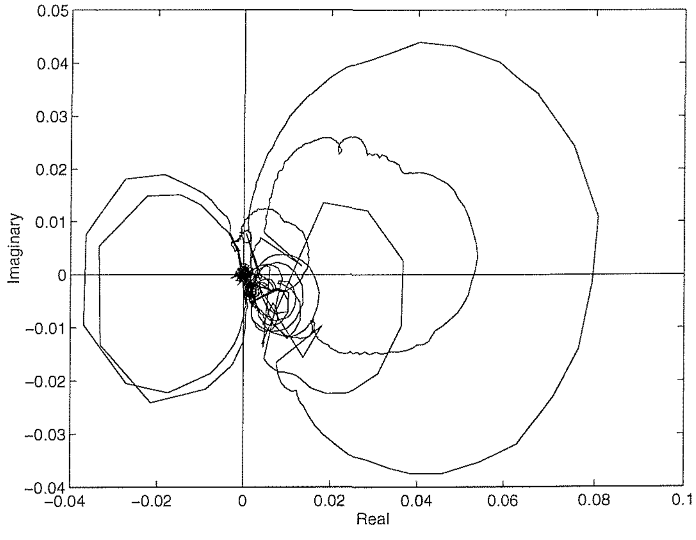

Figure 4.38. Nyquist plot of the eigenvalue $\lambda_1$ of the plant response **G**.

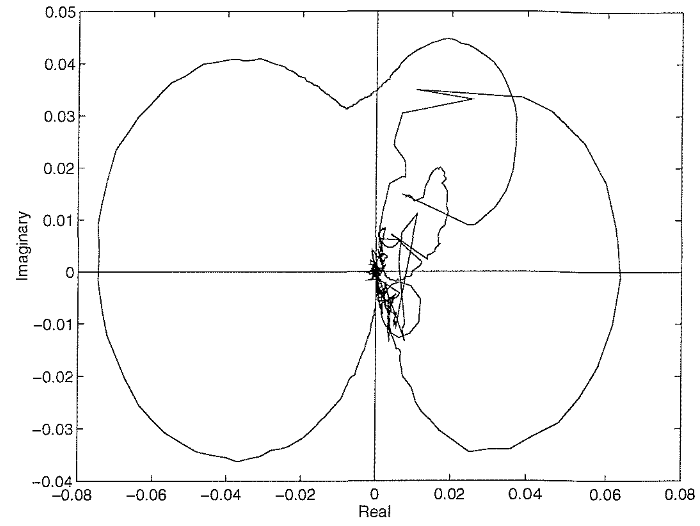

Figure 4.39. Nyquist plot of the eigenvalue $\lambda_2$ of the plant response **G**.

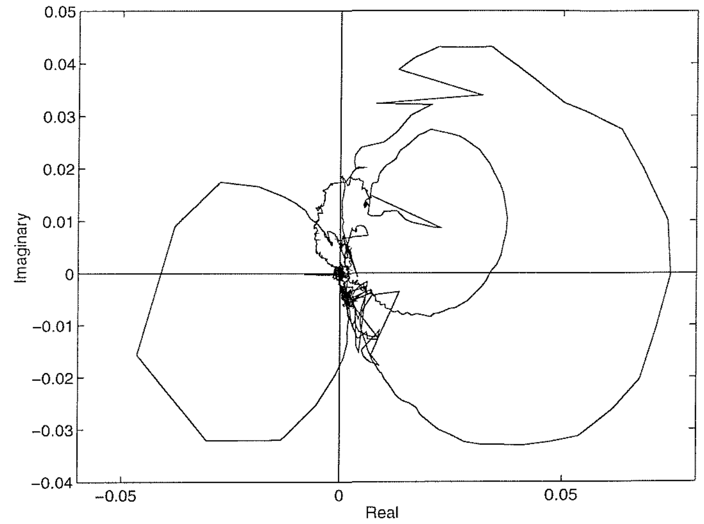

Figure 4.40. Nyquist plot of the eigenvalue $\lambda_3$ of the plant response **G**.

The Nyquist plot of the first eigenvalue in Figure 4.38 presents clear similarities with the Nyquist plot of $G_{11}$ as two large loops cross the negative real axis at 46.5 Hz and 55.5 Hz. The whole locus is however much larger than for $G_{11}$ since the other control loops and specially the third one also contribute to the whole response $\lambda_1$. The Nyquist plot of $\lambda_3$ also presents a large loop in the unstable half plane which crosses the negative real axis around 53 Hz. However, for an equal gain control, the gain limitation is to be found in the Nyquist plot of $\lambda_2$ which exhibits a loop crossing the negative real axis at 90 Hz, at the inertial actuator resonance, as already observed in the analysis of $G_{22}$. The inertial actuator dynamics are directly involved here and the overall gain is limited to a maximum value of 13.4.

### 4.6.2. Control performance

Figures 4.41, 4.42 and 4.43 present the force-normalised velocity at the three control points, similarly defined as for single-channel control, when three-channel equal gain control is simulated for a maximum gain of 13.4. The control responses are compared with the corresponding passive responses as for single-channel control.

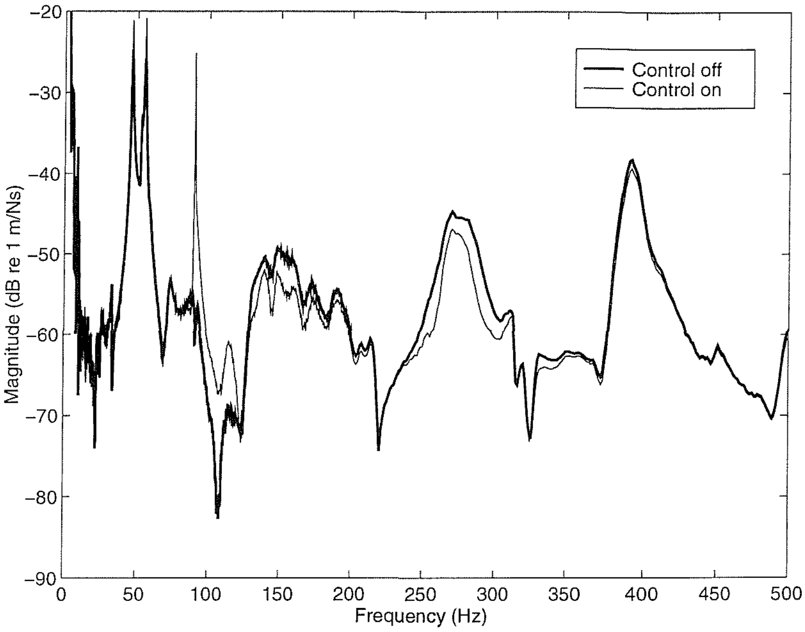

Figure 4.41. Measured passive velocity response $V_{01}$ and simulated controlled velocity response at point 1 for maximum gain multichannel control.

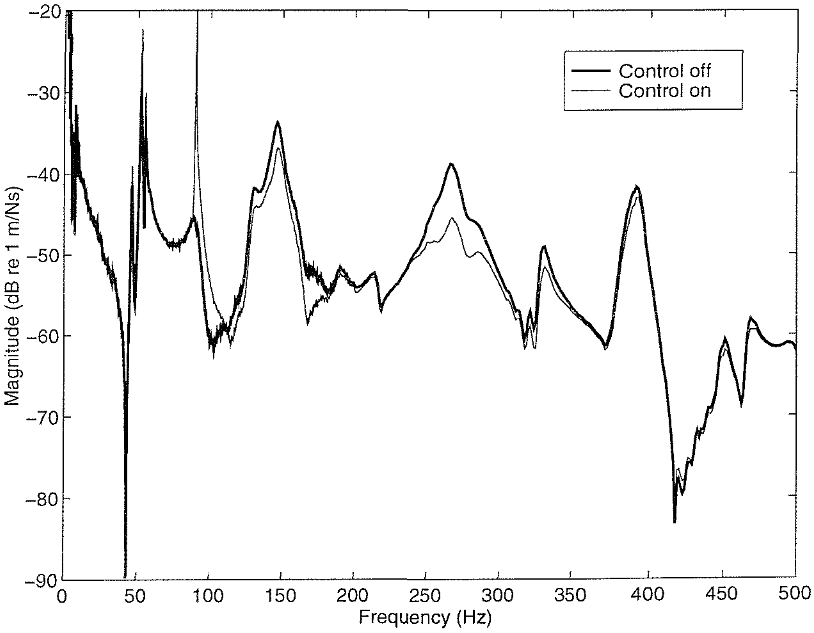

Figure 4.42. Measured passive velocity response $V_{02}$ and simulated controlled velocity response at point 2 for maximum gain multichannel control.

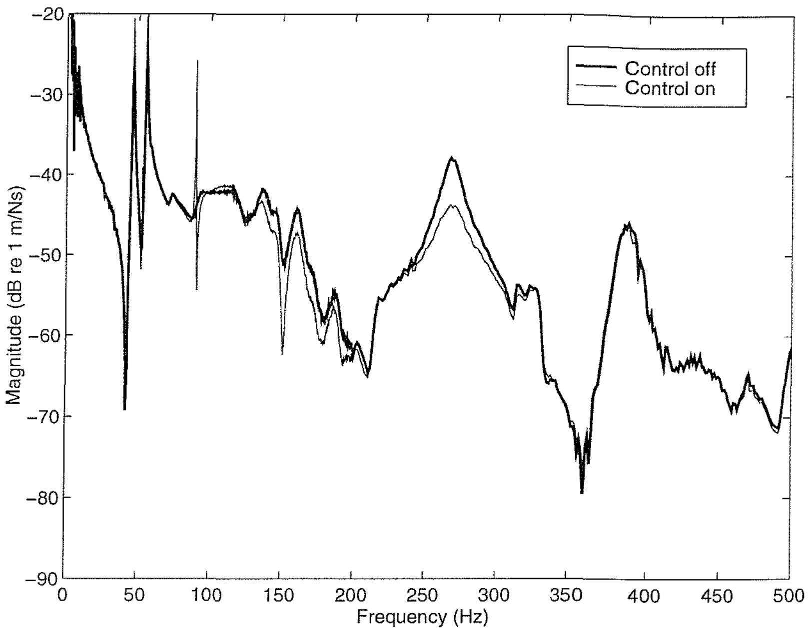

Figure 4.43. Measured passive velocity response $V_{03}$ and simulated controlled velocity response at point 3 for maximum gain multichannel control.

The first thing which is clear from these figures is the significant amplifications in the disturbance which occur at about 90 Hz, which is the frequency at which the system would go unstable if the feedback gain was slightly higher. The three-channel controller prevents any vibration amplification at high frequencies at the control points where only vibration attenuation is observed above 120 Hz. The control is then very likely to generate a global attenuation of the composite panel vibration at high frequencies. The vibration reduction is, however, strongly limited by the small feedback gain applied to the control system. Results are thus only displayed for the frequency range [0 - 500 Hz] as no significant control improvements are noticed above 500 Hz. As expected from the previous analysis, the attenuation is maximum in the band [250 Hz - 300 Hz]. At 270 Hz, 2 dB attenuation is achieved at point 1, 7 dB at point 2 and 6 dB at point 3. As for the single-channel controller study, the vibration energy attenuation above 100 Hz has been calculated at the three control locations to help in the estimation of the high frequency efficiency of the equal gain multichannel controller. The results are listed in Table 4.4.

| | Point 1 | Point 2 | Point 3 |
|---|---|---|---|
| *Attenuation* | 28.4% | 42.9% | 20.5% |

Table 4.4. Percentage of vibration kinetic energy attenuation at the mount junctions on the composite panel in the band [100 Hz - 1 kHz] for maximum gain multichannel control.

Again the attenuation is maximum at point 2. One should note that the attenuation at point 3 goes up to 36.0% when it is estimated from 120 Hz. It would, however, be impossible to use these attenuations in practice because of the amplification at 90 Hz.

## 4.7. Conclusions

The analysis of the different control systems simulated and implemented in this chapter bears out the conclusion reached in chapter 3, that instability and therefore gain limitation are inherent to the use of inertial device in DVFB control. This first appears obvious since it is well know to be difficult to generate a force, at low frequencies, by reaction against a free mass. Section 3.3, however, clearly defined the dominant role of the secondary actuator in the plant response and this chapter extends this conclusion to the general case of flexible structure on multi-mount system. It also illustrates very clearly how the inertial devices split the frequency range into two distinct regions. The low frequency band, below $\omega_a$, is the band of control amplification and, above $\omega_a$, the control is expected to enhance the passive isolation performance. The smaller the inertial actuator damping, the more this statement is satisfied and the quicker the control will implement perfect skyhook damping at high frequencies. As the control becomes efficient, at high frequencies, a simple velocity feedback loop seems not only to apply local control but also to lead, to a certain extend, to an overall reduction of the vibration level of the equipment panel, even if no reduction of a specific mode of the mounted equipment panel has been observed. This suggestion would need to be checked by estimating the control effect at other positions on the equipment panel or the power input in the panel at the mount junctions.

Such a control implementation could be damaging to the suspended system because of the large increase of the low frequency vibration. One can then think of increasing the gain margin by lowering the resonance $\omega_a$ but this may induce an unreasonable addition of weight in the inertial actuator. The inertial implementation of DVFB control thus faces strong low frequency limitations, even though such an active isolation is designed to supplement the poor performance of passive isolations at low frequencies. For many practical cases, an inertial implementation of DVFB control does not appear to be the right strategy when passive/active isolation has to be designed. It offers, however, a greater potential in reducing high frequency vibration on structures not connected to any passive isolation since it can easily be built as a self-contained control unit to be positioned at any location on a vibrating structure in order to apply local control. It must be highlighted, moreover, than only a rather crude and basic control system has been considered here, in which no place is allocated for any operation on the control signal. The use of appropriate compensators to modify the phase response of the plant at low frequencies could thus be considered and may partly remove the control limitations to the expense of reduction of the attenuation at higher frequencies. This would, however, lead to an increase of the gain margin and possibly to an overall enhancement of the control system performance. This is not within the direct scope of the present study which is focused on the mechanical aspect of DVFB control, but it does offer an interesting suggestion for further work and developments.

# Chapter 5

# Reactive implementation of DVFB control on a mounted flexible equipment: Simulations

## 5.1. Introduction

It has been seen that DVFB using inertial actuation leads to enhancement of the vibration at low frequencies compared with that provided by an existing passive isolation. In chapter 3, a reactive control force was shown, however, to give very robust control and high degree of vibration isolation when implemented to a rigid suspended equipment, even though the base structure was considered to be flexible. The final two chapters will thus focus on a reactive implementation of the strategy of DVFB control, extended to a multi-mount system for the isolation of a flexible suspended equipment. This study will enable a assessment of the performance of reactive DVFB control, faced with a practical system in which no simplifying assumption can be made. The test rig designed to carry out this study is similar to the one presented in chapter 4, and so comparisons will be possible between reactive and inertial actuation for the strategy of DVFB control. Prior to any real implementation of the control, a full model of the experimental isolation system has been developed in parallel with passive measurements. Chapter 5 is thus focused on the model description and on the performance of the control resulting from pure simulations whereas chapter 6 will show the results obtained from an experimental implementation of DVFB for both single and multichannel controls. Before discussing the model, this chapter gives a brief description of the test rig. It is followed by a discussion on the general expression of the plant response for reactive control of a flexible equipment panel mounted on a single passive isolator. The structure of the model is then developed and validated by a set of passive measurements carried out on the experimental rig. The performance of the different single-channel controls and of the decentralised multichannel control obtained by the model are finally discussed, setting an useful framework for a safe implementation and a good understanding of the experimental control results.

The objective of the control is to improve the efficiency of a passive mounting system in reducing the equipment out-of-plane vibration due to flexural bending waves transmitted to the supported structure by the rubber mounts. A reactive implementation of DVFB control was shown in chapter 3 to be unconditionally stable and thus to provide very promising performance. However, the control is now faced to four main changes.

*a-* The equipment structure is no longer rigid and thus does not simply behave as a suspended mass. This modifies the expression of $M_e$ defined in section 3.2. The question of the effect of the equipment flexibility on the expression of the plant response is addressed in section 5.2.

*b-* The equipment structure is connected to the base structure by several mounts. In the case of an inertial secondary actuation, this does not really affect the plant response compared to a single-mount connection. However, a secondary force reacting in parallel with the $i^{th}$ mount generates a disturbance in the flexible base which is transmitted back to junction $i$ on the equipment via the other mounts. This mechanical feedback introduces an extra delay in the plant which is an extra factor for plant destabilisation.

*c-* Resonances in the mount now have to be taken into account in the frequency range covered by the active control analysis. The mounts can not be simply modelled by the single impedance term $Z_m$. This may also constitute a factor of control destabilisation.

*d-* Not only axial but also rotational excitations $\theta_x$ and $\theta_y$ in the mount are transmitted to the equipment. These excitations can not be tackled by an axial active force device such as the reactive actuators used. This limits the control to one of the three components responsible for equipment bending vibration. This may, however, not be exactly true as these three components (1 translation and 2 rotations) are coupled together.

## 5.2. Effect of the equipment flexibility on the plant response

The effect of the equipment flexibility can be approached by going back to equation (3.13), which gives the general expression of the total mobility for a single channel DVFB control using a reactive secondary force in parallel with a single massless isolator. The dynamics of the flexible base and equipment are modelled by the uncoupled input mobility at the mount junction $M_b$ and $M_e$ respectively, as defined in chapter 3. The equipment structure, like the base structure, can now be described as a linear combination of structural modes defined by their modal stiffness, damping and mass: respectively $k_{en}$, $c_{en}$ and $m_{en}$ for the $n^{th}$ mode. Similarly, for the base structure, $k_{bm}$ is the modal stiffness, $c_{bm}$ is the modal damping and $m_{bm}$ is the modal mass of the $m^{th}$ mode.

The dynamics of the mounted equipment can thus, in principle, display three types of behaviour. It can be mass controlled, damping controlled or stiffness controlled.

### 5.2.1 Mass controlled equipment

If the equipment is mass controlled, the mobility $M_e$ can be approximated by,

$$M_e = \frac{1}{j\omega m_{en}} \tag{5.1}$$

This comes back to the case of rigid body control, which was proved to be unconditionally stable (section 3.2.1).

### 5.2.2. Damping controlled equipment

If the equipment is damping controlled, the mobility $M_e$ can be approximated by,

$$M_e = \frac{1}{c_{en}} \tag{5.2}$$

The expression for $M_{total}$ in equation (3.13) is now using $Z_m = c + \frac{k}{j\omega}$,

$$M_{total} = \frac{1}{c_{en} + \left(c + {}^{k}\!/_{j\omega}\right)\left(1 + c_{en} M_b\right)} \tag{5.3}$$

As already performed for the analysis of rigid equipment control, and noting that $M_b$ is an input mobility, it can be written that

$$-\frac{\pi}{2} < \angle\left(1 + c_{en} M_b\right) < \frac{\pi}{2} \tag{5.4}$$

so that using expression (3.20)

$$-\pi < \angle\left[\left(c + {}^{k}\!/_{j\omega}\right)\left(1 + c_{en} M_b\right)\right] < \frac{\pi}{2} \tag{5.5}$$

The first damping term $c_{en}$ in the denominator of equation (5.3) does not modify the phase limits and then,

$$-\frac{\pi}{2} < \angle M_{total} < \pi \tag{5.6}$$

The control system is still, in principle, unconditionally stable when the equipment is damping controlled

### 5.2.3. Stiffness controlled equipment

If the equipment is stiffness controlled, the mobility $M_e$ can be approximated by,

$$M_e = \frac{j\omega}{k_{en}} \tag{5.7}$$

and equation (3.13) is now

$$M_{total} = \frac{1}{{}^{k_{en}}\!/_{j\omega} + \left(c + {}^{k}\!/_{j\omega}\right)\left(1 + {}^{k_{en}M_b}\!/_{j\omega}\right)} \tag{5.8}$$

No direct conclusion comes out of this expression unless assumptions on the base dynamics are made.

*Stiffness controlled base*

If the base is stiffness controlled,

$$M_b = \frac{j\omega}{k_{bm}} \tag{5.9}$$

and then equation (5.8) is now

$$M_{total} = \frac{1}{{}^{k_{en}}\!/_{j\omega} + \left(c + {}^{k}\!/_{j\omega}\right)\left(1 + {}^{k_{en}}\!/_{k_{bm}}\right)} \tag{5.10}$$

Going through the process of phase analysis it turns out that,

$$-\frac{\pi}{2} < \angle\frac{1}{M_{total}} < 0 \tag{5.11}$$

and so

$$0 < \angle M_{total} < \frac{\pi}{2} \tag{5.12}$$

which shows that the control is fully passive and thus unconditionally stable when both equipment and base structures are stiffness controlled. In this configuration, only vibration reduction is then achieved.

***Mass controlled base***

If the base is mass controlled,

$$M_b = \frac{1}{j\omega m_{bm}} \tag{5.13}$$

and equation (5.8) can be rewritten as,

$$M_{total} = \frac{1}{k_{en}/j\omega + \left(c + k/j\omega\right)\left(1 + k_{en}/(j\omega)^2 m_{bm}\right)} \tag{5.14}$$

so that

$$\frac{1}{M_{total}} = c + \frac{k + k_{en}}{j\omega} + \frac{k_{en}c}{(j\omega)^2 m_{bm}} + \frac{kk_{en}}{(j\omega)^3 m_{bm}} \tag{5.15}$$

The phase of the total mobility is now such as

$$0 < M_{total} < \frac{3\pi}{2} \tag{5.16}$$

In this configuration, the system is potentially unstable and therefore gain limited when the following two relationships are satisfied:

$$Re\left(M_{total}\right) < 0 \quad \text{and} \quad Im\left(M_{total}\right) = 0 \tag{5.17, 5.18}$$

Using equation (3.13), these two expressions can be shown to be equivalent to

$$\omega < \sqrt{\frac{k_{en}}{m_{bm}}} \quad \text{and} \quad \omega = \sqrt{\frac{kk_{en}}{m_{bm}\left(k + k_{en}\right)}} \tag{5.19, 5.20}$$

Equation (5.19) is automatically satisfied if equation (5.20) is satisfied. Under the conditions that the equipment structure is stiffness controlled and the base structure is mass controlled, the control of a suspended flexible structure can only lead to instability at frequencies given by equation (5.20). In practice, the modal stiffness $k_{en}$ becomes rapidly much larger than the mount stiffness $k$ as the modal order $n$ increases. Expression (5.20) quickly tends to $\omega_c = \sqrt{\frac{k}{m_{bm}}}$ for higher modes. For an uniform plate in bending, $\omega_c$ is a constant, as the modal mass is constant, independent of the modal order so that instability can only occur at rather low frequencies.

Assuming the control is gain limited so that equation (5.20) is satisfied, using equation (5.14) it can be calculated that when the phase of $M_{total}$ is equal to $\pi$,

$$M_{total} = -\frac{k}{ck_{en}} \tag{5.21}$$

The higher the modal order of the equipment structure resonance, the smaller the loop crossing the negative real axis of the Nyquist plot and the larger the maximum feedback gain tolerated by the control system.

### *Damping controlled base*

If the base is damping controlled,

$$M_b = \frac{1}{c_{bm}} \tag{5.22}$$

and equation (5.8) can be rewritten as

$$M_{total} = \frac{1}{{}^{k_{en}}\!/_{j\omega} + \left(c + {}^{k}\!/_{j\omega}\right)\left(1 + {}^{k_{en}}\!/_{j\omega c_{bm}}\right)} \tag{5.23}$$

A phase analysis of equation (5.23) shows that

$$0 < \angle M_{total} < \pi \tag{5.24}$$

The control is then, once again, unconditionally stable. It is interesting to note that as the frequency increases, the wavelength in the base structure becomes small compared to the dimensions of the base which starts to behave as an infinite structure. The base dynamics is therefore damping-like and its input mobility is purely real and frequency dependent. For example, the input mobility of an infinite plate in bending is equal to $1/8\sqrt{D\rho h'}$, where $D$ is the bending stiffness, ρ is the density and $h'$ is the thickness of the plate. This shows that a reactive implementation of DVFB control does not present any sign of high frequency instability. This observation can also be extended to the case of multi-mount systems since the mechanical coupling between two control channels, due to the multi-transmission paths, decreases with frequency as the spacing between two mounts becomes much larger than the wavelength in the base or in the equipment structure.

Even though reactive DVFB control is not unconditionally stable when applied on a flexible structure mounted on a single mount, this discussion on the phase response of the total mobility function presents the reactive actuation as a strategy with good potentials for DVFB control. Instability can only occur at low frequencies as the base structure is mass controlled and the equipment is stiffness controlled. This must, however, be balanced since it comes from the analysis of perfect mass-like, damping-like or spring-like behaviour of the elements composing the isolation system, whereas a combination of the three types of behaviour should be theoretically investigated. Moreover, modal overlap is observed in practise. Finally, this short analysis does not include the other hypothesis pointed in points *b*, *c* and *d* in the introduction.

## 5.3. Isolation system description

The experimental test rig is similar to the one investigated in chapter 4, except that the inertial actuators have been replaced by reactive actuators. The rig is composed of a composite equipment panel set on three rubber mounts which provide passive isolation from the vibrating flexible base. The equipment panel is a composite honeycomb plate of the same structure as the one in chapter 4. The mounts are cylindrical pieces of rubber. To help in deriving an analytical model of the base structure, the U-beam has been replaced by a long aluminium plate on which the reactive actuators are bolted to. Figure 5.1 shows a schematic and a photograph of the global system and Table 5.1 lists the main geometrical and physical parameters of the main three elements of the rig. Like in the system investigated for the implementation of inertial control, both the equipment panel and the base plate present free-free boundary conditions.

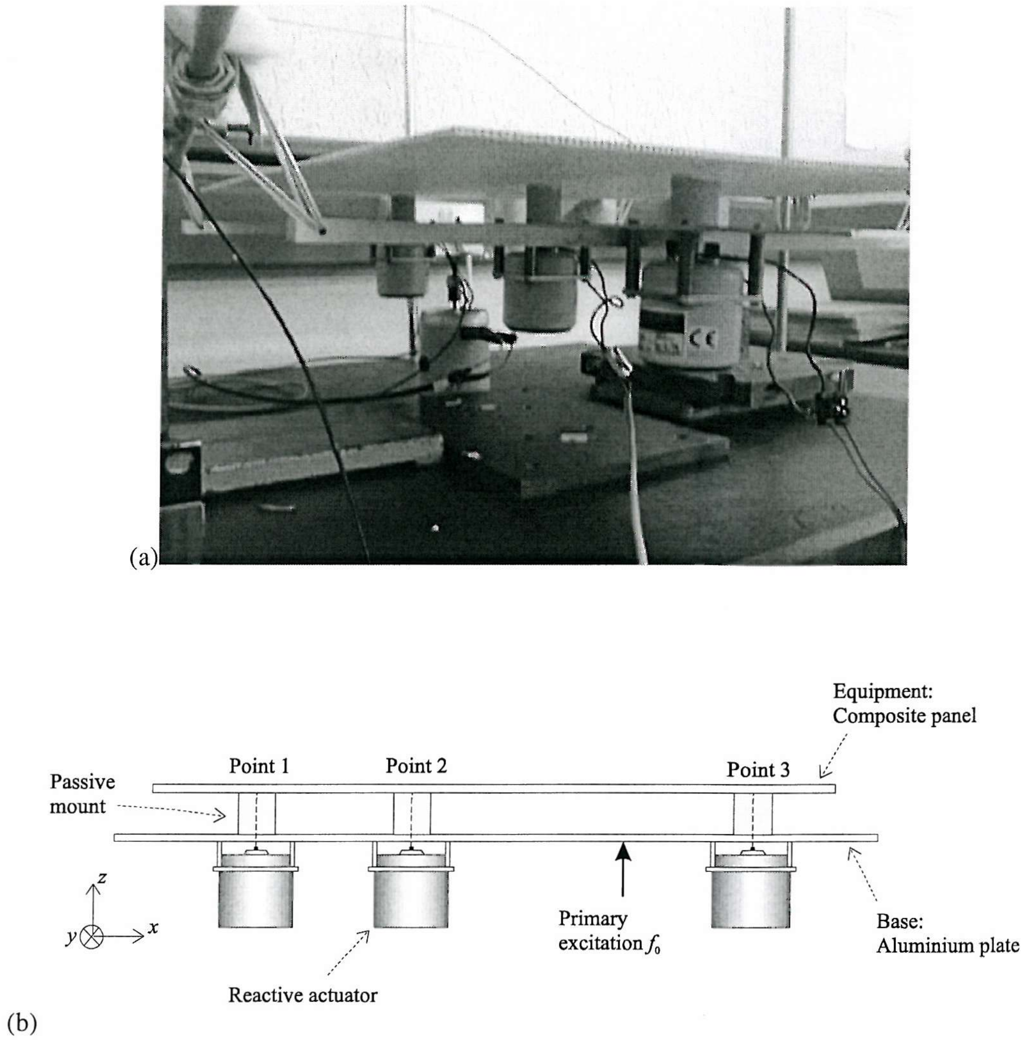

Figure 5.1. Photograph (a) and schematic (b) of the experimental test rig for reactive control.

| | Main dimensions (mm) | Material |
|---|---|---|
| Equipment panel | 710 x 500 x 4 | Composite fibre |
| Base plate | 803 x 100 x 3 | Aluminium |
| 3 mounts | $\varnothing_{ext} = 30$, $\varnothing_{in} = 10$, $h = 30$ | Soft rubber |

Table 5.1. Main characteristics of the elements of the isolation system.

The main differences with the inertial control test rig are due to the type of secondary actuation. The inertial shakers have been removed and replaced by three secondary shakers bolted on the aluminium base plate. They are rather powerful force generators relative to the dynamics of the system under control. They can thus easily generate the control force required but their mass, of 0.91 Kg each, strongly affect the dynamics of the base plate, whose mobility is significantly lowered. This does not completely remove, however, the hypothesis of a flexible base structure, since it still presents significant dynamics with very low frequency resonances as shown in the passive analysis of the system below. Referring to the practical example of the double shell fuselage of a standard civil aircraft, the external aluminium shell, coupled to different sets of stiffeners, has a high impedance in comparison with the internal composite panel. The difference in impedance may not be as large as the one encountered in the system under investigation, but many other practical situations present such a mobility difference between the base and the equipment structures.

In order to apply reactive secondary forces as in chapter 3, the mounts have been moulded as hollow cylinders to insert a thin metallic stinger which can transmit the axial force generated by one control shaker to the top disc of each rubber mount which is rigidly connected to the composite panel. The stinger, as shown in Figure 5.2, is made of a wire, very flexible in rotation, to prevent any transmission of moment excitation due to rotation at the tips of the mount. The secondary actuation can thus only transmit axial efforts. Acting in parallel with the passive isolation, the stiffness of the actuator suspension can be neglected compared to the axial static stiffness of the mounts. The mounts are made of a rubber material, which are easy to mould at relatively low temperature. They are therefore soft in comparison with the isolators generally used in the aeronautic industry. A strip of tape has then be wrapped around each of them to increase their axial stiffness to 42 kN/m. A soft mounting can make the control more challenging for a reactive implementation of DVFB since it gives rise to rather low frequency resonances in the mounts.

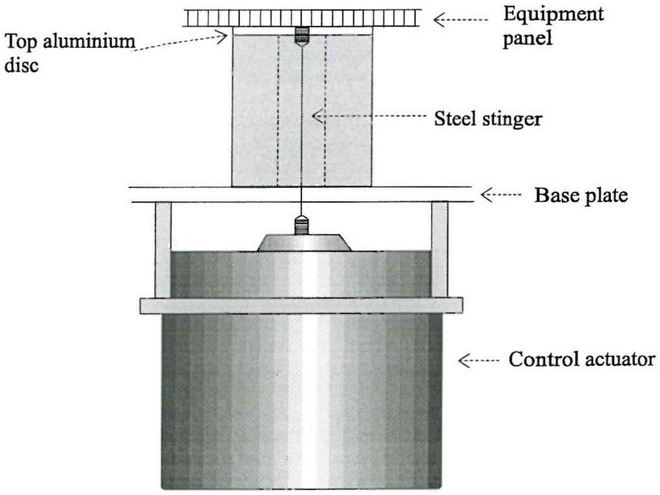

Figure 5.2. Schematic of one active mount

The experimental rig has been designed to avoid any symmetry that could condition the control system. The spacing between two consecutive control actuators is not the same and the three mounts, aligned along the *x*-direction, are connected to the equipment panel off the centre line and off the main nodal lines of the equipment panel, so that all the low frequency modes of the equipment panel can be excited. The primary excitation $f_0$, represented in Figure 5.1, is located off the centre line of the base structure so that a maximum base dynamics, including rotational excitation around the *y*-axis, can be obtained. Table 5.2 lists the positions of the mount junctions on the base plate and on the equipment panel relative to a local reference position whose axis are shown on Figure 5.1.

| Point | Position $(x,y)$ in mm on the base | Position $(x,y)$ in mm on the equipment |
|---|---|---|
| 1 | (160,50) | (120,220) |
| 2 | (350,50) | (310,220) |
| 3 | (680,50) | (640,220) |

Table 5.2. Mount positions on the base plate and on the equipment composite panel.

## 5.4. The model

### 5.4.1. Global modelling

The purpose of modelling the mechanical system under control is to enable an estimation of the whole equipment dynamics by calculating, at each frequency, the power input by the mounts into the equipment. Performing this calculation when the system only undergoes a primary excitation and when the controller is running thus provides a global performance of the controller in reducing the whole equipment out-of-plane vibration. Experimentally, using conventional accelerometers and no force or moment sensors, only a rough estimation of the kinetic energy of the equipment can be achieved by monitoring the response at different locations.

The model is based on a mobility-impedance formulation. It is to a large extend a modified version of the model developed and discussed by Gardonio [25] in the study of active transmission reduction between two flexible plates mounted on multiple isolators.

At each junction *j* with the mounting system, the velocity and force related to the six degrees of freedom on the base and the equipment structures can be gathered respectively in a kinematic vector $\mathbf{v}_j$ and in a dynamic vector $\mathbf{f}_j$ as,

$$\mathbf{v}_j^T = \{\dot{u}_j \quad \dot{v}_j \quad \dot{w}_j \quad \dot{\theta}_{xj} \quad \dot{\theta}_{yj} \quad \dot{\theta}_{zj}\} \text{ and } \mathbf{f}_j^T = \{N_{xj} \quad N_{yj} \quad N_{zj} \quad M_{xj} \quad M_{yj} \quad M_{zj}\} \qquad (5.25, 5.26)$$

where $\dot{u}_j$, $\dot{v}_j$ and $\dot{w}_j$ are the complex amplitudes of the linear velocities respectively along the $x$, $y$ and $z$-axis, $\dot{\theta}_{xj}$, $\dot{\theta}_{yj}$, $\dot{\theta}_{zj}$ are the complex amplitudes of the angular velocities respectively around the $x$, $y$ and $z$-axis, $N_{xj}$, $N_{yj}$, $N_{zj}$ are the complex amplitudes of the forces respectively in the $x$, $y$ and $z$-directions and finally $M_{xj}$, $M_{yj}$ and $M_{zj}$ are the complex amplitudes of the moment referred respectively to the $x$, $y$ and $z$-axis.

Only the out-of-plane motion resulting from bending vibration in the base and equipment structures are considered so that the vectors $\mathbf{v}_j$ and $\mathbf{f}_j$ can be reduced to

$$\mathbf{v}_j^T = \{\dot{w}_j \quad \dot{\theta}_{xj} \quad \dot{\theta}_{yj}\} \text{ and } \mathbf{f}_j^T = \{N_{zj} \quad M_{xj} \quad M_{yj}\} \qquad (5.27, 5.28)$$

since only the rotation $\dot{\theta}_x$, $\dot{\theta}_y$ and therefore the moments $M_x$ and $M_y$ are coupled to the resulting out-of-plane motion $\dot{w}$.

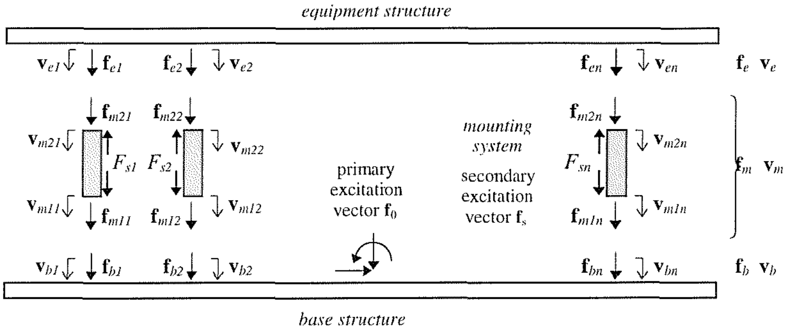

Figure 5.3. Scheme of a general isolating system for base vibration.

As suggested by the notation in Figure 5.3, the different force and velocity vectors can be grouped into a base velocity vector $\mathbf{v}_b$ and in a base force vector $\mathbf{f}_b$ and similarly for the equipment where $\mathbf{v}_e$ is the equipment velocity vector and $\mathbf{f}_e$ is the equipment force vector. Considering 3 mounts,

$$\mathbf{f}_b = \begin{Bmatrix} \mathbf{f}_{b1} \\ \mathbf{f}_{b2} \\ \mathbf{f}_{b3} \end{Bmatrix} \quad \mathbf{v}_b = \begin{Bmatrix} \mathbf{v}_{b1} \\ \mathbf{v}_{b2} \\ \mathbf{v}_{b3} \end{Bmatrix} \qquad \mathbf{f}_e = \begin{Bmatrix} \mathbf{f}_{e1} \\ \mathbf{f}_{e2} \\ \mathbf{f}_{e3} \end{Bmatrix} \quad \mathbf{v}_e = \begin{Bmatrix} \mathbf{v}_{e1} \\ \mathbf{v}_{e2} \\ \mathbf{v}_{e3} \end{Bmatrix} \qquad (5.29, 5.30)$$

where $\mathbf{v}_{bj}$ is the 3x1 velocity vector on the base structure at the junction with the $j^{\text{th}}$ mount as defined in equation (5.27), $\mathbf{f}_{bj}$ is the 3x1 force vector on the base structure at the junction with the $j^{\text{th}}$ mount as defined in equation (5.28) and similarly for $\mathbf{v}_{ej}$ and $\mathbf{f}_{ej}$.

A similar dynamic description can be obtained for the velocity and force components at the two ends of each passive mount so that,

$$\mathbf{v}_m^T = \left\{ \mathbf{v}_{m11}^T \quad \mathbf{v}_{m12}^T \quad \mathbf{v}_{m13}^T \quad \mathbf{v}_{m21}^T \quad \mathbf{v}_{m22}^T \quad \mathbf{v}_{m23}^T \right\} \tag{5.31}$$

$$\mathbf{f}_m^T = \left\{ \mathbf{f}_{m11}^T \quad \mathbf{f}_{m12}^T \quad \mathbf{f}_{m13}^T \quad \mathbf{f}_{m21}^T \quad \mathbf{f}_{m22}^T \quad \mathbf{f}_{m23}^T \right\} \tag{5.32}$$

where $\mathbf{v}_{m1j}$ and $\mathbf{f}_{m1j}$ represent the 3x1 velocity and force vectors of the $j^{\text{th}}$ mount at the junction with the base structure and $\mathbf{v}_{m2j}$ and $\mathbf{f}_{m2j}$ represent the 3x1 velocity and force vectors of the $j^{\text{th}}$ mount at the junction with the equipment structure.

Considering a primary excitation vector $\mathbf{f}_0$ acting on the base structure, the velocity and force vectors of the base can be related to each other using the mobility matrix approach by

$$\mathbf{v}_b = \mathbf{M}_{b1}\mathbf{f}_b + \mathbf{M}_{b2}\mathbf{f}_0 \tag{5.33}$$

where $\mathbf{M}_{b1}$ is the matrix of the mobilities between the different junction locations on the base and $\mathbf{M}_{b2}$ is the matrix of mobilities between the excitation points and the response at the mount junctions on the base structure. Similarly for the velocity and force vectors of the equipment structure.

$$\mathbf{v}_e = \mathbf{M}_{e1}\mathbf{f}_e \tag{5.34}$$

where $\mathbf{M}_{e1}$ is the matrix of mobilities between the different mount junctions on the equipment structure.

Each elements of these matrices, $\mathbf{M}_{b1}$, $\mathbf{M}_{b2}$, $\mathbf{M}_{e1}$ are themselves 3 by 3 matrices of mobility functions accounting for the three coupled degrees of freedom considered. More details can be found in section 5.4.2, which is focused on the plate dynamics modelling. The base and equipment structure equations in expressions (5.33) and (5.34) can then be grouped in an unique equation as,

$$\mathbf{v}_{be} = \mathbf{M}_{be1}\mathbf{f}_{be} + \mathbf{M}_{be2}\mathbf{f}_0 \tag{5.35}$$

where $\mathbf{M}_{be1}$, the global mobility matrix associated to an excitation at the mounting junctions on the base and equipment structures and $\mathbf{M}_{be2}$, the global mobility matrix between the primary excitation locations on the base structure and the response at the mounting junctions on the base and equipment structures are defined as,

$$\mathbf{M}_{be} = \begin{bmatrix} \mathbf{M}_{b1} & 0 \\ 0 & \mathbf{M}_{e1} \end{bmatrix} \quad \text{and} \quad \mathbf{M}_{be2} = \begin{bmatrix} \mathbf{M}_{b2} \\ 0 \end{bmatrix} \qquad (5.36, 5.37)$$

and the global junction velocity and force vectors are given by

$$\mathbf{v}_{be} = \begin{Bmatrix} \mathbf{v}_b \\ \mathbf{v}_e \end{Bmatrix} \; \mathbf{f}_{be} = \begin{Bmatrix} \mathbf{f}_b \\ \mathbf{f}_e \end{Bmatrix} \qquad (5.38, 5.39)$$

The dynamics of the mountings are expressed using an impedance approach. The reactive secondary forces acting in parallel with the passive isolators can also be defined at this stage so that,

$$\mathbf{f}_m = \mathbf{Z}_m \mathbf{v}_m + \mathbf{f}_s \qquad (5.40)$$

where $\mathbf{Z}_m$ is the mount impedance matrix, detailed in section 5.4.5 and $\mathbf{f}_s$ is the secondary force vector which, for DVFB control, is

$$\mathbf{f}_s = \mathbf{K}\mathbf{v}_m \qquad (5.41)$$

where **K** is the control gain matrix.

When the three component, base, isolators and equipment are coupled together, the velocity continuity condition and the force equilibrium principle at each junction impose the conditions that

$$\mathbf{v}_m = \mathbf{v}_{be} \quad \text{and} \quad \mathbf{f}_m + \mathbf{f}_{be} = 0 \qquad (5.42, 5.43)$$

so that equation (5.40) becomes

$$\mathbf{f}_{be} = -(\mathbf{Z}_m + \mathbf{K})\mathbf{v}_{be} \qquad (5.44)$$

Combining equations (5.44) with (5.35),

$$\mathbf{v}_{be} = -\mathbf{M}_{be1}(\mathbf{Z}_m + \mathbf{K})\mathbf{v}_{be} + \mathbf{M}_{be2}\mathbf{f}_0 \qquad (5.45)$$

or

$$\mathbf{v}_{be} = \left(\mathbf{I} + \mathbf{M}_{be1}(\mathbf{Z}_m + \mathbf{K})\right)^{-1}\mathbf{M}_{be2}\mathbf{f}_0 \qquad (5.46)$$

and the global force vector can now be calculated using equation (5.44)

$$\mathbf{f}_{be} = -(\mathbf{Z}_m + \mathbf{K})\left(\mathbf{I} + \mathbf{M}_{be1}(\mathbf{Z}_m + \mathbf{K})\right)^{-1}\mathbf{M}_{be2}\mathbf{f}_0 \qquad (5.47)$$

Knowing both the velocity and force vectors at each mount junction on the equipment structure, it is easy to determine the global power input in the equipment, $P_{in}$, by the axial and rotational excitations from the mounts.

$$P_{in} = \frac{1}{2} Re\{\mathbf{f}_e \mathbf{v}_e^H\} \qquad (5.48)$$

This also enables us to discriminate between the "axial power" and the "rotational power" and to evaluate the control effect on each of this quantities so that a global performance of DVFB in limiting vibration transmission through a passive isolation can be estimated.

Knowing $\mathbf{f}_e$, it is simple to compute a mobility matrix $\mathbf{M}_r$ between the mount junctions on the equipment structure regarded as excitation points and other points on the equipment structure to calculate the out-of-plane velocity at desired locations.

$$\mathbf{v}_r = \mathbf{M}_r \mathbf{f}_e \qquad (5.49)$$

where $\mathbf{v}_r$ is the velocity response vector at the points of interest on the equipment structure.

### 5.4.2. Plate mobility matrices

As already mentioned, each element constituting the different equipment and base mobility matrices presented above, for example $\mathbf{M}_{e1}(k, l)$, are themselves sub-matrices relating a point of excitation $k$ to a response at $l$ for the three degrees of freedom considered in the model so that,

$$\mathbf{M}(k,l)=\begin{bmatrix} M^{kl}_{wNz} & M^{kl}_{wMx} & M^{kl}_{wMy} \\ M^{kl}_{\dot{\theta}xNz} & M^{kl}_{\dot{\theta}xMx} & M^{kl}_{\dot{\theta}yMx} \\ M^{kl}_{\dot{\theta}yNz} & M^{kl}_{\dot{\theta}yMx} & M^{kl}_{\dot{\theta}yMy} \end{bmatrix} \qquad (5.50)$$

the different mobility terms in equation (5.50) illustrated in Figure 5.4, are calculated using an usual modal decomposition for thin isotropic plate based on Warburton's theory [34] and using the Bishop and Johnson mode shape functions [35] as detailed in [25] and already used in [16].

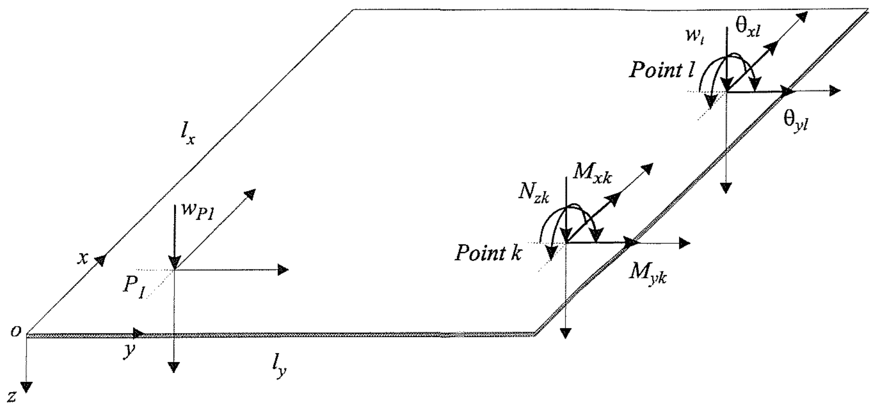

Figure 5.4. Notation of the displacement $w$ at positions $P_1$ and at point $l$, and of the rotations $\theta_x$, and $\theta_y$, at point $l$ when a plate is excited in flexure by a point force $N_z$ and point moments $M_x$, and $M_y$, at position $k$.

Assuming the harmonic motion with time dependence of the form $exp(j\omega t)$ the individual mobility terms are given by the following modal formulae.

$$M^{kl}_{wNz}=\frac{\dot{\tilde{w}}_l(\omega)}{\tilde{N}_k(\omega)}=j\omega\sum_{m=1}^{\infty}\sum_{n=1}^{\infty}\frac{\phi_{mn}(l)\phi_{mn}(k)}{\Lambda_{mn}\left[\omega_{mn}^2(1+j\eta)-\omega^2\right]} \qquad (5.51)$$

$$M^{kl}_{wMx}=\frac{\dot{\tilde{w}}_l(\omega)}{\tilde{M}_{xk}(\omega)}=j\omega\sum_{m=1}^{\infty}\sum_{n=1}^{\infty}\frac{\phi_{mn}(l)\psi^{(x)}_{mn}(k)}{\Lambda_{mn}\left[\omega_{mn}^2(1+j\eta)-\omega^2\right]} \qquad (5.52)$$

$$M^{kl}_{wMy}=\frac{\dot{\tilde{w}}_l(\omega)}{\tilde{M}_{yk}(\omega)}=j\omega\sum_{m=1}^{\infty}\sum_{n=1}^{\infty}\frac{\phi_{mn}(l)\psi^{(y)}_{mn}(k)}{\Lambda_{mn}\left[\omega_{mn}^2(1+j\eta)-\omega^2\right]} \qquad (5.53)$$

$$M^{kl}_{\theta xNz}=\frac{\dot{\tilde{\theta}}_{xl}(\omega)}{\tilde{N}_k(\omega)}=j\omega\sum_{m=1}^{\infty}\sum_{n=1}^{\infty}\frac{\psi^{(x)}_{mn}(l)\phi_{mn}(k)}{\Lambda_{mn}\left[\omega_{mn}^2(1+j\eta)-\omega^2\right]} \qquad (5.54)$$

$$M^{kl}_{\theta xMx}=\frac{\dot{\tilde{\theta}}_{xl}(\omega)}{\tilde{M}_{xk}(\omega)}=j\omega\sum_{m=1}^{\infty}\sum_{n=1}^{\infty}\frac{\psi^{(x)}_{mn}(l)\psi^{(x)}_{mn}(k)}{\Lambda_{mn}\left[\omega_{mn}^2(1+j\eta)-\omega^2\right]} \qquad (5.55)$$

$$M^{kl}_{\theta xMy}=\frac{\dot{\tilde{\theta}}_{xl}(\omega)}{\tilde{M}_{yk}(\omega)}=j\omega\sum_{m=1}^{\infty}\sum_{n=1}^{\infty}\frac{\psi^{(x)}_{mn}(l)\psi^{(y)}_{mn}(k)}{\Lambda_{mn}\left[\omega_{mn}^2(1+j\eta)-\omega^2\right]} \qquad (5.56)$$

$$M^{kl}_{\theta yNz} = \frac{\dot{\tilde{\theta}}_{yl}(\omega)}{\tilde{N}_k(\omega)} = j\omega \sum_{m=1}^{\infty}\sum_{n=1}^{\infty} \frac{\psi^{(y)}_{mn}(l)\phi_{mn}(k)}{\Lambda_{mn}\left[\omega^2_{mn}(1+j\eta)-\omega^2\right]} \tag{5.57}$$

$$M^{kl}_{\theta yMx} = \frac{\dot{\tilde{\theta}}_{yl}(\omega)}{\tilde{M}_{xk}(\omega)} = j\omega \sum_{m=1}^{\infty}\sum_{n=1}^{\infty} \frac{\psi^{(y)}_{mn}(l)\psi^{(x)}_{mn}(k)}{\Lambda_{mn}\left[\omega^2_{mn}(1+j\eta)-\omega^2\right]} \tag{5.58}$$

$$M^{kl}_{\theta yMy} = \frac{\dot{\tilde{\theta}}_{yl}(\omega)}{\tilde{M}_{yk}(\omega)} = j\omega \sum_{m=1}^{\infty}\sum_{n=1}^{\infty} \frac{\psi^{(y)}_{mn}(l)\psi^{(y)}_{mn}(k)}{\Lambda_{mn}\left[\omega^2_{mn}(1+j\eta)-\omega^2\right]} \tag{5.59}$$

where $\omega_{mn}$ is the resonance frequency of the mode ($m,n$), $\phi_{mn}$ is the axial mode shape function of the mode ($m,n$) used to derive $\psi^{(x)}_{mn}$ and $\psi^{(y)}_{mn}$ the rotational mode shape functions associated with $\theta_x$ and $\theta_y$. $m$ and $n$ are the modal indices related to the number of nodal lines in the $x$ and $y$-directions respectively, $\eta$ is the hysteretic damping coefficient identical for all the modes and $\Lambda_{mn}$ is the modal normilsation factor of the mode ($m$, $n$).

### 5.4.3. The equipment modelling

A modal decomposition of isotropic systems implies to define global parameters such as Young modulus $E$ (stiffness), Poisson's ratio $\nu$, density $\rho$ (mass) and damping coefficient (which has been assumed to be of hysteretic type for both the base and the equipment modelling). Although the modal decomposition of the base plate using the well known characteristics of aluminium is straightforward, the honeycomb equipment panel, however, has not an homogeneous structure. An equivalent Young modulus, global density and Poisson ratio have then to be defined provided the composite panel behaves as an isotropic system undergoing flexural vibration in the low frequency range of interest. Fahy discussed the propagation of transverse waves [36] in similar sandwich materials where the core, the central honeycomb layer, is thick compared to the face plates. At low frequencies, the transverse wave propagation is controlled by the whole bending stiffness of the panel, whose behaviour can then be approximated to the one of a uniform plate in bending. At intermediate frequencies, the transverse wave propagation is controlled by the shear stiffness of the core, which means that the shear deformation in the material is significant and at very high frequencies, the propagation is controlled by the bending stiffness of the individual face plates. In other words, at very high frequencies, the two thin composite face plates encompassing the honeycomb layer bend as two independent systems coupled by the core. A modal decomposition of the equipment panel using flexural modes with suitable global parameters is thus only reliable in the low frequency region.

The dispersion curve for transverse wave propagation has been measured on a strip of honeycomb material similar to the one constituting the equipment plate. It has been placed in between two anechoic terminations made of foam, as shown in Figure 5.5, in the attempt to avoid any reflection at the tips of the strip so that, in principle, a single outgoing wave propagating from the excitation point towards to tips of the composite strip can be considered.

Two accelerometers have been positioned on the strip, separated by a distance $\Delta_t$, to evaluate the phase delay $\varphi_{12}$ between two sensor positions caused by the wave propagating in the material. For an harmonic excitation of frequency $\omega$,

$$\varphi_{12} = k_t \Delta_t \tag{5.60}$$

and then

$$k_t = \frac{\varphi_{12}}{\Delta_t} \text{ or } c_t = \frac{\omega \Delta_t}{\varphi_{12}} \tag{5.61, 5.62}$$

where $k_t$ is the transverse wave number and $c_t$ is the phase speed of the transversal wave. One should note that equations (5.61) and (5.62) do not assume anything about the nature of the wave propagating in the material.

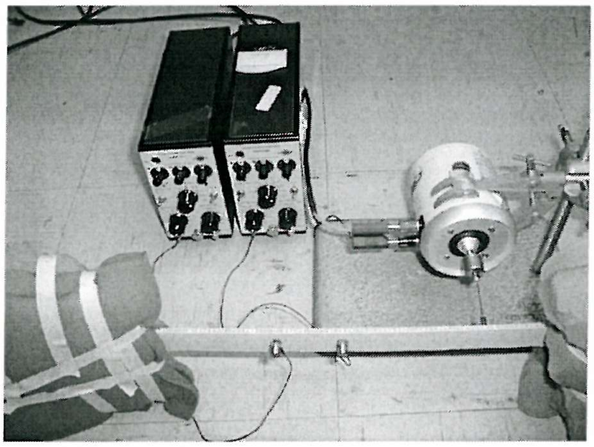

Figure 5.5. Experimental setting for the characterisation of the dispersion of transverse wave in a strip of composite material.

Figure 5.6 shows the experimental dispersion curve obtained using the setting described above. In the low frequency region, below 4 kHz, the curve follows reasonably well the theoretical dispersion curve of pure bending wave in an uniform beam. Then it starts to increase linearly with frequency in a similar way as shear waves in a beam. Even though the equipment panel is not made of exactly the same material as the one considered here, it appears from this experiment to be reasonable to attempt to model the equipment plate in the frequency range of interest [0-1kHz] by a standard modal description of the flexural vibration.

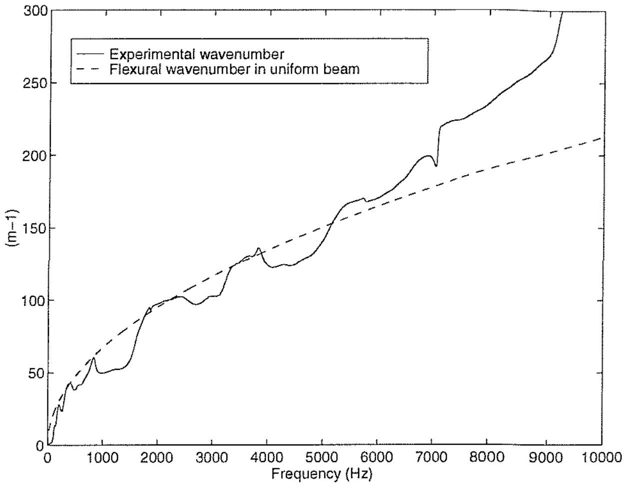

Figure 5.6. Dispersion curve for transverse wave propagation in a composite material beam.

The Young modulus, $E_e$, Poisson's ratio $\nu_e$ and density $\rho_e$ of the equipment panel have been estimated experimentally. The density has been obtained by simply measuring the mass of the equipment panel. This implies an uniform mass distribution as well as the modal decomposition implies an uniform stiffness distribution, which is satisfied at low frequencies. Moreover, one should note that the mass per surface unit is constant over the equipment. $\nu_e$ and $E_e$ were obtained by measuring the response of the equipment panel to an out-of-plane excitation. The first bending mode of the equipment panel was identified to be the mode (1,1) and the second one to be the mode (2,0). Using Warburton's expression for rectangular plate resonance frequencies, it appears that the ratio between two resonance frequencies does not depend on the Young' modulus, neither on the density of the material but only on the Poisson ratio and the modal order $(m,n)$. The equivalent Poisson ratio $\nu_e$ has thus been estimated to be equal to 0.56. This rather large value is not surprising for an honeycomb structure material [37]. The Young's modulus has then be calculated to fit the first measured resonance of the equipment plate. Finally a constant modal hysteretic damping coefficient of 0.05 as been considered. These global parameters being defined, it was possible to model the low frequency dynamics of the composite panel in bending by a simple modal decomposition.

### 5.4.4. Base modelling

The base structure dynamics in bending was described by a standard modal decomposition for thin isotropic plate. The control shakers are bolted to the plate by four screws, one at each corner of the shaker, separated by 60 mm. In the frequency range of interest, they tend to clamp the plate surface between the four connection points. The effective length of the base in the model as therefore been reduced in the $x$-direction to a value of 623 mm. The control shakers are then modelled as extra point masses located at the mount junctions, each of them being characterised by its mass $m_{act}$ and its moments of inertia $I_{xxact}$ and $I_{yyact}$. It is in fact easy to account for the local inertial effect of the control actuators in the modelling, since it turns out that the inertia effect due to $m_{act}$, $I_{xxact}$ and $I_{yyact}$ simply has to be added to the value of the input impedance of each mount at the junction with the base structure, as shown in section 5.4.5.

### 5.4.5. Mount modelling

To account for resonances in the mounting system, the rubber isolators have been modelled as one dimensional distributed elements in which longitudinal and flexural waves can propagate. The elements of the matrix $\mathbf{Z}_m$ are then themselves impedance sub-matrices since three forms of propagation in the mount are considered: due to the axial force $N_z$ and to the two moment $M_x$ and $M_y$. Considering a single mount as represented in Figure 5.7

$$\mathbf{Z}_m = \begin{bmatrix} \mathbf{Z}_{m11} & \mathbf{Z}_{m12} \\ \mathbf{Z}_{m21} & \mathbf{Z}_{m22} \end{bmatrix} \quad \text{where } \mathbf{Z}_{mjl} = \begin{bmatrix} Z^{jl}_{Nzw} & 0 & 0 \\ 0 & Z^{jl}_{Mx\theta x} & 0 \\ 0 & 0 & Z^{jl}_{My\theta y} \end{bmatrix} \qquad (5.63, 5.64)$$

and

$$Z^{jl}_{Nzw}(\omega) = \frac{\tilde{N}_{zj}(\omega)}{\dot{\tilde{w}}_l(\omega)} \qquad (5.65)$$

$$Z^{jl}_{Mx\theta x}(\omega) = \frac{\tilde{M}_{xj}(\omega)}{\dot{\tilde{\theta}}_{xl}(\omega)} \qquad (5.66)$$

$$Z^{jl}_{My\theta y}(\omega) = \frac{\tilde{M}_{yj}(\omega)}{\dot{\tilde{\theta}}_{yl}(\omega)} \qquad (5.67)$$

The impedance elements in equation (5.64) are based on the Euler-Bernoulli model for second order and fourth order equations of longitudinal and flexural waves propagation in a beam [38]. In principle, the impedance matrix $\mathbf{Z}_m$ is a 12 x 12 matrix as, ideally, six kinematic parameters and six dynamic parameters at each mount junction should be accounted for. In the special case of neglecting 3 of the 6 degrees of freedom related to in -plane vibration as explained in 5.4.1, $\mathbf{Z}_m$ becomes a 6 x 6 impedance matrix whose terms can not generally be directly extracted from the 12 x 12 impedance matrix since some of the impedance terms in the 6 x 6 impedance matrix are coupled with the neglected degrees of freedom unlike in the 12 x 12 matrix.

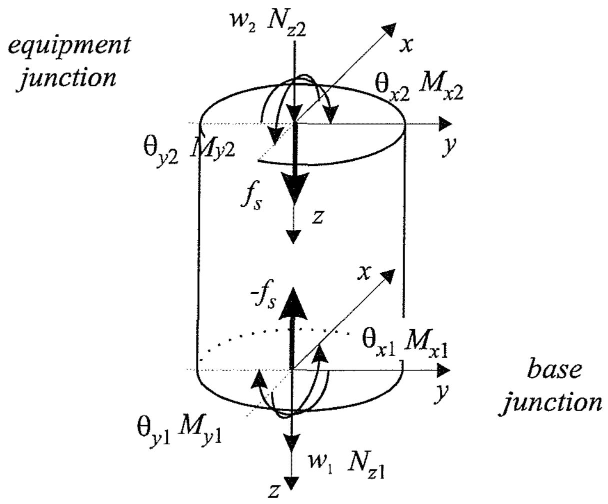

Figure 5.7. Notation of the displacement $w$ and rotations $\theta_x$ and $\theta_y$, point force $N_z$ and point moments $M_x$ and $M_y$ at the top and bottom junctions of one mount of the modelled isolation system.

The statement of "neglecting three degrees of freedom" can cover two physical interpretations:

either $\dot{u} = \dot{v} = \dot{\theta}_z = 0$ and $N_x \neq 0, N_y \neq 0, M_z \neq 0$, in which pinned boundary conditions at the ends of the mount are assumed.

or $N_x = N_y = M_z = 0$ and $\dot{u} \neq 0, \dot{v} \neq 0, \dot{\theta}_z \neq 0$, in which free boundary conditions at the ends of the mount are assumed.

This type of boundary conditions does not affect the expression of the impedance terms related to the longitudinal waves in equation (5.65) and

$$Z_{Nzw}^{11}(\omega) = Z_{Nzw}^{22}(\omega) = \frac{1}{j\omega}\frac{E_m A_m k_{lm} \lambda_1}{\lambda_2} \tag{5.68}$$

$$Z_{Nzw}^{12}(\omega) = Z_{Nzw}^{21}(\omega) = -\frac{1}{j\omega}\frac{E_m A_m k_{lm}}{\lambda_2} \tag{5.69}$$

where $E_m$ is the Young's modulus of elasticity, $A_m$ is the mount cross sectional area. $k_{lm} = \omega / c_{lm} = \omega / \sqrt{E_m / \rho_m}$ is the longitudinal wave number, $c_{lm}$ is the phase velocity of longitudinal waves and $\rho_m$ is the density of the rubber material. $\lambda_1$ and $\lambda_2$ are given by

$$\lambda_1 = cos\, k_{lm} h_m \text{ and } \lambda_2 = sin\, k_{lm} h_m \tag{5.70, 5.71}$$

However, the other impedance terms are not the same for pinned or free boundary conditions. Referring to the results obtained by Gardonio [25], it was decided to chose free-free mount boundary conditions on both ends of the mount. The 6 x 6 impedance matrix can then be obtained by inversion of the corresponding 6 x 6 mobility matrix whose terms are, in this special case, equal to the corresponding terms of the 12 x 12 mobility matrix, since the mobility terms are all defined considering the dynamic vector to be equal to zero. Expressions for these impedance terms related to the rotations are given below. A more detailed discussion on the modelling of distributed mounts can be found in [25].

$$Z^{11}_{Mx\theta x}(\omega)=Z^{22}_{Mx\theta x}(\omega)=Z^{11}_{My\theta y}(\omega)=Z^{22}_{My\theta y}(\omega)=\frac{1}{j\omega}\frac{E_m I_m k_{fm}\varphi_3\varphi_6}{\varphi_6^2-\varphi_7^2} \quad (5.72)$$

$$Z^{12}_{Mx\theta x}(\omega)=Z^{21}_{Mx\theta x}(\omega)=Z^{12}_{My\theta y}(\omega)=Z^{21}_{My\theta y}(\omega)=-\frac{1}{j\omega}\frac{E_m I_m k_{fm}\varphi_3\varphi_7}{\varphi_6^2-\varphi_7^2} \quad (5.73)$$

where

$$\varphi_3=\cos k_{fm}h_m \cosh k_{fm}h_m-1 \quad (5.74)$$

$$\varphi_6=\cos k_{fm}h_m \sinh k_{fm}h_m+\sin k_{fm}h_m \cosh k_{fm}h_m \quad (5.75)$$

$$\varphi_7=\sin k_{fm}h_m+\sinh k_{fm}h_m \quad (5.76)$$

and $k_{fm}=\omega/c_{fm}=\sqrt[4]{\omega^2 m'/B}$ is the flexural wave number, $c_{fm}=\sqrt{\omega}\sqrt[4]{B/m'}$ is the phase velocity of flexural waves, $B=E_m I_m$ is the bending stiffness of one mount, $I_m=I_{xx}=I_{yy}=\pi a_m^4/4$ is the area moment of inertia of the circular mount cross section with radius a, $m'=\rho_m A_m$ is the density per unit area of the material.

The mounts in the experimental test rig are as wide as they are high and therefore the Timoshenko beam model should have ideally been used. However, it was assumed that such a Euler-Bernoulli modelling was sufficient to perform a meaningful assessment of the control effects on the system.

As mentioned in section 5.4.4, the inertial effect of each control actuator has been accounted for in the mount bottom input impedance. It can be shown that the inertia effect of a mass at on end of the mount can be simply modelled by adding to the corresponding mount input impedance the additive inertial terms. The input impedance terms of each mount at the junction with the base can then be written as

$$\mathbf{Z}_{m11} = \begin{bmatrix} Z^{11}_{Nzw} + j\omega m_{act} & 0 & 0 \\ 0 & Z^{11}_{Mx\theta x} + j\omega I_{xxact} & 0 \\ 0 & 0 & Z^{11}_{My\theta y} + j\omega I_{yyact} \end{bmatrix} \tag{5.77}$$

The small inertia effect of the aluminium disc fixing the shaker stinger between the top of each mount to the composite panel was similarly accounted for in $\mathbf{Z}_{m22}$.

### 5.4.6. Summary of the system element properties

Table 5.3 summarises the physical parameters used in the simulations, for each element constituting the isolation system.

| | Base plate | Equipment panel | Mount |
|---|---|---|---|
| Young's modulus (N/m$^2$) | 7.1e10 | 1.27e9 | 1.93e5 |
| Poisson's ratio | 0.33 | 0.56 | 0.33 |
| Density (Kg/m$^3$) | 2798 | 170 | 909 |
| Hysteretic modal damping coefficient | 0.015 | 0.05 | 0.05 |

Table 5.3. Summary of the main physical parameters of the isolation system elements.

## 5.5 Passive analysis of the system

Simulations of the passive response of the isolation system are performed first. In order to estimate properly any passive isolation effect of the rubber mounts and to be able to carry on a full analysis of the control performance, it is useful to look at the dynamics of the base and of the equipment structure when uncoupled from the global system. Figure 5.8 shows an axial input mobility $M_{wNz}$ simulated at a point of coordinate (0.094,0.078) on the composite panel. The corresponding measurement is also displayed as a measure of the model reliability.

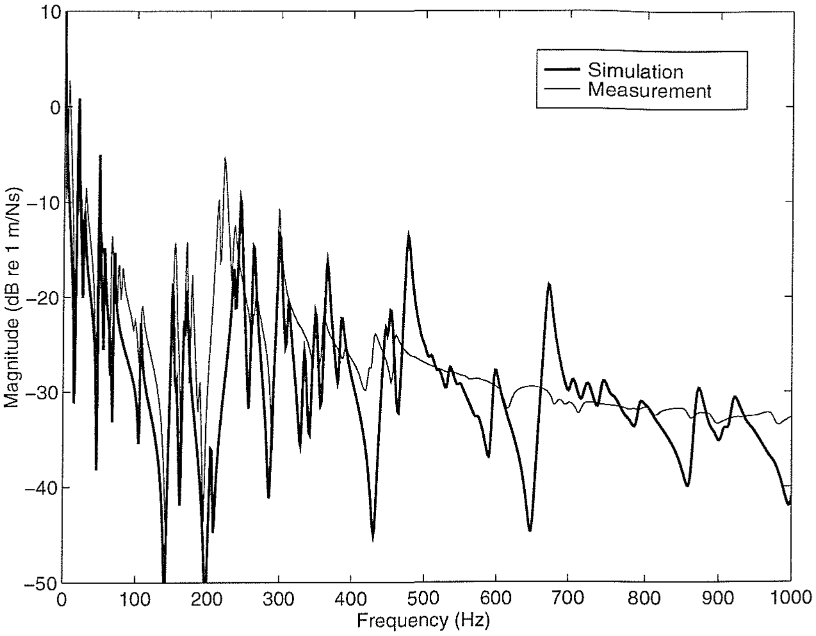

Figure 5.8. Composite panel input mobility at point (0.094,0.078).

The first observation to be made is to notice the good agreement between the two curves at low frequencies where the simulated and measured resonances match very well together. Above 200 Hz, the simulation manages to track the global trend of the measured plate response which is, however, more damped than that in the simulation. If the hysteretic modal damping is replaced by a viscous effect, the improvement in the modelling is not significant. This suggests that a non-constant modal damping should ideally be considered. Unmodelled shear effects may also start to contribute to the out-of-plane plate vibration at frequencies as low as 1 kHz. The model globally gives a satisfactory representation of the plate dynamics up to 1 kHz. The first modes in the equipment plate occur at 20 Hz, 30 Hz and 48 Hz according to both the model and the measurements. The equipment system is a very light and resonant system which fully fits the requirements of the design of a very flexible mounted structure in the scope of a full assessment of DVFB control. Above 500 Hz, the plate modes are less distinct because of modal overlapping and the composite panel starts to behave as an infinite structure.

Figure 5.9 shows a transfer mobility $M_{wN_z}$ measured and simulated on the base structure between the point of primary excitation $f_0$ and the location of the 3rd rubber mount junction. Once again a good agreement between the simulation and the experiment is achieved, especially at low frequencies where the simulated resonances match the measured ones. Because of the large inertial loading caused by the control shakers, the first base resonances occur at very low frequencies: 16 Hz, 42 Hz, 68 Hz for the first three modes. Two large resonances around 270 Hz and 660 Hz dominate the base structure response in the intermediate frequency range.

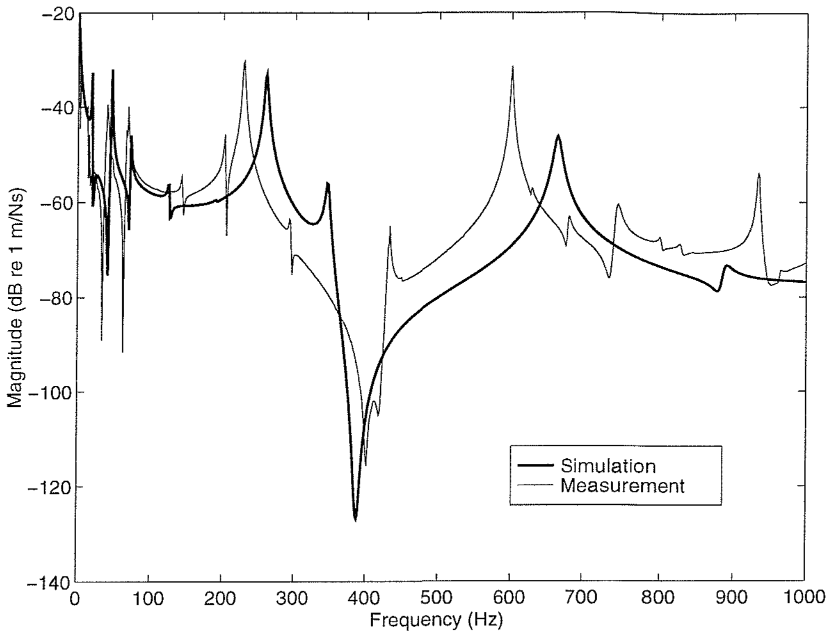

Figure 5.9. Mobility function on the base structure at point 3 for an excitation $f_0$ at point 0.

The modal density is rather low as the width of the aluminium base plate is very small compared to its length so that the base structure can be regarded as a beam at low frequencies. Despite the low frequency resonances, the base dynamics are limited as the mass of the control shakers significantly increases the base impedance. The overall value of the base mobility in Figure 5.9 is 30 dB lower than the composite panel mobility presented in Figure 5.8, such that in some frequency bands, the base structure can almost be considered as rigid compared to the equipment panel. This partly removes the assumption of a flexible base and brings back to the well known case of perfect velocity control and its skyhook effect as the secondary force can react against a rigid ground. The base mobility is, however, not negligible over the whole frequency range [0-1kHz]. Moreover, even in the frequency range in which there is a large difference between the base and the equipment panel mobilities, the interest of estimating the performance of a local DVFB control implementation over the whole equipment panel remains unchanged.

The full coupled system is now considered and Figure 5.10 shows the velocity response on the composite equipment panel at point 1 per unit primary excitation $f_0$ on base plate. Using control terminology, this quantities is called the force normalised disturbance, $D_1$. Once again, the corresponding measured quantity is overlaid to the simulation which exhibits good agreement with the experimental check. This implies a good modelling of the passive isolators which seems to have the typical vibration amplification effect expected from a passive isolation located around 300 Hz. Figure 5.10 is however not sufficient to draw definite conclusion about the passive mount effects as both the base and the composite panel dynamics are large in the band [250 Hz - 300 Hz]. Apart from illustrating the satisfactory passive results of the model, Figure 5.10 shows that the system response on the equipment is dictated to a large extend by the base dynamics. Because of its large impedance, the base tends to drive the mounted panel: the peak observed at 255 Hz is related to the large base plate resonance observed on Figure 5.9. This also true for the resonances at 16 Hz and to a less extend at 660 Hz which is more significantly noticed in the response at points 2 and 3 as shown in Figure 5.11.

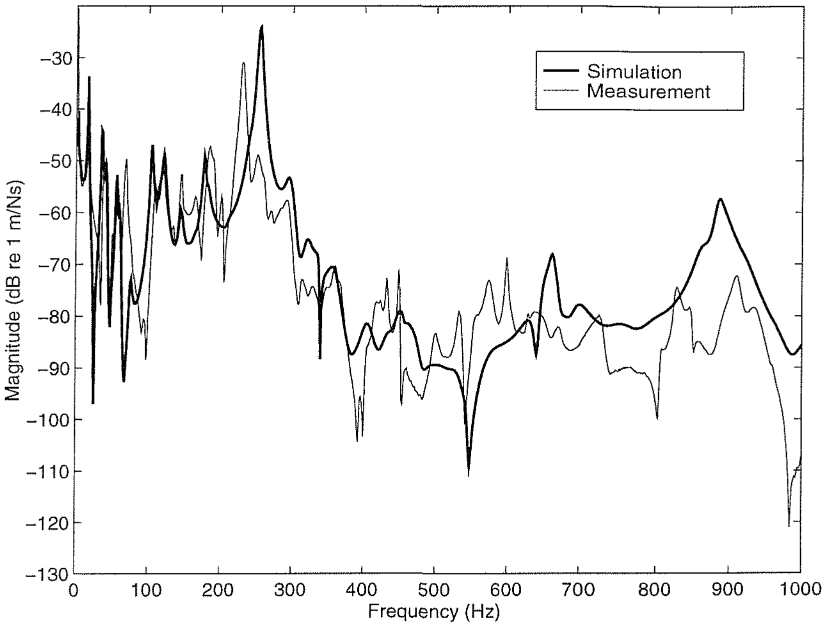

Figure 5.10. Velocity response on the coupled equipment panel at point 1 per unit primary excitation $f_0$.

In order to estimate the true impact of the passive mounts on the equipment panel isolation, Figure 5.11 shows the simulated force normalised velocity responses on the equipment and on the base structure at the three mount junctions 1 (a), 2 (b) and 3 (c) respectively. This representation is preferred to a dimensionless ratio between the base and equipment structure velocities at one mount location since the flexibility of the base does not allow to define a proper transmissibility term. Such plots, however, give an insight into the effect of the passive isolation on the equipment vibration.

The passive isolation effect is obvious at point 1 on Figure 5.11(a) as the vibration transmission is greatly amplified from 120 Hz to 400 Hz / 500 Hz. This is much less noticeable at point 2 and 3 as the equipment motion appears to be mainly dictated by the base plate motion, as already pointed out. The importance of the base plate dynamics can also be observed by comparing the base plate response in Figure 5.11(c) to the base plate response in Figure 5.9 when uncoupled from the rest of the system. Both curves are very similar which means that, at point 3, the coupled equipment structure has very little effect on the base structure. This is the consequence of the large impedance of the base structure. No real vibration attenuation is observed below 1 kHz, even at point 1. Simulations were thus performed up to 5 kHz in order to identify more clearly the attenuation effect of the passive mounts.

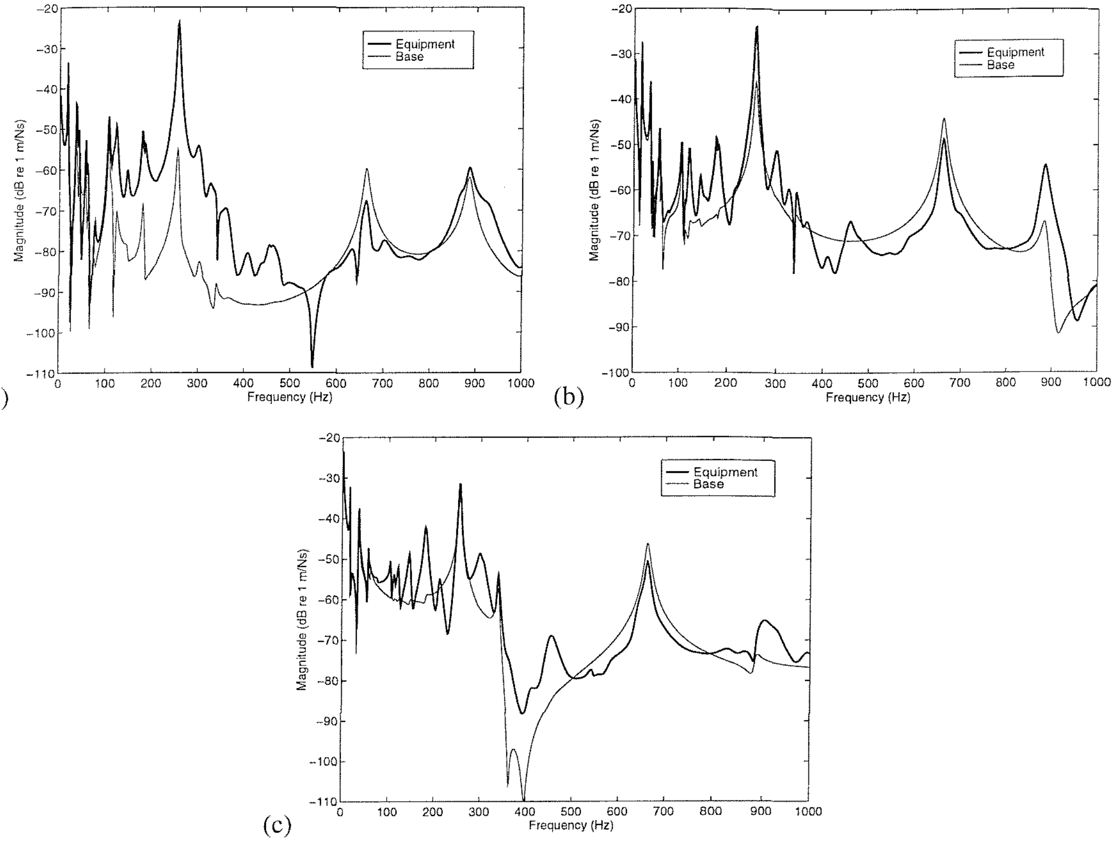

(a) (b) (c)

Figure 5.11. Simulated velocity responses on the equipment and the base structures at mount junctions 1 (a), 2 (b) and 3 (c) per unit primary excitation $f_0$.

Figure 5.12 shows the same quantities as Figure 5.11 but for the extended frequency range [0-5 kHz]. No vibration amplification is generated by the passive isolation above 500 Hz. The passive isolation is efficient above 1 kHz as the base motion at the mount junctions gets much larger than on the equipment structure with increasing frequency. Above 1 kHz, the equipment velocity at the mount junctions significantly decreases with frequency so that [0-1 kHz] appears to be the frequency band in which the controller can make a significant contribution to reducing the composite panel vibration.

It can also be deduced from the simulations on the passive system that the power input in the equipment was largely due, over the whole frequency range [0-1 kHz], to the axial excitation from the mounts, so that no real control limitations caused by a large rotational excitation of the suspended panel are expected which answers point *d* discussed in the introduction.

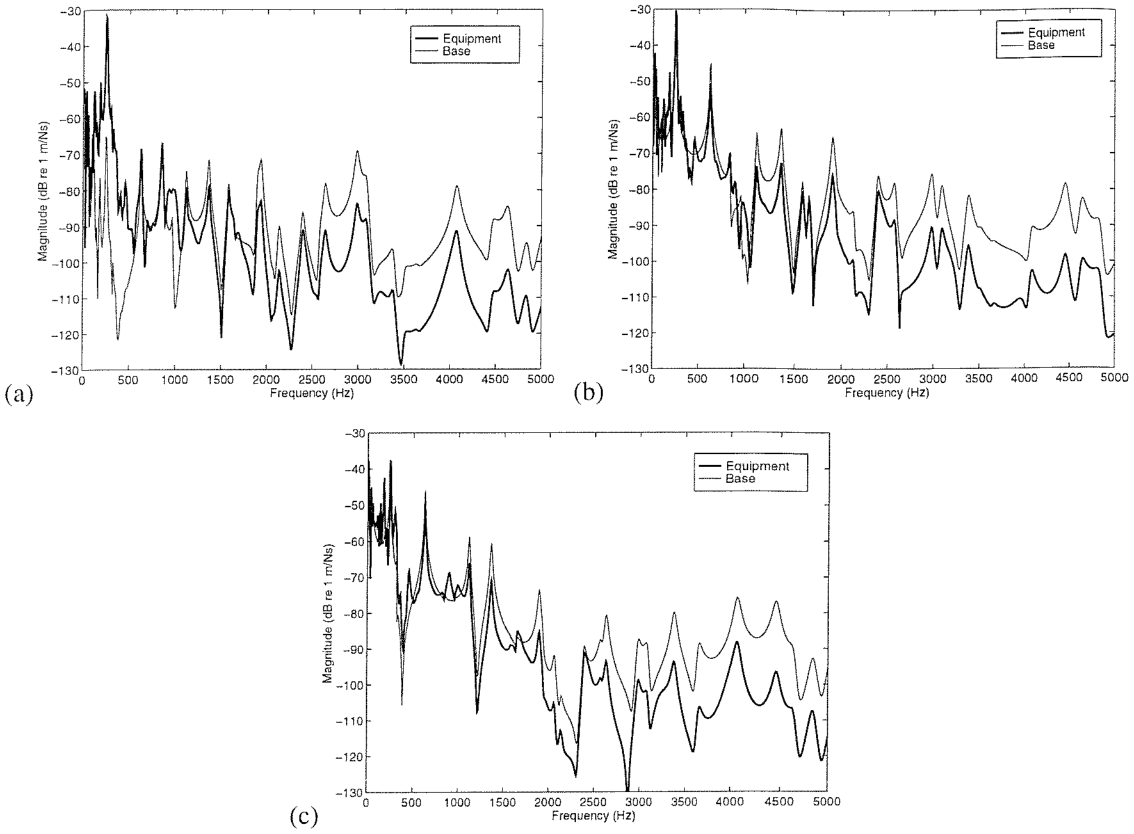

Figure 5.12. Simulated velocity responses on the equipment and the base structures at mount junctions 1 (a), 2 (b) and 3 (c) per unit primary excitation $f_0$.

## 5.6. Simulations for single-channel control

### 5.6.1. Plant responses and stability analysis

Referring to the mechanical system under investigation, three different single-channel controllers can be implemented by closing one of the three control loops acting in parallel with each passive isolator. The simulation model was first used to derive the plant response of each of the three-single channel controllers in order to assess the stability and the expected performance of each control system. The control stability is studied over the frequency range of interest defined in the passive analysis of the mechanical system as [0-1 kHz]. Figure 5.13 (a), 5.14 (a) and 5.15 (a) show the magnitude and phase of the three simulated plant responses $G_{11}$, $G_{22}$ and $G_{33}$ over the whole frequency range [0-1 kHz] and Figure 5.13 (b), 5.14 (b) and 5.15(b) show the corresponding Nyquist plots.

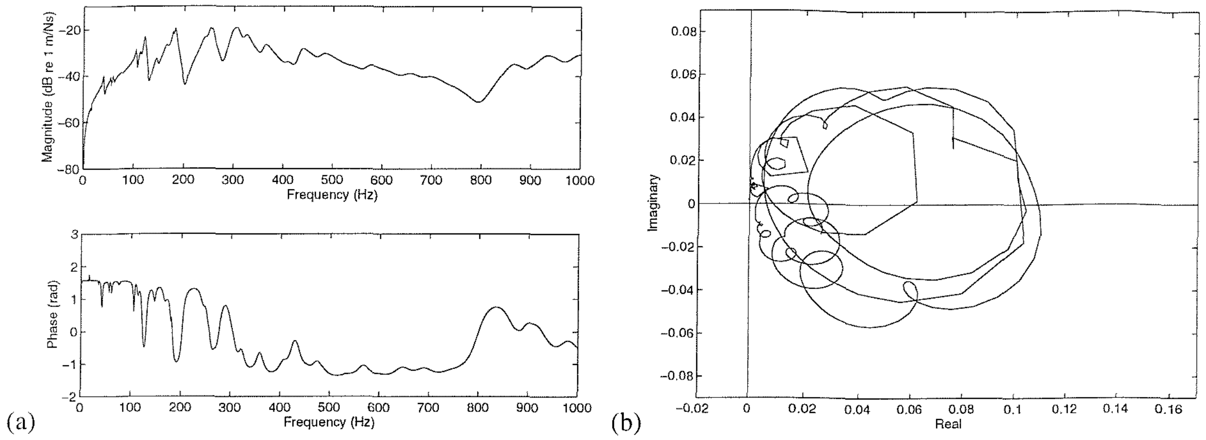

Figure 5.13. Magnitude and phase responses (a) and Nyquist plot (b) of the simulated plant response $G_{11}$.

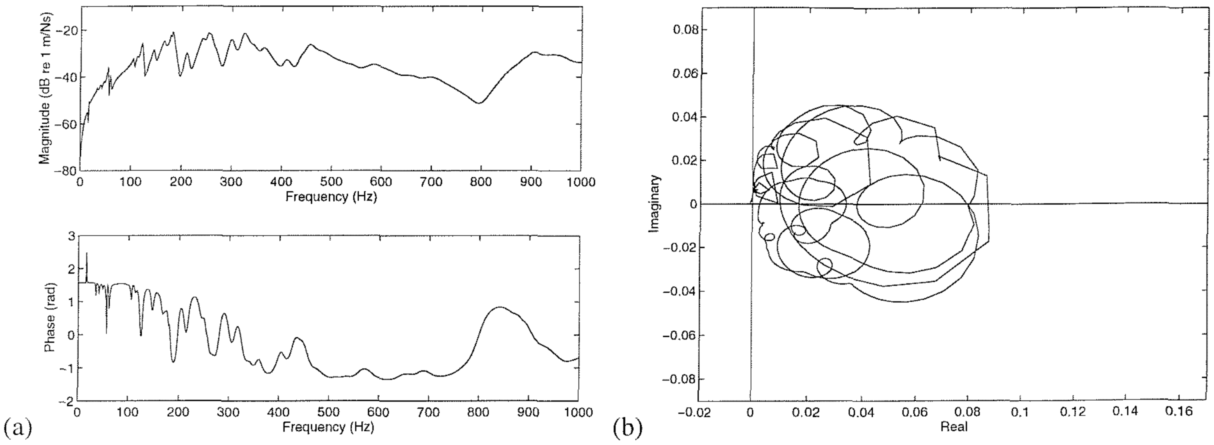

Figure 5.14. Magnitude and phase responses (a) and Nyquist plot (b) of the simulated plant response $G_{22}$.

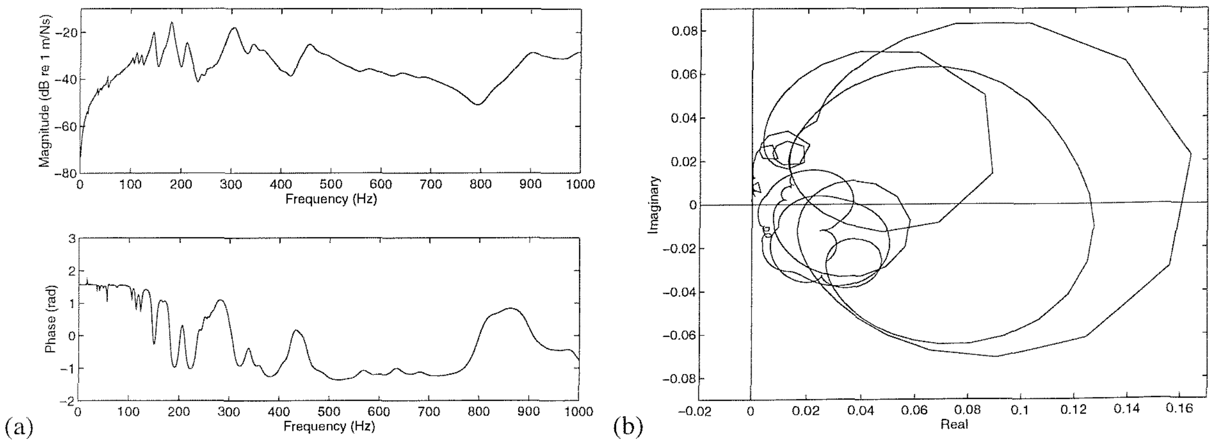

Figure 5.15. Magnitude and phase responses (a) and Nyquist plot (b) of the simulated plant response $G_{33}$.

The global characteristics of the three plant responses are very similar. The three control loops first appear to be very stable as shown on the different Nyquist diagrams as the plots almost fully lie in the positive real part half plane, except at low frequencies as discussed below. The plant responses are dominated by the frequencies range [100 Hz - 400 Hz] as the passive isolation increases the vibration transmission to the equipment. In this frequency band, the trend of the phase responses is shifted from $\pi/2$ to $-\pi/2$ as the passive mount amplification effect starts to give place to the high frequency attenuation characterising passive isolations. The dynamics of the base plate and composite panel generate some fluctuations on the global variation but without threatening the control stability. The largest vibration reduction is therefore expected in the frequency band [100 Hz - 400 Hz]. Around 850 Hz, the magnitude and phase responses of the plant significantly increase again. This is the result of the first longitudinal mount resonance. The effect of the longitudinal mount resonances are clearly represented in Figure 5.16 showing the magnitude and phase of the plant response $G_{11}$ up to 5 kHz.

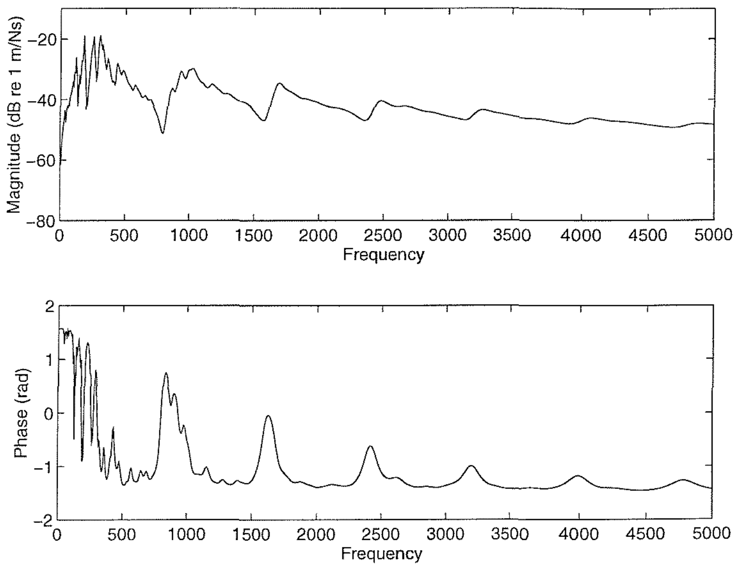

Figure 5.16. Magnitude and phase of the simulated plant response $G_{11}$ for a control at point 1.

Referring to the mount modelling presented in section 5.4.5 and assuming that each single mount boundaries are clamped by the base and the equipment structures loading effect, the expression for the longitudinal resonances is given by Bishop and Johnson [35] as

$$f_{nl} = \frac{n\sqrt{E_m/\rho_m}}{h_m} \tag{5.78}$$

where $n$ is the modal order of the resonance.

| Modal order | Frequency (Hz) |
|---|---|
| 1 | 794 |
| 2 | 1589 |
| 3 | 2383 |
| 4 | 3178 |
| 5 | 3972 |
| 6 | 4767 |

Table 5.4. First six longitudinal mount resonances assuming clamped boundary conditions.

The first six mount longitudinal resonances according to equation (5.78) are listed in Table 5.4 These resonances appear quite clearly in Figure 5.16 and are very close to the values calculated using the simple expression in equation (5.78). If resonances in the mount generate an increase of the equipment response, they do not destabilise the control, as the phase is pushed back in the stable region. This can be explained by decomposing the reacting secondary force in two individual components as done in chapter 3. The control velocity is therefore the summation of two contributions: the force acting on the composite panel and the force acting on the base plate. As the frequency increases, the contribution of the force acting on the base plate becomes much smaller than the effect of the collocated force on the composite panel so that, at high frequencies, the control can be approximated to a collocated control which is known to be fully passive. The longitudinal resonances in the mount occurring sufficiently high in frequency, they do not threaten the control whose collocated characteristics provide very good stability properties.

The favourable characteristics of the control systems are, however, somewhat debased by the low frequency behaviour of the plants. In order to identify the low frequency control limitations, Figures 5.17, 5.18 and 5.19 zoom on the magnitude, phase and Nyquist plots of the three plant responses $G_{11}$, $G_{22}$ and $G_{33}$. Several sharp peaks comes out of the magnitude plots at low frequencies. The first one occurs at very low frequency around 0.5 Hz and is the largest one, for all the three single channel controls. It is associated with a phase shift of $\pi$ which causes the Nyquist plot of $G_{22}$ and $G_{33}$ to cross the negative real axis and thus sets the maximum control gain to an approximate value of 165 and 140 for control at point 2 and 3 respectively. However, it does not destabilise the control at point 1 which is unconditionally stable. This sharp resonance is probably due to the pitching mode around the $y$-axis of the base and equipment structures behaving as rigid masses. The very low bending stiffness of the mounts and the large moment of inertia created by the reactive shakers around the y-axis explain the very low value of the resonance.

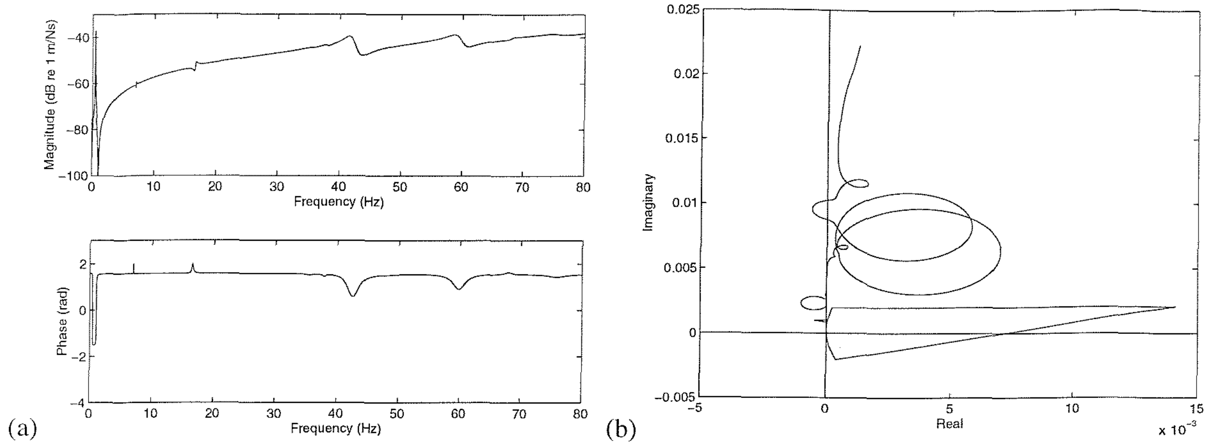

Figure 5.17. Zoom of the magnitude and phase responses (a) and Nyquist plot (b) of the simulated plant response $G_{11}$.

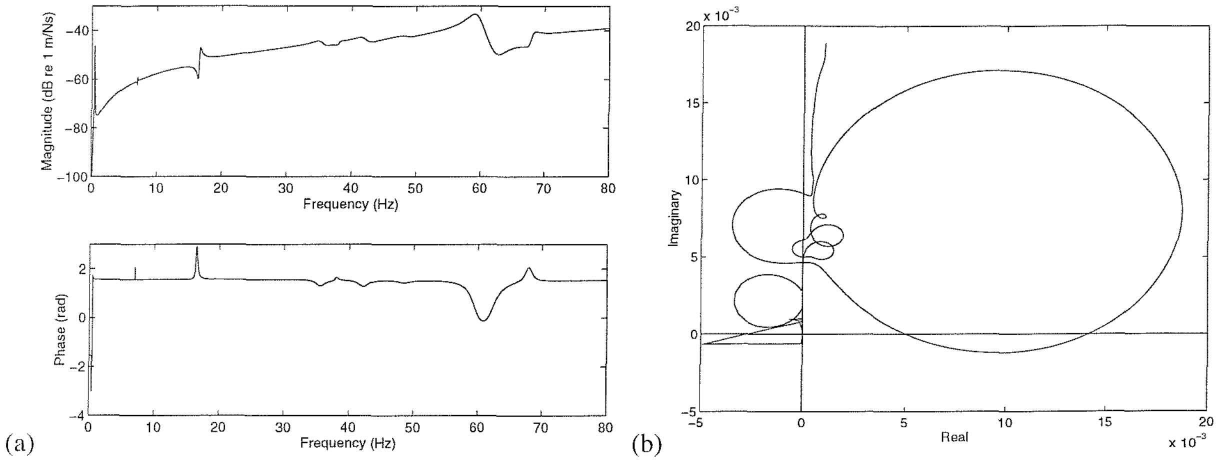

Figure 5.18. Zoom of the magnitude and phase responses (a) and Nyquist plot (b) of the simulated plant response $G_{22}$.

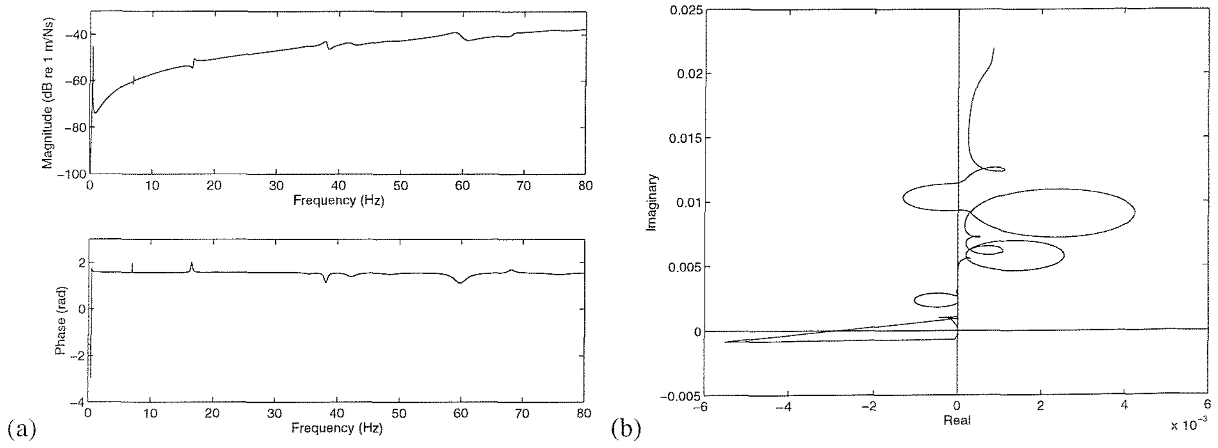

Figure 5.19. Zoom of the magnitude and phase responses (a) and Nyquist plot (b) of the simulated plant response $G_{33}$.

A second sharp peak is noticed at 16.5 Hz on each magnitude plot. It is associated with an increase of the phase response which brings the phase of $G_{22}$ close to $\pi$. This local peak is represented on the three Nyquist plots by a small loop in the unstable half plane which does not cross the negative real axis of the Nyquist diagrams. This 16.5 Hz peak is not a resonance but may correspond to a configuration of the system discussed in section 5.2.3. where the base structure is mass controlled and the equipment panel stiffness controlled. This is what happens at 16.5 Hz as the first resonances of the base and equipment structures are respectively equal to 16 Hz and 20 Hz. This occurs in conjunction with the fact that the dynamics of the base plate is significant compared to the dynamics of the composite panel at this frequency. This illustrates that the base structure does not act as a rigid base at any frequency and that its dynamics has to be considered even if it is globally much smaller than the one of the composite panel. If it does not constitute a direct limitation to the control gain, large amplifications can be expected from the controller around 16 Hz, especially for a control implementation at point 2. Moreover, any additive delay in a real control loop caused by the electronics, as observed in chapter 3, may destabilise the control. The same phenomenon appears to cause the maximum noticed at 67.5 Hz on $G_{22}$ and very weakly on $G_{11}$ and $G_{33}$. This is not observed higher in frequencies as expected from the analysis of the expression of the plant response in section 5.2.3. A small peak also appears at 7 Hz. It seems to be the result of the rotational excitation of the equipment.

For each single channel controller, the performance is limited at low frequencies whereas, at high frequencies, the reactive actuators seem to implement collocated control and therefore skyhook damping control. The gain is strongly limited for a control at point 2 and at point 3 whereas an implementation at point 1 is, in principle, unconditionally stable. However, vibration amplification is expected around 7 Hz and 16 Hz from any of the three controllers. This analysis demonstrates that the stability of a reactive implementation of DVFB is strongly related to the dynamics of the elements constituting the system unlike for an inertial implementation whose performance was shown to rely on the actuator dynamics instead of on the isolation system dynamics.

### 5.6.2. Control performance

For each single-channel controllers, the control results are simulated for two values of control gain $h$ as listed in Table 5.5. The second control gain $h_1$ has been arbitrarily chosen in order to be of the order of magnitude of the maximum gain for a control at point 2, $h_{2max}$, and at point 3, $h_{3max}$.

| Control location | 1st control gain | 2nd control gain |
|---|---|---|
| Point 1 | 40 | 150 |
| Point 2 | 40 | $h_{2max} = 160$ |
| Point 3 | 40 | $h_{3max} = 140$ |

Table 5.5. Control gains for simulation of the implementation of reactive single-channel controllers.

The performance resulting from each control implementation is presented under three different forms.

*a*- The simulated control results on the equipment are shown at the control point and at the two other mount junctions using the force normalised velocity spectra $V_{ij}$ compared to the passive response $V_{0j}$ as defined in chapter 4 ($i$ is the location of control and $j$ is the location of measurement). This allows us to estimate the local effect of the control at the mount junctions on the equipment.

*b*- The total (axial and also rotational) power input in the equipment is estimated over the range [0-1 kHz]. This provides the exact estimation of the controller effect over the whole equipment panel. Using the standard expression of the power,

$$P = \frac{1}{2} Re\{f^* v\} \tag{5.79}$$

the power related to a specific degree of freedom, or to one mount could also be easily obtained.

*c*- For a control at point $i$, a frequency dependent estimation of the energy over the equipment panel, $E_i$, is derived using the velocity responses $V_{ij}$ at five randomly chosen locations on the equipment panel (points 4, 5, 6, 7 and 8). It is compared to the same quantity when the controller is turned off. The location of the five points listed in Table 5.6 correspond to the 5 measurement points on the test rig where the control results were also experimentally monitored. This energy estimate is defined as

$$E_i = \frac{1}{5}\sum_{j=4}^{8}\left|V_{ij}\right|^2 \tag{5.80}$$

| Point | Position $(x,y)$ in mm |
|---|---|
| 4 | (100,100) |
| 5 | (220,350) |
| 6 | (540,420) |
| 7 | (500,170) |
| 8 | (660,50) |

Table 5.6. Location of response points on the equipment for energy estimation.

The estimate of the energy, $E_i$, is based on force normalised velocity responses so that it is itself normalised by the primary excitation. Five points are probably not sufficient to precisely assess the controller effect over the whole composite panel, unlike the power estimation presented above. However, if good agreement can be observed on the control performance between the simulated energy estimation and the calculated input power, it will be possible to extend the observation made on the energy estimate determined experimentally to an interpretation of the global effect of the experimental control on the equipment panel. This can thus be very useful since such a power quantity can not be obtained using the test rig available, since it would require to monitor the force and moments at the mount junctions on the equipment.

### *Control point 1*

The local effect of the single channel control at point 1 is shown in Figure 5.20. Only vibration reduction is obtained over the frequency range of interest except at 16.5 Hz where the velocity response is amplified by 1 dB. Large attenuation are still observed at 1000 Hz. The larger the control gain, the larger the attenuation. The peak of the system response at 255 Hz goes down by 25 dB. Further reduction could be obtained by increasing the feedback gain as the control is unconditionally stable but, as expected from the stability analysis, a larger increase could occur at 16.5 Hz where the response is already relatively large. The control effect at points 2 and 3 is very small as shown in Figures 5.21 and 5.22, especially at point 3. The 255 Hz maximum is reduced by 5 dB at point 2 and by 3 dB at point 3 which is the main significant effect of the control, together with the 8 dB reduction of the 0.5 Hz resonance. The influence of the control on the 0.5 Hz resonance at the other mount junctions tends to emphasise that it is a rigid body mode of the mounted composite panel. A 2 dB attenuation is also obtained at 885 Hz as the result of the first mount longitudinal resonance. The small amplification noticed at 16.5 Hz is also observed at points 2 and 3.

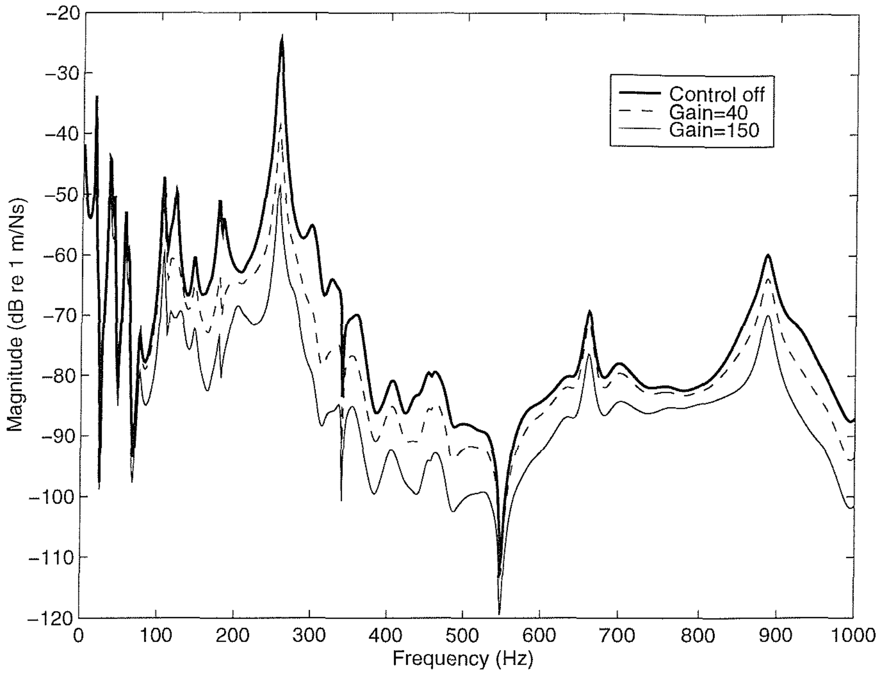

Figure 5.20. Simulated velocity at point 1 per unit primary force for a control at point 1.

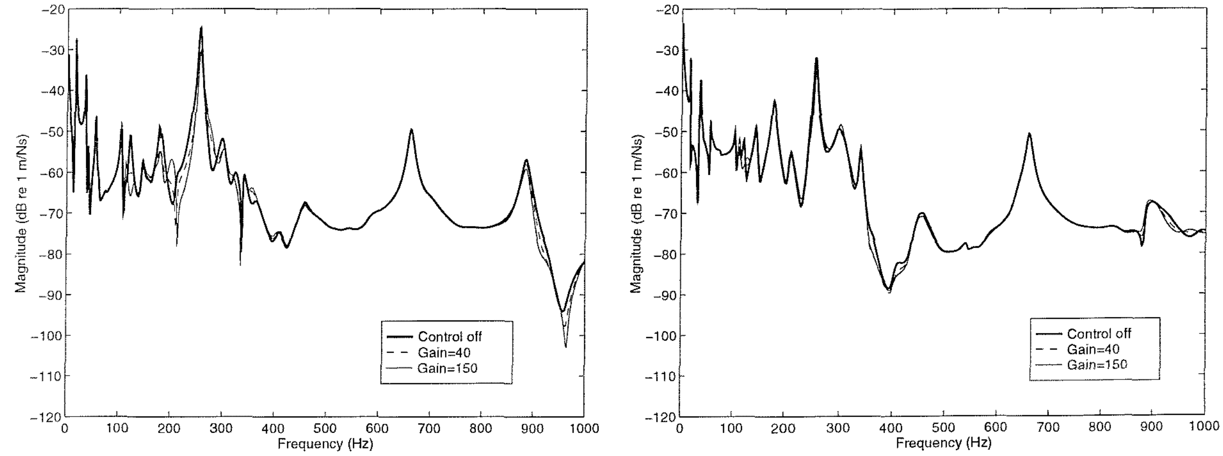

Figure 5.21. Simulated velocity at point 2 per unit primary force for a control at point 1.

Figure 5.22. Simulated velocity at point 3 per unit primary force for a control at point 1.

The local effect of the control is born out by the spectrum of the energy estimate in Figure 5.23 and also by the total input power spectrum in Figure 5.24 which illustrates that the reduction of the very low resonance and of the 255 Hz peak by 6 dB are the only global effect of the control with the amplification at 16.5 Hz. Reduction around 900 Hz is also observed in the power spectrum.

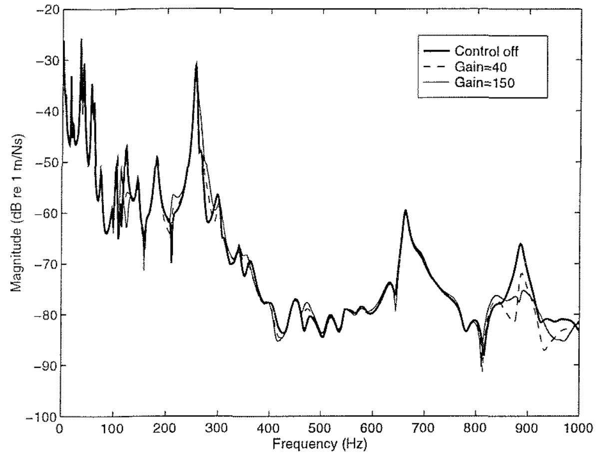

Figure 5.23. Simulated energy estimate for a control at point 1.

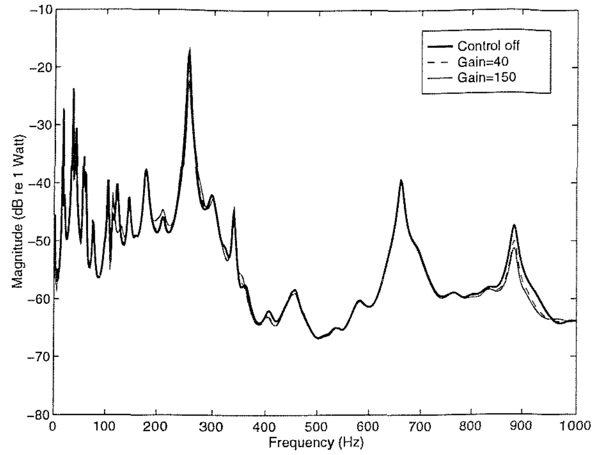

Figure 5.24. Simulated power input in the equipment panel for a control at point 1.

The control is only very efficient at the control location, as it provides very high reduction of the velocity at point 1. The small 16.5 Hz increase, however, may balance this conclusion if the feedback gain was set too high as any control reduction appears to be very local whereas any sharp control amplification is spread all over the equipment structure. The energy estimate seems to provide results relatively similar to the input power which shows it as a good quantity for the assessment of the equipment dynamics.

### *Control at point 2*

The local effect of the control is shown in Figure 5.25. As for a single-channel control at point 1, large reduction is observed over the frequency range except at 0.5 Hz and 16.5 Hz where the level is increased by 4 dB and 5 dB respectively for a gain of 160. A maximum reduction of 25 dB is achieved at 255 Hz and a 12 dB is till observed at 1000 Hz. The effect of the control at point 1 and 3 are now relatively significant, especially at point 1 which is quite close to point 2. The fact that no further reduction at point 1 is observed above 500 Hz tends to demonstrate again the local effect of the control which can be recovered at location not too distant from the control point compared to a structural wavelength in the composite panel.

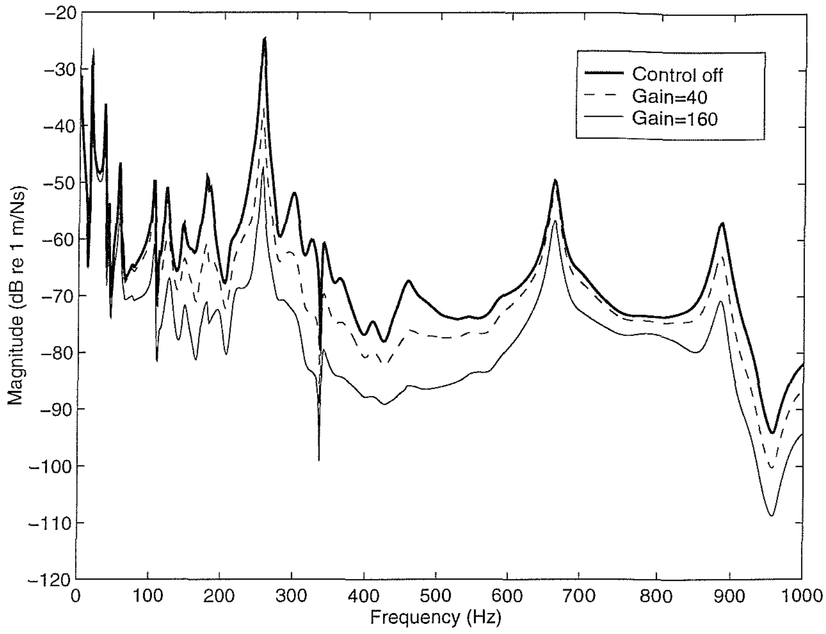

Figure 5.25. Simulated velocity at point 2 per unit primary force for a control at point 2.

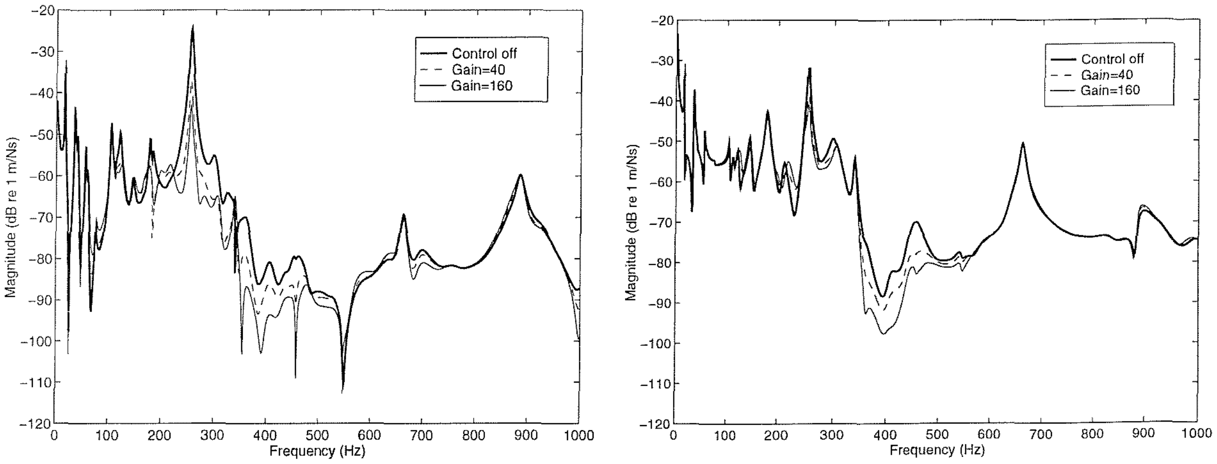

Figure 5.26. Simulated velocity at point 1 per unit primary force for a control at point 2.

Figure 5.27. Simulated velocity at point 3 per unit primary force for a control at point 2.

As shown on the input power spectrum in Figure 5.29, the control seems to generate some reduction over the equipment plate even if the reduction in the range [300 Hz - 600 Hz] will not have any significant effect on the global composite panel vibration as the passive level is already low. The peak at 255 Hz is attenuated by up to 8 dB on both the energy and the power spectra. Both amplification at 0.5 Hz and 16.5 Hz are observed in the energy and power quantities which balances the efficiency of the control as the associated passive level is already high at these frequencies.

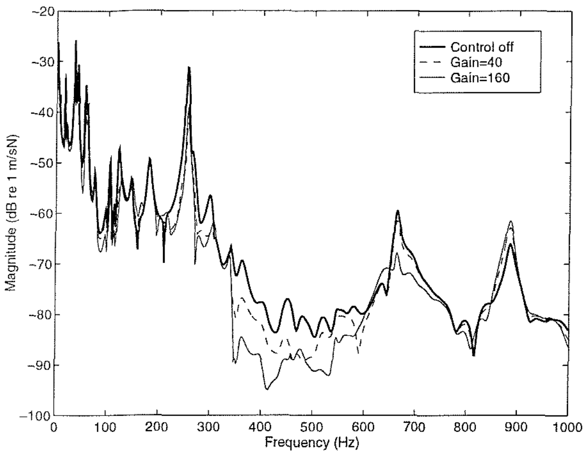

Figure 5.28. Simulated energy estimate for a control at point 2.

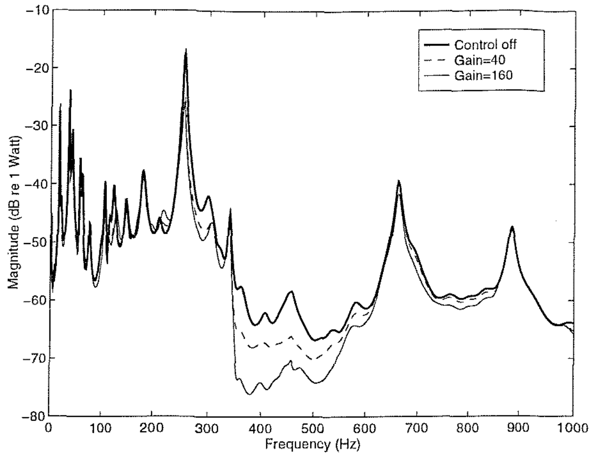

Figure 5.29. Simulated power input in the equipment for a control at point 2.

### *Control at point 3*

The control provides again very large local broad band attenuation over the band [0-1 kHz] which is balanced by the possibility of instability at 0.5 Hz and small amplification at 16.5 Hz, which sets the low frequency range to high vibration level as already observed for a control at point 2. These two amplifications are general to the whole equipment dynamics as they are noticed at the other mount junctions and on the energy and input power spectra as shown in Figures 5.33 and 5.34. Even though 4 dB reduction are obtained at 255 Hz at point 1 and 2 and for the energy and power quantity, isolation is again only obtained locally.

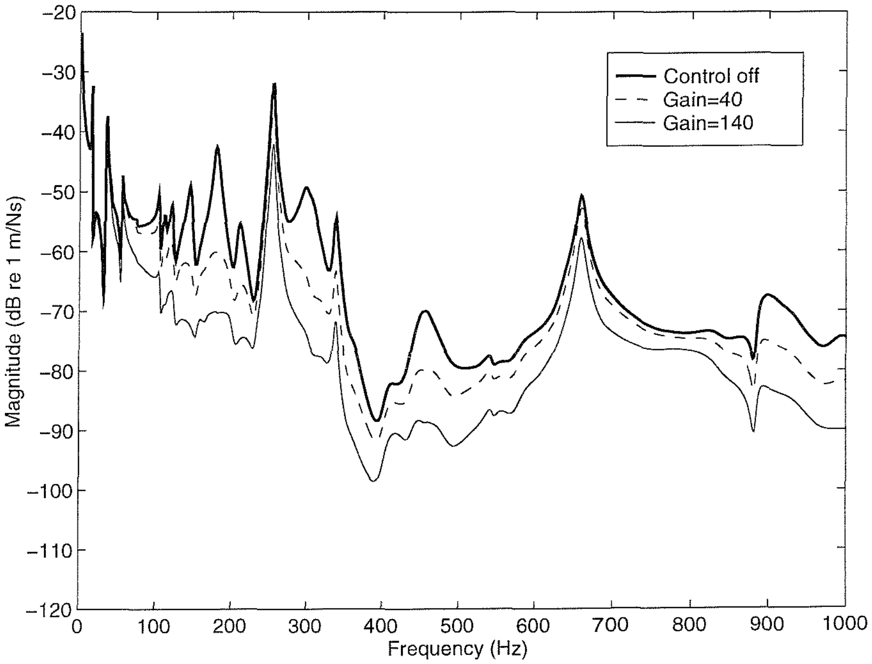

Figure 5.30. Simulated velocity at point 3 per unit primary force for a control at point 3.

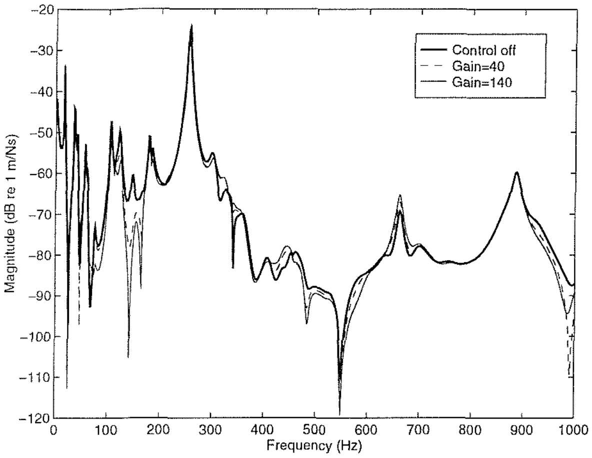

Figure 5.31. Simulated velocity at point 1 per unit primary force for a control at point 3.

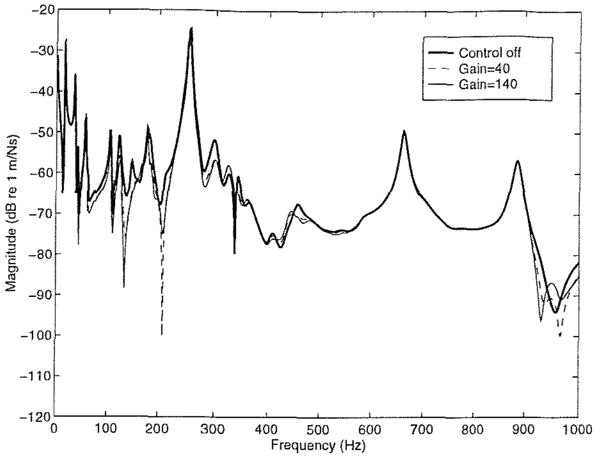

Figure 5.32. Simulated velocity at point 2 per unit primary force for a control at point 3.

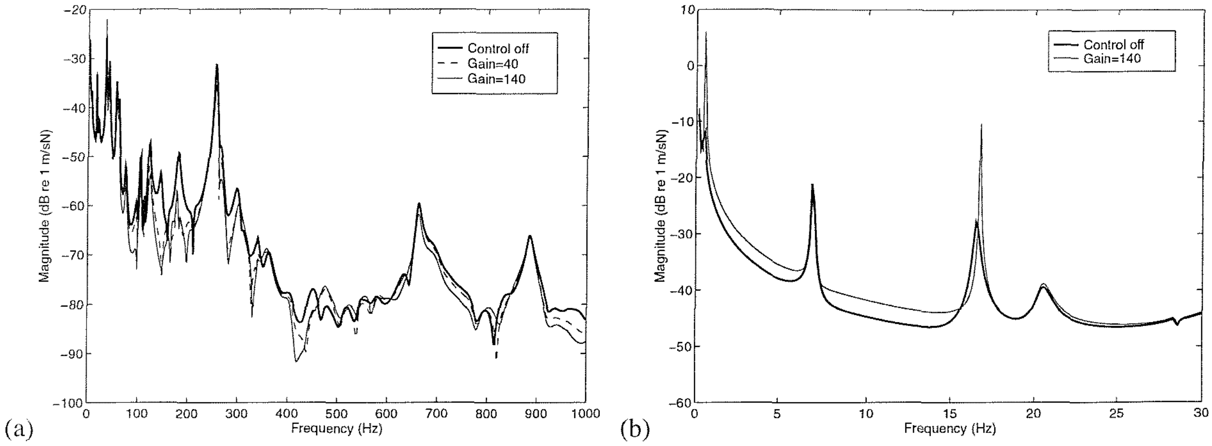

(a) (b)

Figure 5.33. Simulated energy estimate for a control at point 3 over the range [0-1 kHz] (a) and zoom picture (b).

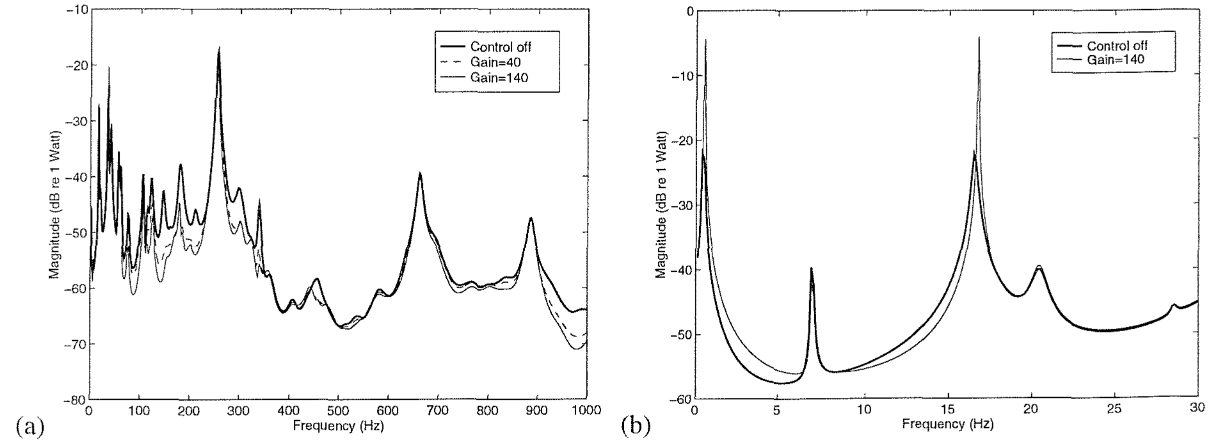

(a) (b)

Figure 5.34. Simulated power input in the equipment for a control at point 3 over the range [0-1 kHz] (a) and zoom picture (b).

### *Conclusions*

At the control point, the implementation of the single channel controllers provides large broad band vibration attenuation. As the frequency increases, the plant appears to become very stable as the bottom component of the reacting force become negligible compared to the top one, thus implementing collocated control and therefore skyhook damping. Several low frequency peaks, whose velocity magnitude is already high, are, however, strongly amplified and for a control at point 2 and 3, the system is close to instability for the maximum gains used. This cancels the benefit brought by the control at higher frequencies as these amplifications are spread over the equipment structure unlike the isolation effect which appears to be local. To be really efficient, the control loops would require some signal processing at low frequencies or the estimation of an optimal gain limiting the low frequency amplification.

The similarities observed between the energy and power quantities demonstrate that the energy estimate provides good information on the dynamics of the whole equipment structure. The energy estimate used experimentally in chapter 6 can thus be expected to be a reliable parameter to measure the global performance of the experimental controllers.

## 5.7. Multichannel control

### 5.7.1. Plant response and stability analysis

The objective is now to implement three decentralised control channels, closing simultaneously the three control loops discussed in section 5.6 in order to recover the maximum isolation performance over the whole equipment panel. Considering equal gain control, the stability of the multichannel controller requires us to apply the Nyquist method to the frequency dependent eigenvalues of **G**, the matrix of the plant response. This method is detailed in chapter 2 and has already been used in chapter 4. Figures 5.35, 5.36 and 5.37 show the magnitude and phase responses and the Nyquist plot of the three frequency dependent eigenvalues of **G**, $\lambda_1$, $\lambda_2$ and $\lambda_3$ for the frequency range [0-1 kHz]. No risk of control amplification are instability is expected above [0 - 1 kHz] as the eigenvalues are all in the positive real side of the complex plane.

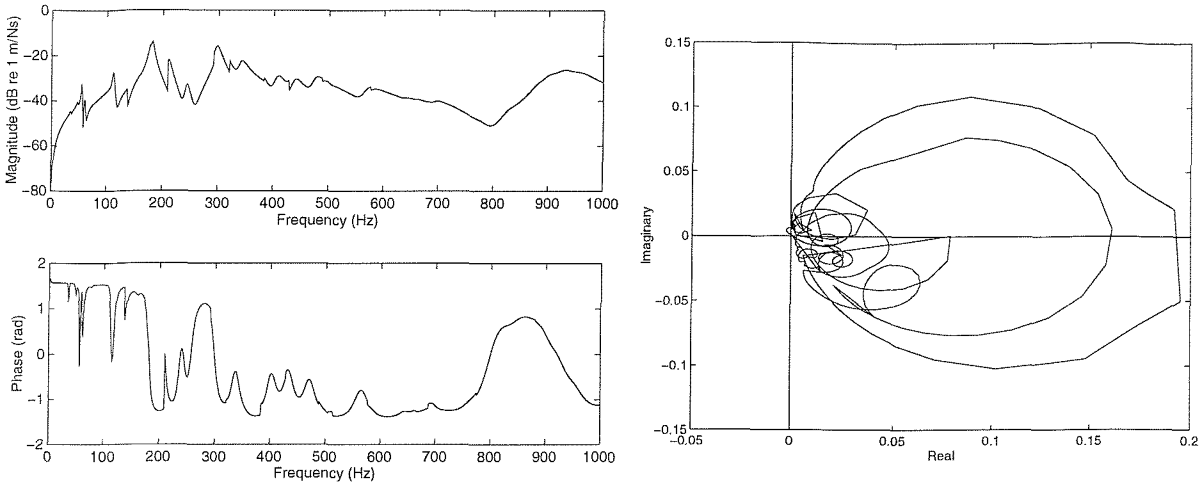

(a) (b)

Figure 5.35. Magnitude and phase responses (a) and Nyquist plot (b) of $\lambda_1$ estimated from the simulated data.

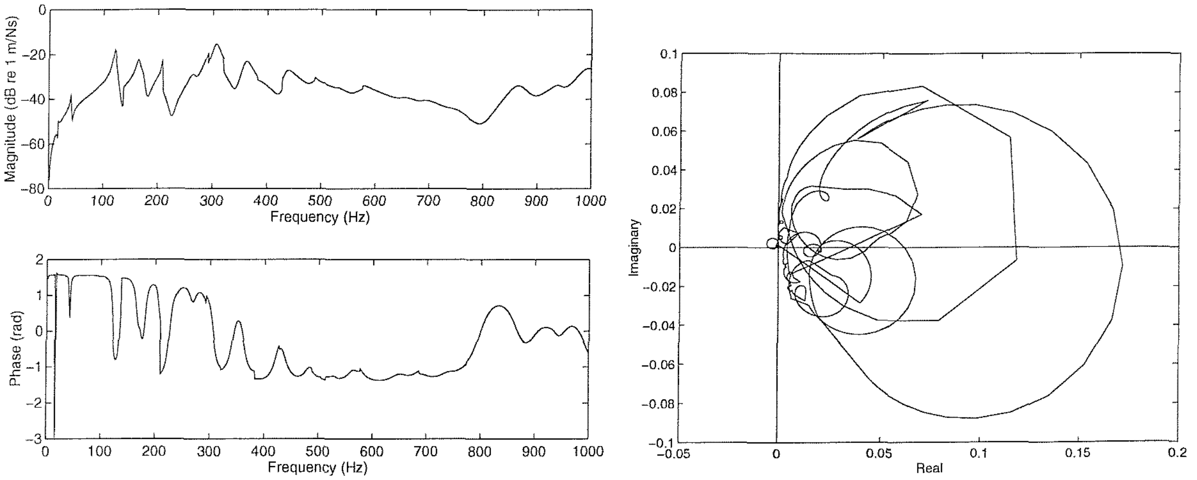

(a) (b)

Figure 5.36. Magnitude and phase responses (a) and Nyquist plot (b) of $\lambda_2$ estimated from the simulated data.

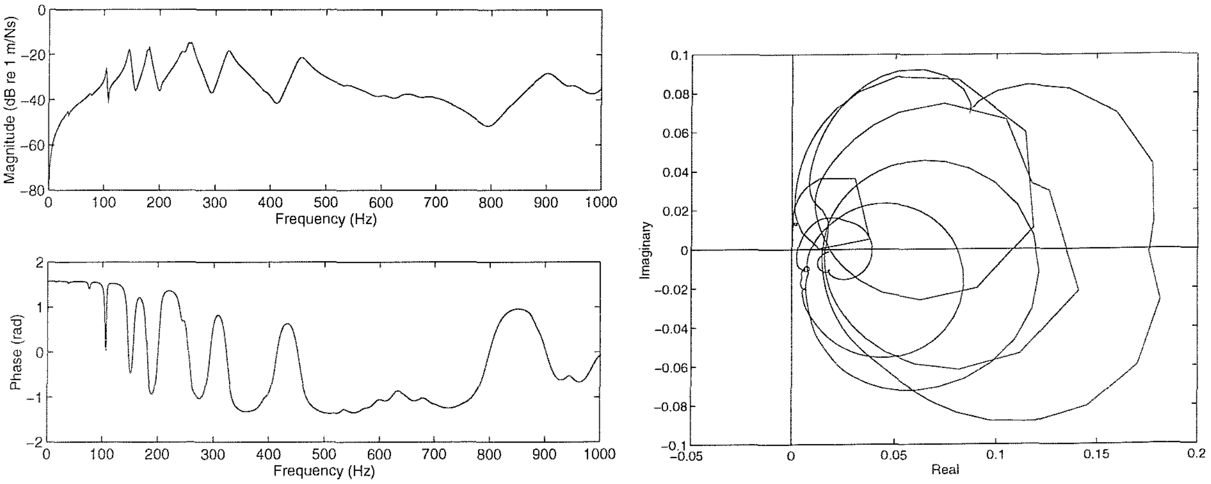

(a) (b)

Figure 5.37. Magnitude and phase responses (a) and Nyquist plot (b) of $\lambda_3$ estimated from the simulated data.

The three eigenvalues first display very stable characteristics. No sign of instability or even amplification is to be found at high frequencies where strong reduction can be expected thanks to the first mount longitudinal resonance which increases the level of the plant response around 850 Hz. As noticed in the simulations of the single-channel control implementations, the maximum reduction is expected in the range [100 Hz - 400 Hz] where the control will attenuate the adverse effect of the passive isolation. Instability is, however, present in the multichannel control, again, at low frequencies as seen in $\lambda_2$ in Figure 5.36. Figure 5.38 is a zoom on the low frequency range [0 - 100 Hz] to display more accurately the behaviour of $\lambda_2$. The Nyquist plot crosses the negative real axis for a frequency of 16.5 Hz. This is the only frequency that is able to generate instability in the system. Vibration amplification was already noticed in the single-channel control analysis at 16.5 Hz and was explained to be caused by the fact that the base structure is mass controlled whereas the equipment panel is stiffness controlled. No stability problem is noticed for multichannel control at 0.5 Hz, which was identified as a rigid body mode of pitching of the global system. Control at channel 1 was not subject to stability issue at 0.5 Hz, and it may be that the whole system is stabilised as the three loops are closed simultaneously. The gain is therefore limited to a maximum value of 230. Vibration amplification is also expected at 7 Hz as a small loop inside the unstable half plane is noticed in the Nyquist plot of $\lambda_1$ in Figure 5.39.

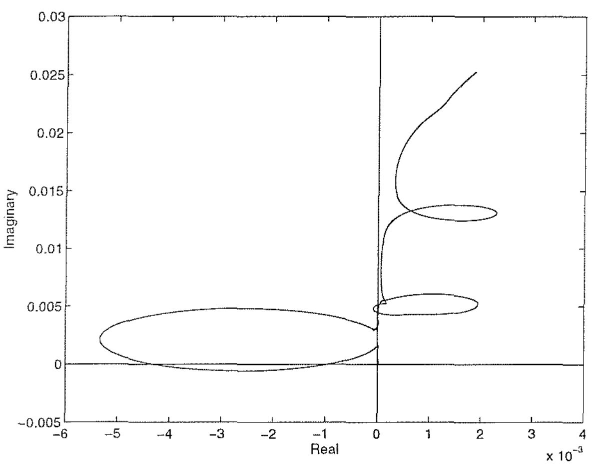

Figure 5.38. Nyquist plot of $\lambda_2$ for the range [0 - 100 Hz] estimated from simulated data.

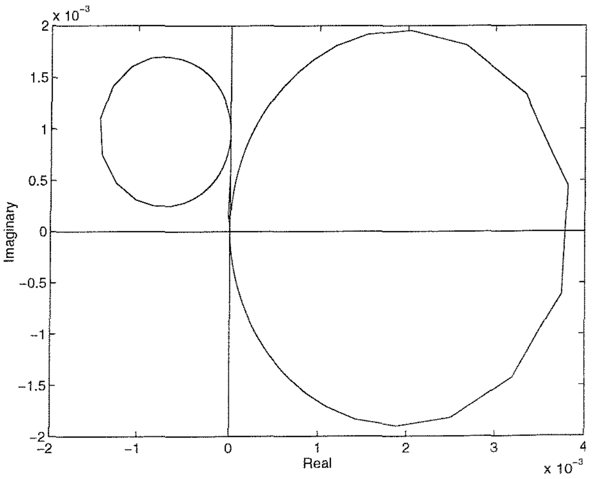

Figure 5.39. Nyquist plot of $\lambda_1$ for the range [0 - 100 Hz] estimated from simulated data.

### 5.7.2. Control performance

The performance of the multichannel equal gain control are simulated for the maximum value of control gain tolerated by the system, 230 and for an intermediate value, 40. The different responses of the control system are normalised by the primary force excitation and compared to the equivalent passive quantities. The local effect of the control is first shown in Figures 5.40, 5.41 and 5.42 giving the force normalised velocity responses at points 1, 2 and 3, in a similar way to the analysis of the single-channel controllers.

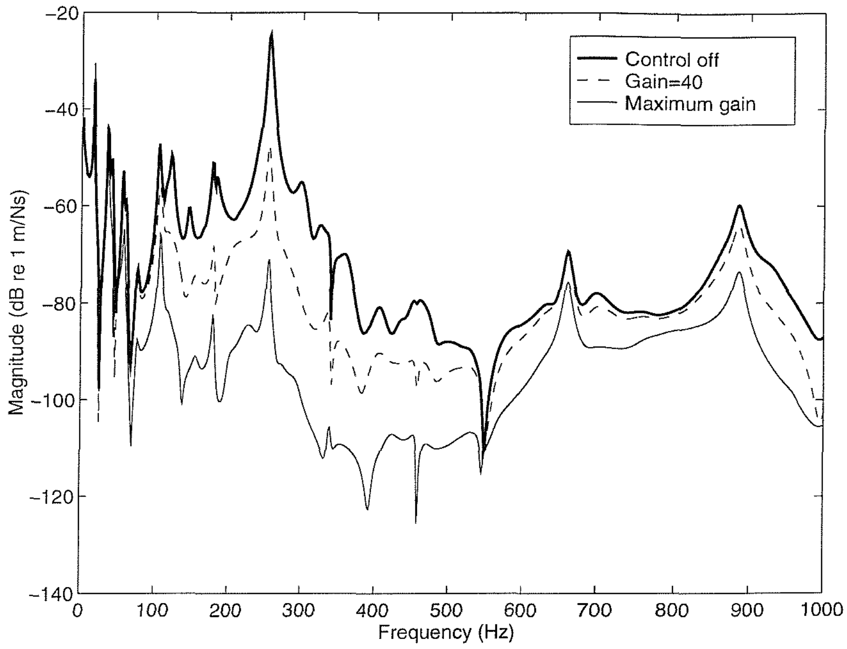

Figure 5.40. Simulated velocity at point 1 per unit primary force when no control is applied and for two values of feedback gain with a decentralised multichannel control system.

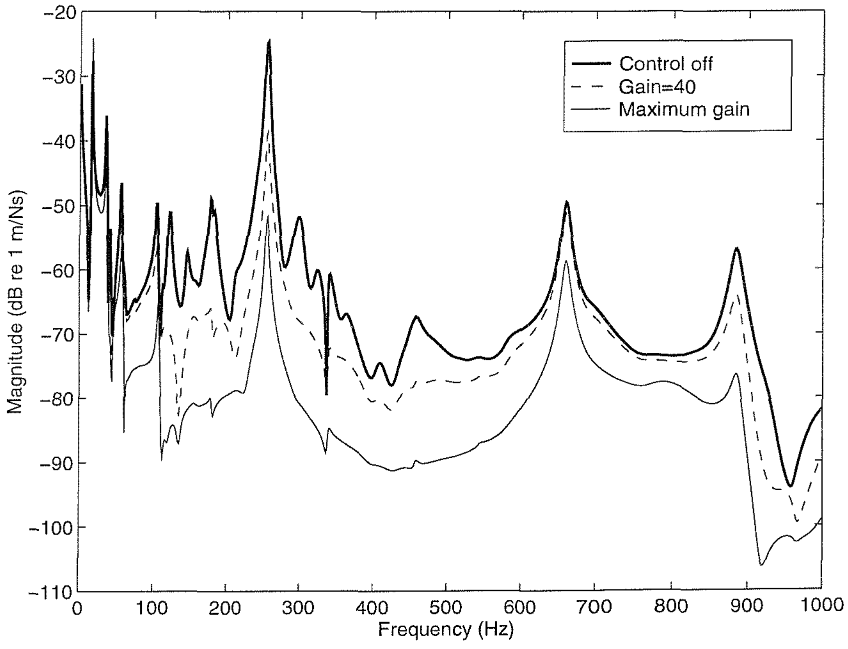

Figure 5.41. Simulated velocity at point 2 per unit primary force when no control is applied and for two values of feedback gain with a decentralised multichannel control system.

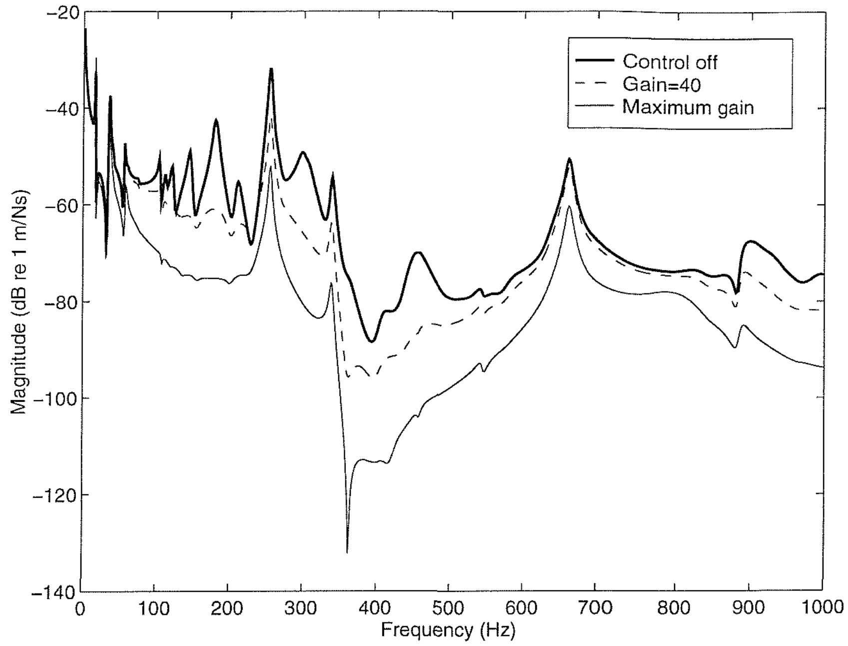

Figure 5.42. Simulated velocity at point 3 per unit primary force when no control is applied and for two values of feedback gain with a decentralised multichannel control system.

Except from the amplification noticed at 16.5 Hz, the control generates very large reduction of the vibration level at the control locations over the whole frequency range of interest. The most significant results are obtained in the frequency range [100 Hz - 450 Hz] where the vibration level goes down by 10 dB to up to 40 dB for a gain of 230. The maximum equipment response at 255 Hz is attenuated by up to 27 dB at point 2, 20 dB at point 3 and even 45 dB at point 1. 15 dB to 20 dB reduction are still observed at 885 Hz so that the effect of the first longitudinal resonance in the mount is strongly attenuated. The local maximum at 600 Hz, which is generated by a resonance of the base plate, is also damped. The attenuation is especially large at point 1 which was shown in the passive analysis to be the junction that is the most subject to the amplification from the passive isolation in the range [100 Hz - 500 Hz].

Figure 5.43 shows the estimate of the kinetic energy over the equipment plate as defined in section 5.6 and Figure 5.44 shows the total power input in the composite panel by the active mounts. In this multichannel case, the good isolation performance observed locally appears to be generalised to the whole equipment. At 255 Hz, the power is reduced by 25 dB and the energy estimate by 20 dB. The local reduction obtained with a single-channel control was shown above to generate only small reduction of the total input power. Distributing several control loops over the equipment plate provides local reduction at each mounting position, which are able to generate a global reduction of the suspended structure vibration. The large isolation effect of the control can also be explained by the fact that such a multichannel control applies a local correction at each of the disturbance paths implementing a control at the sources of the disturbance.

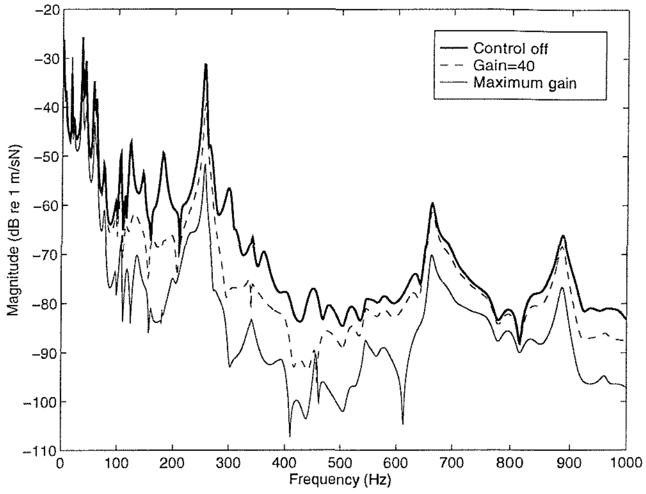

Figure 5.43. Simulated energy estimate when no control is applied and for two values of feedback gain with a decentralised multichannel control system.

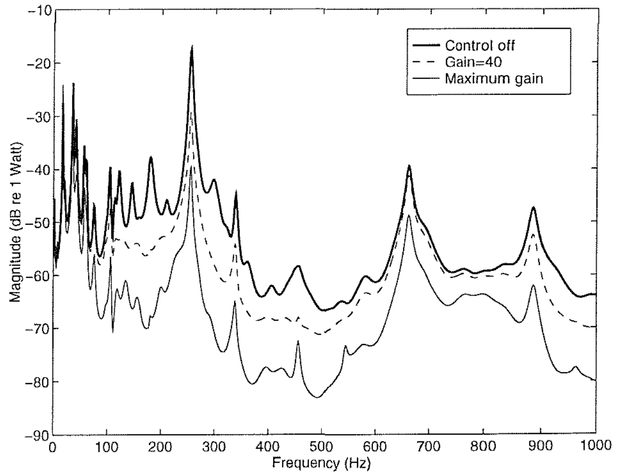

Figure 5.44. Simulated power input in the equipment when no control is applied and for two values of feedback gain with a decentralised multichannel control system.

The onset of instability is, however, largely noticed locally in Figure 5.45, and spreads to the whole equipment structure as shown in the zoomed spectrum of the input power in Figure 5.46. The sharp increase generated at 16.5 Hz prevents the use of a control gain value close to the maximum gain as it may cancel all the benefit obtained at higher frequencies by the control. No other significant amplifications are noticed at low frequencies.

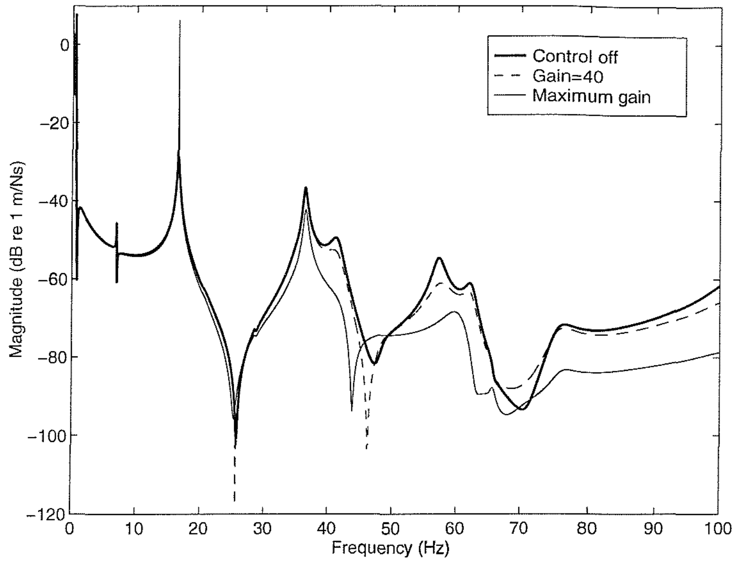

Figure 5.45. Simulated velocity at point 1 per unit primary force when no control is applied and for two values of feedback gain with a decentralised multichannel control system. Zoomed picture.

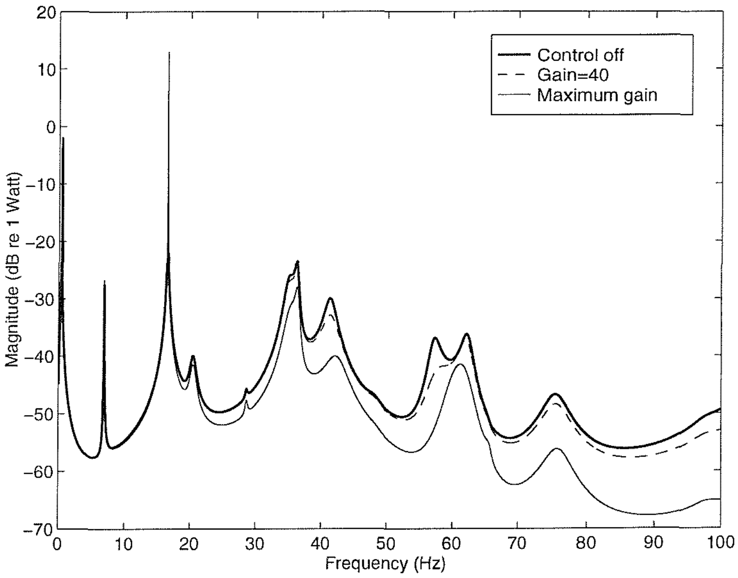

Figure 5.46. Simulated power input in the equipment when no control is applied and for two values of feedback gain with a decentralised multichannel control system. Zoomed picture.

The control limitation is again centred at low frequencies. It may be possible to design appropriate filters in order to balance the large increase observed at 16.5 Hz..

# Chapter 6

# Reactive implementation of DVFB control on a mounted flexible structure: Experiments

## 6.1. Introduction

This chapter presents the results obtained from the experimental implementation of the single channel controllers and of the multichannel controller whose simulations have been presented in chapter 5. The main mechanical characteristics of the system have been identified and discussed in chapter 5. The model, however, is based on simplification and extra unmodelled mechanical features are likely to partly modify the conclusions reached from the simulations. The simulated control results also assumed a perfect control loop and the use of perfect control sensors and actuators. In this chapter, the question of the limitations encountered by the electronics involved in the control channels is addressed and their effects on the control performance are discussed. In a first part, the description of one experimental control loop is given. The control results obtained on the test rig by the experimental implementation of the control systems simulated in chapter 5 are then presented. This involves three single-channel control systems, one at each of the mount junctions and the equal gain decentralised multichannel control system.

## 6.2. The experimental test rig

The whole isolation system was suspended by very soft elastic strings connected to light sticks of wood supporting the rig from the base as shown in Figure 5.1. The extra inertial effect of the supporting pieces of wood were also accounted for in the model. Such a setting satisfies rather well the conditions of free boundary conditions and should not affect the dynamics of the base plate. The passive analysis of the system has been partly carried out in chapter 5, in which the passive system response at point 1, as well as the uncoupled equipment and plate response calculated by the model, were compared to the equivalent simulated quantities. Figure 6.1 shows the out-of-plane velocity per unit primary excitation $f_0$ measured at the mount junctions 1, 2 and 3 on the base structure and on the equipment structure. This enables us to estimate the effect of the passive isolation and therefore to have an insight into the frequency range where the control is likely to be effective and useful.

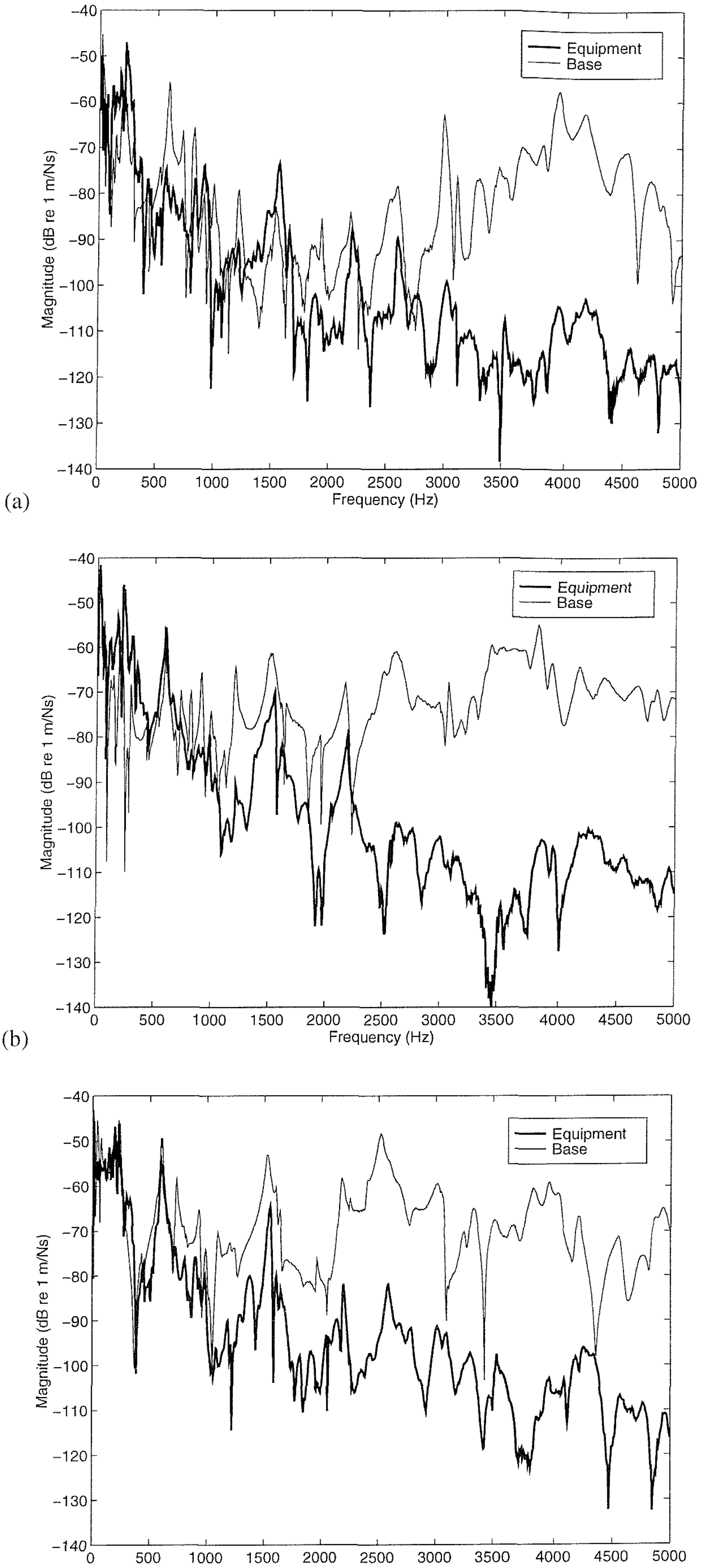

Figure 6.1. Measured velocity responses on the equipment and base structures at mount junction 1 (a), 2 (b) and 3 (c) per unit primary excitation.

The passive isolation effect is obvious from these three plots. As observed from the simulated results, no real isolation improvement is provided by the passive isolators below 1 kHz. The vibration level is strongly amplified in the range [100 Hz - 400 Hz] at points 1 and 2 but not at point 3, whose motion is dictated by the base dynamics. No real amplification effect was noticed either at point 3 in the simulations. From 300 Hz the vibration level on the equipment decreases rapidly with frequency so that, above 3 kHz, the measurements start to be slightly corrupted by noise. The base velocity response is however rather constant with frequency. Above 2000 Hz the vibration level on the base is much greater than on the equipment, especially at point 2 and 3 so that the control is very unlikely to have any extra isolation effect on the equipment above this frequency. As determined from the simulations in chapter 5, the frequency band in which addition control is required appears to be [0-1 kHz] particularly in the range [100 Hz - 400 Hz].

## 6.3. The experimental control loop

Since the multichannel control implemented is a decentralised control, the discussion of the effect of the electrical devices in the control loop on the experimental plant responses can be carried out both single and multichannel controls looking simply at a single independent control channel.

As already presented in chapter 2, the plant response for single-channel control tends to be defined as the transfer function between the input electrical signal in the control actuator, $u$ and the response at the output of the control sensor, $y$. This allows us to consider the control force device and the sensor as part of the plant. For a perfect actuator and a perfect sensor, with flat frequency responses, the plant response $G$ is therefore proportional to the total mobility, the quantity relating the control force to the velocity response of the mechanical system at the control location. Usually, however, the dynamics of the actuator and the response of the control sensor can not be neglected and have a significant effect on the control system.

Each control loop of the experimental control is composed as shown in Figure 6.3. The velocity signal is obtained by measuring the acceleration at the control point using a small accelerometer, B&K type 4375, whose signal is integrated through a charge amplifier B&K type 2635 to obtain a velocity signal. The equivalent velocity sensor to consider as part of the plant is therefore the accelerometer coupled to the charge amplifier. If the frequency response of the accelerometer is very flat down to very low frequency, the integration implies a low frequency filtering process which add a phase shift to the sensor response at low frequencies. This is the results of the difficulty in measuring the velocity at low frequencies, as already discussed in chapter 3.

Figure 6.2. Photograph of the mechanical setting for a single control channel.

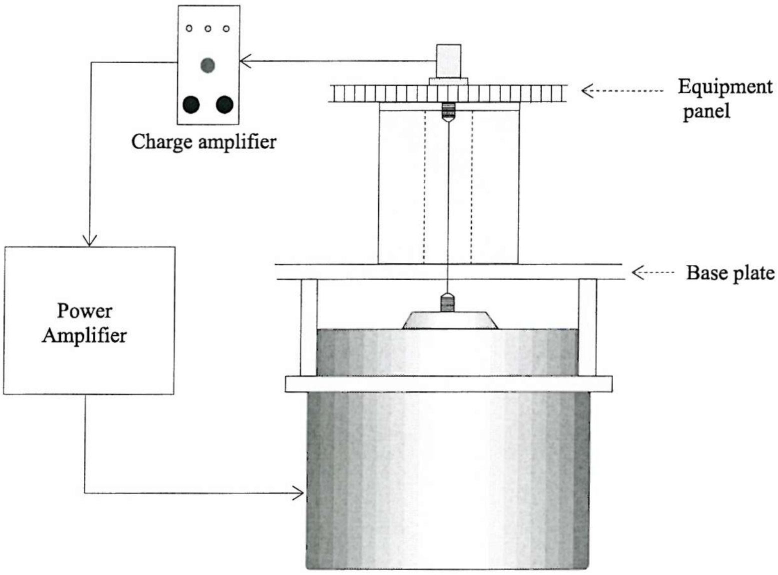

Figure 6.3. Schematic of one experimental control loop.

Not only the plant but also the controller is subject to the non-perfect response of the electronics involved in the control. The power amplifier used in the loop cannot provide a perfect gain constant with frequency. Figure 6.4 shows the response of one channel of one of the two power amplifiers used, from which it is clear that extra phase shift is introduced into the control loop at low frequencies. The gain response of the power amplifier as well as the response of the control actuator and sensor have been included in the expression of the measured plant response so that, as in chapter 4, the controller can be regarded as a perfect amplifier of constant gain $h$.

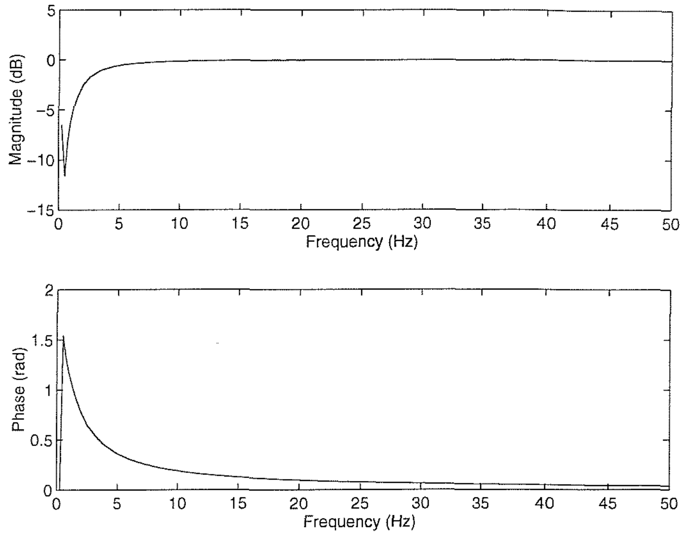

Figure 6.4. Normalised transfer function of one power amplifier channel.

## 6.4. Single channel control

### 6.4.1. Plant responses and stability analysis

*Control at point 1*

Figure 6.5 shows the experimental plant response $G_{11}$ in the frequency range of interest for the control.

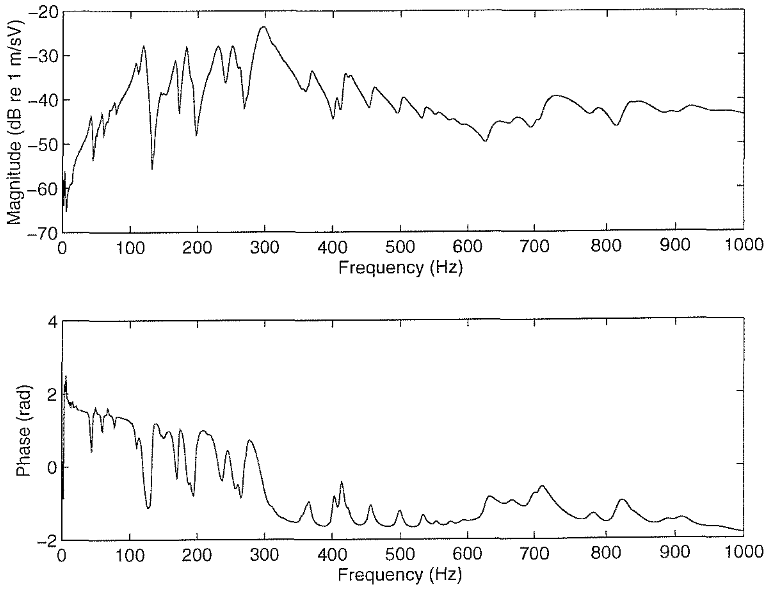

Figure 6.5. Magnitude and phase of the measured plant response $G_{11}$.

It looks very similar to the simulated one but with a different magnitude as the input quantity is now the control shaker input voltage. The plant response has a maximum in the range [100 Hz - 400 Hz] as the result of the passive isolation amplification effect. It slightly increases again around 700 Hz as the first longitudinal resonance occurs in the mount as noticed at 850 Hz in the simulations. The phase globally varies from $\pi/2$ to $-\pi/2$ under the passive mount effect so that the Nyquist plot in Figure 6.6 largely lies in the stable half plane.

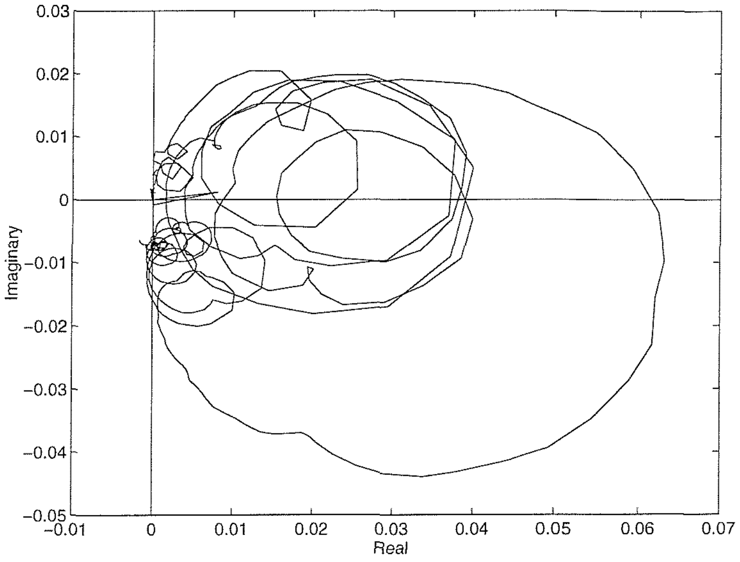

Figure 6.6. Nyquist plot of the measured plant response $G_{11}$.

Looking closer at the low frequencies range in Figure 6.7, a very low resonance can be noticed around 4 Hz. This is likely to be due to the rigid body pitching mode of the ensemble identified in the simulation, but the attenuation caused by the charge amplifier and power amplifier responses, the poor resolution and therefore the low coherence means that it is not possible to precisely diagnose the low frequency behaviour of the system. This resonance does not seem to be able to destabilise the system by itself but the phase shifts introduced at low frequencies by both the charge amplifier and the power amplifier in the control loop make the Nyquist plot to cross the negative real axis of the Nyquist diagram as shown in Figure 6.8. Some of the small jumps in amplitude and phase observed in the simulations at 7 Hz, 16.5 Hz or 67.5 Hz are also noticeable but do not appear to be a threat to the control stability.

A danger of instability was also to be found at higher frequencies, however. It first appeared that the phase response was gradually falling off below $-\pi/2$ in Figure 6.5 as the result of the frequency dependent electrical impedance of the control shaker, $Z_e$.

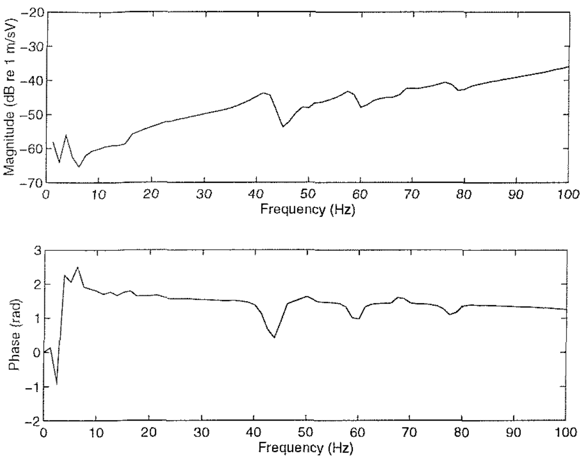

Figure 6.7. Zoomed picture of the magnitude and phase of the measured plant response $G_{11}$.

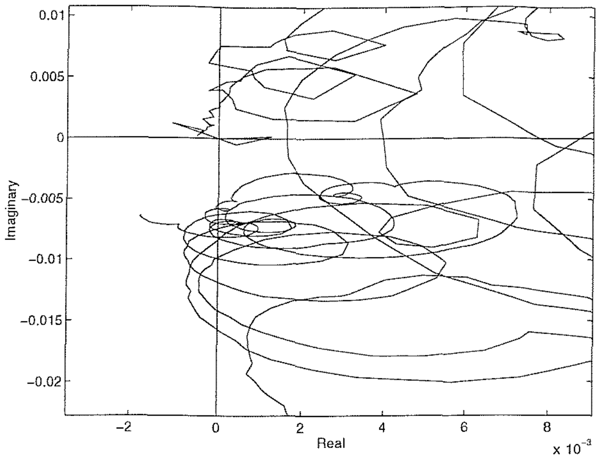

Figure 6.8. Nyquist plot of the measured plant response $G_{11}$. Zoomed picture around the origin.

$$Z_e = R_e + j\omega L_e \tag{6.1}$$

As the frequency becomes higher the inductance term $j\omega L_e$ increases so that the control force is no longer proportional to the control voltage. The early effect of this phase shift can be observed around 1 kHz on the Nyquist plot in Figure 6.8. Figure 6.9 shows the measured electrical impedance of the unloaded control shaker.

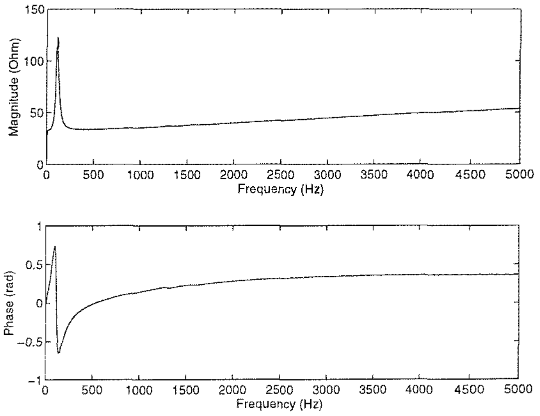

Figure 6.9. Measured electrical impedance of the unloaded control shaker.

It was therefore decided to investigate the plant response up to 5 kHz in order to determinate any instability even if control was restricted to the range [0-1 kHz]. The dashed line curve in Figure 6.10 shows the plant response obtained as the control accelerometer was located on the top panel of the composite plate as shown in Figure 6.3. Two large resonances at 2600 Hz and 4500 Hz drive the phase response down through two consecutive $\pi$ phase shifts. Since the first resonance at 2600 Hz was quite large, this constituted a direct threat to the control system, setting the maximum control gain to a rather low value. This resonance was found to be caused by a mass/spring effect of the accelerometer on the axial stiffness of the core of the composite plate. A hole was therefore made on the plate to glue the accelerometer on the top disc of the mount, so that the control sensor is collocated with the top component of the reactive force. The new plant response is shown as the solid line in Figure 6.10. This modification to the system did not remove the second resonance, which may be due to a longitudinal resonance in the steel stinger transmitting the reactive control force from the shaker or to a rocking mode in the aluminium top disc between the isolator and the composite panel. It is significantly amplified by the modification performed to reduce the first resonance.

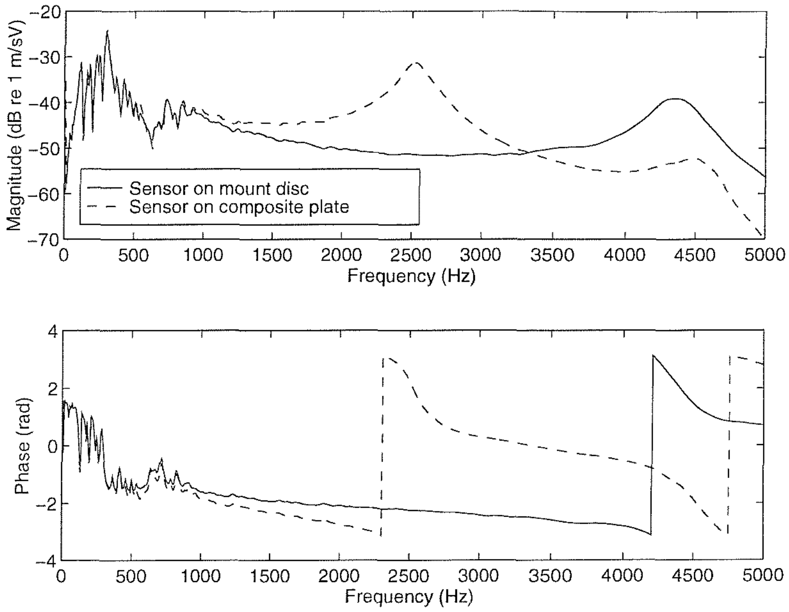

Figure 6.10. Magnitude and phase of the measured plant response $G_{11}$ up to 5 kHz before and after modification of the sensor location.

The Nyquist plot of the modified plant response is shown in Figure 6.11 in the range [0 - 5 kHz]. The maximum control gain is estimated to be 118, which is limited at high frequency by the 4500 Hz resonance, which is represented in the Nyquist plot by the larger loop in the unstable half plane.

Setting the charge amplifier cut-off frequency to 3 kHz appeared to be another means of increasing the control stability. The Nyquist plot of this new plant response in Figure 6.12 shows that the undesired loop is significantly shrunk as the filtering process attenuates the 4500 Hz resonance.

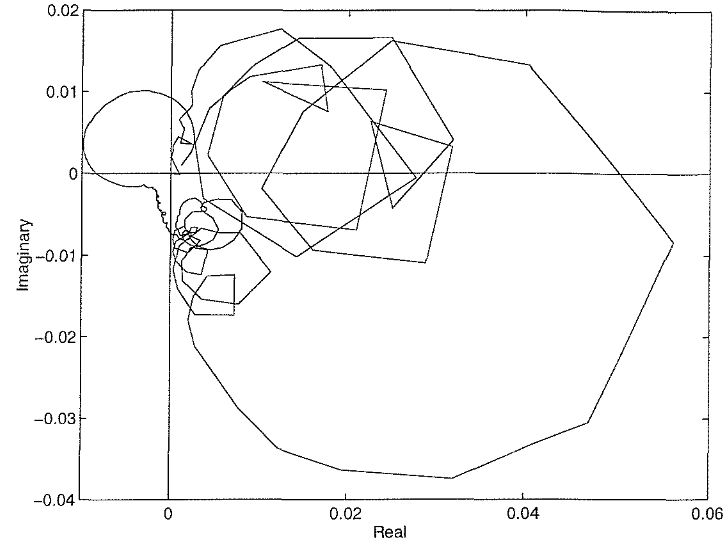

Figure 6.11. Nyquist plot of the measured plant response after modifications up to 5 kHz

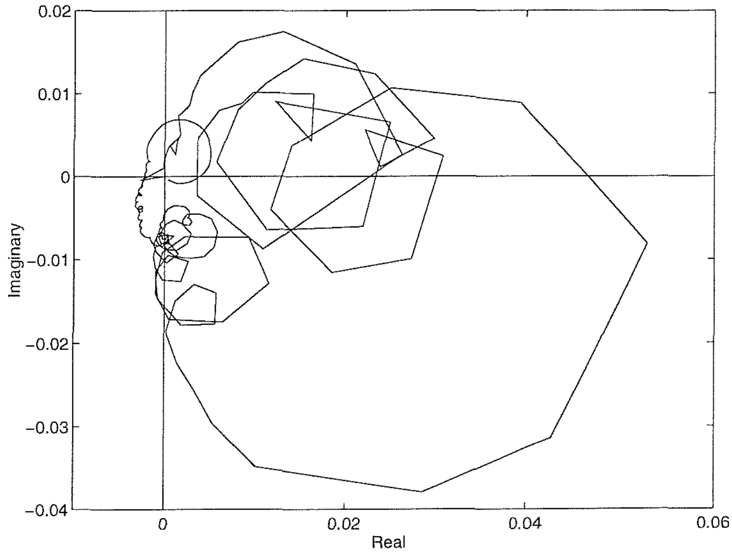

Figure 6.12. Nyquist plot of the measured plant response $G_{11}$ up to 5 kHz after modification and with the cut-off frequency of the charge amplifier set to 3 kHz.

It is now difficult to discriminate whether it is the very low frequency response or the high frequency response that is going to generate instability. The control gain can, however, be increased rather safely to values around 300, even if it is difficult to draw definite conclusions at low frequencies because of the poor resolution and coherence of the measurements. Moreover, at high frequencies, the amplitude of the resonance at 4500 Hz appeared to be sensitive to small change such as a small modification of the control sensor location.

The plant is very stable all over the range [70 Hz- 1000 Hz] and large attenuation are expected in the range [100 Hz- 400 Hz].

### *Control at point 2*

The same general observation made in the analysis of $G_{11}$ can be made for the analysis of the plant response $G_{22}$ shown in Figure 6.13 and 6.14 for the frequency range [0-1 kHz].

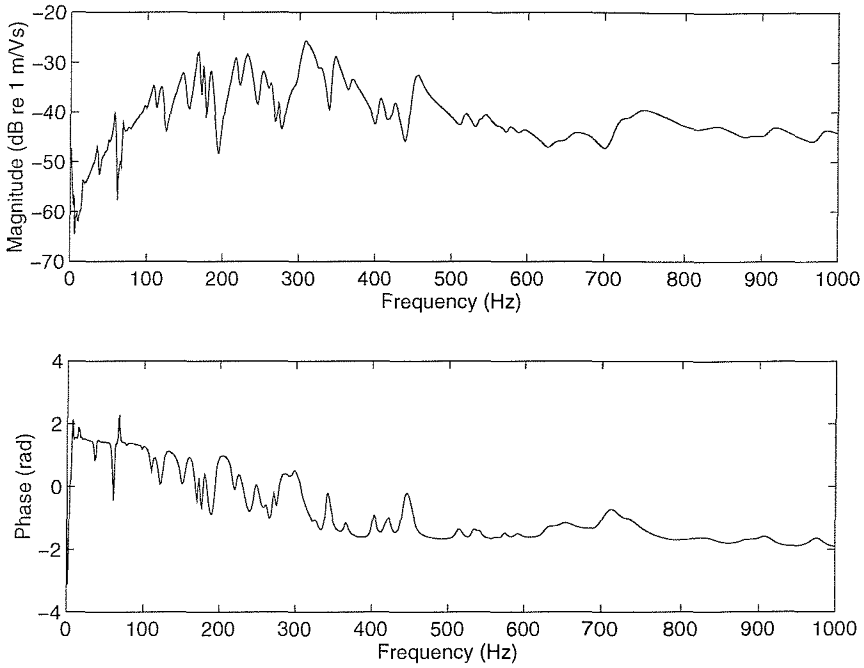

Figure 6.13. Magnitude and phase of the measured plant response $G_{22}$.

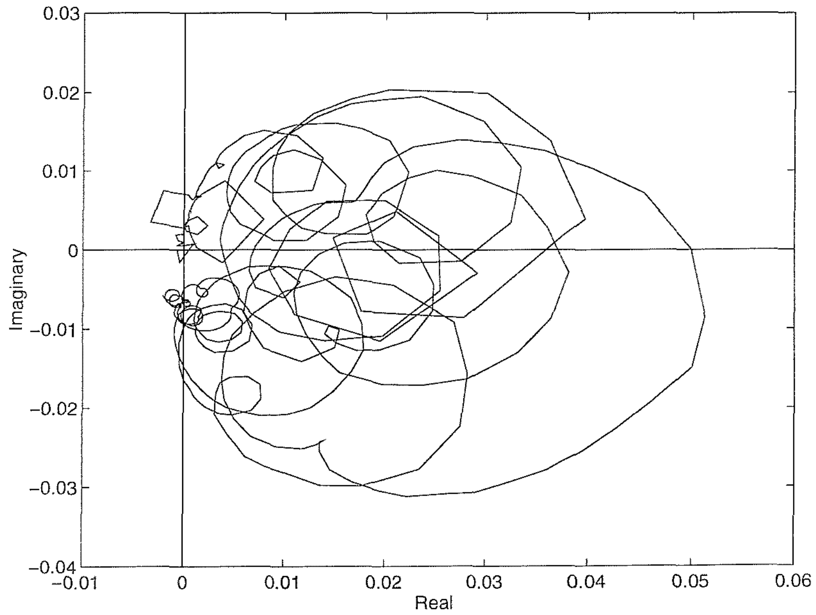

Figure 6.14. Nyquist plot of the measured plant response $G_{22}$.

The passive mounts generate a maximum response in the band [100 Hz - 400 Hz]. The same high frequency resonances were observed at 2000 Hz and 4500 Hz and the same modification was carried out to suppress the first one. The second one sets the maximum control gain to a value of 159. The only difference come at low frequencies where the "jumps" at 7 Hz, 16.5 Hz and 67.5 Hz are larger than in $G_{11}$. The sharp response at 67.5 Hz is represented in Figure 6.14 by a small loop in the unstable half plane which does not seem to cross the negative real axis. However, as already noticed in the simulations, it may cause large amplifications but the frequency resolution renders difficult the extraction of any clear features.

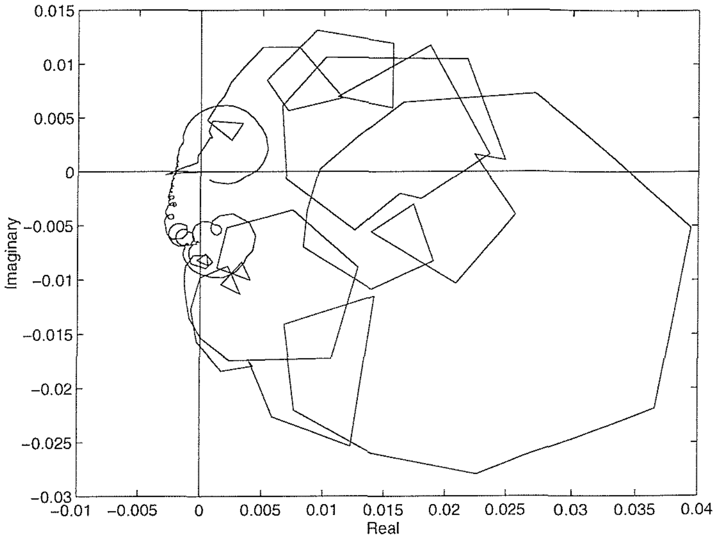

Figure 6.15. Nyquist plot of the plant response $G_{22}$ up to 5 kHz with the cut-off frequency of the charge amplifier set to 3 kHz.

The high frequency resonance can be attenuated by again setting the charge amplifier cut-off frequency to 3 kHz. Figure 6.15 shows the Nyquist plot of the new plant response. Again this allows to increase the maximum gain tolerated by the control system to value greater than 300 but it again appears difficult from figure 6.15 to know if the low or high frequency region is going to set the control limitation.

### *Control at point 3*

The plant response $G_{33}$ is, once again, very similar to $G_{11}$. The passive isolation generates the same global trend with an amplitude maximum in the range [100 Hz - 400 Hz] where good control is expected. The Nyquist plot in Figure 6.17 crosses the negative real part axis at very low frequencies but this is associated with a very low level, as already explained, so that the control limitation once again first appears to be due to the 4500 Hz resonance which is also observed at point 3 after performing similar modification as at the two other control points. The maximum control gain is then estimated to be equal to 170 and is improved approximately to 390 as the high cut-off frequency of the charge amplifier is set to 3 kHz.

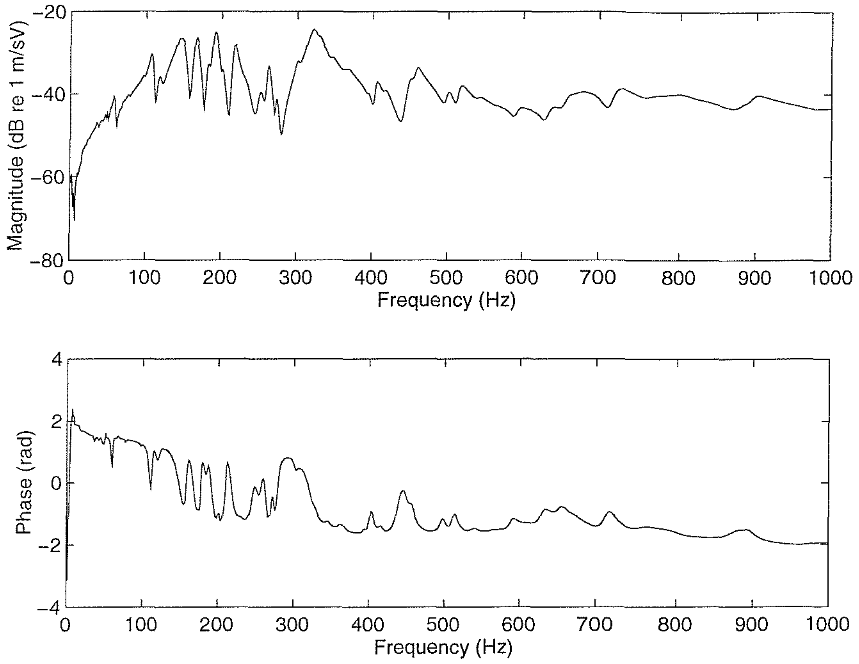

Figure 6.16. Magnitude and phase of the measured plant response $G_{33}$.

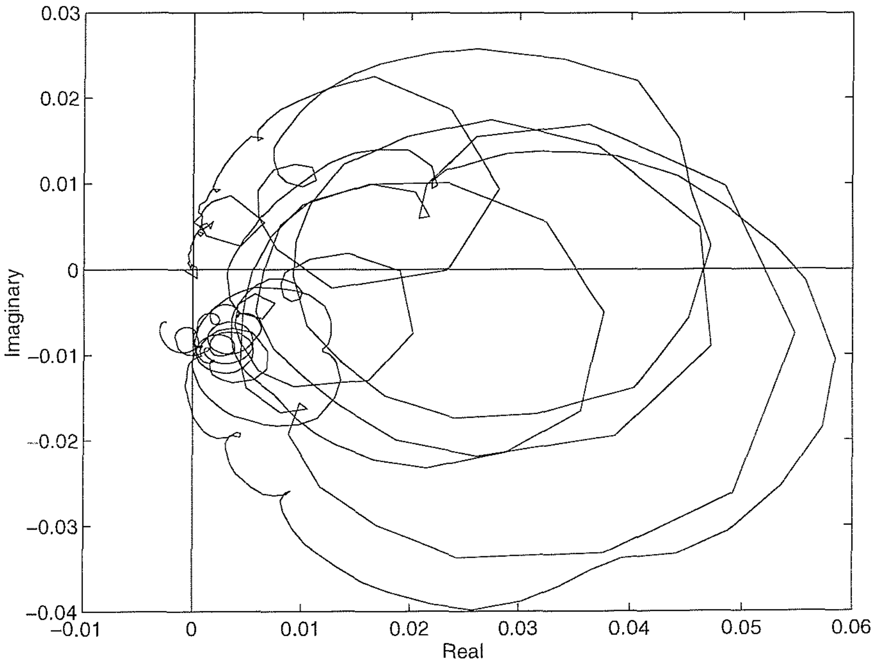

Figure 6.17. Nyquist plot of the measured plant response $G_{33}$.

Figure 6.18 shows the Nyquist plot for such a setting. Again, no clear evidence on the frequency region limiting the control can be extracted comparing Figure 6.17 to Figure 6.18 as the frequency resolution is not high enough.

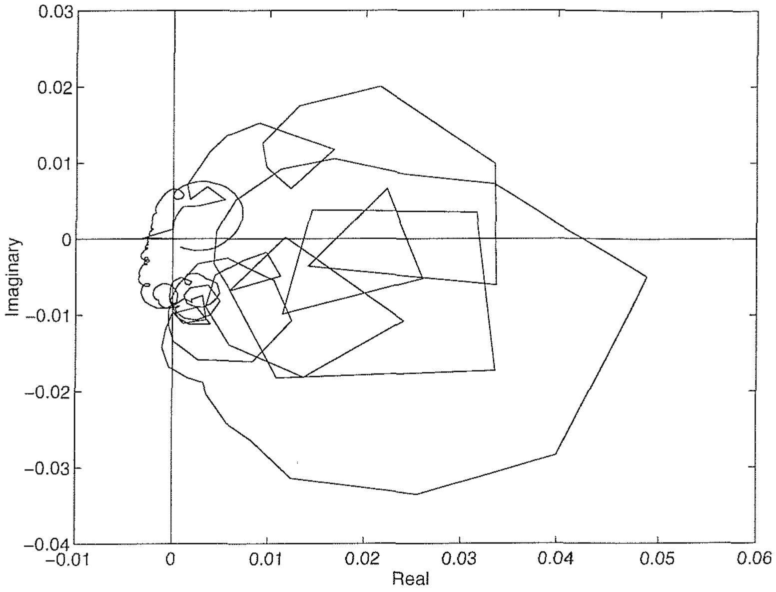

Figure 6.18. Nyquist plot of the measured plant response $G_{33}$ up to 5 kHz with the cut-off frequency of the charge amplifier set to 3 kHz.

***Conclusions***

Good local performance is expected in the frequency range [100 Hz - 400 Hz] for any of the three single-channel control systems, which is the first objective of the control implementation. The control effect at higher frequencies will have, however, to be carefully monitored up to 5 kHz in the experimental implementation as well as in the low frequency region where the bad coherence does not allow to make a clear prediction of the control system behaviour. The low frequency resonance observed in chapter 5 from the model at point 2 and 3 may have an unexpected amplification effect hidden to the plant response measurements.

### 6.4.2. Single-channel control performance

A single-channel system control was experimentally implemented at each of the three mount junctions individually. For each of them, the composite panel response was monitored at the three mount junctions. The equipment response was also monitored at the five points mentioned in chapter 5 for the estimation of the plate energy, but only for an implementation of the control at point 3 which seemed to tolerate, from the stability analysis, the larger control gain. The estimate of the plate energy was therefore only obtained for a control at point 3, assuming, from the simulations carried out, that it would provide general results on the effect of an experimental single-channel controller over the mounted composite panel.

The local effect of the controls is again given in terms of the out-of-plane velocity normalised by the primary force excitation, as performed in the simulation in chapter 5 and also in chapter 4. The quantities $V_{ij}$ when control is applied are thus compared to the primary disturbances $V_{0j}$ in the different plots presented below.

During the experimental implementation of the different controls, the high cut-off frequency of the charge amplifier was set to 3 kHz in the attempt to recover maximum values of control gain.

### *Single-channel control implementation at point 3*

The maximum gain tolerated by the system in the experiment is equal to 240. Figure 6.19 shows the effect of the control at the control point over the frequency range [0-1 kHz] for two values of feedback gain. Significant broad-band attenuation is achieved from 20 Hz to 1000 Hz with maximum reduction in the range [100 Hz - 400 Hz], as clearly predicted from the plant response analysis. The peak at 230 Hz is attenuated by 12 dB for a gain of 240 and reduction greater than 20 dB is obtained around 200 Hz.

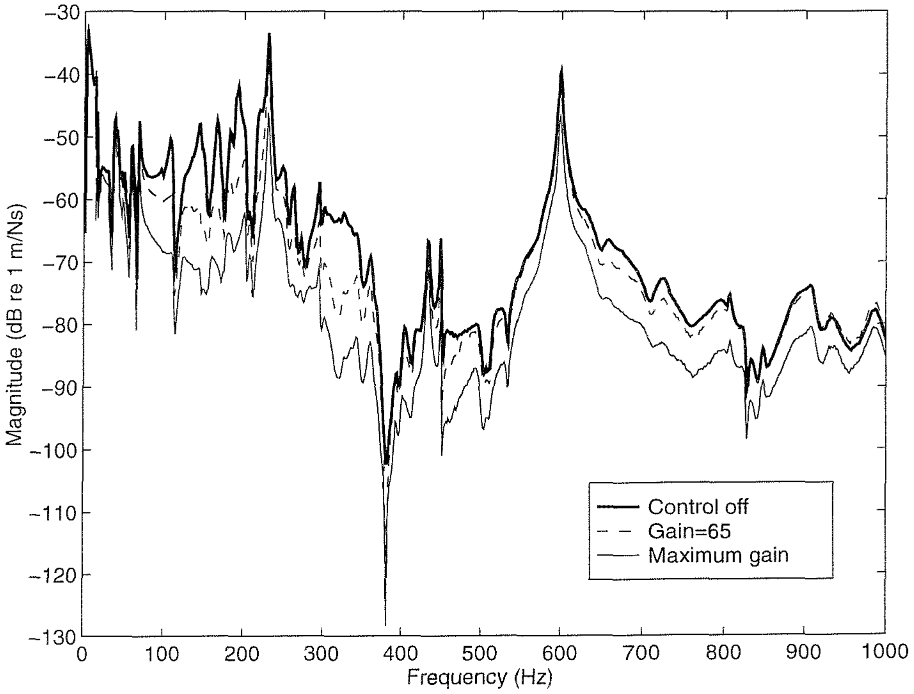

Figure 6.19. Measured velocity at point 3 per unit primary force for experimental control at point 3.

Looking at Figure 6.20, the control isolation efficiency appears to stop at 1500 Hz. Above this frequency, the controller with the maximum gain generates large vibration amplification in the band [2 kHz - 4 kHz].

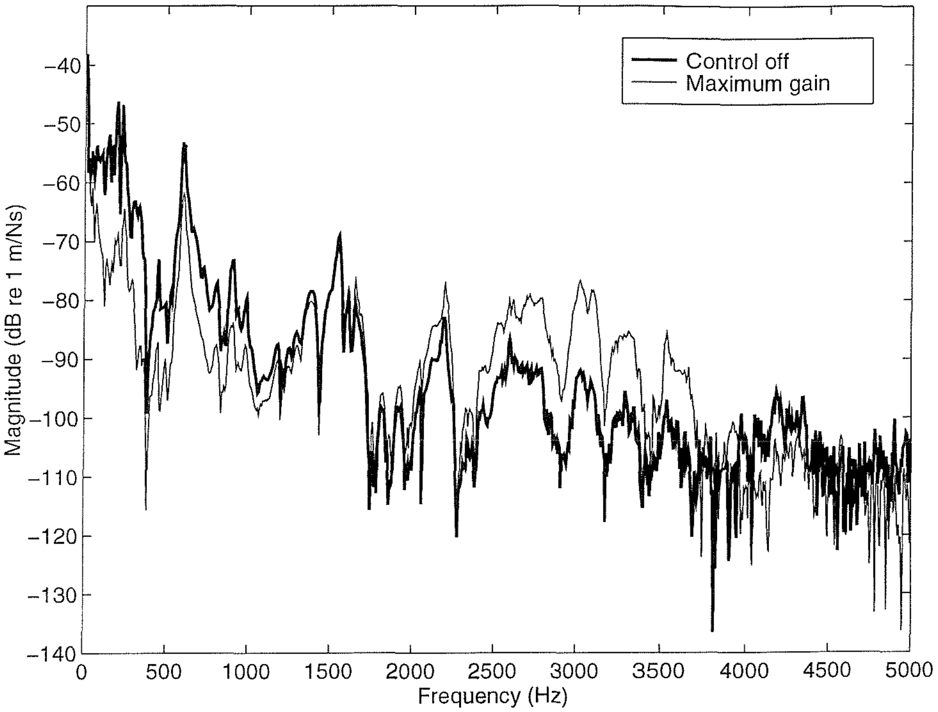

Figure 6.20. Measured velocity at point 3 per unit primary force for experimental control at point 3 over the range [0-5 kHz].

It is difficult to make any conclusion on the nature of the instability experienced as it does not clearly come out of the two plots in Figures 6.19 and 6.20. The plant response was found to be very sensitive to the position of the accelerometer, which could thus significantly modify the value of the maximum control gain tolerated by the system. The gain could, moreover, only be increased by steps, so that the sign of instability could be missed. Finally, it is difficult to draw any interpretation of the system response at low frequencies, below 20 Hz, where the local vibration level first appears unchanged by the control as the plant response magnitude is very low at these frequencies. A small 1 dB increase is observed at 16.5 Hz. The poor coherence at these frequencies may hide some important information on the system stability.

Figures 6.21 and 6.22 show the effect of the control at point 2 and 3 up to 1 kHz for the maximum value of control gain, 240. As already observed in chapters 4 and 5, the control seems only to have a local effect, and even if the level is reduced somewhat in the range [100 Hz - 400 Hz] at point 2 and 3, the passive responses are not significantly modified under the action of the controller. 5 dB attenuation is obtained at 230 Hz at point 1 and 2 dB at point 2. No real amplification which could give information on the onset of instability can be observed on these two plots.

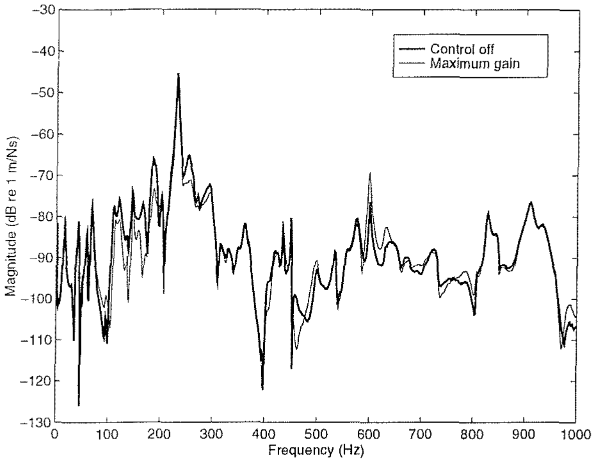

Figure 6.21. Measured velocity at point 1 per unit primary force for experimental control at point 3.

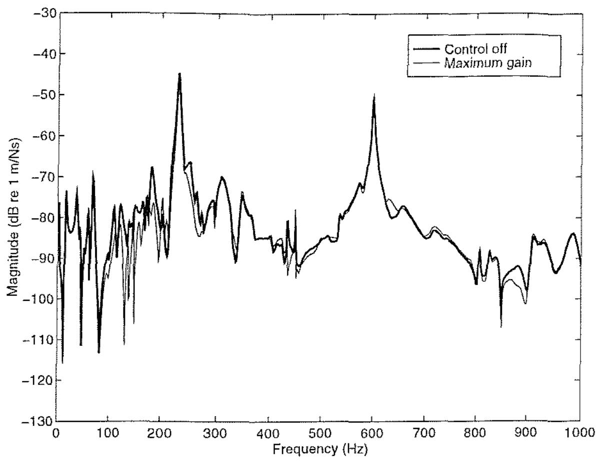

Figure 6.22. Measured velocity at point 2 per unit primary force for experimental control at point 3.

The plot of the energy estimate in Figure 6.23 provides useful information on the control effect on the whole equipment panel. The attenuation appears to be relatively small, as noticed at point 1 and 2. Although attenuation is observed in the range [100 Hz - 300 Hz] and a 3 dB attenuation is seen at 230 Hz, it does not seem to have a large effect on the global system vibration. Again, the equipment panel dynamics under control seem to be unchanged at very low frequencies but the poor quality of the measurement limits the observation. Any small amplification of the low frequency composite panel vibration could generate a large global amplification of the system response.

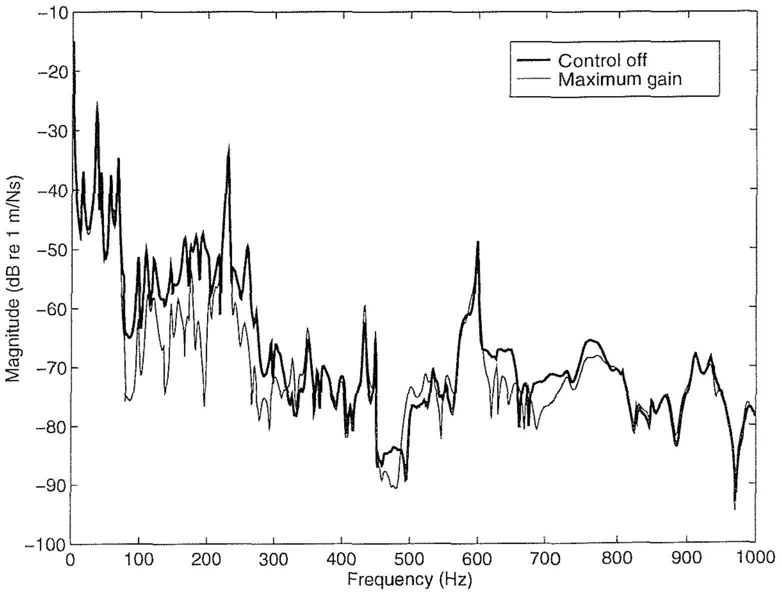

Figure 6.23. Estimate of the kinetic energy obtained from measurements for experimental control at point 3.

The control provides large vibration reduction at the control location even if it is significantly gain limited. The amplification observed at higher frequencies do not appear to debase this isolation improvement too much. However, instability was experienced so that even if it has not been identified by the measurement, the optimistic conclusions on the control efficiency at the control point must be balanced. Single-channel DVFB control appears, once again, to generate only a local isolation effect.

### *Single-channel control implementation at point 1*

Figure 6.24 shows the control result at point 1 for two values of control gain: the maximum gain value implemented experimentally, 348 and an intermediate value of 94. As for a control at point 3, large reduction are obtained over the range displayed and especially in the band [100 Hz - 400 Hz] of amplification effect of the passive isolators where the level goes down by 10 to more than 20 dB for the use of the maximum gain. 18 dB reduction is achieved at the 230 Hz peak. As the frequency increases, the reductions are less significant. The controller starts to generate amplification around 2000 Hz as shown in Figure 6.25 and as predicted from the plant response analysis, but no clear sign of instability appears on the plot even though it was experienced. A 5 dB amplification occurs at very low frequencies, around 4 Hz but, once again, any interpretation is difficult in this frequency region.

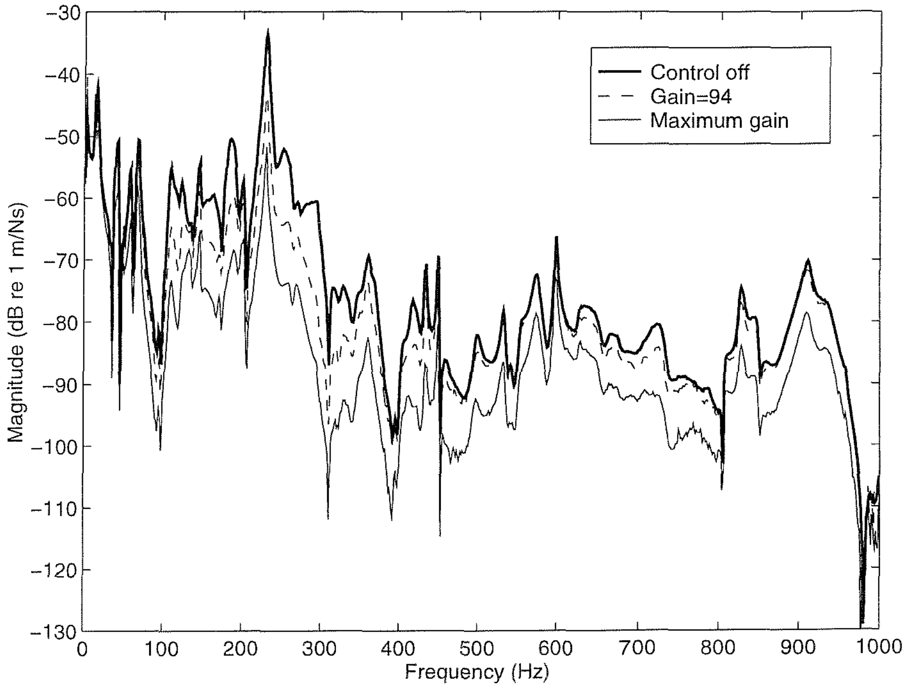

Figure 6.24. Measured velocity at point 1 per unit primary force for experimental control at point 1.

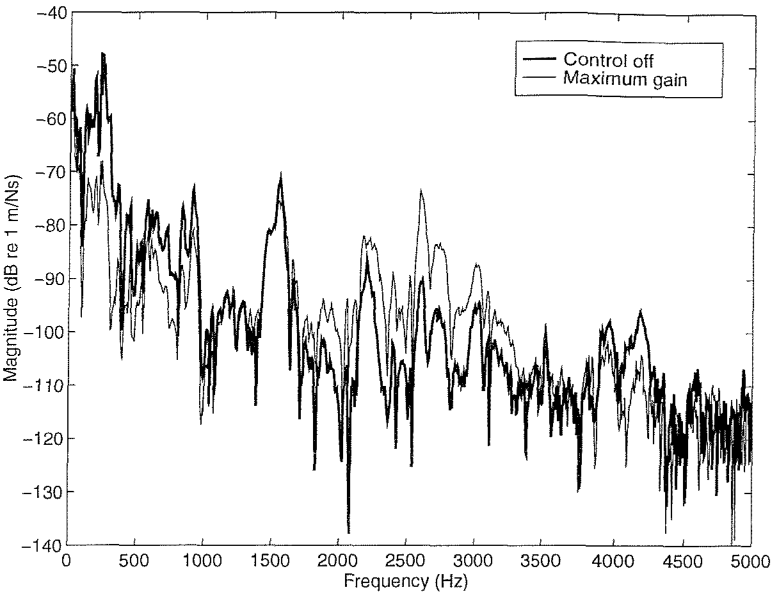

Figure 6.25. Measured velocity at point 1 per unit primary force for experimental control at point 1 over the range [0-5 kHz].

The control does not seem to affect the vibration level at the two other mount junctions where the level is either weakly reduced or weakly amplified along the band [0-1 kHz] as shown in Figures 6.26 and 6.27. The control effect is slightly more obvious at point 2 with a 5 dB reduction at 230 Hz for a 2 dB reduction at point 3. Point 2 being closer from point 1 than point 3, this can be explained by the local effect of the control. The increase noticed at the control point at very low frequencies is not observed in Figures 6.27 and 6.28 so that it is unlikely to be associated with a stability issue, which may be introduced around 2600 Hz. This would suggest that the instability really occurs at high frequencies which is consistent with the fact that the experimental gain value is close to the one estimated in the analysis of the plant response. Moreover, the simulation in chapter 5 did not identified any stability limitation at very low frequencies for a single-channel control at point 1.

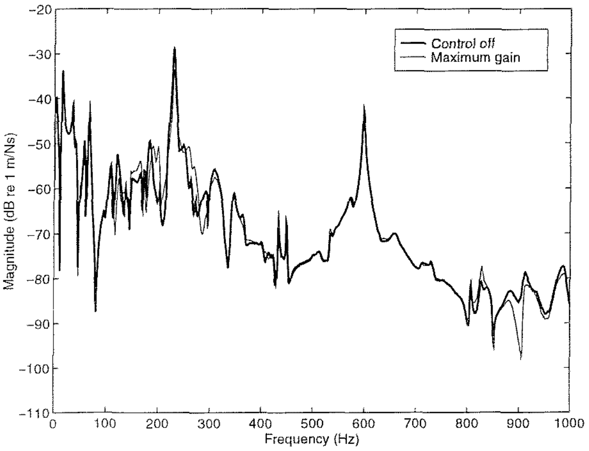

Figure 6.26. Measured velocity at point 2 per unit primary force for experimental control at point 1.

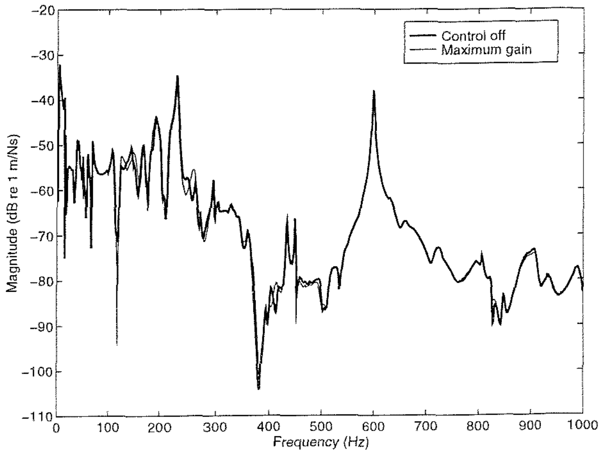

Figure 6.27. Measured velocity at point 3 per unit primary force for experimental control at point 1.

### *Single-channel control implementation at point 2*

Figure 6.28 shows the control result at point 2 for two values of control gain: the maximum gain value implemented experimentally, 225 and an intermediate value of 45.

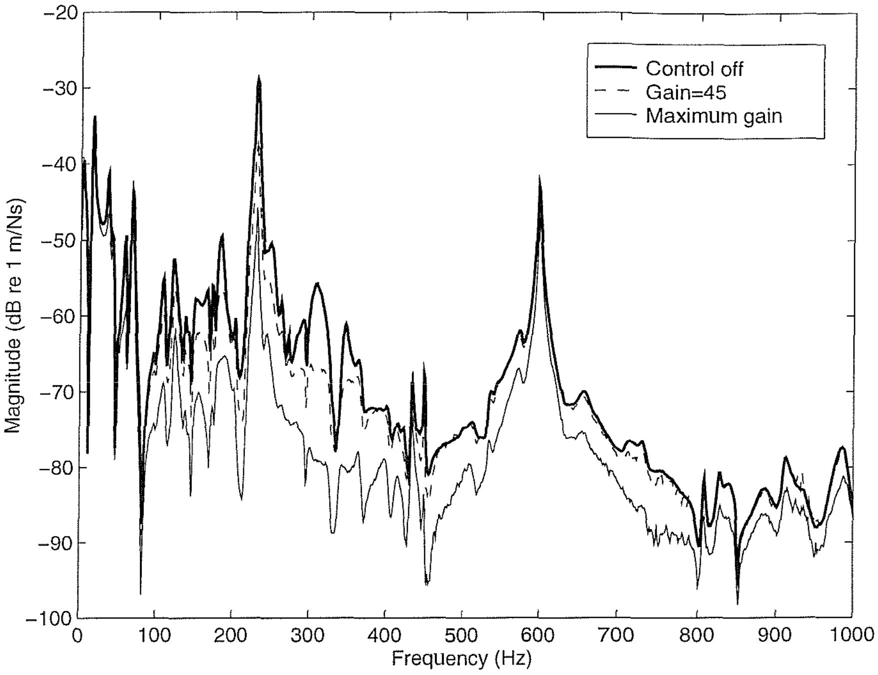

Figure 6.28. Measured velocity at point 2 per unit primary force for experimental control at point 2.

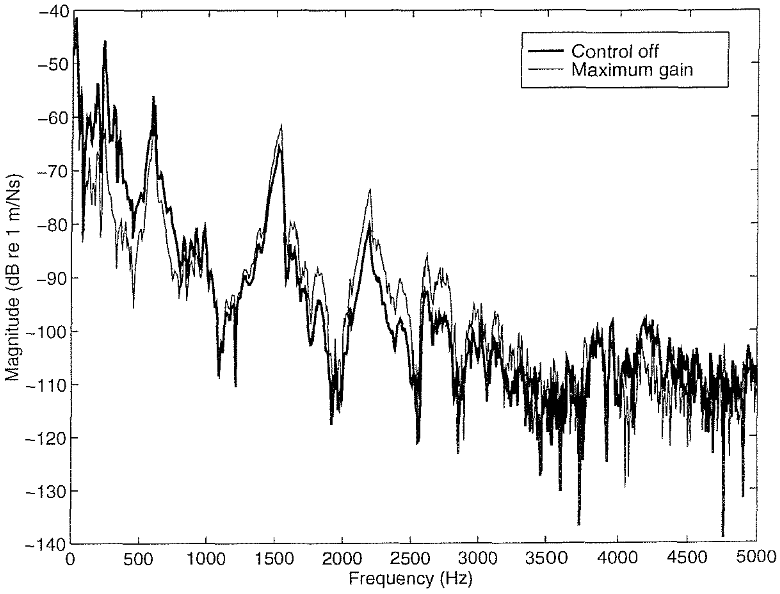

Figure 6.29. Measured velocity at point 2 per unit primary force for experimental control at point 2 over the range [0-5 kHz].

Similarly at the two other control implementations, large reduction is achieved at the control point in the range [0-1 kHz]. The level is reduced by up to 17 dB at 230 Hz and by up to 25 dB around 300 Hz. A small amplification is noticed at 37.5 Hz which was partly anticipated by the analysis of the plant response. The plate is also subject to vibration amplification at higher frequencies in the band [1 kHz - 3 kHz] as seen in Figure 6.29 but the amplitude of the increase does not suggest high frequency instability. The low frequency domain is here more likely to be the reason of the instability encountered in the experimental implementation of the control. This would bear out the conclusion drawn in the interpretations of the simulated results.

It appears from Figure 6.30 that a control at point 2 leads to significant change in the response at point 1. This agrees with the characteristics of local efficiency of a single channel DVFB control as point 1 is located only 190 mm away from point 2. Vibration reduction is thus observed between 200 Hz and 300 Hz with a 8 dB improvement at 230 Hz. A small but sharp amplification is noticed at 67.5 Hz at point 1, but also at point 3, as well as other very small amplifications at low frequencies which are difficult to interpret but may imply a low frequency limitation of the control. This would be reasonable as the maximum experimental feedback gain is significantly lower than the one estimated from the plant response analysis. As for the two other single-channel control systems, if any higher gains than the ones applied were used, the fuses in the control shaker quickly blew.

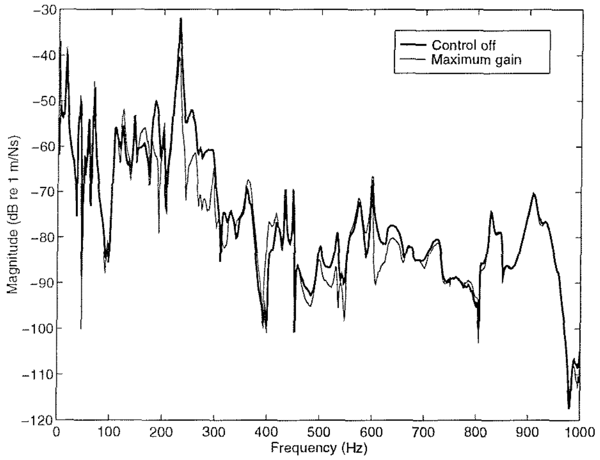

Figure 6.30. Measured velocity at point 2 per unit primary force for experimental control at point 1.

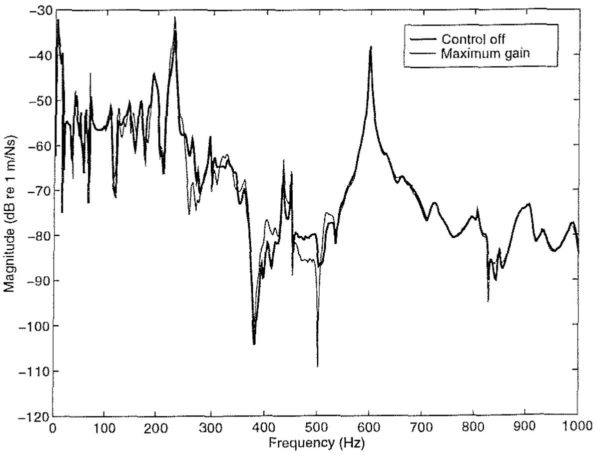

Figure 6.31. Measured velocity at point 3 per unit primary force for experimental control at point 1.

*Conclusions*

The three different control implementations exhibited very similar characteristics providing relatively strong attenuation in the frequency range of interest [0-1 kHz] balanced by the onset of instability. The instability has not been clearly identified but seems to be caused by the high frequency behaviour of the system at point 1 and by the low frequency behaviour of the system at 2 and 3, as suggested by the simulations. Appropriate low frequency or high frequency filtering could therefore, in principle, increase the stability and thus the local efficiency of the controllers. The reduction that can be obtained by single channel DVFB seems to give some benefit in the region near the control point. This local efficiency of DVFB control has already been outlined in the simulations presented in chapter 6.

## 6.5. Experimental implementation of multichannel control

### 6.5.1. Plant response and stability analysis

The three control loops are closed to implement a three-channel decentralised control. Using equal gains, the control stability is investigated by applying the Nyquist method to the frequency dependent eigenvalues of the measured plant response matrix **G**. Figures 6.32, 6.33 and 6.34 display the magnitude and phase and the associated Nyquist plot of each of the eigenvalues up to a 5 kHz with the high cut-off frequency of the charge amplifier set to 3 kHz. They look very similar to each others and also very similar to the plant responses for single-channel control, especially at high frequencies since, above 1 kHz, the cross terms of **G** are very small compared to the diagonal terms. It appears from these three figures that the control will be quite efficient in the frequency range of interest ([0-1 kHz]) but once more limited by the resonance at 4500 Hz, even though it is attenuated by the low-pass filter of the charge amplifier.

Concentrating the analysis in the range [0-1 kHz], the first eigenvalue $\lambda_1$ in Figure 6.35 shows a rather strong peak at 67.5 Hz associated with a sharp increase of the phase, already noticed in the single channel control analysis. This is represented on the Nyquist plot by a small loop which is truncated by the insufficient frequency resolution and should be slightly larger than it appears. This seems to set the real limit to the control gain to an approximate value of 150/200. The response of the system at 7 Hz and at very low frequencies may also cause some amplifications. This was mentioned in the simulations but did not give rise to any significant amplification. The measurement coherence at these frequencies again prevents any accurate analysis.

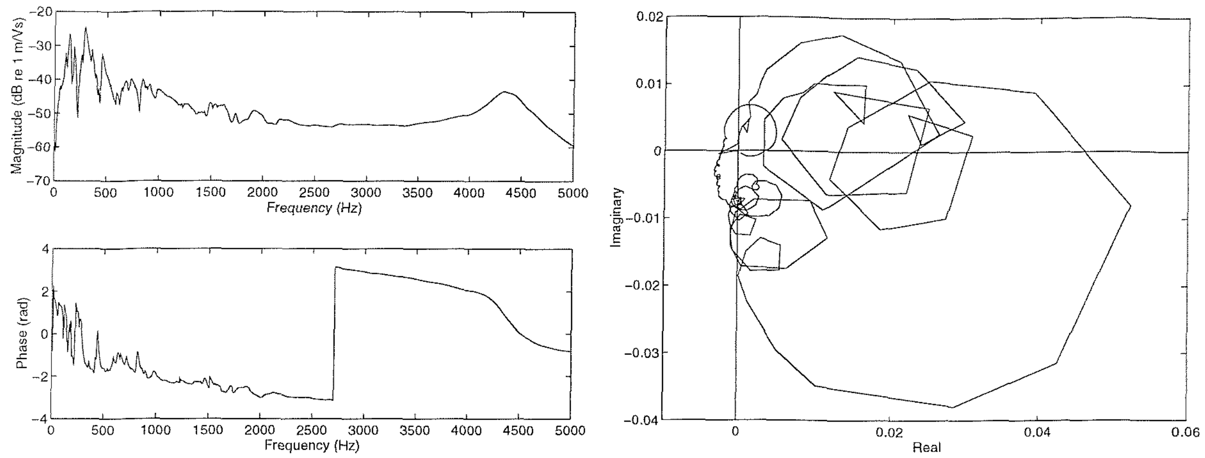

(a) (b)

Figure 6.32. Magnitude and phase responses (a) and Nyquist plot (b) of the first eigenvalue $\lambda_1$ for a charge amplifier cut-off frequency set to 3 kHz estimated from the measured plant response.

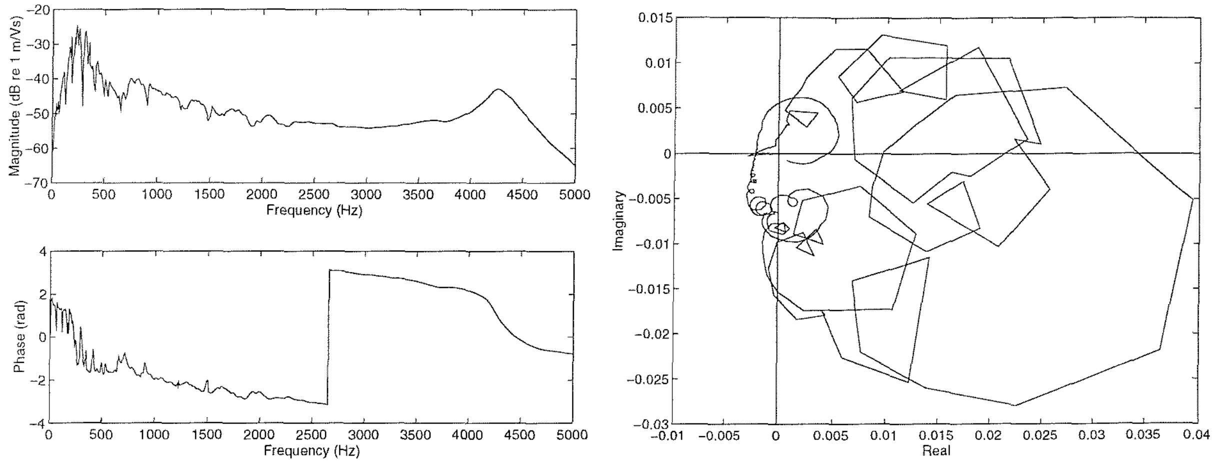

(a) (b)

Figure 6.33. Magnitude and phase responses (a) and Nyquist plot (b) of the second eigenvalue $\lambda_2$ for a charge amplifier cut-off frequency set to 3 kHz estimated from the measured plant response.

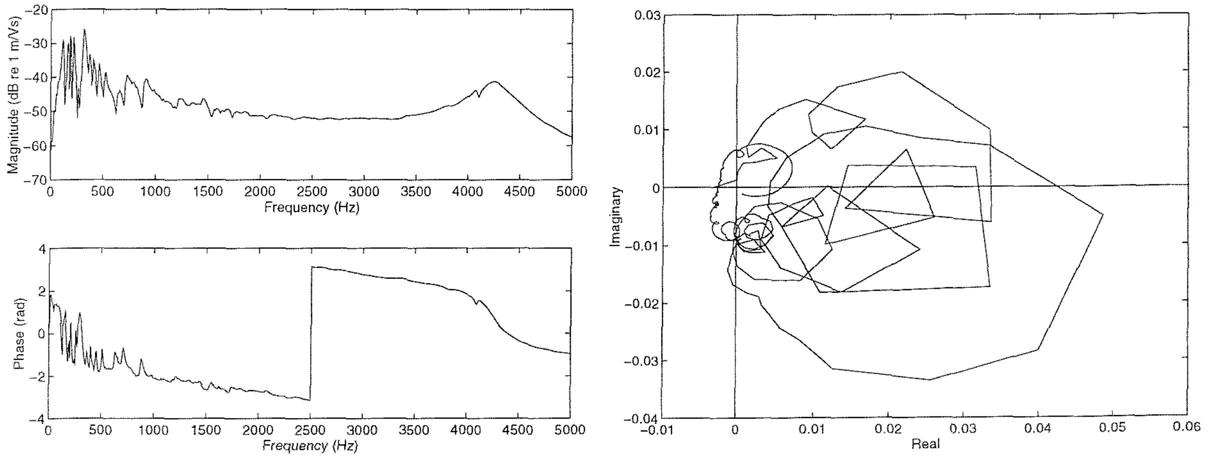

(a) (b)

Figure 6.34. Magnitude and phase responses (a) and Nyquist plot (b) of the third eigenvalue $\lambda_3$ for a charge amplifier cut-off frequency set to 3 kHz estimated from the measured plant response.

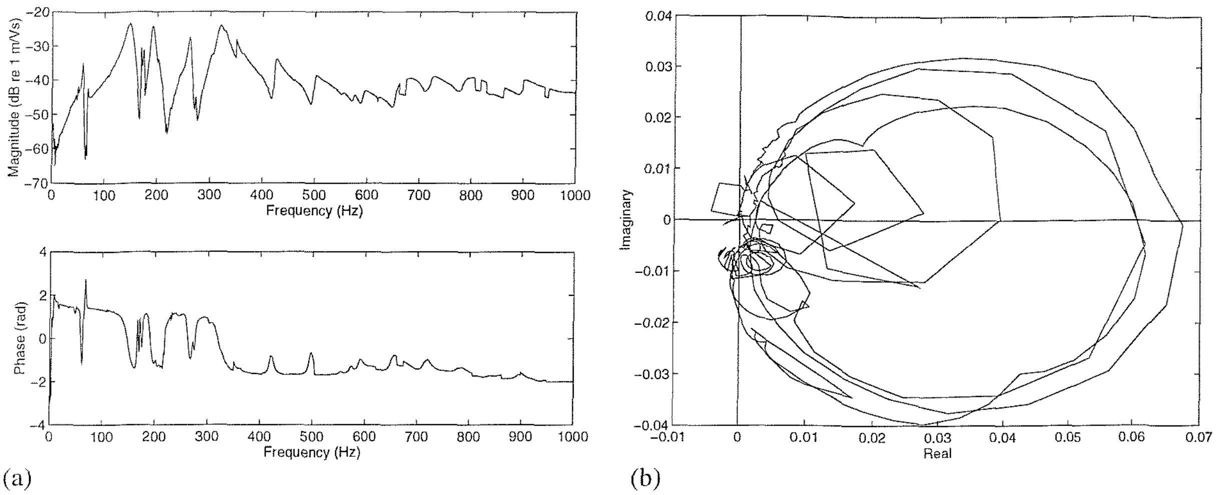

(a) (b)

Figure 6.35. Magnitude and phase responses (a) and Nyquist plot (b) of the first eigenvalue $\lambda_1$ up to 1 kHz for a charge amplifier cut-off frequency set to 3 kHz estimated from the measured plant response.

### 6.5.2. Multichannel control performance

The local performance of the multichannel control system is presented at points 1, 2 and 3, up to 1 kHz for the maximum experimental gain value implemented, 127 and an intermediate gain value equal to 93 by comparison with the associated passive responses in Figures 6.36, 6.37 and 6.38 respectively.

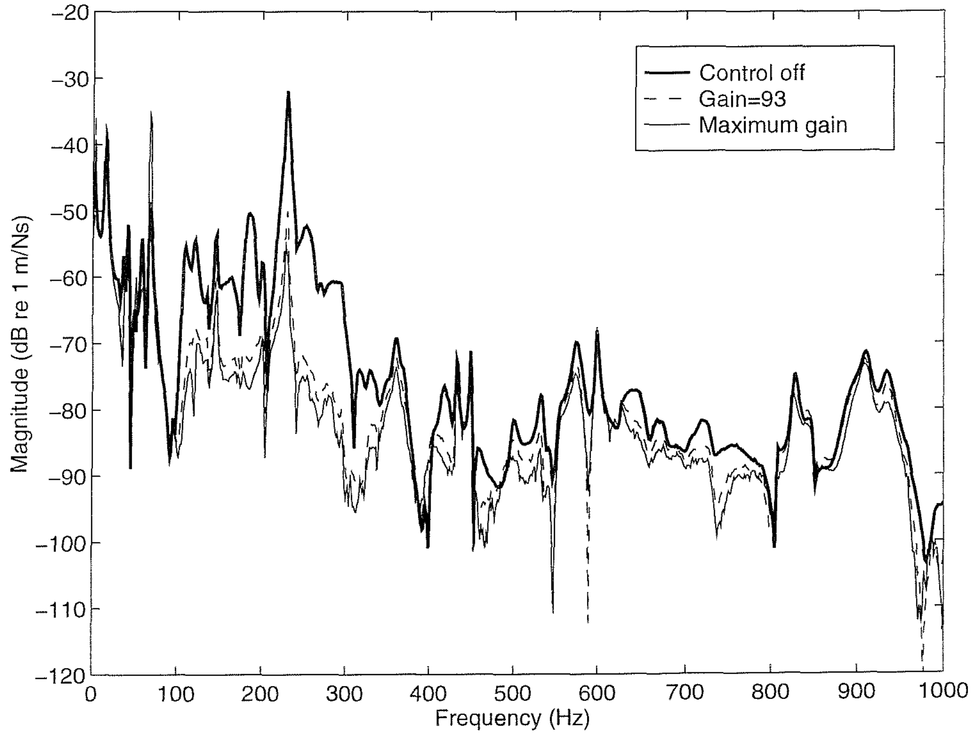

Figure 6.36. Measured velocity at point 1 per unit primary force for experimental multichannel control.

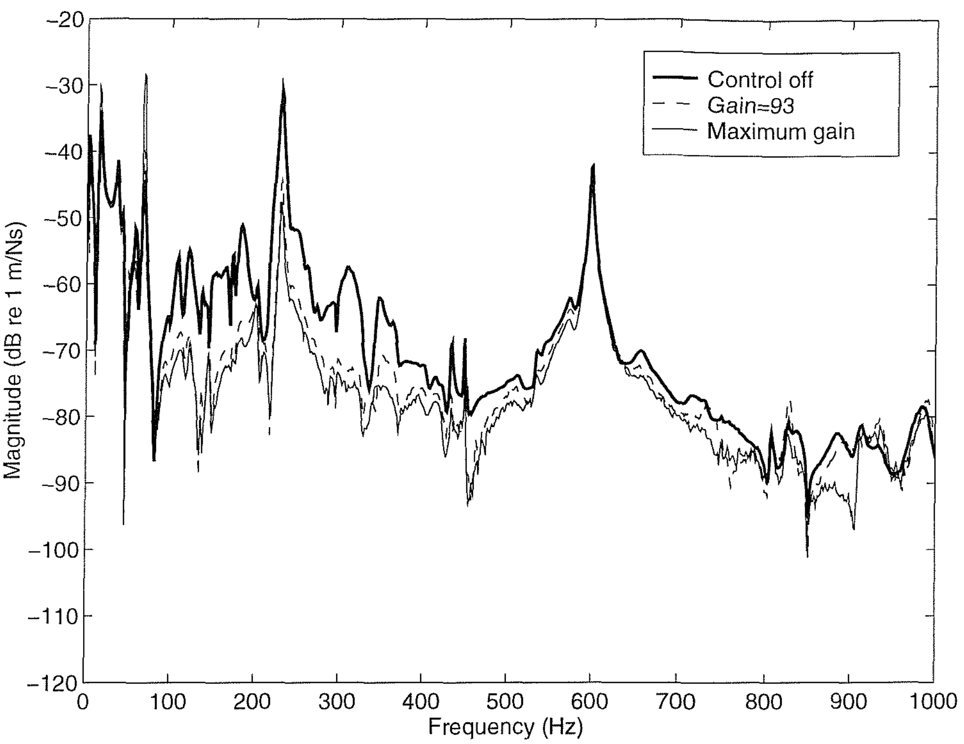

Figure 6.37. Measured velocity at point 2 per unit primary force for experimental multichannel control.

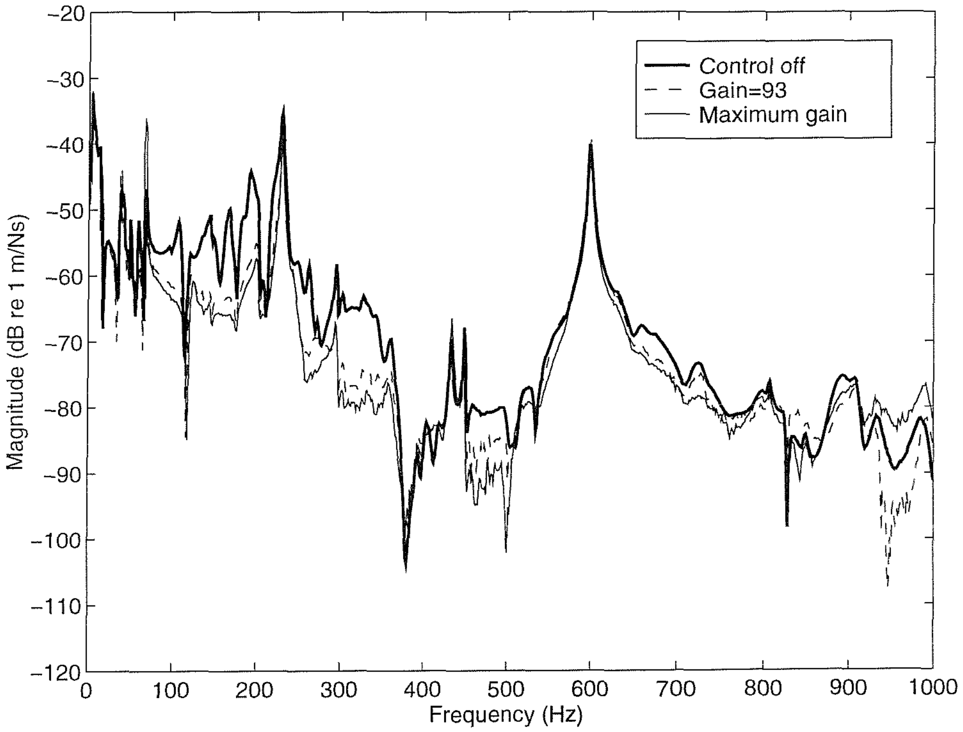

Figure 6.38. Measured velocity at point 3 per unit primary force for multichannel control.

[0-1 kHz] is clearly the range of control efficiency which decreases gradually up to 1 kHz where no more real attenuation is observed. The control provides large local reduction in the band [100 Hz -

400 Hz] as noticed for the experimental implementation of single-channel control systems and in the simulations. The onset of instability is here very clear at 67.5 Hz. The peak at 230 Hz is reduced by up to 25 dB at point 1, 12 dB at point 2 but only 3 dB at point 3. Attenuation in the band [100 Hz - 400 Hz] goes roughly from 5 dB to 15 dB at each point and up to 20 dB at point 1, which shows the greater vibration reduction as already noticed in the simulation. This can be explained by the proximity of point 2, so that two local isolation effects are generated in the vicinity of point 1 and 2. It is also explained by the fact that the amplification due to the passive isolation in [100 Hz - 400 Hz] is very large at point 1, as mentioned in the passive analysis of the system. The control does not have much effect at low frequencies. It generates some small amplifications or reductions without incidence on the system vibration except at point 1 where a 8 dB amplification is noticed at 3 Hz for a gain equal to 93. It does not give any sign of instability but may affect the system response as the passive dynamics of the equipment panel is already quite large at low frequencies.

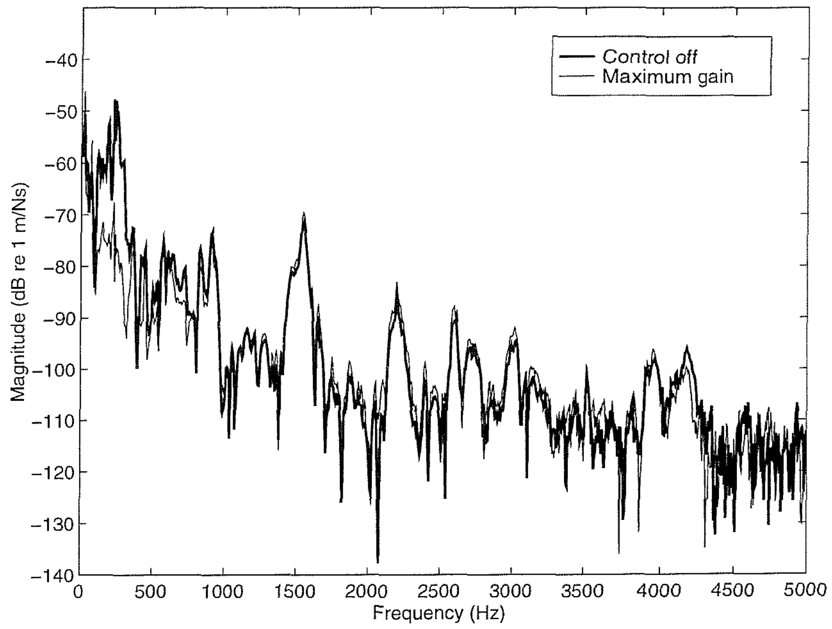

Figure 6.39. Measured velocity at point 1 per unit primary force for experimental multichannel control.

Figure 6.39 displays the control results at point 1 up to 5 kHz. No extra control benefit is recovered above 1 kHz but the response is slightly amplified in the range [2 kHz - 4 kHz], but the amplitude of the amplification is now very small compared with the one encountered for the implementation of single-channel controllers. This bears out the conclusion that the multichannel control is not limited by the high frequency response of the system. These amplifications have no effect on the response at point 1, as the passive isolation keeps them to a small level. A similar response is observed at points 2 and 3 so that the high frequency range above 1 kHz does not have to be considered in any interpretation of the multichannel control efficiency.

Figure 6.40 shows the spectrum of the kinetic energy estimate calculated using the system responses at the five measurement points presented in Table 5.6.

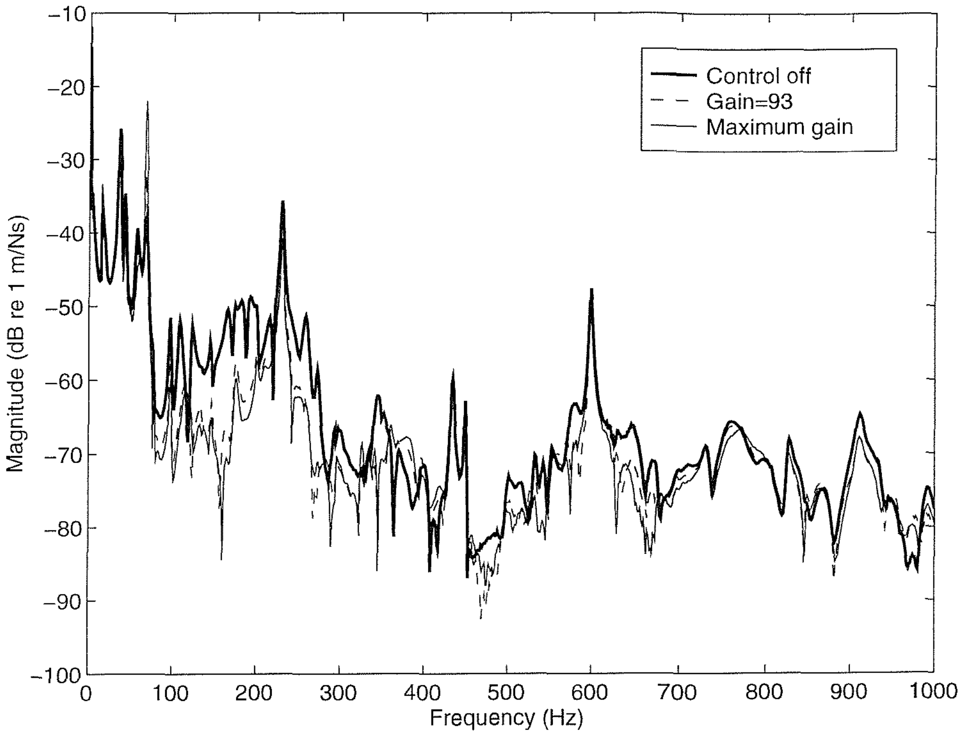

Figure 6.40. Estimate of the kinetic energy obtained from measurements for multichannel control.

It shows that the control has a global isolation effect in the frequency range [80 Hz - 350 Hz] where attenuations of up to 15 dB are observed. The level at 230 Hz goes down by only 6 dB for both control gains as this peak is due to a base structure resonance and not only to an amplification effect of the passive isolation. The same observation can be made at 430 Hz or 600 Hz where the composite panel motion is dictated by the base plate resonances. No more real improvement is recovered above 500 Hz. The onset of instability which is spread to the whole system is clear at 67.5 Hz. The attenuation of the energy estimate seems however to be slightly smaller than the improvement recovered at the control points. Above a certain frequency limit, as the independent control loops do not appear to be able to destabilise each other, global control can be achieved by positioning several local control loops, whose local effect can spread to a certain extend over the whole equipment panel. It is, moreover, sensible to apply such a control strategy at the sources of disturbance, here at the mount junctions.

## 6.6. Summary of the local performance of the experimental control systems

As already performed in chapter 4 for the inertial implementation of DVFB control, the reductions generated by a reactive implementation of DVFB have been estimated control in term of the attenuation of the local vibration kinetic energy in the frequency range [100 Hz - 1 kHz]. This was calculated at the three mount junctions on the composite panel according to equation (4.20), for the three different single-channel control systems and for the equal gain decentralised multichannel control system, considering, for each control, the largest experimental feedback gain applied. The percentages of local attenuation are listed in Table 6.1, which provides a summary of the effects of each control systems at the three different mount junctions.

| Vibration attenuation | Control at 1 | Control at 2 | Control at 3 | Multichannel control |
|---|---|---|---|---|
| at point 1 | 98.7% | 75.5% | 56.5% | 99.1% |
| at point 2 | 62.6% | 96.5% | 30.4% | 93.5% |
| at point 3 | 12.0% | -59.2% | 92.5% | 72.8% |

Table 6.1. Percentage of vibration kinetic energy attenuation at the mount junctions on the composite panel in the band [100 Hz - 1 kHz] for the different control systems implemented experimentally.

For a single-channel control, the diagonal terms in Table 6.1 are dominant as the result of the local efficiency of the strategy of DVFB control. They show very large local attenuations. The cross-terms are rather significant, as a good isolation effect from one single-channel control can be recovered at the other mount junctions. This is not clear from the different velocity response spectra discussed. These attenuations are largely due to the reduction of the 230 Hz peak which dominates the response of the composite panel in the band [100 Hz - 1 kHz] and whose small reduction at the three mount junctions is the only significant global effect of single-channel control systems as noticed in the analysis of the different plots. This reduction effect is particularly large at point 2 for a control at point 1 and reciprocally, at point 1 for a control at point 2, which highlights again the local effect of DVFB control. The rather small amplification of the 230 Hz peak at point 3 for a control at point 2 generates a global amplification of the vibration at point 3 as noticed by the negative value quoted in Table 6.1.

The implementation of a multichannel control generates very large vibration reduction at the three mount junctions in the range [100 Hz - 1 kHz]. As for the single-channel control systems, point 3 exhibits the smallest control performance since the response at point 3 on the equipment panel is particularly dictated by the motion of the base structure, especially by the two base resonances at 230 Hz and 600 Hz. Point 3 is also rather distant from the two other control locations.

According to Table 6.1, a reactive implementation of DVFB control offers larger vibration attenuation of the response of the composite panel at the three mount junctions than the inertial implementation discussed in chapter 4 (Tables 4.3 and 4.4).. It would, however be impossible to use these attenuations in practice because of the amplifications at low frequencies.

# Chapter 7

# Conclusions

## 7.1. Conclusions

The work presented in this thesis has investigated the real potential of the strategy of Direct Velocity Feedback control in enhancing the performance of passive isolations. This study was motivated by the simplicity offered by such a control strategy, which had demonstrated very strong broad band isolation effect on the control of rigid body modes of suspended systems [14-16].Other feedback strategies for broad-band control, such as internal model control, require much more complicated controllers, whose design involves system identifications and signal processing techniques. In order to carry out a clear and strict assessment of the potentials of DVFB control, the analysis was focused only on the dynamics of the different systems, without considering any signal processing treatment which could have been easily coupled to the control loops. The different controls implemented were thus kept as simple as possible without any low frequency filtering process which could have increased the stability of the control system. Similarly, in order to retain control simplicity, multichannel control was implemented using decentralised controllers with identical feedback gain in each channel. DVFB control has thus been tested through both simulations and experiments to assess:

- The conditions under which skyhook damping effect could be obtained.

- The effect of local skyhook damping on the global dynamics of the equipment.

This was performed for both rigid and flexible mounted equipments.

### DVFB applied to rigid pieces of equipment

The implementation of DVFB control on a mass mounted on a single mount allowed us first to concentrate on the types of actuation available in practise to implement the control: an inertial actuation where the secondary force reacts against a suspended extra mass and a reactive actuation where the secondary force reacts against the vibrating base. The inertial control was shown to be strongly limited in term of control gain because of the low frequency dynamics of the actuator that can not provide a reliable secondary effort. However, above the actuator resonance frequency, an inertial device can implement perfect skyhook damping. The interest in DVFB, however, is generally to act at low frequencies to supplement the bad characteristics of passive isolators.

Unlike inertial control, a reactive control provides a plant response which is very dependent on the dynamics of the system under control, as derived in equation (3.13). For a single-mount system and a rigid equipment structure, a reactive control is, however, unconditionally stable and generates very strong local vibration reduction regardless of the base dynamics. In the case of a rigid equipment, the local effect of the control can easily give global control of the suspended equipment vibration. It thus appears to be a very promising practical control implementation for the reduction of the rigid body modes of mounted equipment, even if attention should be paid in case of multi-mount isolation system if the base structure presents large dynamics.

### DVFB applied to flexible equipment

Generalised to the multi-mount system for the isolation of flexible equipment, the experimental implementation of an inertial control showed the same characteristics of instability as the single-mount system for isolation of a rigid structure, since the stability of the control is not dependent on the mechanics of the system involved but on the actuator dynamics. This presents, however, the interesting features of a control system which is almost fully predictable from the analysis of the actuator dynamic.

Much larger attenuation was obtained using a reactive control of the flexible equipment plate. The rotational excitation from the mount did not appear to have a large effect on the out-of-plane response of the composite plate so that an axial control force was sufficient to have a good control authority on the system. However, unlike for the implementation on a rigid equipment mounted on a single mount, it was possible for the control system to become unstable at low frequencies and the feedback gain was significantly limited. These low frequency instabilities are generated by two different phenomena. The first can occur in a specific configuration where the equipment behave as a stiffness and the base as a mass. Then the base does not offer a safe ground for the secondary force to react off. This direct effect of the bottom component of the reactive secondary force is discussed in chapter 5 and decreases with frequency. The second reason for low frequency instability is the multiple transmission paths created by an isolation system made of several mounts. The excitation of the base generated by one reactive secondary force can propagate through another mount back to the control sensor, creating a mechanical feedback that may be able to destabilise the system. This threat also gradually disappears with frequency as the structural wavelengths in the equipment and base structures get smaller so that the bottom component of the reactive force becomes negligible compared to the collocated one. It thus appears that, like inertial control, a reactive implementation of DVFB tend to implement, in principle, perfect skyhook damping at high frequencies. For both types of actuation the control encounters mechanical limitations at low frequencies but provides a very healthy plant to control as the frequency increases.

The other threats to the control stability come from the sensor and the actuator. The actuator sets a high frequency limitation to the control efficiency since it is not to able to generate a force perfectly in phase with the input voltage as the frequency increases. The sensor sets a very low frequency limitation since velocity is a quantity which is difficult to monitor at low frequencies, and this gives rise to phase shifts in the integrators used with the practical accelerometers.

### Global isolation effect of local DVFB control

Both the simulations and the experiments showed that the vibration reduction obtained from the implementation of a control loop at a mount junction had a large local attenuation effect above 100 Hz. Small corresponding attenuation could be observed in the input power and also in the energy estimate but to a much smaller extent than at the control points. The multichannel reactive control offered, however, significant global vibration isolation as the result of the addition of the different local benefits provided by each channel. This was also largely achieved by the fact that the control was operating at the mount junction, which were the sources of the disturbance to the equipment panel. This suggests that, providing the independent control loops do not significantly destabilise each others, global control can be obtained from a proper distribution of several control loops over the mounted equipment structure. A reactive implementation of the control is, however, mainly restricted to the location of the mounts, but an inertial controller can be positioned anywhere on the suspended structure to generate local control.

## 7.2. Further work

The maximum feedback gain of the control loops were reduced by the operation of integration and amplification of the accelerometer signal. The stability limitations were shown to be concentrated at low frequencies, well below the range of maximum vibration amplification caused by the passive isolation, for both reactive and inertial implementations. There is therefore a good framework for

further work, consisting in analysing the improvements achievable by operating appropriate signal processing to the original control loops.
Referring to the need of low frequency isolation, an inertial control does not seem to be appropriate to supplement the performance of a passive isolation. It is, however, very easy to implement on any system, regardless of the dynamics of the system to control which makes it very attractive in practice. The use of inertial DVFB control is therefore to be sought for high frequency problems. This would require to design proper compensators in order to modify the low frequency response of the actuator. Such a filtering process could increase very significantly the gain margin of the control and thus the performance of inertial DVFB control.

As far as the reactive control is concerned, modification could be carried out on the test rig to perform extra sets of measurements.

- Lighter reactive actuators, more appropriate to the system under control, should be designed. The control actuators used experimentally had a too large effect on the global system dynamics.

- The composite panel could be replaced by an aluminium plate to test the different controllers on an uniform and isotropic system.

- Acoustic measurement could also be performed to determine the influence of the control on the sound radiation.

# References

[1] Van Santen, G.W. (1958). *Mechanical vibration.* Cleaver-Hume Press, London.

[2] Tong, K.N. (1960). *Theory of Mechanical Vibration.* John Wiley and Sons, New York.

[3] Tse, F.S., Morse, I.E. and Hinkle, R.T. (1963). *Mechanical Vibrations.* Prentice-Hall, London.

[4] Thomson, W.T. (1973). *Theory of Vibration (with applications).* Prentice-Hall, New Jersey.

[5] White, R.G. and Walker, J.G. (1982). *Noise and Vibration.* Ellis Horswood, Chichester.

[6] Lalanne, M., Berthier, P. and Der Hagopian, J. (1983). *Mechanical Vibrations for Engineers.* John Wiley and Sons, Chichester.

[7] Bies, D.A. and Hansen, C. H. (1988). *Engineering Noise Control.* Unwin Hyman, London.

[8] Fuller, C.R., Elliott S.J. and Nelson, P.A. (1996). *Active Control of Vibration.* Academic Press, London.

[9] Collins, S.A. and von Flotow, A.H. (1991). Active vibration isolation for spacecraft. Paper No.IAF-91-289, presented at *the 42nd Congress of the International Astronautical Federation*, Montreal, Canada.

[10] Nelson, P.A. and Elliott, S.J. (1992). *Active Control of Sound.* Academic Press, London.

[11] Jenkins, M.D., Nelson, P.A., Pinnington, R.J. and Elliott, S.J. (1993). Active isolation of periodic machinery vibrations. *Journal of Sound and Vibration*, **166**(1), 117-140.

[12] Gardonio, P. and S. J, Elliott and Pinnington R. J., 1997. Isolation of structural vibration on a multiple-degree-of-freedom system, part II: Effectiveness of active control strategies. *Journal of Sound and Vibration*, **207**(1), 95-121.

[13] Karnopp, D., Crosby, M.J. and Harwood, R.A (1974). Vibration control using semi-active force generators. *American Society of Mechanical Engineers Journal of Engineering in Industry*, **96**, 619-626.

[14] Schubert, D.W. (1991). Characteristics of an active vibration isolation system using absolute velocity feedback and force actuation. Proceedings of *the Conference on Recent Advances in Active Control of Sound and Vibration*, Blacksburg, Virginia. Technomic Press, Lancaster, Pennsylvania, 448-463.

[15] Serrand, M. and Elliott, S.J. (2000). Multichannel feedback control for the isolation of base-excited vibration. *Journal of Sound and Vibration*. To be published in July 2000.

[16] Serrand, M. (1998). *Active isolation of base vibration*. MSc Thesis, University of Southampton.

[17] Elliott, S.J. and C. C. Boucher, C.C. (1994). Interaction between multiple feedforward active control systems.*IEEE Transactions on Speech and Audio Processing* **2**, 521-530.

[18] Nayroles, B. (1987). Functional monotony and diagonal control in synchronous vibration absorption. *Journal de mécanique théorique et appliquée* (special issue) **6** (suppl.), 23-38.

[19] Beard, A.M., von Flotow, A.H. and Schubert, D.W. (1994). A practical product implementation of an active/passive vibration isolation system. *IUTAM Symposium on the active control of vibration*, University of Bath, U.K.

[20] Balas, M.J. 1978 Feedback control of flexible structures. *Institute of Electrical and Electronical Engineers Transactions on Automatic Control*. **AC-23**, 673-679.

[21] Pinnington, R.J. and White, R.G. (1980). Power flow through machine isolators to resonant and non-resonant beams. *Journal of Sound and Vibration* **75**(1), 179-197.

[22] Goyder, H.G.D. and White, R.G. (1980). Vibrational power flow from machines into built-up structures, part I: introduction and approximate analyses of beam and plate-like foundations. *Journal of Sound and Vibration* **68**(1), 59-75.

[23] Pinnington, R.J. (1987). Vibrational power transmission to a seating of a vibration isolated motor. *Journal of Sound and Vibration* **118**(3), 515-530.

[24] Gardonio, P., Elliott, S.J. and Pinnington, R.J. (1997). Isolation of structural vibration on a multiple-degree-of-freedom system, part I: The dynamics of the system. *Journal of Sound and Vibration*, **207**(1), 61-93.

[25] Gardonio, P. and Elliott, S.J. (1999). Active control of structural vibration transmission between two plates connected by a set of active mounts. Proceedings of *the 1999 International Symposium on Active Control of Sound and Vibration*, Fort Lauderdale, FL, USA, **1**, 117-128.

[26] Johnson, M.E. and Elliott, S.J. (1995). Active control of sound radiation using volume velocity cancellation. *Journal of the Acoustical Society of America*, **98**, 2174-86.

[27] Sors, T.C. and Elliott, S.J. (1999). Modelling and feedback control of sound radiation from a vibrating panel. *Journal of Smart Materials and Structures*, **8**, 301-314.

[28] Meirovitch, L. (1990). *Dynamics and Control of Structures*. Wiley, New York.

[29] Franklin, G.F., Powell, J.D. and Emami-Naeini, A. (1994). *Feedback Control of Dynamic Systems*, 3rd edn. Addison Wesley, Reading, Massachusetts.

[30] Skogestad, S. and Postlethwaite, I. (1996). *Multivariable Feedback Control.* Wiley, Chichester.

[31] Balas, M.J. (1979). Direct velocity feedback control of large space structures. *Journal of Guidance and Control* **2**, 252-253.

[32] Elliott S.J., Serrand M. and Gardonio, P. (2000). Feedback stability limits for active isolation systems with reactive and inertial actuators. *Submitted to the Journal of the American Society of Mechanical Engineering.*

[33] Gardonio, P., Elliott, S.J. and Pinnington, R.J. (1996). User manual for the isolating system with two active mounts constructed at the ISVR for the ASPN Project final experiment. *ISVR Technical Memorandum* No. 801.

[34] Warburton, G.B. (1951). The vibration of rectangular plates. Proceedings of *the institute of Mechanical engineering* **168**, 371-381.

[35] Bishop, R.E.D. and Johnson, D.C. (1960). *The Mechanics of Vibration.* University Press, Cambridge.

[36] Fahy, F.J. (1987). *Sound and Structural Vibration: radiation, transmission and response.* Academic Press, London.

[37] Gibson, L.J. and Ashby, M.F. (1988). *Cellular solids - Structure and Properties.* Pergamon Press, Oxford.

[38] Cremer, L., Heckl, M. and Ungar, E.E. (1988). *Stucture-Borne Sound*, 2nd edn. Spriger-Verlag Berlin Heidelberg, New-York.